Surface processes and deformation in orogenic settings: quantification and modeling

Philippe Steer

To cite this version:

Philippe Steer. Surface processes and deformation in orogenic settings: quantification and modeling. Earth Sciences. Université Paris-Sud 11, 2010. English. NNT: . tel-00602341

HAL Id: tel-00602341
https://theses.hal.science/tel-00602341

Submitted on 22 Jun 2011

HAL is a multi-disciplinary open access archive for the deposit and dissemination of scientific research documents, whether they are published or not. The documents may come from teaching and research institutions in France or abroad, or from public or private research centers.

L'archive ouverte pluridisciplinaire **HAL**, est destinée au dépôt et à la diffusion de documents scientifiques de niveau recherche, publiés ou non, émanant des établissements d'enseignement et de recherche français ou étrangers, des laboratoires publics ou privés.

Surface processes and deformation in orogenic settings: quantification and modeling

---

Processus de surface et déformation en contexte orogénique: quantification et modélisation

THÈSE DE DOCTORAT

Présentée par

PHILIPPE STEER

Pour l'obtention du grade de
Docteur de l'Université Paris-Sud 11
Spécialité : Géosciences
École Doctorale MIPEGE - 534
Préparée au Laboratoire Géosciences de l'Université Montpellier 2
et au Laboratoire de Géologie de l'École Normale Supérieure

Soutenue le 25 Novembre 2010
Devant le jury composé de:

M. BRAUN Jean,	Rapporteur
M. CARRETIER Sébastien,	Rapporteur
M. CATTIN Rodolphe,	Directeur de thèse
M. LAVÉ Jérôme,	Co-directeur de thèse
M. TUCKER Gregory,	Examinateur
M. ZEYEN Hermann,	Examinateur

N° attribué par la bibliothèque
⊔⊔⊔⊔⊔⊔⊔⊔⊔⊔⊔⊔⊔

Résumé

Parmi les processus d'érosion, l'incision des rivières est classiquement décrit comme un processus clé contrôlant l'érosion des paysages. L'efficacité de l'incision est principalement influencée par le climat et par l'érodabilité. Ce dernier paramètre ne dépend pas seulement de la nature du substratum rocheux, mais aussi de sa déformation passée qui affecte ses propriétés rhéologiques équivalentes. Les principaux objectifs de cette thèse sont: (1) de mieux contraindre les relations entre propriétés équivalentes et érodabilité, et (2) de quantifier l'influence de l'érosion et de l'érodabilité sur la formation ou la décadence, spatiale et temporelle, de la topographie.

Plusieurs outils numériques sont développés. Un formalisme 1D d'évolution des paysages est proposé, prenant en compte simultanément l'incision des rivières avec une distribution stochastique des débits en eau et l'érosion des versants par glissements de terrain. Un nouvel algorithme de remaillage appelé Surface Lagrangian Remeshing (SLR) est développé. Il permet de prendre en compte l'érosion à long terme dans les codes numériques 2D Lagrangiens basés sur des éléments finis triangulaires.

Ensuite, la possibilité de mesurer in-situ l'érodabilité avec un marteau de Schmidt (R) est évaluée pour: l'orogène actif de Taiwan, les grès diagénétique d'Annot et la zone de faille de St Clement. Les résultats suggèrent un fort contrôle de R par les propriétés équivalentes des roches testées. Un modèle linéaire, basé sur la théorie des milieux équivalents, est appliqué à une zone de faille avec une résolution inégalée (750 mesures, 25 mesures par mètre carré). Le modèle permet de corréler avec succès la densité de fracture et R. Ces résultats démontrent empiriquement que l'élasticité équivalente ainsi que l'érodabilité sont sensibles à la densité et à la nature des fractures.

Enfin j'étudie les conditions d'érosion et de rhéologie qui permettent de reproduire l'évolution des chaînes de montagnes post-orogéniques. Un modèle couplant érosion en surface et soulèvement isostatique régional est compatible avec les observations. Les taux de décroissance topographique et de diminution du rapport de l'élévation de surface sur l'épaisseur de racine crustale sont contrôlés au premier ordre par la géométrie initiale de la chaîne de montagne et par l'efficacité de l'érosion. Ce nouveau modèle met en évidence le contrôle du climat et de l'érodabilité sur la décroissance topographique et de la rhéologie lithosphérique sur la persévérance des racines crustales.

Abstract

Among erosion processes, river incision is classicaly described as a key process controlling erosion of landscapes. Incision efficiency is mainly influenced by climate and erodibility. This latter is not only dependent on the nature of the bedrock, but also on its past deformation, which affects its rheological effective properties, such as fracture density. The main objectives of this thesis are: (1) to better constrain the relationship between effective properties and erodibility, and (2) to quantify the influence of erodibility and erosion on both the temporal and spatial building or decay of the topography.

Several numerical tools are developed. A $1D$ formalism of landscape evolution is introduced, including river incision with stochastic distribution of water discharge and hillslope landsliding. A new remeshing algorithm called Surface Lagrangian Remeshing (SLR) is developed as a complement to remeshing algorithms dealing with internal elements. It allows one to take into account long-term erosion into $2D$ Lagrangian numerical codes based on triangular finite elements.

Then the potentiality of measuring erodibility in-situ using a Schmidt hammer (R) is assessed for the active orogen of Taiwan, the diagenetic Annot sandstones and St Clement fault zone. Results suggest a strong control of R by effective properties. A linear model based on effective medium theory is applied to a fault zone with an unmacthed resolution (750 measures, 25 measures per square meter). The model successfully correlates R to fracture density. These results demonstrate that effective elasticity as well as erodibility are sensitive to the density and type of fractures.

Finally I focus on the erosional and rheological conditions that allows reproducing post-orogenic evolution of mountain belts. A model coupling surface erosion and regional isostatic uplift is consistent with observations. The topographic decay and decrease of the ratio of surface elevation over crustal root thickness is at first order controlled by the initial geometry of the mountain belt and erosion efficiency. This new model highlights the control of climate and erodibility on the topographic decay and of lithospheric rheology on the perseverance of crustal roots.

Contents

II Measuring Rock Erodibility with a Schmidt Hammer 83

Résumé étendu

Notre compréhension de la planète Terre est fortement limitée par l'échelle temporelle d'observation humaine. Par exemple, considérons un documentaire d'1h30 décrivant l'histoire de la Terre depuis 4.5 Ga avec 25 images par seconde. L'histoire humaine, soit environ 3000 ans, ne représenterait qu'une seule image du documentaire. Seriez-vous capable de comprendre une film avec une seule image? Cela illustre la difficulté de la tâche à accomplir par les chercheurs en géosciences. Heureusement pour nous, des empreintes de l'état passé de la Terre ont été enregistrées. En particulier la surface de la Terre représente la plus accessible et complète source d'information sur la planète, et ouvre des perspectives vers la compréhension de la Terre, de son évolution et des mécanismes qui la gouvernent. L'exemple le plus spectaculaire et le plus convaincant est probablement le relief des orogènes continentales, qui apparaissent, depuis l'Espace, comme des cicatrices à la surface de la Terre. Ces reliefs, situés aux frontières de plaques tectoniques convergentes, sont le résultat d'interactions complexes entre la déformation tectonique, les processus de surface, comme l'érosion et la sédimentation, et le climat.

Parmi les processus de surface, l'incision des rivières est classiquement décrite comme un processus clé contrôlant l'érosion des paysages. En effet, Les taux d'incision des rivières, dans les vallées, dictent l'activité des processus de versants, en abaissant les niveaux de base locaux. L'efficacité de l'incision est principalement influencée par le climat et par l'érodabilité, qui traduit le contrôle exercé par la lithologie sur les taux d'incision. Ce dernier paramètre ne dépend pas seulement de la nature du substratum rocheux, mais aussi de sa déformation passée qui affecte ses propriétés rhéologiques équivalentes. Les principaux objectifs de cette thèse sont: (1) de développer des outils numériques adaptés à l'étude des interactions tectonique-érosion, (2) de mieux contraindre les relations entre propriétés équivalentes du substratum rocheux et érodabilité, et (3) de quantifier et modéliser l'influence de l'érosion et de l'érodabilité sur la formation ou la décadence, spatiale et temporelle, de la topographie.

Développements d'Outils Numériques pour Étudier l'Érodabilité, l'Érosion et la Déformation

Dans une première partie je présente la physique, ainsi que les méthodes numériques de modélisation associées, de la rhéologie de la lithosphère, des transferts de chaleur, et des processus de surface en traitant notamment les lois d'érosion. Deux principales familles de lois d'érosion sont proposées dans la littérature: (1) les lois empiriques basées sur des principes hypothétiques des processus qui gouvernent la physique de l'érosion, comme la contrainte cisaillante de l'eau; (2) les lois basées

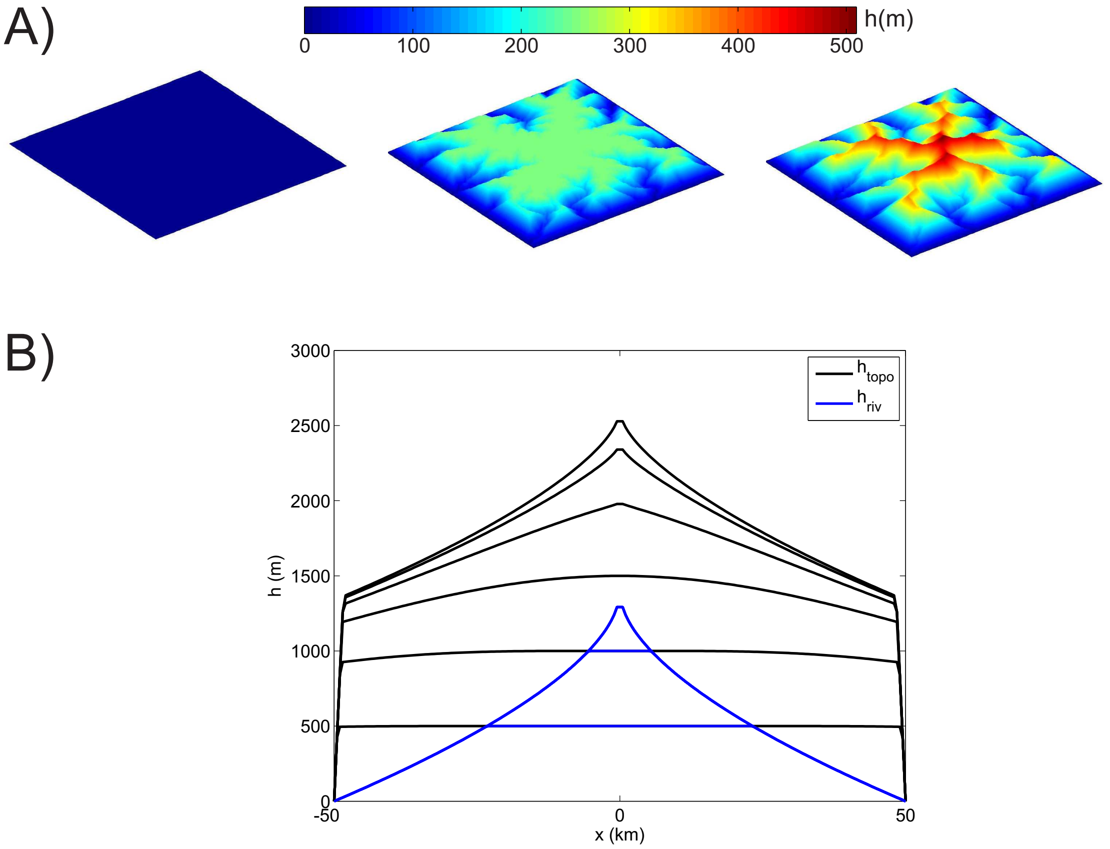

Figure 1: Exemples d'évolution temporelle d'un modèle d'évolution des paysages (A) en $2D$, et (B) en $1D$. Le formalisme $1D$ présente l'avantage de pouvoir être aisément couplé avec un code de déformation $2D$.

sur la mécanique des processus d'érosion, comme l'abrasion par impacts de galets. Les lois d'érosion s'expriment classiquement comme des équation différentielles de l'élévation de la surface et sont ici modélisées à l'aide de méthodes en différences finies. Un modèle $2D$ d'évolution des paysages, prenant en compte aussi bien les processus d'incision à l'aide d'un formalisme en *stream-power*, que les processus de versants, modélisés à l'aide d'une pente critique, est développé et présenté. Ce modèle planaire est ensuite intégré analytiquement dans une des directions de l'espace, afin d'exprimer l'érosion des paysages comme une fonction $1D$ de l'espace (*Lavé*, 2005) (Fig. 1). En outre, le caractère stochastique de la charge en eau des rivières est ici pris en compte (e.g., *Lague et al.*, 2005). Ce nouveau formalisme $1D$ d'évolution des paysages présente l'avantage de pouvoir être aisément couplé aux modèles thermo-mécaniques $2D$ décrivant la Terre solide (*Willett*, 2010).

D'autre part, les différences finies sont aussi employées pour modéliser les transferts de chaleur par advection et diffusion. La rhéologie de la lithosphère est modélisée par la méthode des éléments finis, qui permet de prendre en compte simultanément l'élasticité, la viscosité et la plasticité des roches. Dans cette dernière approche, lorsque la déformation cumulée, ou que le gradient de déformation, deviennent importants, le remaillage des éléments finis devient nécessaire pour maintenir

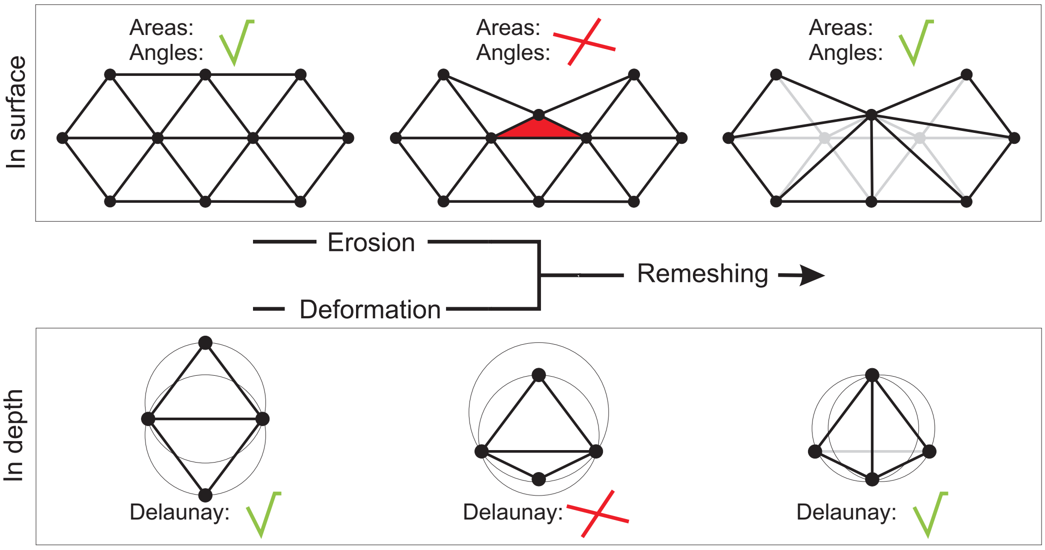

Figure 2: Présentation des algorithmes de remaillage local développés pour les modèles lagrangiens aux éléments finis: (A) *Surface Lagrangian Remeshing* (SLR) (*Steer et al.*), dédié à la prise en compte de la distorsion en surface induite par l'érosion, et (B) *Dynamical Lagrangian Remeshing* (DLR) (*Braun and Sambridge*, 1994), dédié à la prise en compte de la distorsion associée à la déformation en profondeur. Dans le cas du SLR, les éléments de surface présentant des critères de distorsion importants (angle ou surface faible) voient leurs noeuds n'appartenant pas à la surface éliminés. Seuls l'élément distordu et ses voisins directs sont ensuite remaillés par une triangulation de Delaunay.

la qualité de la solution numérique. Je présente donc un nouvel algorithme de remaillage local, intitulé *Surface Lagrangian Remeshing* (SLR), dédié à la prise en compte de la distorsion des éléments en surface, induite par l'érosion, dans les modèles $2D$ ou $3D$ (thermo-) mécaniques (Fig. 2). Le SLR présente l'avantage d'être à la fois précis, en permettant par exemple de suivre avec précision la surface libre du modèles ou en minimisant la diffusion numérique inhérente au remaillage, et efficace, en induisant un gain de temps de calcul considérable par rapport aux méthodes classiques de remaillage global. Le SLR représente donc un algorithme de remaillage local, permettant de coupler efficacement et précisément, l'érosion à long terme avec la déformation dans les modèles lagrangiens aux éléments finis triangulaires. Cette dernière partie fait l'objet d'un article sous presse à *Computers & Geosciences*.

Acquisition de Données in-situ: Rebond au Marteau de Schmidt, Érodabilité et Propriétés Équivalentes

Dans une seconde partie, j'examine la potentialité de mesurer l'érodabilité in-situ à l'aide d'un marteau de Schmidt, et quantifie l'influence des fractures sur l'érodabilité. L'érodabilité est classiquement déterminé à l'aide d'un canal circulaire permettant de reproduire, en laboratoire, des conditions réalistes de transport et d'érosion fluviale (*Attal and Lavé*, 2009). Les résultats de *Attal and Lavé* (2009) suggèrent que l'érodabilité est, au premier ordre, fonction de la lithologie. Les valeurs

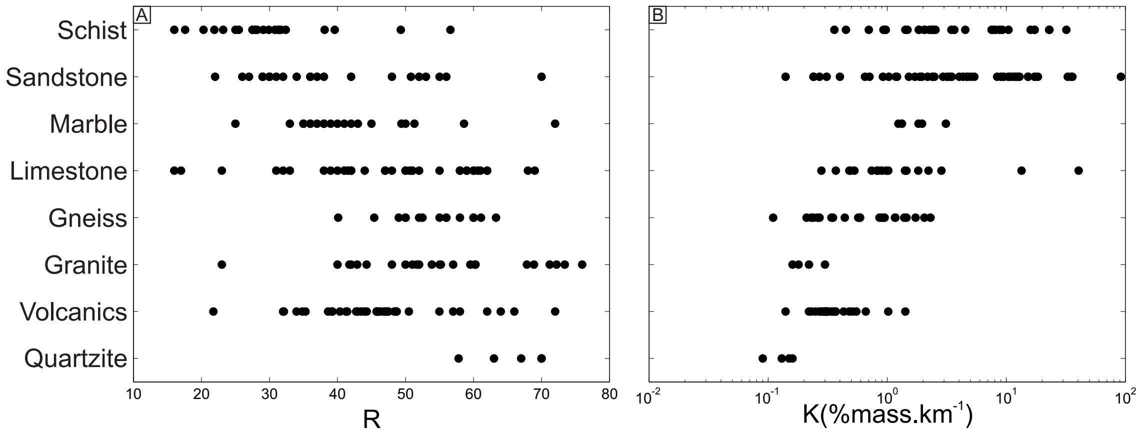

Figure 3: Variation (A) du rebond au marteau de Schmidt R, et (B) de l'érodabilité K en fonction de la lithologie. L'érodabilité est extraite des travaux de *Attal and Lavé* (2009), alors que le rebond au marteau de Schmidt est compilé à partir de la littérature (e.g., *Aydin and Basu*, 2005). Qualitativement, érodabilité et rebond sont anti-corrélés.

d'érodabilité (K) ainsi obtenues sont ensuite comparées avec des valeurs de rebond (R) au marteau de Schmidt (Fig. 3), compilées depuis la littérature (e.g., *Aydin and Basu*, 2005). R et K sont qualitativement anti-corrélées, avec les fortes valeurs de rebond associées à de faibles valeurs d'érodabilité. Un modèle novateur, basé sur la dérivation mécanistique des processus d'incision (*Sklar and Dietrich*, 2001, 2004) et combiné à des relations empiriques (*Aydin and Basu*, 2005) reliant contrainte à la rupture et R, est développé. Ce modèle permet de relier quantitativement les jeux de données d'érodabilité K et de rebond au marteau de Schmidt R, sous la forme d'une loi exponentielle ou en puissance. Ces relations fournissent un cadre théorique et empirique à l'étude de l'érodabilité, mesurée à l'aide d'un marteau de Schmidt.

Le marteau de Schmidt est ensuite utilisé pour contraindre in-situ l'érodabilité dans différents contextes naturels. Tout d'abord j'applique cette méthode pour réaliser un transect d'érodabilité à travers la chaîne de montagne de Taïwan. Les résultats révèlent un faible contrôle de R et de K par la lithologie, et suggèrent un fort contrôle par le degré de fracturation. Je présente aussi les résultats d'une étude de terrain dédiée à la compréhension de l'influence de la diagénèse des Grès d'Annot sur R et K. A partir d'un jeu de données pétrogénétiques et pétrophysiques (*Labaume et al.*, 2008a), j'évalue le contrôle du grade diagénétique sur R, en m'affranchissant de possibles variations induites par la lithologie. Les résultats suggèrent un contrôle de R et K par la diagénèse, notamment à travers la cohésion des roches étudiées. Ce contrôle est qualitativement contre-balancé par le degré de fracturation, lui aussi fonction croissante de la diagénèse. De ces deux études préliminaires, il ressort clairement que les fractures représentent un contrôle tout aussi prépondérant que la lithologie sur l'érodabilité, mesurée à l'aide d'un marteau de Schmidt.

Je présente ensuite les résultats d'une expérience dédiée à l'étude de la relation entre densité de fractures et rebond au marteau de Schmidt R. La zone de faille de

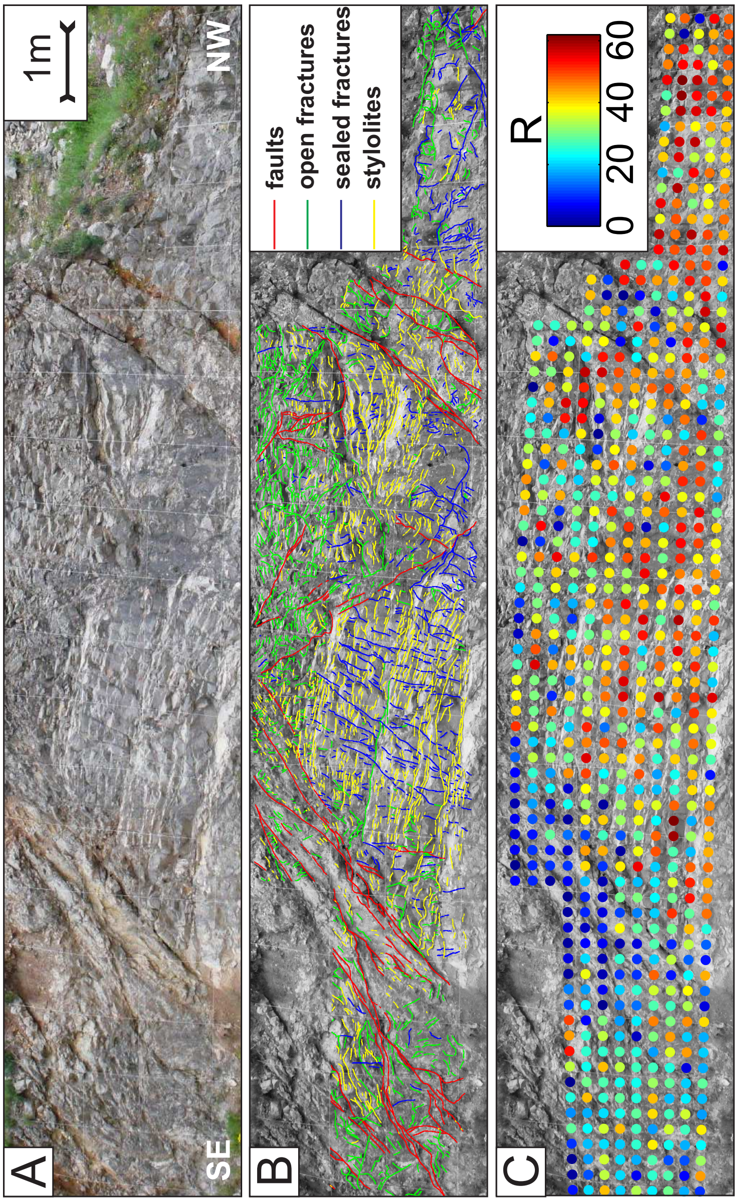

Figure 4: (A) L'affleurement de St Clément comporte principalement des calcaires entrecoupés de parties marneuses ou cataclasitiques, respectivement localisés dans les zones de failles secondaires du SE ou du NE de l'affleurement. (B) Quatres types de fractures sont considérées: les failles (lignes rouges), les fractures ouvertes (lignes vertes), les fractures scellées (lignes bleues) et les stylolites (lignes jaunes). (C) Distribution spatiales des valeurs de rebond R au marteau de Schmidt.

St Clément, qui présente une lithologie à dominance calcaire, permet partialement de s'affranchir d'éventuelles variations induites par la lithologie. Une image haute résolution (25 mesures par m^2) de R à l'échelle de l'affleurement est réalisée ainsi qu'un relevé des fractures, incluant les failles secondaires, les fractures ouvertes ou scellées, et les stylolites (Fig. 4). Un modèle linéaire, issu de la théorie des milieux élastiques équivalents (*Hudson*, 1980, 1981), est proposé. Ce modèle, reliant R à la densité de fracture pour chaque type de fracture, est utilisé dans une série d'inversion et d'optimisation. Les images modélisées par inversion à partir des images de densités de fractures, sont significativement corrélées à l'image de données R. Cela démontre d'une part que la partie la plus significative des variations de R à l'échelle de l'affleurement peuvent être associées à des variations de densité de fracture. D'autre part, l'inversion du modèle permet aussi de quantifier la pondération exercée par la densité de fracture pour chaque type de fracture sur l'élasticité équivalente et R. Les résultats suggèrent que les failles et les fractures ouvertes ont un effet négatif sur R, alors que les fractures scellées on un effet neutre voire positif. Ces résultats illustrent le contrôle excercé par les fractures sur l'érodabilité des roches, comme cela a été suggéré par *Molnar et al.* (2007). De plus, en comparaison avec les experiences classiques d'abrasion (*Sklar and Dietrich*, 2001; *Attal and Lavé*, 2009), R capture les propriétés équivalentes des roches à une échelle correspondant aux processus d'érosion, entre 1 et 30 cm environ. Cette dernière étude, qui a été soumise à *Journal of Structural Geology*, ouvre en outre de nouvelles perspectives sur le rôle des cycles diagénétiques dans la rhéologie des zones de failles.

Modélisation Numérique: Érosion, Rheologie et Évolution Post-Orogénique

Dans cette dernière partie j'étudie, à l'aide de la modélisation numérique, la relation entre érodabilité et morphologie des paysages en temps et en espace. D'abord, j'explore la relation entre érodabilité et longueur d'onde des paysages, en utilisant le modèle planaire d'évolution des paysages développé dans la première partie du manuscrit. Ce modèle permet de considérer à la fois l'érosion fluviale par *stream-power* et l'érosion associée aux glissements de terrains, ici modélisée via un angle critique de stabilité des versants. Ce modèle simpliste permet de produire des topographies synthétiques au stade d'équilibre dynamique entre les taux d'érosion à la surface et le taux de soulèvement imposé. Ces topographies synthétiques présentent une périodicité contrainte par l'agencement du réseau fluvial. la périodicité des topographies synthétiques obtenues est une fonction puissance à exposant positif du rapport du taux de soulevement divisé par l'érodabilité. Ce résultat est cohérent avec la théorie du *stream-power*. Je démontre aussi que les indices classiquement utilisés pour déterminer la longueur d'onde du paysage, tels que la densité de drainage basée sur un seuil arbitraire de l'aire drainée, ne sont pas adéquats pour évaluer le lien entre longueur d'onde du paysage et l'érodabilité ou le taux de soulèvement.

La dernière étude a pour objectif de contraindre les conditions d'érosion en surface et les mécanismes de déformation lithosphérique qui permettent de repoduire la diminution du rapport de l'élévation sur l'épaisseur de la racine crustale R, lors de la phase post-orogénique (*Fischer*, 2002). Les chaînes de montagnes post-orogéniques sont caractérisées par des élévationx plus faibles que les chaînes orogéniques (Fig.

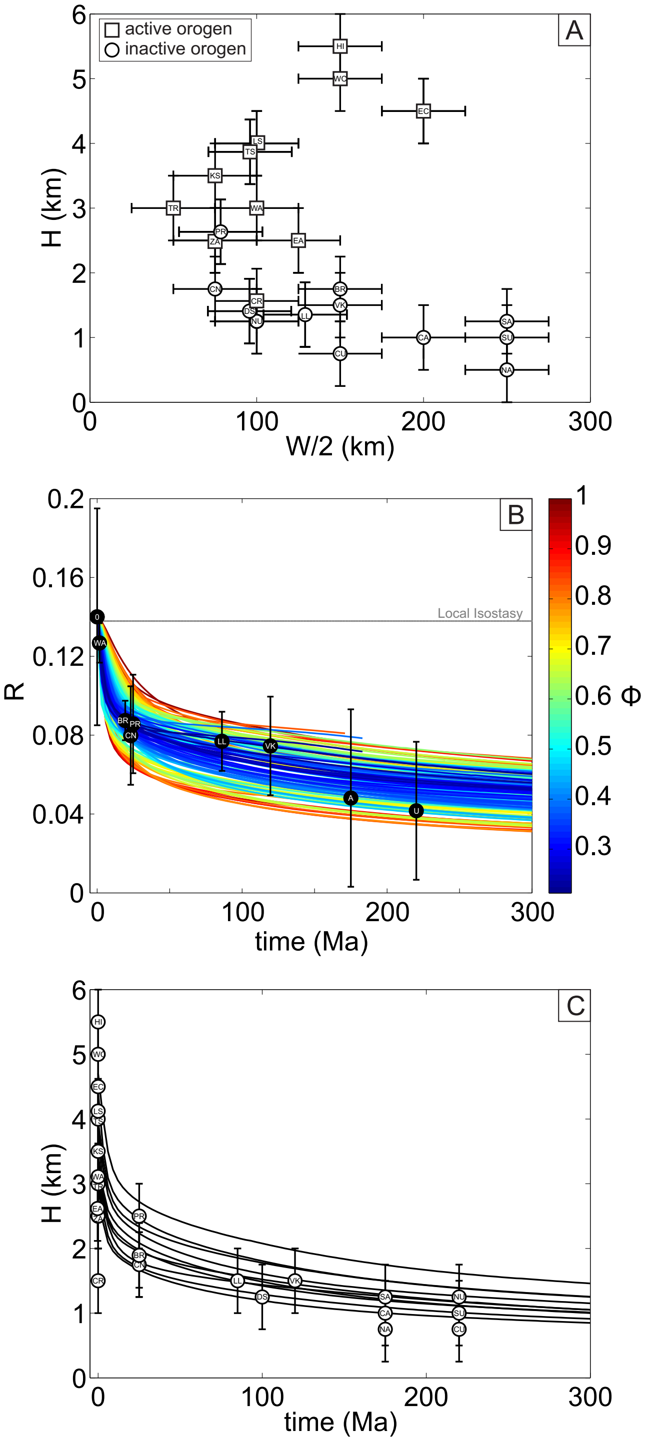

Figure 5: (A) Élévation (H) et demi-largeur ($W/2$) des orogènes actives et inactives, mis à part celles présentant une topographie de type plateau. (B) Evolution comparée du rapport de l'élévation de la topographie divisée par l'épaisseur de la racine crustale (R), pour les orogènes actives et inactives d'après *Fischer* (2002), et pour les meilleurs modèles, i.e. les modèles présentant les meilleurs accords avec les données. Un misfit Φ faible signifiant un bon accord. (C) Evolution de la décroissance de l'élévation (H) de la topographie au centre de la chaîne pour les dix meilleurs modèles vis à vis de l'inversion, et distribution de l'élévation des orogènes en fonction du temps. Le nom des chaînes de montagne est donné dans le texte en bas de page [2].

5 A). Cependant la persistance des reliefs post-orogéniques, pendant plusieurs centaines de millions d'années, met en défaut les concepts classiques d'érosion et de déformation lithosphérique (*Baldwin et al.*, 2003). Un modèle aux éléments finis, ADELI (*Hassani et al.*, 1997), couplant processus de surface, déformation mécanique et évolution thermique, est utilisé pour étudier l'évolution à long terme des chaînes de montagne post-orogéniques. En utilisant une gamme de valeurs réalistes pour la géométrie initiale des chaînes de montagnes, ainsi que pour le coefficient d'efficacité de l'érosion et pour les conditions thermiques, nous montrons qu'une décroissance topographique contrôlée par l'érosion et partiellement compensée par isostasie régionale est compatible avec la diminution temporelle de R observée (Fig. 5 B). Un échantillonnage de l'espace des modèles avec un algorithme uniforme Monte-Carlo associé à un critère de moindre valeur absolue, permet de contraindre les combinaisons de paramètres compatibles avec une diminution temporelle de R. Le première facteur qui contrôle la qualité des modèles vis à vis des données est le coefficient d'efficacité de l'érosion, avec les meilleurs modèles associés à des valeurs modérées à élevées. Le deuxième facteur est la géométrie initiale de la chaîne de montagne, avec les montagnes les plus élevées ou les plus étroites nécessitant les coefficients d'efficacité de l'érosion les plus faibles. Toutefois une diminution temporelle de R est atteinte indépendamment de la géométrie initiale. La viscosité équivalente de la croûte ne ressort pas comme un facteur déterminant de la qualité des modèles. Les meilleurs accords entre modèles et données, sont obtenus pour des chaînes où la décroissance de la topographie est contrôlée par l'érosion, et non pas par un éventuel effondrement gravitaire. Ce dernier mécanisme n'étant pas associé à une diminution temporelle de R. Enfin, les meilleurs modèles présentent une décroissance topographique qui est à posteriori en accord avec la distribution de l'élévation des chaînes de montagnes post-orogénique en fonction de leur âge (Fig. 5 C). Cette étude, qui a été soumise à *Journal of Geophysical Research*, illustre le rôle de l'érodabilité, à travers l'efficacité de l'érosion, dans la persévérance des reliefs terrestres.

Études en Cours et Perspectives

Métamorphisme et Évolution Post-Orogénique: D'autres modèles géodynamiques d'évolution à long terme des chaînes de montagne post-orogéniques ont été proposés dans la litérature (*Fischer*, 2002; *Baldwin et al.*, 2003; *Pelletier*, 2004). *Fischer* (2002) notamment, suggère que la densification de la racine crustale, par réactions métamorphiques, est un facteur déterminant de l'évolution post-orogénique. En effet, une densification de la racine crustale se traduit géodynamiquement par une diminution de sa flottabilité. Cet effet pourrait être responsable de la décroissance temporelle du rapport de l'élévation de surface sur l'épaisseur de la racine

---

[2] Suite de la légende de la figure 5: HI, Himalaya; WC, Cordillère Ouest Andine; EC, Cordillère Est Andine; LS, Longmen Shan; TS, Tien Shan; KS, Kunlun Shan; WA, Alpes Occidentales d'Europe; EA, Alpes Orientales d'Europe; ZA, Alpes du Sud de la Nouvelle-Zélande; TR, Montagne de Taiwan; CR, Carpates; PR, Pyrenées Centrales; BR, Chaîne de Brooks; CN; Cordillère Cantabrique; LL, Lachlan Orogène; DS: Dabie Shan; VK, Monts de Verkhoïansk; SA, Appalaches du Sud; CA, Appalaches Centrales; NA: Appalaches du Nord; NU, Oural du Nord; CU, Oural Central; SU, Oural du Sud. O, moyenne pour les orogènes actives; A, moyenne pour les Appalaches; U, Moyenne pour l'Oural.

crustale *R*. Il s'agit d'un mécanisme alternatif ou complémentaire à celui proposé au cours de cette thèse. Pour tester les effets relatifs et les limites des deux approches, une modélisation couplant érosion en surface, déformation lithosphérique, évolution thermique et variations de densité associées au métamorphisme, est requise. L'approche développée par *Hetényi et al.* (2010) permet de prendre en compte, dans le modèles numériques aux éléments finis, des variations de densité induites par métamorphisme, et ce tout en respectant la conservation de la masse. Cet algorithme a été inclut à ADELI au cours de cette thèse, et une étude préliminaire a déjà été réalisée.

Variations Spatio-Temporelles d'Érodabilité et Orogénèse: Concernant l'évolution à long terme des orogènes, *Beaumont et al.* (1992) et *Willett* (1999) ont mis en évidence, par modélisation numérique, le contrôle majeur exercé par le climat sur l'évolution géodynamique des orogènes: les roches profondes étant advectées au cours de l'orogène vers les zones en surface présentant les taux de précipitation et d'érosion les plus élevés. Je propose que des variations spatiales ou temporelles d'érodabilité pourraient avoir des impacts tout aussi majeurs sur la dynamique orogénique. En effet l'érodabilité, étant une fonction de la lithologie (*Sklar and Dietrich*, 2001; *Attal and Lavé*, 2009), varie spatialement à la surface de la plupart des orogènes (par exemple les Himalayas, Pyrénées, Alpes européennes, Andes, Taiwan, la Sierra Nevada), mais aussi temporellement avec la déformation, la diagenèse ou le métamorphisme (Fig. 6). Cette perspective, qui a déja été abordée numériquement dans le cas des chaînes inactives lors de cette thèse, mérite surtout d'être traitée dans le cas des chaînes actives.

Fractures, Élasticité Équivalente, et Chargement Intersismique: A plus courte échelle de temps, les résultats obtenus par l'étude de l'élasticité équivalente de la zone de faille de St Clément ont potentiellement des implications sur la dynamique des cycles sismiques. Un résultat important de cette étude a été de mettre en évidence que les fractures scellées contribuent moins à la baisse de rigidité que les fractures ouvertes ou les failles. Je suggère que l'évolution de l'élasticité équivalente autour d'une faille majeure, par la création de fracture au cours de la phase cosismique et postsismique et par le scellement de ces mêmes fractures pendant la phase intersismique d'un cycle sismique, peut avoir des répercussions géodynamiques. De tels processus pourraient induire des variations temporelles de rigidité dans la zone d'endommagement et par conséquent mener à des variations du taux de chargement des contraintes sur le plan principal de la faille, au cours de la phase intersismique.

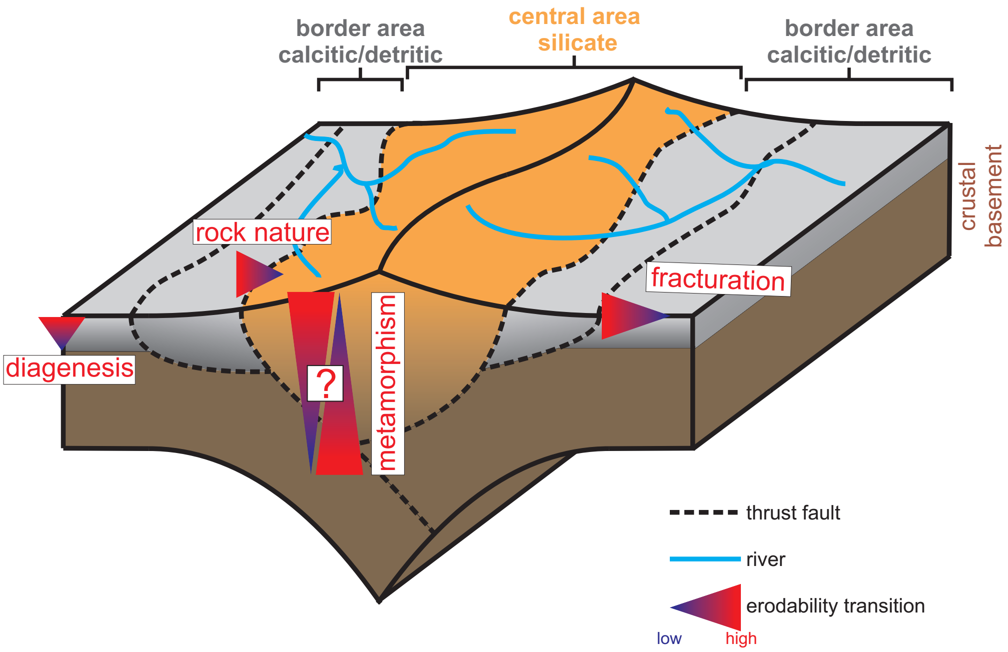

Figure 6: Schéma des principaux processus affectant l'érodibalité des roches en contexte orogénique et post-orogénique. Ici, nous supposons que la zone axiale de la chaîne de montagnes est dominée par des silicates, alors que ses piédmonts sont de nature calcitique ou détritique. L'érodibilité varie dans l'espace en fonction de la nature des roches de surface: les roches calcitiques ou détritiques étant généralement plus sensibles à l'érosion qu'un granite ou un gneiss. La diagenèse diminue l'érodabilité en augmentant la densité, en diminuant la porosité, et en cimentant les pores inter-grains et les fractures. L'effet du métamorphisme (supposé ici prograde) sur l'érodabilité est double, d'une part il tend à augmenter la densité de la roche, d'autre part il crée des fragilités par acquisition de linéation ou de foliation. Les fractures ont pour effet d'affaiblir mécaniquement les roches et ainsi augmentent l'érodabilité vis à vis de l'abrasion, favorisant ainsi l'érosion par *plucking* (*Molnar et al.*, 2007).

Introduction

The time scale of human observation is a real limit to our understanding of the planet Earth. For instance, comparing Earth history since its creation 4.5 Ga ago, with the story of a 1h30-long movie with 25 fps, our records during human history $\sim$ 3000 yr would only represent one tenth of a single frame. Would you be able to understand a movie with only one snapshot? This is the difficult task that geoscientists have to challenge. Fortunately for them, some fingerprints of the past states of the Earth have been recorded. In particular the Earth's surface offers the most accessible and complete observations of the planet, and gives some insights on its evolution and on the governing mechanisms that shape it. The most spectacular and convincing example is the relief of continental orogens, which appears as scars which affect Earth's surface topography (Fig. 7). Orogenic relief results from complex interactions between climate, surface processes, tectonic motion and solid Earth deformation. This manuscript is an attempt to contribute towards a better understanding of these processes and interactions that shape Earth's surface, with a particular focus on the role of the lithology and rock effective properties.

In Part 1, I try to give an overview of the physical processes that controls the shape and the evolution of Earth's surface elevation in orogenic settings, with a particular focus on the erosional and lithospheric deformation mechanisms that create, support and remove orogenic reliefs. A focus is made on the numerical methods that allow one to study these processes and their interactions, in one, two and three dimensions. I also present a new local remeshing algorithm dedicated to the implementation of surface erosion in numerical modeling using triangular finite elements.

In Part 2, I investigate the potentiality and limits of measuring the resistance of rock masses to erosion, i.e. erodibility, with a in-situ method: the Schmidt hammer, which is documented to offer an empirical relation between rock properties, such as elasticty or strength, and its rebound. First I empirically and theoretically analyse and review the relation between Schmidt hammer and erodibility. Then I apply this method to perform a transect of rock erodibility accross the Taiwan mountain belt, and to explore the relation between Schmidt hammer rebound and the diagenetic grade of the Annot Sandstone. From these two preliminary experiments, it appears that fractures and their densities have a dominant control on Schmidt hammer rebound. Thus in a dedicated experiment, I study the influence of fractures type and density on Schmidt hammer rebound in a fault zone.

In Part 3, I use and develop numerical models to study the influence of rock erodibility on landscapes morphology and temporal evolution. In particular I first focus on the control of landscapes wavelength by rock erodibility, and I assess the limits of drainage density to predict such control. Second, taking advantage of the remeshing algorithm developed, I employ a $2D$ numerical model, to investigate the

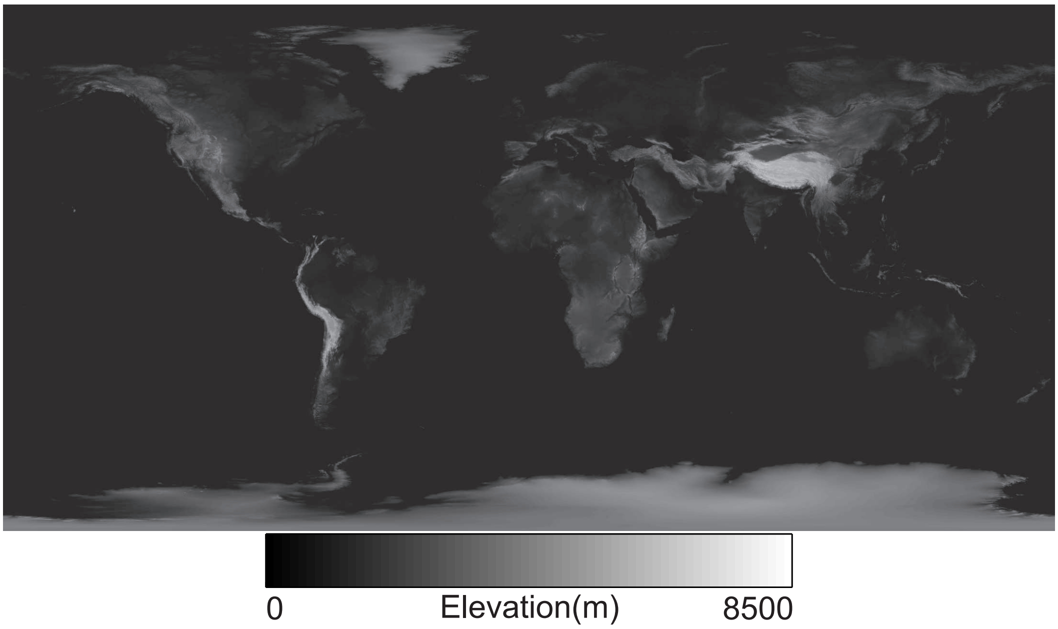

Figure 7: Elevation of the topography of the Earth's land surface relative to sea level. The data come from the NASA and are initially from the Shuttle Radar Topography Mission 30-arcsecond data (SRTM30) and the RadarSat Antartic Mapping Project Digital Elevation Model Version 2 (RAMP2). The data in the cylindrical equidistant projection, utilizing the WGS-84 datum.

evolution of old mountain belts that are no longer in a context of tectonic plate convergence, i.e. post-orogenic mountain belts. These belts have two remarkable properties: (1) they maintain high elevation during an unexpectedly long perdiod of time (above 100 Ma), (2) they are underlain by very thick crustal roots in respect to their surface elevation. I numerically explore the conditions of surface erosion and of lithospheric deformation that are compatible with both of these properties. In particular, I focus on the influence of erosion efficiency and erodibility on their evolution and on the decay time of the relief of these post-orogenic belts. Based on this study I reassess general models of post-orogenic evolution.

Finally, after a conclusion, I briefly present some future work that needs to be developed in the coming years.

Part I

Surface Processes, Solid Earth Rheology and their Modeling

Résumé

Dans cette partie je présente la physique, et les méthodes numériques de modélisation associées, de la rhéologie de la lithosphère, des transferts de chaleur, et des processus de surface en traitant notamment les lois d'érosion. Deux familles principales de lois d'érosion existent: (1) les lois empiriques basées sur des principes hypothétiques des processus qui gouvernent la physique de l'érosion, comme la contrainte cisaillante de l'eau; (2) les lois basées sur la mécanique des processus d'érosion, comme l'abrasion par impacts de galets. Les lois d'érosion, qui s'expriment classiquement comme des équation différentielles de l'élévation de la surface, sont modélisées à l'aide de la méthode des différences finies. Les différences finies sont aussi utilisées pour modéliser les transferts de chaleur par advection et diffusion. D'autre part la rhéologie de la lithosphère est modélisée par la méthode des éléments finis, qui permet de prendre en compte simulaténement l'élastictité, la viscosité, et la plasticté. Dans cette dernière approche, lorsque la déformation cumulée, ou que le gradient de déformation, deviennent importants, le remaillage des éléments finis devient nécessaire pour maintenir la qualité de la solution numérique. J'introduis donc un nouvel algorithme de remaillage local qui permet de coupler efficacement l'érosion avec la déformation dans les modèles lagrangiens avec des éléments finis triangulaires. Cette dernière partie fait l'objet d'un article sous presse à *Computers & Geosciences*.

Abstract

In this first part I present the physics, and associated numerical modeling methods, of lithospheric rheology, heat transfer, and surface processes with a focus on erosion laws. Two main classes of physical erosion law exist: (1) empirical erosion laws that are based on hypothetical principles of the processes that govern physics of erosion, such as water shear-stress; (2) process-based erosion laws that are based on the mechanics of the processes, such as abrasion by pebble impacts. Erosion laws, classicaly expressed as differential equations of surface elevation, are modeled with finite differences methods. Finite differences are also employed to model heat transfers, with advection and diffusion. On the other hand, lithospheric rheology is modeled with the finite element method, which allows one to consider elasticity, viscosity and plasticity into a single approach. In this latter approach, when facing large cumulated deformation, or deformation gradient, remeshing of the finite elements becomes necessary to maintain the quality of the numerical solution. I thus introduce a new local remeshing algorithm that allows one to efficiently couple erosion to lithospheric deformation in lagrangian models with triangular finite elements. This last part has been published in *Computers & Geosciences*.

Chapter 1

Numerical modeling of Erosion and Lithospheric deformation: processes and interactions

Earth's surface topography corresponds to the frontier between internal and external envelopes. Its evolution is governed by the transfer of rock: tectonics advects rocks which are then transported and redistributed at the surface after erosion. This system is subjected to feedbacks and interactions, as it is now well accepted that mass transfer at the surface affect tectonics, and that tectonics partly controls erosion by modifying elevation and its spatial derivatives. Earth's surface evolution is also sensitive to transfers of water coming from the atmosphere, as water or ice are considered as the main agents of erosion and transport.

In this chapter, I briefly present the numerical methods that allow modeling of surface processes and lithospheric deformation. The aim is to offer the reader an overview, rather than an exhaustive review, that will help him to understand the key topics addressed in this manuscript. For further details, we invite the reader to refer to these following books:

- Quantitative Modeling of Earth Surface Processes (*Pelletier*, 2008);
- Geodynamics (*Turcotte and Schubert*, 2002);
- Deformation of Earth Materials (*Karato*, 2008);
- Numerical Geodynamic Modelling (*Gerya*, 2009);
- The Finite Element Method for Solid and Structural Mechanics (*Zienkiewicz et al.*, 2005);
- The Nature of Mathematical Modeling (*Gershenfeld*, 1999);
- Numerical Recipes in Fortran (*Press et al.*, 2007).

First I describe surface processes and their numerical modeling in $1D$ and $2D$, then I focus on lithospheric deformation and the finite element method in $2D$. Next I address the question of numerical modeling of the interactions between surface processes and lithospheric deformation and I present a new local remeshing algorithm dedicated to this problem.

1 Mathematical Representation of a Physical System and Numerical Modeling

Before addressing scientific questions, it is essential to define what is a physical system, a physical model, a numerical model, an analytical model and to assess their respective limits. A **physical system** is a system that is governed by physical processes, which can be observed and described or not by physical laws. A **physical model** is as a copy of a physical system, which translates the physics into a mathematical (or analogical) description. It is mainly limited by the physical representation of the system. A physical model can be simulated with analytical or numerical model. An **analytical model** is the *perfect* mathematical representation of the physical system, as it does not suffer from any approximation. On the other hand a **numerical model** is a computer program that *attempts* to simulate the physical model, and is not an exact copy as it suffers from numerical approximation. Clearly when possible analytical models are preferable to numerical models, even if many numerical methods minimize approximation errors.

When considering a complex physical systems such as the Earth's surface and its evolution, the limits of its simulation are manifold:

- First the physical model only approximates the physical system. For instance only empirical laws exist to describe erosion of a fluvial system.
- The physical model can not be defined without a large set of equations that includes the first-order physics: conservations or continuity equations (mass, energy, momentum), constitutive equations of rock material (e.g., elasticity, viscosity, plasticity, heat), erosion and transport equations. Many of these equations exhibit temporal or spatial partial derivatives at different orders, which prevents one from having a general analytical solution.

From this last statement two classical strategies are possible to solve the problem:

- Simplifying the physical model (which is already a simple view of the physical system) by making hypothese on the conditions that apply to the system (e.g., boundary conditions) in order to obtain an anlytical solution. Generally the stronger the assumptions are, the simpler it is to get a solution. This strategy offers a mathematically *perfect* solution to a *weak* physical model that strongly approximates the physical system.
- Conserving the physical model, but solving the set of equations with mathematical schemes (e.g., finite differences) implemented into a numerical model. This offers an *approximate* mathematical solution to a *strong* physical model.

In the following I mainly adopt the second strategy. Indeed, I consider that existing numerical methods to have sufficient quality to reduce numerical approximations and thus offer practical solutions to a wide range of problems with varying boundary conditions and constitutive laws. The main drawback of numerical modeling is its inherent high computational cost.

It is also important to clearly define what is the dimension of a model: what is a one- ($1D$) two- ($2D$) or three-dimensional ($3D$) model. Following (*Pelletier*, 2008)

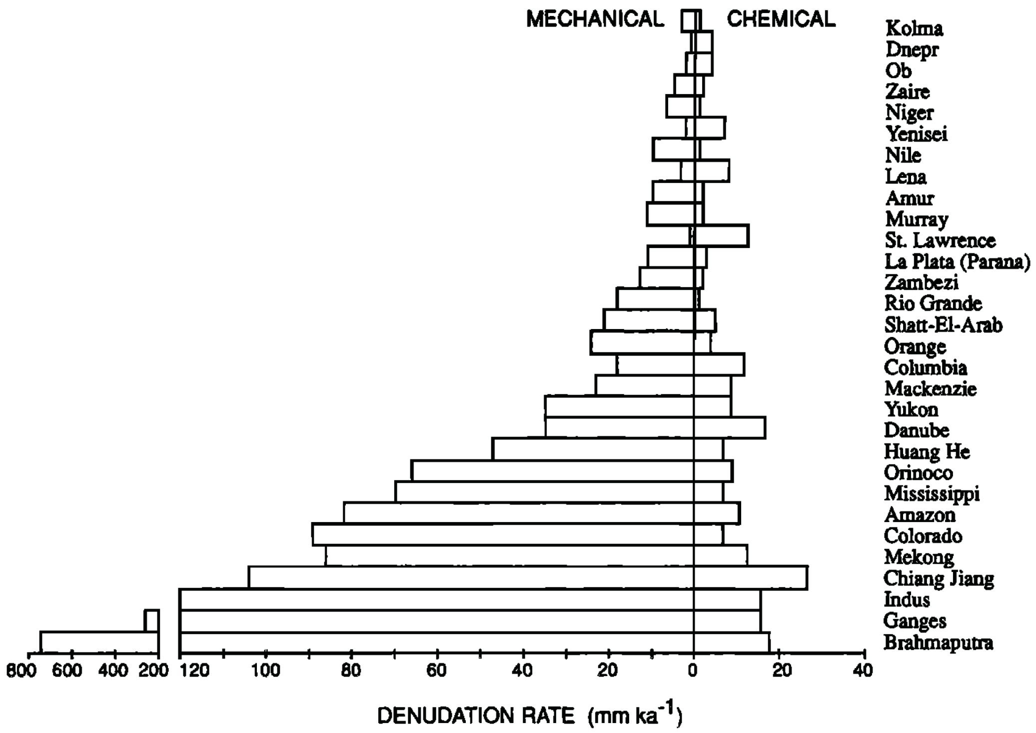

Figure 1.1: Histograms comparing mechanical and chemical denudation/weathering rates for the main drained basins of the world (*Summerfield and Hulton*, 1994). Mechanical erosion is clearly the dominant erosion process.

I use the convention that the dimensionality of the problem refers to the number of independent spatial variables. Therefore, Earth's surface elevation $h(x, y, t)$, which is the main variable used to describe geomorphologic systems, is a function of 2 independent spatial variables x and y: it is a $2D$ function. Concordingly a topographic profile $h(x, t)$ is a $1D$ function. Solving the temperature of the lithosphere in a volume is a $3D$ problem as it is a function of 3 independent spatial variables $T(x, y, z, t)$.

In the following we introduce the physical system that is investigated in this manuscript and present the numerical methods that are suitable to model it.

2 Numerical Modeling of Surface Processes

Surface processes can be defined as all the processes that redistribute mass at the surface of the Earth: erosion, transport and deposition. In this manuscript I focus mainly on erosional processes.

2.1 A General Overview of Erosional Processes in Orogens

In active orogens, the intensity of mechanical erosion is several orders of magnitude higher than chemical weathering (Fig. 1.1). Among mechanical processes glacier erosion, fluvial incision and hillslope erosion are preponderant. Glacier erosion can play an important role in sculpting landscapes, especially by limiting the maximum elevation of mountain belts (*Brozovic et al.*, 1997; *Whipple and Tucker*, 1999). However in the following I focus only on the interactions between tectonics and erosion in non-glaciated mountain belts. Thus I don't describe in detail the dynamics of glacier erosion. I invite the reader to refer to *Herman and Braun* (2008) for details on the numerical implementation of glacier erosion. In this section I briefly present the physics of fluvial incision and hillslope erosion at different spatial scales: from the physical scale, the scale at which processes take place, to the scale of landscapes, the appropriate scale for modeling interactions between tectonics and erosion.

2.1.1 Physical Scale

Erosion is the result of two complex process. The first group comprises those which accomplish the disintegration of the rocks, reducing them to fragments, pebbles, sand and clay. The second comprises those processes which remove the debris and carry it away to other parts of the world. Dutton (1882)

2.1.1.a River Erosion

Mechanical fluvial erosion processes of bedrock vary considerably between field settings: abrasion by bed load and suspended load; plucking of joint rocks; cavitation (e.g., *Whipple et al.*, 2000). For instance, the Hérault river, located in the South of France, exhibits evidence of both bedrock abrasion and plucking (Fig. 1.2), which are the two dominant mechanical erosion processes. As it is classically defined in geomorphology, bedrock abrasion consists of the mechanical erosion of a bedrock surface by friction and impacts with moving particles transported by the river water flow. On the other hand, plucking consists of the formation and extraction of blocks from the bedrock. These two processes correspond to the physical system of river erosion. Here we attempt to describe from the physical system, a set of equations that allows to define a physical model of river erosion at the scale of the processes.

Cavitation Erosion by cavitation is the consequence of the creation of air bubbles in turbulent flow areas of low pressure, and their implosion in flow areas of high pressure. If implosion occurs at the contact with rock, it induces rock damages following an increase of pressure and temperature (e.g., *Arndt*, 1981; *Momber*, 2003). However it not clear whether or not cavitation is an active process of river bedrock erosion (*Hancock et al.*, 1998; *Whipple et al.*, 2000).

Abrasion In orogens, river bedrock abrasion mainly occurs by the repetitive saltation of bed load and its resulting impacts (e.g., *Sklar and Dietrich*, 2004). However in special conditions, such as rivers with fine sediments, steep slopes and large floods, abrasion by suspended load also takes place (*Lamb et al.*, 2008).

Bed load saltation induces abrasion of bedrock during impacts, in particular by the formation of a network of cracks after multiple impacts (*Engel and Ling*, 1978). In brittle materials, the volume of eroded material V_i per impact is scaled by the vertical kinetic energy of the impacting particle and by the capacity of the bedrock

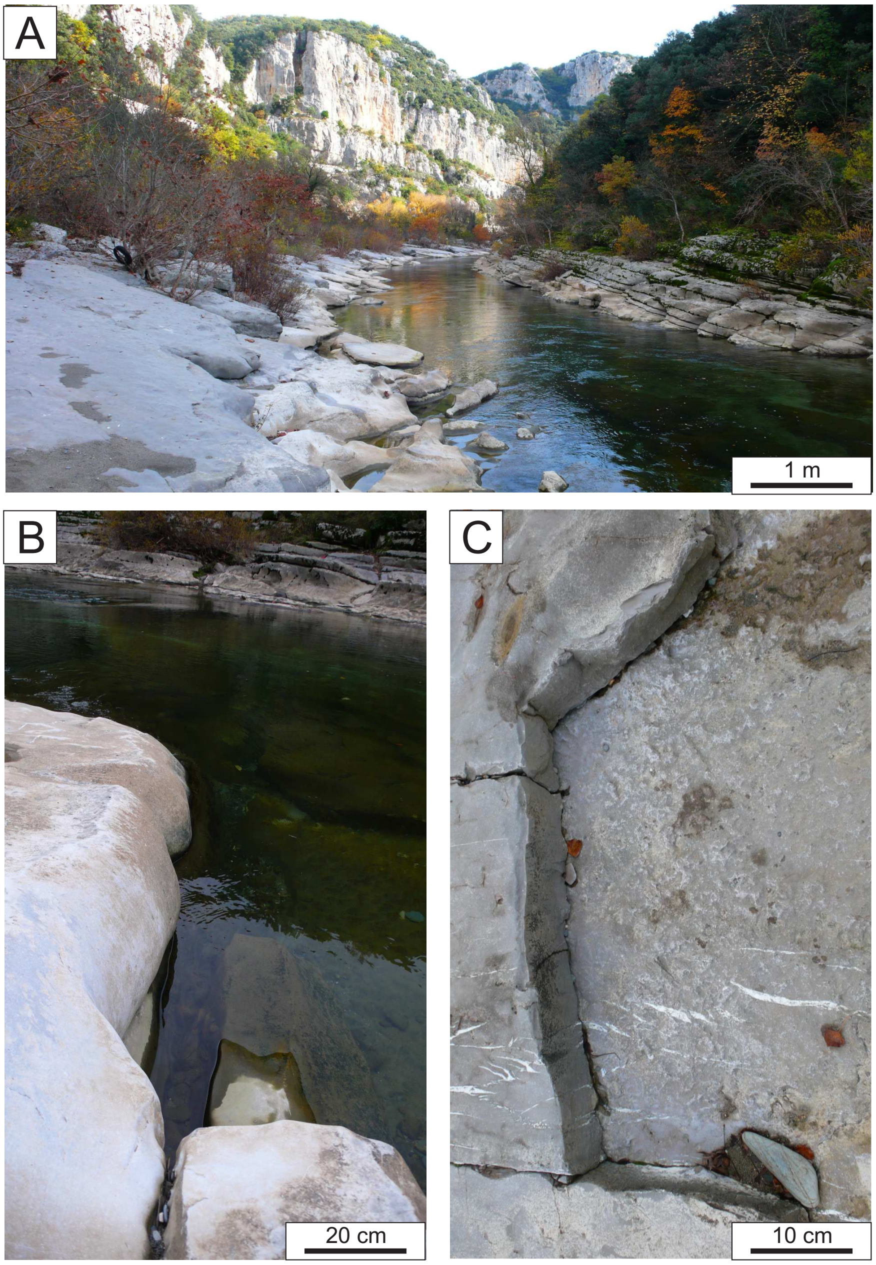

Figure 1.2: Pictures of the Herault river, South of France. A: The Hérault river in the in the Gorges de l'Hérault . B: Abrasion dominated part of the river (flowing from right to left), illustrated by rounded bedrocks which are geometrically orthogonal to the water flow . C: Location of a bedrock block that has been previously plucked (water flowing from bottom to top). Note the presence of fractures.

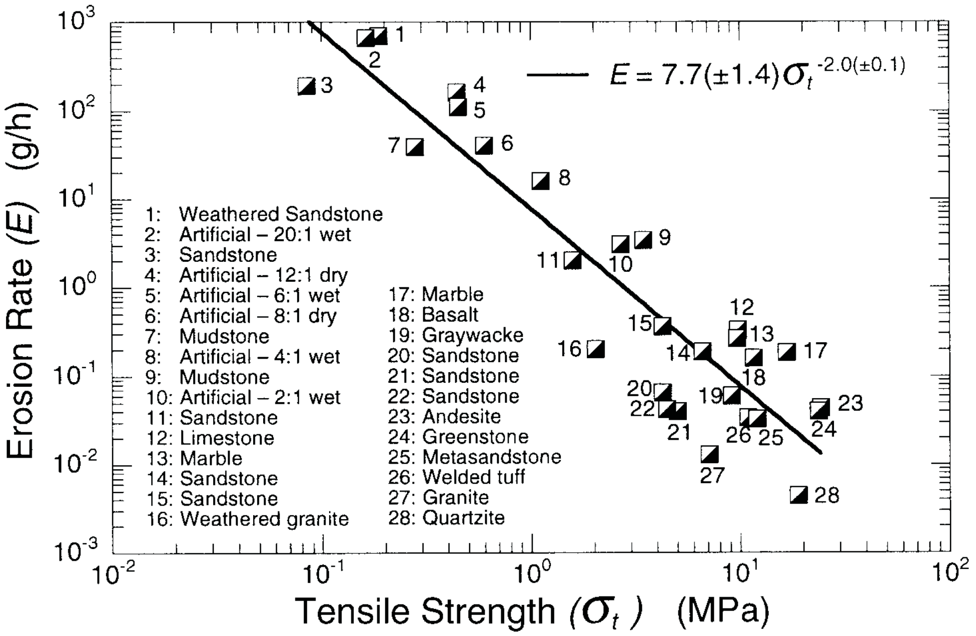

Figure 1.3: Variation of erosion rate by abrasion with rock tensile strength of bedrock (*Sklar and Dietrich*, 2001). Abrasion rates are inversely proportionnal to the square of the tensile strength.

to store the impact energy into elastic energy (*Bitter*, 1963; *Sklar and Dietrich*, 2004):

$$V_i = \frac{\pi \rho_p \phi_p^3 v_p^2 Y}{6 k_p \sigma_T^2}, \tag{1.1}$$

with ρ_p the impacting particle density, ϕ_p its diameter and v_p its vertical velocity, k_p a dimensionless coefficient that depends on the mechanical properties of the impacting particle, Y the Young's modulus of the impacted susbtrate and σ_T its tensile strength. This relation, which was derived for elastic brittle materials, is supported by experimental abrasion of artificial materials (glass, plastic, metals) with sub-millimiter non-natural erodents (steel shot, alumina, ceramics) at very high velocities. It is unknown whether these results can be applied to ductile river bedrock or to abrasion by low-velocity pebbles with a wide range of sizes. In particular, concerning the controls that exert the mass of the impacting particle $\pi\rho_p\phi_p^3$, its vertical velocity (tangential velocity is important in ductile materials), and the elastic-plastic substrate rheology.

Two major experimental studies clarify the factors that control abrasion of bedrock close to realistic conditions:

- *Sklar and Dietrich* (2001) deduced from bedrock abrasion mill experiments that V_i is inversely proportional to σ_T^2 when compiling a large range of lithologies (Fig. 1.3). Thus at first order the equation of abrasion (Eq. 1.1) is correct with respect to σ_T.
- Using a circular flume with realistic flow velocity ~ 1 m.s^{-1} and rounded sediments, *Attal and Lavé* (2009) found an empirical relation between the attrition

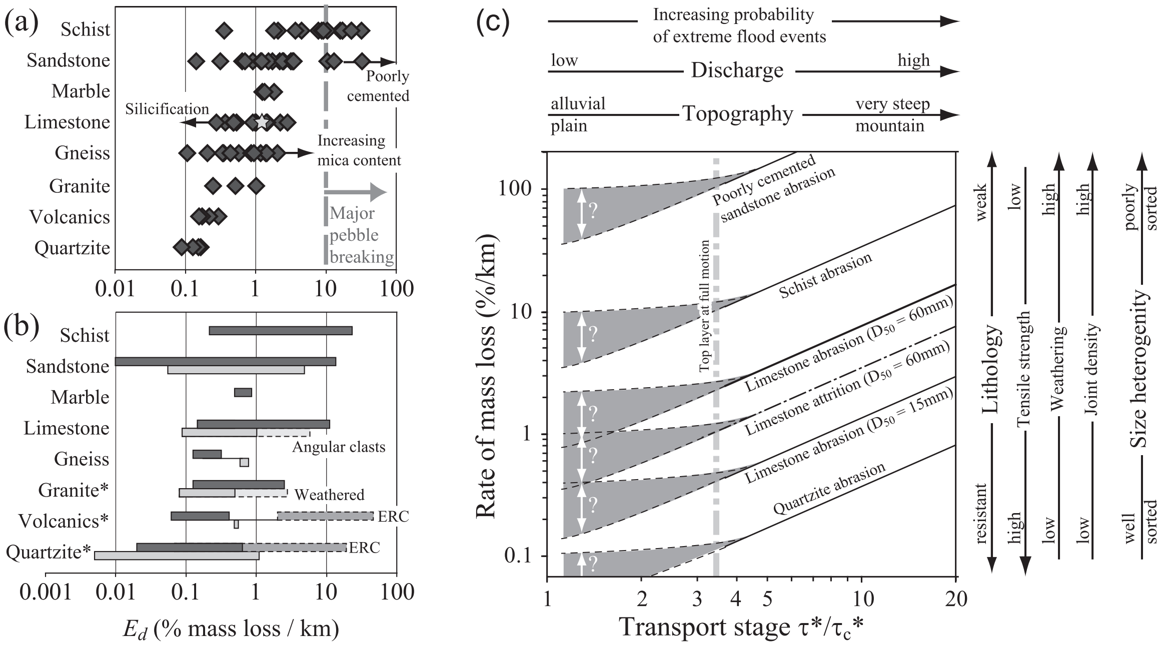

Figure 1.4: Influence of lithology and transport conditions on abrasion rates (*Attal and Lavé*, 2009). Comparision of abrasion rates between (a) *Attal and Lavé* (2009) and (b) a compilation of previously published experimental abrasion results for similar lithologies. (c): Schemi-schematic diagram of the abrasion rate dependency on the transport stage). Both the lithology and the transport condition have a first order control of the abrasion rates of river bedrock. The transport stage $\tau^\star/\tau_c^\star$ is the ratio of the Shield stress on its critical value for particle entrainment.

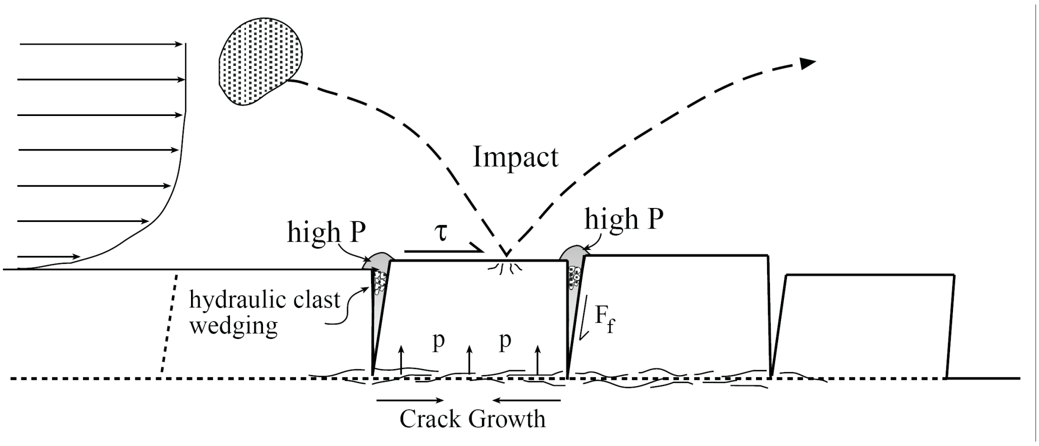

Figure 1.5: Simplified schematic illustration of the processes and forces contributing to erosion by plucking (*Whipple et al.*, 2000). Impacts by large pebbles drive crack propagation. Eventually opening of existing fractures by clast wedging occurs. Surface drag forces and differential pressures accross the block could act to lift it. After removal of a block, it is probably easier to remove its neighbors.

rate (i.e. the inter-pebble abrasion rate) and the square of pebble velocity, quite independently of the mass of pebbles. This confirms the proportionality between abrasion rate and the square of the velocity of the particle, even if here the velocity corresponds to the mean velocity during the experiment and not to the vertical velocity just before the impact (Eq. 1.1). Moreover these results also depend on the transport capacity of the flow and on the probability of inter-particle collision, which are both related to the number and size of pebbles at constant flow speed.

It remains that the factors that control the physics of real river bedrock abrasion, which is the most common erosion process, is still an on-going issue. Still it is by far better understood than plucking, which is considered as the second most common erosion process.

Plucking

Plucking of bedrock requires the validation of different physical stages to occur: rock discontinuities (e.g., fractures, joints) propagation around the block in $3D$ (the pre-conditioning phase) and block extraction (the erosion phase) (*Whipple et al.*, 2000). Many uncertainties remain on the physics of plucking. In particular it is not clear:

- During pre-conditioning, whether bedrock fracturation by bed load impact is important, or if pre-fracturation by tectonics processes and associated deformation is sufficient to isolate blocks from the bedrock;
- During erosion, whether detachment and quarrying of isolated blocks is controlled by flow conditions and local pressure effects, or by bed load impacts.

Plucking-dominated river bedrock exhibits moderate to high fracture density (with a spacing below a few meters), whereas plucking has not been documented for bedrock with low fracture density. Thus it appears that the pre-conditioning phase that produces mechanically discontinuous block at bedrock surface is a necessary condition for plucking, but it is probably not a sufficient condition depending mainly on flow conditions and bed load characteristics.

The other necessary condition for plucking is the entrainment of the mechanically isolated block. Following *Whipple et al.* (2000) let's consider a rectangular block of thickness h, width w, length l, and density ρ_s (Fig. 1.5). This block is surrounded by bedrock. Forces resisting vertical entrainment are the normal component of block buoyant weight in the water with a density ρ_w, friction on the lateral F_l, upstream F_u and downstream F_d block edges, and the averaged pressure force that applies at the surface of the block P_s. In the case of vertical entrainment, the vertical force F_{lift} that is required to lift the block is,

$$\frac{F_{lift}}{wl} \geq P_s + (\rho_s - \rho_w)gh + 2F_l\frac{h}{w} + (F_u + F_d)\frac{h}{l} \ . \tag{1.2}$$

It has been proposed that this lifting force could be the fluid pressure under the block that occurs when a set of discontinuities has formed around the block. Now let's consider the same setting, but with the downstream neighbour being already plucked (*Hancock et al.*, 1998). In this setting entrainment is horizontal, and the horizontal force F_{slide} required to slide the block is,

$$\frac{F_{slide}}{wl} \geq \mu(\rho_s - \rho_w)gh + 2F_l\frac{h}{w} \ , \tag{1.3}$$

with μ the coefficient of basal friction, which mainly depends on the ruggedness of the basal surface. The forces that could slide the block are the shear stress generated by water flow or large pebble impacts with velocity vector with a horizontal component.

This simple analysis reveals that plucking is favored by blocks with a low height, and by a low ratio of height over width or length. It confirms that the efficiency of plucking increases with fracture density if the network of fractures exhibits at least 3 different orientations.

During this thesis I have started to investigate the mechanics of erosion by plucking using both experimentation based on circular flume (*Attal and Lavé*, 2009) and numerical modeling. However the results are too preliminary to be efficiently presented in this manuscript.

Competition between Plucking and Abrasion: The Hérault river

The Hérault river offers both plucking and abrasion dominated environments. Moreover, at some locations, both erosion processes are simultaneously active. Figure 1.6 presents an interpreted picture of a location where both plucking and abrasion are active. Plucking occurs only for relatively low limestone layer thickness, as it uses the interlayer interface as a mechanical discontinuity that eases block removal. This confirms that the density of mechanical discontinuities is a controlling factor on plucking efficiency. Abrasion increases where water height, and consequently shear stress, increases.

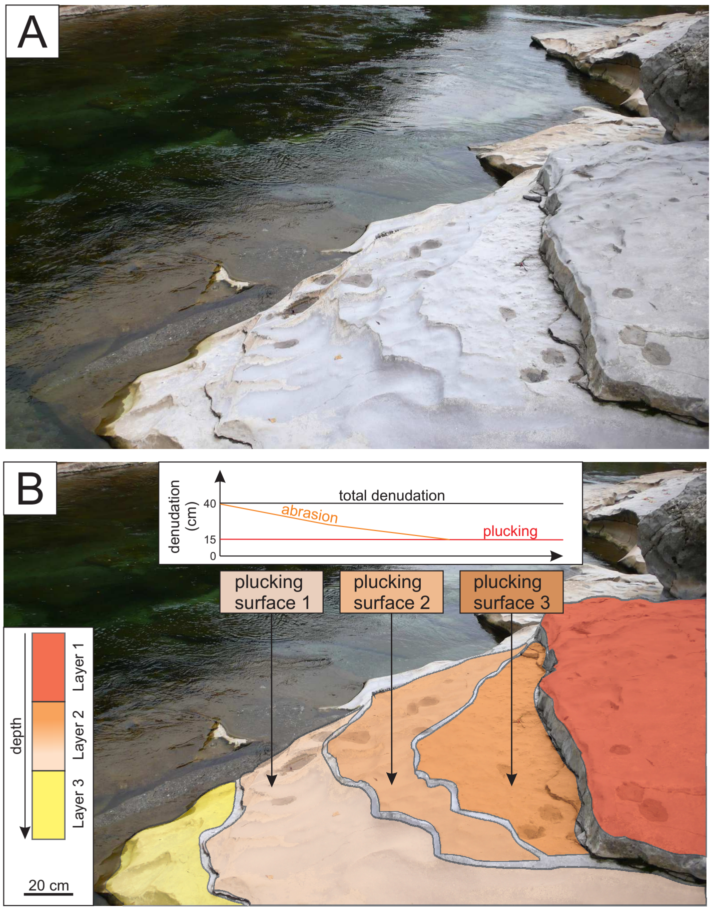

Figure 1.6: Picture of the Hérault river (A) and its geomorphological interpretation (B). The river flows downward. At this location 3 limestone layers are present, and the total erosion increases from right to left. The red layer ($\sim$ 15 cm thick) is above the two other layers, the orange one ($\sim$ 40 cm thick) is intermediate, and the yellow one ($\sim$ 50 cm thick) sets the base. It is interesting to note that only the red layer shows evidences of plucking, and it correlates with a lower layer thickness. On the other hand, the orange and yellow layers only exhibit evidences of abrasion. However abrasion of these layers is strongly influenced by the chronology of plucking events, which has set the starting time of abrasion of these layers. At least two other evidences of plucking are present on the orange layer. Interestingly, plucking results in the exhumation of the inter-layer roughness which can be used as a time-marker of erosion. Roughness decreases at the present surface of the orange layer from right to left, which indicates that total abrasion, which smoothes this rougnhess, is more intense close to the river and/or that plucking of the red layer is older close to the river.

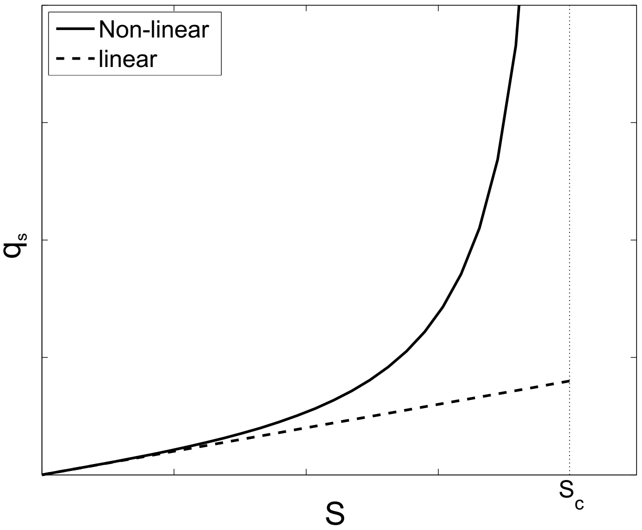

Figure 1.7: Sediment flux q_s as a function of the slope S for the linear (dashed line) and the non-linear (solid line) diffusion models of hillslope erosion. The critical slope S_c above which landsliding occurs is indicated by a dotted line.

2.1.1.b Hillslope Erosion

Hillslope erosion processes are also dependent on the local context: landsliding in steep areas, soil-creeping, burrowing by animals, rainsplash and runoff on soil-mantled hillslopes (*Dietrich et al.*, 1987; *Bryan*, 2000). Splash erosion is driven by rainsplash kinetic energy (*Ekern*, 1950). Its efficiency depends mainly on raindrop characteristics, wind conditions (e.g., *Pedersen and Hasholt*, 1995) and soil properties (*Cruse and Larson*, 1977). Runoff erosion is due to hydraulic flow onto soil. It is dependent on hydraulic flow conditions and on soil conditions which control respectively, erosion forces, and soil response to erosion forces (*Bryan*, 2000). Soil creeping is due to the disturbance of soil by animals and the displacement of soil particles by wetting-drying cycles (*Heimsath et al.*, 2002). Triggering conditions and mechanisms for landslides and debris flows vary between landslide types. Steepness of the slope, fracturation and pore pressure are some common triggering factors of landsliding.

All these processes (i.e., runoff, creep, rainsplash) are termed as disturbances. Hillslope erosion is thus a result of a competition between the energy introduced into the system by these disturbances and gravitational and frictional forces that dissipate energy and act to balance the system. Disturbances are classicaly considered as random and isotropic processes, which can be modeled by a constant power supply at geomorphic time scale.

For soil-mantled hillslopes, transport of soil particles is classicaly described as a diffusive process of the local topographic gradient ∇z (*Culling*, 1960, 1963; *Roering et al.*, 1999),

$$q_s = K\nabla z \ , \tag{1.4}$$

where q_s is the flux of particles (i.e. sediments), and K is the coefficient of diffusion. Field estimates of downslope sediment flux on low to moderate gradient are consistent with linear diffusion over both short (*Schumm*, 1967) and long timescales (*McKean et al.*, 1993).

When considering high local topographic gradient, non-linear diffusion is required, (*Roering et al.*, 1999),

$$q_s = \frac{K\nabla z}{1-(|\nabla z|/S_c)^2} \ , \tag{1.5}$$

with S_c the crictical slope above which landsliding occurs. Figure 1.7 compares sediment fluxes as a function of the topographic gradient for the linear and non-linear diffusion.

Practically, these models of particle transport also assume that soil production rate from regolith is at least equal to the transport rate, so that transport is not limited by production (e.g., *Heimsath et al.*, 1997).

As other diffusion laws, hillslope erosion laws based on diffusion assume that the motion of particles is only dependent of the local properties of the hillslope, i.e. mainly the local topographic gradient ∇z. Here the characteristic transport length for each particle, associated to the diffusion law, is assumed to be small (local) compared to the scale of the hillslope (non-local). This assumption may not hold in the case of steep hillslopes, where non-locality is believed to be an important feature of hillslope transport (*Tucker and Bradley*, 2010). *Foufoula-Georgiou et al.* (2010) derive an anlytical model of hillslope transport based on the assumption of non-locality where the sediment flux at a point is also a function of upslope topography. It is interesting to note that non-locality also results in non-linear diffusion (Eq. 1.5).

2.1.2 Landscape Scale

Upscaling from physical process (10^{-2}-10 m) to the scale of a landscape ($> 10^2$ m) involves taking into account the spatial variability of erosion process, their interactions with solid Earth deformation, and the dynamics of the system at the appropriate time scale (geomorphic timescale). It is uncommon that a single process shapes the morphology of a landscape, and thus it is difficult to extract landscape dynamic properties from its direct observation, from one “snapshot”.

In non-glaciated orogens, landscapes are dissected in several hillslopes by the fluvial network. Thus the characteristic size of hillslopes 10^1-10^3 m, is limited and bounded by rivers. Hillslopes can be described at the scale of a landscape by the laws that are derived for the scale of the processes, i.e., by non-linear diffusion (Eq. 1.5). This is supported by observation of local relief for active orogens which fits non-linear diffusion with respect to their mean slope (*Montgomery and Gran*, 2001a). It is also important to note that under specific conditions, such as in active orogens, hillslopes are dominated by landslides (*Hovius et al.*, 1997) and can be modeled by a critical angle of repose at first order (e.g., *Lavé*, 2005). Thus in the following we only focus on upscaling river erosion to the scale of landscapes.

2.1.2.a Mechanistic Approach

The last decade has seen an increasing awareness of the need for a mechanistic river incision law. *Sklar and Dietrich* (2004) derive from Eq.1.1 a mechanistic model of erosion by saltating bed load abrasion, in which the erosion rate E is defined as the product of the average volume of rock detached per particle-bedrock impact V_i, the rate of particle impacts per unit bed area per unit time I_r, and the fraction of exposed bedrock on the river bed F_e,

$$E = V_i I_r F_e \ . \tag{1.6}$$

The particle impact rate is defined as,

$$I_r = \frac{6q_s}{\pi \rho_p \Phi_p^3 L_s} \ , \tag{1.7}$$

with q_s the particle flux, Φ_p the particle diameter, ρ_s its density, and L_s the hop length. The fraction of exposed bedrock on the river bed varies between completely exposed bedrock to completely alluviated conditions, where the bedrock is protected from a thick layer of bed load which dissipates impact kinetic energy into inter-particles friction. *Sklar and Dietrich* (2004) assumes that F_e varies linearly between these two end-members, so that

$$F_e = 1 - q_s/q_t \ \text{ for } q_s \leq q_t \ , \tag{1.8}$$

where q_t is the transport capacity for a fully-alluviated river bed. Note that it is debated whether F_e should be linearly or exponentially related to q_s/q_t (*Turowski et al.*, 2007). Combining previous equation leads to a mechanistic expression of the rate of river erosion by saltating bed-load abrasion,

$$E = \frac{q_s v_p^2 Y}{L_s k_p \sigma_T^2} \left(1 - \frac{q_s}{q_t} \right) \ . \tag{1.9}$$

Lamb et al. (2008) and *Chatanantavet and Parker* (2009) have extended this mechanistic model to abrasion by suspended load and to plucking, respectively. Such models are able to reproduce many characteristic features of river incision, such as knickpoint migration (*Chatanantavet and Parker*, 2009) or the tools or cover effects (F_e), which are respectively the shortage of abrasive sediments, and the protection of bedock by sediments, respectively (*Sklar and Dietrich*, 1998, 2004, 2006; *Turowski et al.*, 2007). Moreover, it enables predicting river profiles depending on the dominant erosion mechanism. On the other hand, these models are difficult to apply to natural cases or to use in models coupling erosion and tectonics, due to the high number of model parameters, many of which are poorly constrained.

2.1.2.b Empirical Approach

Two main classes of models are classicaly used to model long-term river erosion: transport-limited models (e.g., *Willgoose et al.*, 1991) which assume that the erosion rate is limited by the rate at which sediments are transported, and detachment-limited models (e.g., *Howard and Kerby*, 1983) which assume that erosion rate is not limited by transport but only by the rate of particle-detachment from the bedrock.

Detachment-limited Models In detachment-limited conditions, river incision of the bedrock is classicaly deduced from the so-called stream-power model (*Howard and Kerby*, 1983; *Howard*, 1994; *Whipple and Tucker*, 1999), where the erosion rate of a river E is a power function of the drainage (or contributing, or upslope) area A and of the local channel bed-slope S:

$$E = KA^m S^n \ , \tag{1.10}$$

with K a constant that depends on bedrock erodibility, climate, channel geometry and perhaps sediment supply, m and n are the area and slope empirical exponents. This model was first applied to explain changes in badland topographies (*Howard and Kerby*, 1983).

The stream-power erosion law could be related (empirically) to different mechanistic models of river erosion depending on the value of m and n (*Tucker and Whipple*, 2002):

- bed shear-stress for $m \simeq 0.3$ and $n \simeq 0.7$ (*Howard and Kerby*, 1983);
- stream-power per unit channel length for $m \simeq 1$ and $n = 1$ (*Seidl and Dietrich*, 1992);
- stream-power per unit bed area for $m \simeq 0.5$ and $n \simeq 1$ (*Whipple and Tucker*, 1999);

All these models use an equation 1.10 that has the form of a non-linear advection equation as in $1D$ it can be expressed as,

$$\frac{\partial h}{\partial t} = -KA^m |\frac{\partial h}{\partial x}|^n \ , \tag{1.11}$$

where h is the river channel elevation, and x is along-stream distance.

In Chapter 8 I explore the implications of a detachment-limited erosion law on the wavelength of landscapes.

Transport-limited Models In transport-limited models (e.g., *Willgoose et al.*, 1991), the fluvial sediment volumetric transport capacity Q_t is cast as a power function of slope S and drainage area A,

$$Q_t = KA^m S^n \ , \tag{1.12}$$

where K is the transport efficiency factor, and is a function of grain size and density, bed roughness, climate, hydrology, and channel geometry. Equating volumetric total transport rate Q_s with capacity Q_t, and imposing continuity of mass leads to,

$$\frac{\partial h}{\partial t} = -K\frac{\partial}{\partial x}\left[A^m |\frac{\partial h}{\partial x}|^n / W\right] \ , \tag{1.13}$$

where W is channel width. This equation has a strong diffusive component ($\partial h/\partial t \ \alpha - \partial^2 h/\partial x^2$ for $n = 1$). It is also interesting to note that transport-limited models is also dependent on non-local properties of sediment supply, compared to the detachment-limited model.

We invite the reader to refer to *Tucker and Whipple* (2002) for a detailed comparison between transport- and detachment-limited models, and to *Sklar and Dietrich* (2006) for a complete overview of existing model of river incision. It is important to note that both transport- and detachment-limited models can be extended to include a critical threshold for transport or detachment, respectively.

Last *Gasparini et al.* (2007) demonstrated that the stream-power model can in fact be derived from the mechanistic model of river erosion by bed load abrasion. This implies that the stream-power which is based on simple physics (i.e., for instance erosion rate proportional to shear-stress) reproduces mechanistic erosion with a simple physics and scaling properties. Thus the stream-power model is probably the most suitable model to couple with a tectonics model.

Steady State: A physical system in *steady-state* has numerous properties that are not changing with time. This implies that for any properties of the physical system, for instance the elevation h of the Earth's surface, the partial derivative with respect to time is zero:

$$\frac{\partial h}{\partial t} = 0 \; . \tag{1.14}$$

In many systems, such as the Earth's surface, steady state is not achieved until some time has elapsed after the system is initiated. This initial situation is defined as a *transient state*. By considering the Earth's surface, *Willett and Brandon* (2002) defined 4 properties, relevant to the dynamic of an orogen, able to achieve steady state:

1. Erosional flux steady state, $\partial q_s/\partial t = 0$.
2. Topographic elevation steady state, $\partial h/\partial t = 0$.
3. Subsurface thermal steady state, $\partial T/\partial t = 0$.
4. Exhumational steady state, that characterizes the cooling age of minerals considered as thermochronologic systems.

Surface processes dynamics is mainly constrained by the observation of their resulting spatial properties and scaling at steady-state. For instance a river submitted to uplift and erosion by stream power is expected to exhibit a power-law relation between its local slope and drainage area at steady state (e.g., *Howard*, 1994), The exponent of the power law being dependent on the slope and area exponents.

2.2 Modeling of Fluvial and Hillslope Erosion in $1D$

In the following we present numerical methods that allow modeling of the evolution of hillslopes or river $h(x,t)$ submitted to erosion in $1D$. Numerical schemes based on the finite differences are the most commonly used methods to solve differential equations. It is based on the resolution of a differential equation on a discretized space (for spatial derivative) or time (for temporal derivative) which are called nodes. Finite differences approximate the solutions of differential equations by replacing derivative expressions with approximately equivalent difference quotients. By definition, the first derivative of a function f is,

$$f'(a) = \lim_{a \to 0} \frac{f(x+a) - f(x)}{a} \; , \tag{1.15}$$

and a reasonable approximation for that derivative is,

$$f'(a) = \frac{f(x+a) - f(a)}{a} \ , \tag{1.16}$$

for a small value of a. Intuitively the quality of the approximation depends on the value of a, which is the spacing between the nodes of the discretized space or time. This is called a forward scheme.

Approximation of derivatives can be obtained from Taylor's polynomia of the differentiable function considered,

$$f(x+a) = f(x) + \frac{f'(x)}{1!}a + \frac{f^{(2)}(x)}{2!}a^2 + ... + \frac{f^{(n)}(x)}{n!}a^n + R_n(x) \ , \tag{1.17}$$

where $R_n(x)$ is a remainder term denoting the difference between the Taylor polynomia of degree n and the original function, and characterizes the amplitude of the error due to discretization. Taylor's polynomia allows one to express a derivative of degree n as a function of the derivative of smaller degree between 1 and $n-1$ (for instance first degreee Eq. 1.16).

It is also possible to define a backward scheme for the first derivative,

$$f'(a) = \frac{f(x) - f(x-a)}{a} + \frac{R_1(x)}{a} \ , \tag{1.18}$$

and a centered scheme,

$$f'(a) = \frac{f(x+a) - f(x-a)}{2a} + \frac{R_2(x)}{a} \ . \tag{1.19}$$

2.2.1 Fluvial incision

Here, rather than presenting numerical schemes that allow one to model river incision, we focus on the ones that were used in the following chapters of this manuscript. We invite the reader to refer to *Pelletier* (2008) for a review of the numerical methods that can be used for fluvial incision.

First let's consider once again the generic form of river long-term erosion by stream power,

$$\frac{\partial h(x,t)}{\partial t} = -KA^m |\frac{\partial h(x,t)}{\partial x}|^n \ , \tag{1.20}$$

where h is river elevation, A is the contributing area, and m and n some constant exponents. This is an advection equation, that can be rewritten if considering the exponents of the stream-power erosion per unit bed area ($m = 0.5$ and $n = 1$) as,

$$\frac{\partial h(x,t)}{\partial t} = c\frac{\partial h(x,t)}{\partial x} \ , \tag{1.21}$$

Two partial derivatives are present in this equation, on the left hand side a partial derivative of river elevation $h(x,t)$ with respect to time t, and on the right hand side a partial derivative of river elevation $h(x,t)$ with respect to along-stream distance x. Thus two numerical schemes are required to solve this equation. The discretization is expressed through the j-th index for time, and through the i-th indice for space. The time and space increments are $\Delta t = t_{j+1} - t_j$ and $\Delta x = x_{i+1} - x_i$.

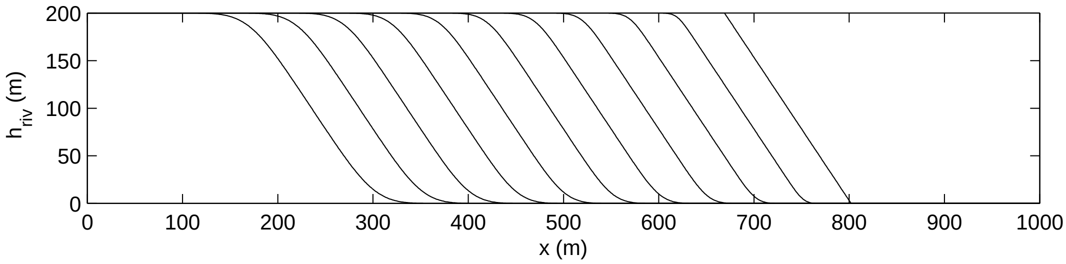

Figure 1.8: Knickpoint advection (from right to left) using the Upwind-difference scheme presented in Eq. 1.27. Note the progressive numerical diffusion of the knickpoint on its edges with time.

To illustrate how to solve the preceding equation, let's consider the evolution of a knickpoint submitted to river incision by stream power assuming a homogeneous A and $n = 1$. Under these conditions the stream-power equation is,

$$\frac{\partial h(x,t)}{\partial t} = -K_{knick} | \frac{\partial h(x,t)}{\partial x} | \ , \tag{1.22}$$

with K_{knick} including both erodibility and drainage area.

Then let's define a numerical scheme for the time derivative. Practically it is convenient to use an explict forward scheme, where the derivative at the timestep j is expressed as,

$$\frac{\partial h(x,t)}{\partial t}|_i = \frac{h(x_i,t_{j+1}) - h(x_i,t_j)}{t_{j+1} - t_j} \ , \tag{1.23}$$

and its compact form is,

$$\frac{\partial h}{\partial t}|_i = \frac{h_i^{j+1} - h_i^j}{\Delta t} \ . \tag{1.24}$$

For the space derivative, the most common scheme is the centered one,

$$\frac{\partial h}{\partial x}|_i = \frac{h_{i+1}^j - h_{i-1}^j}{2\Delta x} \ . \tag{1.25}$$

However it is unconditionally unstable for the advection equation.

Thus it is more appropriate to use an upwind-difference scheme, where the slope is calculated along the direction of transport. Combining both temporal finite difference with the spatial one using Upwind-difference leads to,

$$\frac{h_i^{j+1} - h_i^j}{\Delta t} = K_i^j \frac{h_{i+1}^j - h_i^j}{\Delta x} \quad \text{if} \quad K_i^j > 0 \ , \tag{1.26}$$

$$= K_i^j \frac{h_i^j - h_{i-1}^j}{\Delta x} \quad \text{if} \quad K_i^j < 0 \ . \tag{1.27}$$

Figure 1.8 presents the advection of a knickpoint using this numerical scheme. The knickpoint is advected from right to left, however numerical diffusion occurs on the boundaries of the knickpoint. Following *Pelletier* (2008) it is convenient to use the procedure of *Smolarkiewicz* (1983) to correct this numerical diffusion.

The Upwind-difference scheme is used in Chapter 8, while Smolarkiewicz correction is applied in Chapter 2.

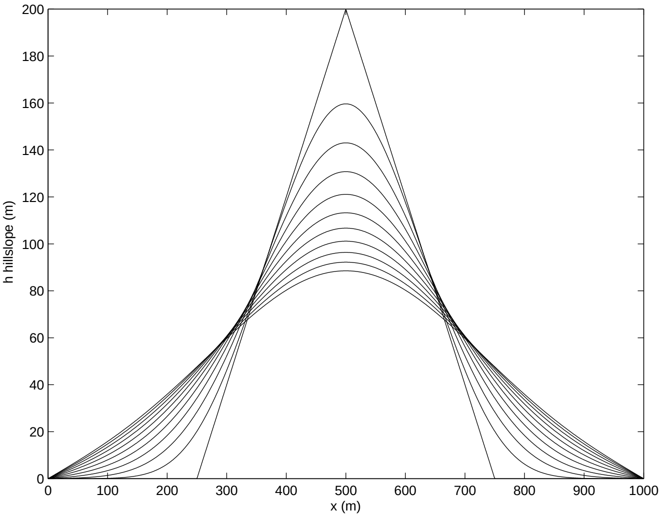

Figure 1.9: Evolution of a hillslope submittted to erosion by diffusion of its elevation. Two spatial boundary conditions are applied as the erosion rate is nul at the both ends of the model.

2.2.2 Hillslope erosion

At first order, soil-mantled hillslope erosion can be modeled by a linear-diffusion law of hillslope elevation h (Eq. 1.4). Combining a transport law proportional to hillslope elevation gradient with conservation of mass leads to the equation of linear diffusion,

$$\frac{\partial h(x,t)}{\partial t} = K\frac{\partial^2 h(x,t)}{\partial x^2} \ , \qquad (1.28)$$

with K the coefficient of diffusion, here assumed homogeneous.

Once again two numerical schemes (time and space) are required to solve this equation. An explicit forward scheme is employed for time discretization, and an explict centered scheme of degree 2 for space discretization,

$$\frac{h_i^{j+1} - h_i^j}{\Delta t} = K_i^j \frac{h_{i+1}^j - 2h_i^j + h_{i-1}^j}{\Delta x^2} \ . \qquad (1.29)$$

Figure 1.9 shows the evolution of a hillslope with this numerical scheme.

2.3 Modeling of Fluvial and Hillslope Erosion in $2D$

In active orogens, the basic units of landscapes are hillslopes, which are separated from each other by the fluvial network (see Fig. 1.10). Hillslope erosion and river erosion are coupled: river erosion lowers the base level of hillslopes, and hillslopes on the other hand are the first source of sediments that erode the river.

2.3.1 Modeling Landscape Evolution

$2D$ plan view models make it possible to investigate the effects of this coupling on the landscape dynamics and morphology. The last two decades have seen

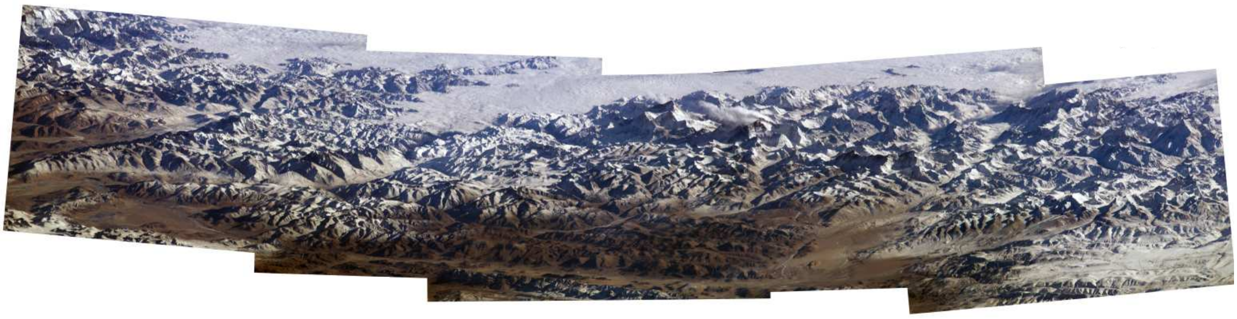

Figure 1.10: Mosaic of aerial pictures of the Himalaya, Nepal (source: NASA). The image is centered on the Everest. Note the presence of rivers which dissect the landscape into isolated hillslopes.

an increasing number of studies using surface processes models (SPM) with both different physics and numerical implementation (*Willgoose et al.*, 1991; *Beaumont et al.*, 1992; *Howard*, 1994; *Braun and Sambridge*, 1997; *Tucker and Slingerland*, 1996; *Tucker et al.*, 2001a; *Pelletier*, 2004; *Perron et al.*, 2008).

The space discretization is either uniform using a square grid composed of regular pixels (e.g., *Pelletier*, 2004), or non-uniform with an irregular and adaptative triangular grid (*Braun and Sambridge*, 1997; *Tucker et al.*, 2001b). This latter option offers more adaptability as the grid can be refined where it is required, for instance rivers. Moreover they can be coupled to numerical codes of solid earth deformation, which employ irregular and adaptative grids that force both the vertical and the horizontal velocity of the surface (*Braun et al.*, 2008).

Evolution of landscape elevation h classicaly follows:

$$\frac{\partial h}{\partial t} = U - E_{riv} - E_{hill} \ , \tag{1.30}$$

with U the uplift rate, E_{riv} and E_{hill} the erosion rate due to river and to hillslope erosion laws, respectively. The degree of complexity of the physics used to model landscape evolution is also very variable, ranging from long-term fluvial erosion by stream power with hillslopes controlled by a crictical slope of landsliding (*Pelletier*, 2004), to stochastic fluvial erosion by stream power and non-linear diffusion of hillslopes (*Tucker et al.*, 2001a). However, as already mentioned, in active orogens hillslopes are dominated by landslides (*Hovius et al.*, 1997) and long-term river erosion is reasonably modeled by a detachment-limited law (*Lavé and Avouac*, 2001). These dominant physical processes of erosion in active orogens are thus taken into account by the modeling approach of *Pelletier* (2004) and *DeLong et al.* (2007).

2.3.2 A Simple Surface Processe Model

Here I present a simple method to model landscape evolution in $2D$. Following *Pelletier* (2004), the surface processes model (SPM) that is developed here assumes that:

- hillslopes are dominated by landslides and follow a critical angle of repose ϕ_c;
- river erosion follows stream-power per unit bed area with $m = 0.5$ and $n = 1$;

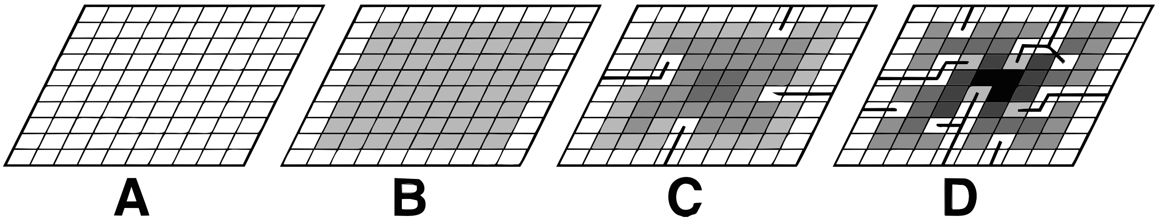

Figure 1.11: Schematic representation of the surface processe model behaviour under constant uplift rate and both fluvial and hillslope erosion (*DeLong et al.*, 2007). Time increases from left to right, solid lines indicates the fluvial network, and pixel elevation is indicated by a gray scale.

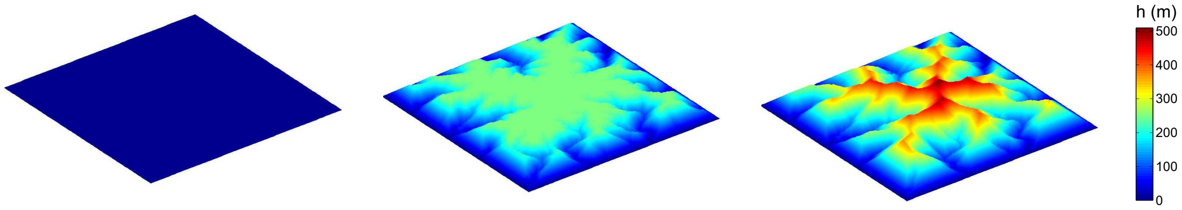

Figure 1.12: Evolution of the elevation h of surface of the SPM model under constant uplift rate and both fluvial and hillslope erosion. Time increases from left to right until reaching topographic steady-state. Surface elevation is indicated by the colormap. The model is a square with 3 km of side length, and includes 10.000 pixels.

- the entire landscape is subjected to a constant and homogeneous uplift rate U, exept at the boundaries of the model where elevation is kept constant at the base level.

Figure 1.11 shows a schematic evolution of the SPM. Drainage area is determined using a bifurcation method that routes flow to multiple downslope directions, weighted by local slope (*Freeman*, 1991; *Pelletier*, 2004).

Numerical implementation of this SPM requires iteration over the following steps:

- Uplift the surface and respect boundary conditions;
- Compute slope and force it to respect the critical slope of landsliding;
- Fill river pits by sedimentation;
- Compute drainage area with the flow algortithm;
- Deduce fluvial erosion rate and modify surface elevation.

To illustrate this SPM, figure 1.12 presents the time evolution of the surface of the model until reaching a topographic steady-state. SPM topographic outcomes allow comparing of predicted topography with real topographies, and offer both a way to constrain the 2D behaviour of erosion laws and to test their transient dynamics.

In Chapter 7 we investigate the relation between erodibility and the wavelength of landscapes using this SPM.

2.4 2D in 1D

Practically $1D$ or $2D$ models of surface processes are compatible with $2D$ or $3D$ solid earth models, respectively. The main benefit of $2D$ solid earth models are their relatively small computational times compared to $3D$ models. However the coupling with surface processes, which is natural with $3D$ models, is not natural with $2D$ models. Indeed the pertinent variable for the upper boundary of a $2D$ solid earth model, which mechanically responds to gravitational forces, is the mean elevation, not the elevation of the river channel (*Godard et al.*, 2006; *Willett*, 2010).

Thus to couple both fluvial and hillslope erosion with a $2D$ solid earth model, it is required to integrate the elevation from $2D$ to $1D$ and to divide by the total lateral length L of the topography considered, in order to get a $1D$ profile of the mean elevation:

$$h_{mean}(x,t) = \frac{1}{L}\int_y h(x,y,t)\,\mathrm{dy}\ . \tag{1.31}$$

In the following we propose to extend the formalism of the integration of landscape evolution of a rectangular watershed from $2D$ to $1D$ described by *Lavé* (2005) to:

- a watershed represented by Hack's law (*Willett*, 2010);
- fluvial incision taking into account a stochastic distribution of water discharge (*Lague et al.*, 2005);

The watershed is composed of the main river that defines the watershed, of its tributaries, and of the hillslopes that make up the non-fluvial reliefs. Compared to *Willett* (2010) we also propose to take into account realistic self-adapting hillslope relief in the tributary basins (*Lavé*, 2005). The methods that we employ numerically solve the evolution of the main river, and consider that tributary rivers (and consequently hillslopes) can be analytically derived using the same evolution law as for the main river.

2.4.1 Geometrical description of the physical system

2.4.1.a Main river and main watershed

The watershed described here follows Hack's law (*Hack*, 1957; *Rigon et al.*, 1996), which provides a relationship between the area of the watershed A and the length of its main (i.e., the longest) river x_l,

$$A = k_a {x_l}^h\ , \tag{1.32}$$

with k_a and h empirical constants.

Main river tributaries, which flow orthogonally to the main river (*Stolar et al.*, 2007) have a length y_l which is deduced from Hack's law,

$$y_l = \frac{1}{2}k_a {x_l}^{h-1}\ , \tag{1.33}$$

Note that it is possible to consider the sinuosity of both the main and tributary rivers by multiplying their cartesian lengths by their averaged sinuosity s_0,

$$x_l = s_0 x\ ,\ \ y_l = s_0 y\ . \tag{1.34}$$

2.4.1.b Tributary fluvial network

In this section we aim to express the length and area of the tributary fluvial network. A classical framework to describe a fluvial network is to use Horton's (*Horton*, 1945) ordering, in which the geometrical caracteristics of the stream segments of order i are related to the upper order stream segments by the following relationships,

$$\frac{n_i}{n_{i+1}} = R_n \ , \ \frac{\Delta L_{i+1}}{\Delta L_i} = R_L \ , \ \frac{A_{i+1}}{A_i} = R_A \ , \tag{1.35}$$

where n_i, ΔL_i and A_i are the number of stream segments of order i, their average length, and their average contributing area, respectively. R_n, R_L and R_A are the bifurcation, length and area ratios. It can be shown that bifurcation, area and length ratios are linked to the order of the stream segment considered by the following expression, $1-\omega = \frac{ln(R_L)-ln(R_N)}{ln(R_A)}$.

The length L of a fluvial network that drains an area A can be expressed as a density function (Fig. 1c *Lavé*, 2005),

$$f_L(A) = K_L A^{-\omega} \ , \tag{1.36}$$

where K_L and ω are constants. This density function strongly depends on the channel organization and branching network. If the drainage density is roughly uniform over the watershed considered (here tributary basins), K_L is proportional to $\frac{A_T}{A_0^{1-\omega}-A_T^{1-\omega}}$, with A_0 the average head source area of the fluvial network considered and A_T the total area of the watershed considered. This last expression reduces to $\sim A_T$ when $\omega > 1$ and $A_T >> A_0$. Note that K_L is uniform and independant of A.

At this stage we have expressed by a density function the length of a fluvial network that comprises an area between A and $A+dA$. Integrating this density function over the total area A_T of a tributary watershed gives the total length of the fluvial network in this watershed,

$$L_{tot} = \int_{A_0}^{A_T} f_L(A)dA \ , \tag{1.37}$$

$$= K_L \int_{A_0}^{A_T} A^{-\omega} dA \ , \tag{1.38}$$

$$= \frac{K_L}{1-\omega}(A_T^{1-\omega} - A_0^{1-\omega}) \ . \tag{1.39}$$

Linking the tributaries to the main watershed gives an expression of the total area of each tributary watershed. Indeed, the length y_l of the longest tributary river is directly dependent on the main river length x_l at its confluence with the tributary. Using Hack's law, the total area of the tributary watershed A_T is,

$$A_T = k_a {y_l}^h \ , \tag{1.40}$$

$$= \frac{1}{2^h} k_a^{h+1} {x_l}^{h(h-1)} \ , \tag{1.41}$$

2.4.1.c Hillslopes

The hillslopes are defined as the non-fluvial part of the main watershed, which corresponds to the non-fluvial part of the tributaries. As a consequence, the proportion of a watershed occupied by hillslopes can be described using the description of the tributary fluvial network.

Dividing the total area A_T of the tributary watershed by two times the total length of its fluvial network L_{tot} roughly gives a characteristic width w_{hill} of hillslopes in the tributary watershed considered,

$$w_{hill} = \frac{A_T}{2L_{tot}} \ , \tag{1.42}$$

$$= \frac{(1-\omega)}{2K_L} \frac{A_T}{(A_T^{1-\omega} - A_0^{1-\omega})} \ , \tag{1.43}$$

Alternatively, a simplified expression of w_{hill} can be obtained by noticing that the head sources of the fluvial network are part of the hillslopes. Thus the hillslope width can be defined from the average head source area, assuming that Hack's law is valid at the head of the fluvial network,

$$w_{hill} = \left(\frac{A_0}{k_a}\right)^{1/h} \ . \tag{1.44}$$

This last expression will be used in the following.

2.4.2 Evolution of the physical system

The physical system that was geometrically described in the previous section, is submitted to both erosion and uplift. The uplift function can be deduced by coupling with a geodynamical model. Erosion occurs along the main river of the watershed, but also along its tributaries, and on the hillslopes.

2.4.2.a Main river erosion

Following *Lavé and Avouac* (2001), we adopt a simple detachment-limited relation that has provided first-order results accross the Subhimalaya. This relation states that the instantaneous bedrock incision rate of a river i is proportional to its unit stream power,

$$i = k \left(\left(\frac{Q}{W}\right)^m S^\alpha - \tau_c \right) \ , \tag{1.45}$$

with S the local channel slope, Q the water discharge, W the width of the river channel, m and α the stream power exponents, τ_c a critical unit stream-power threshold for incision, and k a dimensional erodibility coefficient.

Effective discharge Assuming that Q reflects a long-term effective discharge, we can empirically describe its downstream variations,

$$Q = k_Q A^\xi (\bar{P} - P_0) \ , \tag{1.46}$$

with ξ an exponent, k_Q a dimensional coefficient, P_0 a precipitation threshold, and $\bar{P}$ the upstream spatially averaged precipitation rate P over the drainage area,

$$\bar{P}(A) = \frac{1}{A} \int^A P(A') dA' \ , \tag{1.47}$$

The downstream variations of the river channel width is also empirically described (*Leopold and Maddock*, 1953; *Montgomery and Gran*, 2001b; *Snyder et al.*, 2003),

$$W = k_a Q^{\omega_a} \ , \tag{1.48}$$

with ω_a an exponent and k_a a dimensional coefficient. Combining previous equations and assuming that an effective discharge allows to reproduce long-term river incision rate I, leads to,

$$I = k\left(k_{eff} A^{\gamma} (\bar{P} - P_0)^{\beta} S^{\alpha} - \tau_c\right) \ , \tag{1.49}$$

with $\gamma = \xi m(1-\omega_a)$ the apparent area exponent, $\beta = m(1-\omega_a)$ the apparent precipitation exponent, and $k_{eff} = k_a^{-m} k_Q^{m(1-\omega_a)}$.

Stochastic distribution of discharge Now instead of using an effective water discharge to describe long-term erosion, we rather use an erosion law that reflects instantaneous erosion and integrates it over a stochastic distribution of discharge to express the long-term river erosion law (*Lague et al.*, 2005).

The downstream variation of river width is still expressed by,

$$W_a = k_a \bar{Q}^{\omega_a} \ , \tag{1.50}$$

and its at-a-station temporal variations by,

$$W = W_a \left(\frac{Q}{\bar{Q}}\right)^{\omega_s} \ , \tag{1.51}$$

with Q the instantaneous river water discharge, $\bar{Q}$ the river mean water discharge (averaged over time), and ω_s an exponent. Combining the last two equations leads to,

$$W = k_W Q_\star^{\omega_s} \bar{Q}^{\omega_a} \ , \tag{1.52}$$

with $Q_\star = Q/\bar{Q}$ the normalized water discharge (or water discharge ratio), and k_W a constant. Combining last equation with Eq. 1.45 gives,

$$i = k\left(k_W^{-m} Q_\star^{m(1-\omega_s)} \bar{Q}^{m(1-\omega_a)} S^{\alpha} - \tau_c\right) \ . \tag{1.53}$$

Now we make the assumption that the at-a-station river water discharge temporal variability can be expressed through a power law distribution,

$$pdf(Q_\star) = \frac{\chi^{\chi+1}}{\Gamma(\chi+1))} Q_\star^{-(\chi+2)} \ , \tag{1.54}$$

with χ an exponent, and Γ the Gamma function such that if χ is an integer then $\Gamma(\chi+1) = \chi!$. Then we can integrate the incision rate to express the long-term incision rate,

$$I = \int_{Q_{c\star}}^{Q_{m\star}} pdf(Q_\star) i(Q_\star) dQ_\star \ , \tag{1.55}$$

with i the incision rate defined in Eq. 1.53. $Q_{c\star}$ is the critical water discharge ratio and is defined such that $i(Q_{c\star}) = 0$, i.e. $Q_{c\star}$ is the minimum discharge for which the critical unit stream-power threshold for incision is overcome. $Q_{m\star}$ is the maximum water discharge ratio at the timescale considered. Note that a power law distribution for water discharge is an approximation that holds if the contribution of low discharge events to erosion is negligible, as it does not reproduce the decrease of number of events for discharge below the average discharge (*Lague et al.*, 2005). It is thus a correct approximation when $Q_{c\star}$ is large or when the long-term incision rate is dominated by the largest events. Here we also make the assumption that the previous equation can be integrated with the parameters of the incision law independant of the water discharge, and we obtain for $m(1-\omega_s)-(\chi+1)\neq 1$,

$$I = k\frac{\chi^{\chi+1}}{\Gamma(\chi+1)}\left(k_W^{-m}\bar{Q}^{m(1-\omega_a)}S^{\alpha}\frac{(Q_{m\star}^{m(1-\omega_s)-(\chi+1)}-Q_{c\star}^{m(1-\omega_s)-(\chi+1)})}{m(1-\omega_s)-(\chi+1)}\right.$$
$$\left. -\ \tau_c\frac{(Q_{m\star}^{-(\chi+1)}-Q_{c\star}^{-(\chi+1)})}{-(\chi+1)}\right) . \quad (1.56)$$

At large timescale and in most settings $Q_{m\star}\gg Q_{c\star}$, and if $m(1-\omega_s)-(\chi+1)<1$ (which is likely to be true) then any dependency with $Q_{m\star}$ rapidly vanishes with increasing time in Eq. 1.56, and I converges to a constant whose approximate expression is:

$$I = -k\frac{\chi^{\chi+1}}{\Gamma(\chi+1)}\left(k_W^{-m}\bar{Q}^{m(1-\omega_a)}S^{\alpha}\frac{Q_{c\star}^{m(1-\omega_s)-(\chi+1)}}{m(1-\omega_s)-(\chi+1)}\right.$$
$$\left. +\ \tau_c\frac{Q_{c\star}^{-(\chi+1)}}{\chi+1}\right) . \quad (1.57)$$

In order to simplify previous equation, let's notice that $Q_{c\star}^{m(1-\omega_s)}=k_W^{m}\bar{Q}^{-m(1-\omega_a)}S^{-\alpha}\tau_c$, which gives,

$$I = -k\frac{\chi^{\chi+1}}{\Gamma(\chi+1)}\tau_c Q_{c\star}^{-(\chi+1)}\frac{m(1-\omega_s)}{(\chi+1)(m(1-\omega_s)-(\chi+1))} . \quad (1.58)$$

Ultimately injecting $Q_{c\star}$ and using $\bar{Q}=k_Q A^{\xi}(\bar{P}-P_0)$ in the previous equation leads to,

$$I = \left(\frac{k}{\tau_c'}\right)k_{sto}A^{\gamma'}(\bar{P}-P_0)^{\beta'}S^{\alpha'} , \quad (1.59)$$

with,

$$\tau_c' = \tau_c^{\frac{\chi}{m(1-\omega_s)}} \quad (1.60)$$
$$k_{sto} = -\frac{\chi^{\chi+1}}{\Gamma(\chi+1)}\frac{m(1-\omega_s)}{(\chi+1)(m(1-\omega_s)-(\chi+1))}k_W^{\frac{-(\chi+1)}{(1-\omega_s)}}k_Q^{\frac{(\chi+1)(1-\omega_a)}{(1-\omega_s)}} \quad (1.61)$$
$$\beta' = \frac{(\chi+1)(1-\omega_a)}{(1-\omega_s)} \quad (1.62)$$
$$\gamma' = \xi\beta' \quad (1.63)$$
$$\alpha' = \frac{\alpha(\chi+1)}{m(1-\omega_s)} \quad (1.64)$$
$$(1.65)$$

We can even more simplify previous equation by defining an apparent coefficient of erodibility $k'=k/\tau_c'$, which leads to,

$$I = k'k_{sto}A^{\gamma'}(\bar{P}-P_0)^{\beta'}S^{\alpha'} . \quad (1.66)$$

2.4.2.b Erosion of the fluvial networks and hillslopes of the tributary watersheds

Main river erosion $\dot{h}_{riv}$ drives the evolution of the mean total topography $\dot{\bar{h}}$ through a transfer function. This transfer function is dependent on the erosion of both the tributary rivers $\dot{h}_{trib}$ and the hillslopes $\dot{h}_{hill}$, and on the geometry of the system. To define this function, we first make the assumption that the tributary rivers are subjected to the same erosion law as the main river, and that hillslopes are controlled by a stability angle above which landsliding occurs. In a second case we consider a more complex system, where hillslopes are not only controlled by landsliding, but can also be eroded by diffusion of their elevation when their average slope is below the stability angle. In each case we make the assumption that hillslope erosion is in balance with the local fluvial network.

2.4.2.c Hillslope evolution

Here we assume that hillslopes are controlled by a stability angle ϕ_c, above which landsliding occurs. Combining this definition with the width of the hillslopes (Eq. 1.44) leads to the following expression of the mean hillslope relief,

$$\begin{aligned} \bar{h}_{hill} &= \frac{\tan(\phi_c)}{2} w_{hill} \ , && (1.67) \\ &= \frac{\tan(\phi_c)}{2} \left(\frac{A_0}{k_a}\right)^{1/h} \ , && (1.68) \end{aligned}$$

2.4.2.d Tributary evolution

The volume of topography above a point in a tributary fluvial network $V(A_T)$, can be viewed as the stack of topographic slices. Using the density function defined in Eq. 1.36 each slice has a volume of $Af_L(A)S(A)dA$, with dA the increment of area that defines the slice. Integrating this equation over the total area of the tributary fluvial network gives the volume of topography belonging to this fluvial network,

$$V(A_T) = \int_{A_0}^{A_T} Af_L(A)S(A)dA \ . \tag{1.69}$$

Dividing this volume by the total area of the tributary watershed gives the average fluvial relief in the tributary watershed considered,

$$\bar{h}_{trib} = \frac{V(A_T)}{A_T} \ . \tag{1.70}$$

To explicitly express the slope in Eq. 1.70, we need to make the assumption that the tributary is in steady state, and that $\dot{\bar{h}}_{trib} = u - i = 0$. Using the stream power equation, it is now possible to derive the slope of the tributary fluvial network as a function of the area, assuming that erodibility, uplift, precipitation are uniform in the tributary watershed, for an effective water discharge (Eq. 1.49),

$$S(A) = \left(\frac{u/k + \tau_c}{k_{eff} A^{\gamma} (\bar{P} - P_0)^{\beta}}\right)^{1/\alpha} \ , \tag{1.71}$$

or for a stochastic distribution of water discharge (Eq. 1.66),

$$S(A) = \left(\frac{u/k'}{k_{sto} A^{\gamma'} (\bar{P} - P_0)^{\beta'}} \right)^{1/\alpha'} . \tag{1.72}$$

Combining the previous equation with the expression of the tributary mean fluvial relief and integrating, leads to the following equations for an effective water discharge (Eq. 1.49),

$$\bar{h}_{trib} = \left(\frac{u/k + \tau_c}{k_{eff} (\bar{P} - P_0)^{\beta}} \right)^{1/\alpha} \left(\frac{K_L (A_T^{2-\omega-\gamma/\alpha} - A_0^{2-\omega-\gamma/\alpha})}{(2 - \omega - \gamma/\alpha) A_T} \right) , \quad \text{if } \omega + \gamma/\alpha \neq 2 , \tag{1.73}$$

and

$$\bar{h}_{trib} = \left(\frac{u/k + \tau_c}{k_{eff} (\bar{P} - P_0)^{\beta}} \right)^{1/\alpha} \left(\frac{K_L ln(A_T/A_0)}{A_T} \right) , \quad \text{if } \omega + \gamma/\alpha = 2 , \tag{1.74}$$

or for a stochastic distribution of water discharge (Eq. 1.66),

$$\bar{h}_{trib} = \left(\frac{u/k'}{k_{sto} (\bar{P} - P_0)^{\beta'}} \right)^{1/\alpha'} \left(\frac{K_L (A_T^{2-\omega-\gamma'/\alpha'} - A_0^{2-\omega-\gamma'/\alpha'})}{(2 - \omega - \gamma'/\alpha') A_T} \right) , \quad \text{if } \omega + \gamma'/\alpha' \neq 2 , \tag{1.75}$$

and

$$\bar{h}_{trib} = \left(\frac{u/k'}{k_{sto} (\bar{P} - P_0)^{\beta'}} \right)^{1/\alpha'} \left(\frac{K_L ln(A_T/A_0)}{A_T} \right) , \quad \text{if } \omega + \gamma'/\alpha' = 2 . \tag{1.76}$$

2.4.2.e Denudation Rate of the Mean Topography

As we have previously assumed that the tributaries were at steady state, their incision rates equal their uplift rates. Thus inverting the previous equation gives the expressions of the denudation rate at steady-state, for an effective water discharge (Eq. 1.49),

$$i = k \left(k_{eff} (\bar{P} - P_0)^{\beta} \left(\frac{(2 - \omega - \gamma/\alpha) A_T}{K_L (A_T^{2-\omega-\gamma/\alpha} - A_0^{2-\omega-\gamma/\alpha})} \bar{h}_{trib} \right)^{\alpha} - \tau_c \right) , \quad \text{if } \omega + \gamma/\alpha \neq 2 , \tag{1.77}$$

and

$$i = k \left(k_{eff} (\bar{P} - P_0)^{\beta} \left(\frac{A_T}{K_L ln(A_T/A_0)} \bar{h}_{trib} \right)^{\alpha} - \tau_c \right) , \quad \text{if } \omega + \gamma/\alpha = 2 , \tag{1.78}$$

or for a stochastic distribution of water discharge (Eq. 1.66),

$$i = k' \left(k_{sto}(\bar{P} - P_0)^{\beta'} \left(\frac{(2 - \omega - \gamma'/\alpha')A_T}{K_L(A_T^{2-\omega-\gamma'/\alpha'} - A_0^{2-\omega-\gamma'/\alpha'})} \bar{h}_{trib} \right)^{\alpha'} \right) , \quad \text{if } \omega + \gamma'/\alpha' \neq 2 , \tag{1.79}$$

and

$$i = k' \left(k_{sto}(\bar{P} - P_0)^{\beta'} \left(\frac{A_T}{K_L ln(A_T/A_0)} \bar{h}_{trib} \right)^{\alpha'} \right) , \quad \text{if } \omega + \gamma'/\alpha' = 2 , \tag{1.80}$$

The channel head belongs to both the hillslopes and the tributay fluvial network. Thus it imposes two conditions: (1) the local slope at the channel head in $A = A_0$ is controlled by the stability angle $S(A_0) \leq tan(\phi_c)$; (2) the inverted mean incision rate i computed for the tributary is valid at the channel head and $i(A_0) = i$. Thus the inversion of the tributary mean incision needs to be processed iteratively. The procedure is equivalent using an effective water discharge or using a stochastic distribution of water discharge. Using this iterative algorithm enables to compute the incision rate of the mean topography, and to take into account a source area that balances the incision rate of the tributary.

2.4.2.f Transient and Steady-state Evolution of the River and Mean Topography

Figure 1.13 shows the evolution of the river profile and of the mean topography when subjected to uniform uplift. Similar to $2D$ SPM, erosion by the main river is regressive (from the boundaries to the center of the model). It sets the low points of tributary basins, which are then eroded once the regressive erosion wave of the main river reaches the point of their confluence. At this stage mean topography and main river elevation are no more similar as the local relief of the tributary basins starts to develop.

Topographic steady-state ($E = U$) is reached, first for the main river when the regressive wave has propagated all along the main river up to the main divide. Then the mean topography reached steady-state, when the regressive wave has also propagated up to the divide of the tributary basins, and hillslopes have reached their critical slope.

In Chapter 8, I use the integration of landscape evolution from $2D$ to $1D$ with a stochastic distribution of water discharge to model the topographic decay of post-orogenic mountain belts with a $2D$ deformation model.

3 Numerical Modeling of Lithospheric Thermics, Mechanics and Metamorphism

In the following we introduce the numerical methods that allow modeling of the thermal and mechanical behaviour of the lithosphere. In particular a focus is made

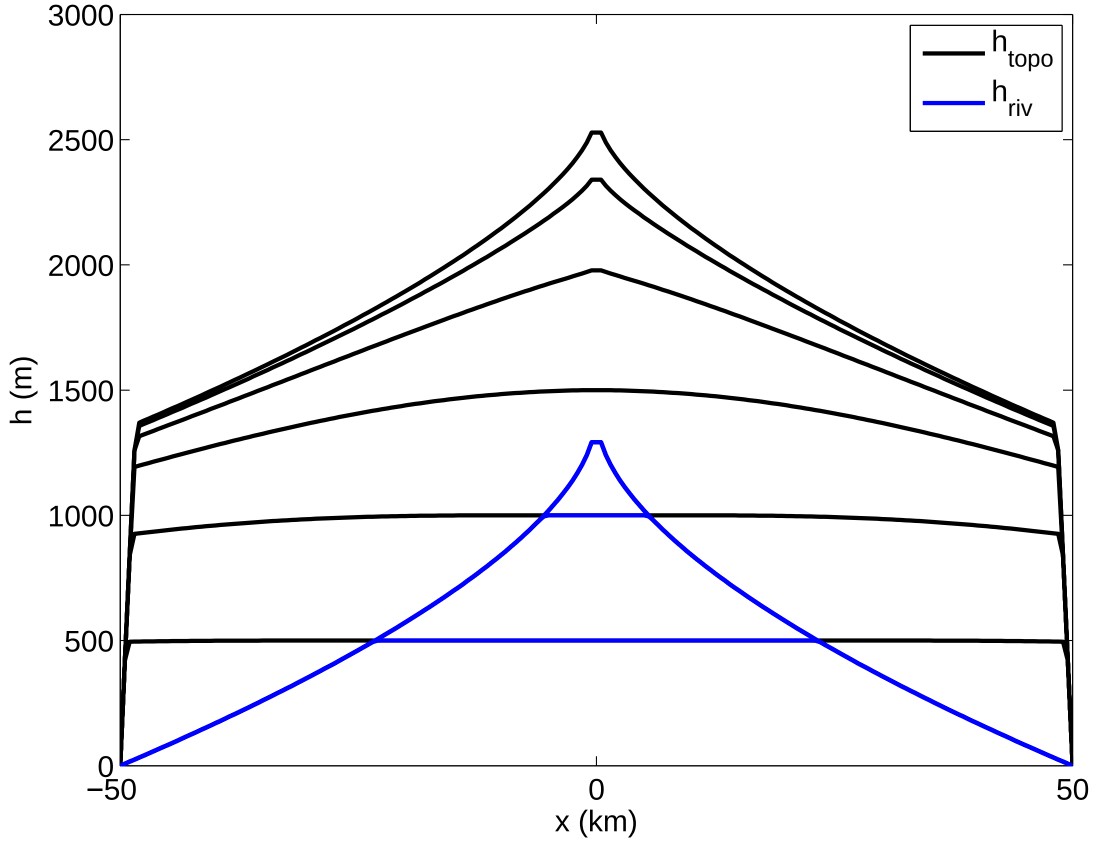

Figure 1.13: Time evolution of the river (blue line) and of the mean topography (black line) with a uniform uplift until reaching steady-state. The initial topography is a triangular surface with a summit of elevation $h = 1$ m at the center. All the parameters of the model are kept constant and uniform. Note that drainage area is not computed assuming a basin's geometry following Hack's law, but for self-similar and rectangular basins (*Lavé*, 2005).

on the finite element solutions to the mechanics of the lithosphere, and it is illustrated with the finite element model (FEM) called ADELI (*Hassani et al.*, 1997). Then I briefly present the thermal behaviour of the lithosphere and its numerical modeling with finite differences.

3.1 Finite Element Models (FEM)

Zienkiewicz et al. (2005): *The limitations of the human mind are such that it cannot grasp the behaviour of its complex surroundings and creations in one operation. Thus the process of subdividing all systems into their individual components or elements, whose behaviour is readily understood, and then rebuilding the original system from such components to study its behaviour is a natural way in which the engineer, the scientist, or even the economist proceeds.*

3.1.1 Principles of Finite Element Modeling

Many physical phenomena in Earth sciences can be described in terms of partial differential equations. Solving these equations by classical analytical methods for arbitrary shapes is almost impossible. The finite element method (FEM) is a numerical approach by which these partial differential equations can be approximately solved.

The finite element method consists of the following five steps:

1. Preprocessing: subdividing the problem domain Ω into finite elements.
2. Element formulation: development of equations for elements.
3. Assembly: obtaining the equations of the entire system from the equations of individual elements.
4. Solving the equations.
5. Postprocessing: determining quantities of interest, such as stresses and strains, and obtaining visualizations of the response.

3.1.1.a The Element

Triangular element was the first finite element proposed for continuous problem in $2D$. Let's consider one triangular element in the coordinate system (x,y) (Fig. 1.14) with three nodes a, b, and c. In a mechanical formulation, the *discretized* displacements U_{nodes} at the nodes of the element, define the degree of freedom of the element considered,

$$U_{nodes} = \begin{pmatrix} u_a^x \\ u_a^y \\ u_b^x \\ u_b^y \\ u_c^x \\ u_c^y \end{pmatrix} .$$

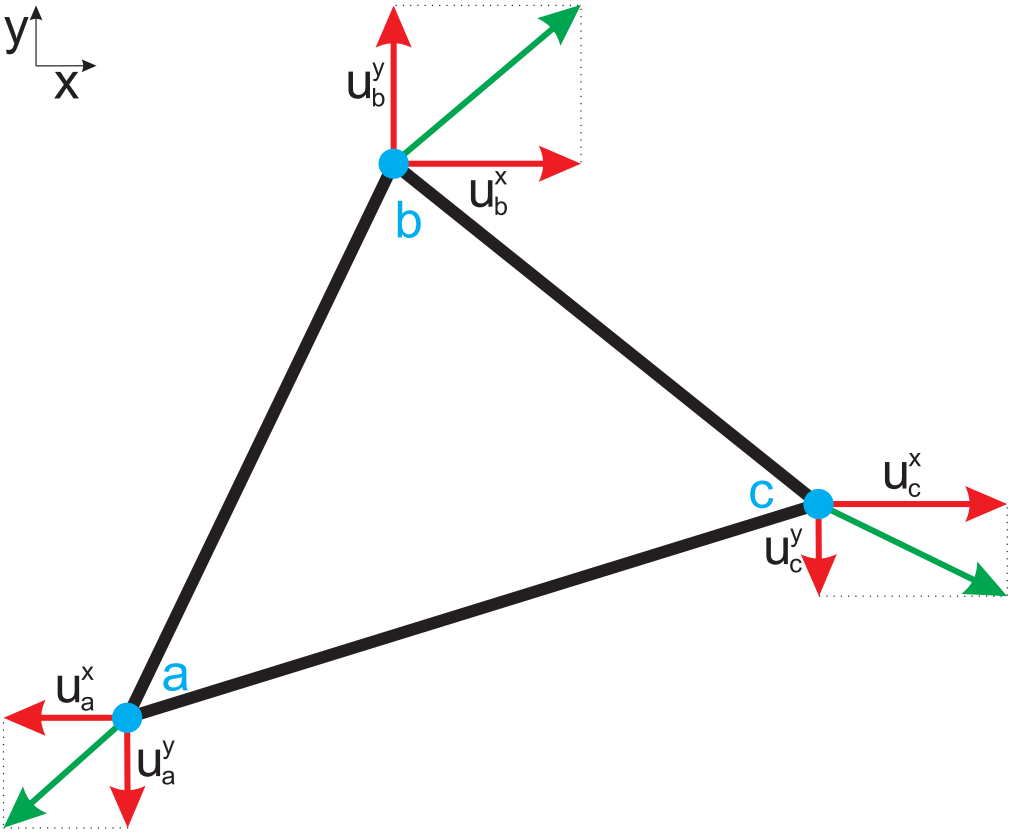

Figure 1.14: Triangular finite element and its associated displacement U_{nodes} at its 3 nodes a,, b and c, in the xy coordinates.

From this *discretized* displacement, it is possible to define a *continuous* displacement u inside the element by interpolation of the nodal values, using a function of interpolation (shape-function hereinafter):

$$u = \begin{pmatrix} u_x \\ u_y \end{pmatrix} = \begin{pmatrix} f_a(x,y)u_a^x + f_b(x,y)u_b^x + f_c(x,y)u_c^x \\ f_a(x,y)u_a^y + f_b(x,y)u_b^y + f_c(x,y)u_c^y \end{pmatrix} ,$$

with $f_a(x,y)$, $f_b(x,y)$ and $f_c(x,y)$ the shape functions that are functions of x and y. For triangular elements common shape function consist of polynomia of first degree with $f_n(x,y) = \alpha_n + \beta_n x + \gamma_n y$. Note that shape functions can also be defined for different shapes of elements, such as rectangular elements.

3.1.1.b Assembly: Example of a a 1D Elastic Bar

Elementary Rigidity Let's consider a linear $1D$ bar made up of linear elements with 2 nodes (Fig 1.15). External forces F_a and F_b are applied at the nodes, and we want to compute the resulting displacement in the bar. In this setting, continuous displacement using a linear interpolation of nodal values is expressed as,

$$u(x) = (L-x)u_a + xu_b \tag{1.81}$$

The bar is assumed elastic with a length L and a section of area A. Stress σ_x in the bar is a linear function of strain ε_x,

$$\sigma_x = E\varepsilon_x , \tag{1.82}$$

where E is the Young's modulus of the elastic bar, $\varepsilon_x = \frac{u_b - u_a}{L}$.

Force balance implies that the external forces F_e (F_a and F_b) applied to the nodes are equal to the internal forces F_i:

$$F_a = -\sigma_x A \text{ and } F_b = \sigma_x A . \tag{1.83}$$

This equation can be developped and expressed in its matricial form,

$$\begin{pmatrix} F_a \\ F_b \end{pmatrix} = -\frac{EA}{L}\begin{pmatrix} 1 & -1 \\ -1 & 1 \end{pmatrix}\begin{pmatrix} u_a \\ u_b \end{pmatrix} ,$$

and in its compact matricial form

$$F_e = KU_{nodes} . \tag{1.84}$$

with F_e the external forces and K the element stiffness (or rigidity) matrix of the element,

$$K = -\frac{EA}{L}\begin{pmatrix} 1 & -1 \\ -1 & 1 \end{pmatrix} .$$

Global Rigidity Now let's consider the same model but with 2 jointing elements, with b the node common to the 2 elements (Fig 1.15). Both elements share the same rigidity matrix. Combining these matrices, through the assembly phase, leads to a single matricial equation,

$$\begin{pmatrix} F_a \\ F_b \\ F_c \end{pmatrix} = -\frac{EA}{L}\begin{pmatrix} 1 & -1 & 0 \\ -1 & 2 & -1 \\ 0 & -1 & 1 \end{pmatrix}\begin{pmatrix} u_a \\ u_b \\ u_c \end{pmatrix} ,$$

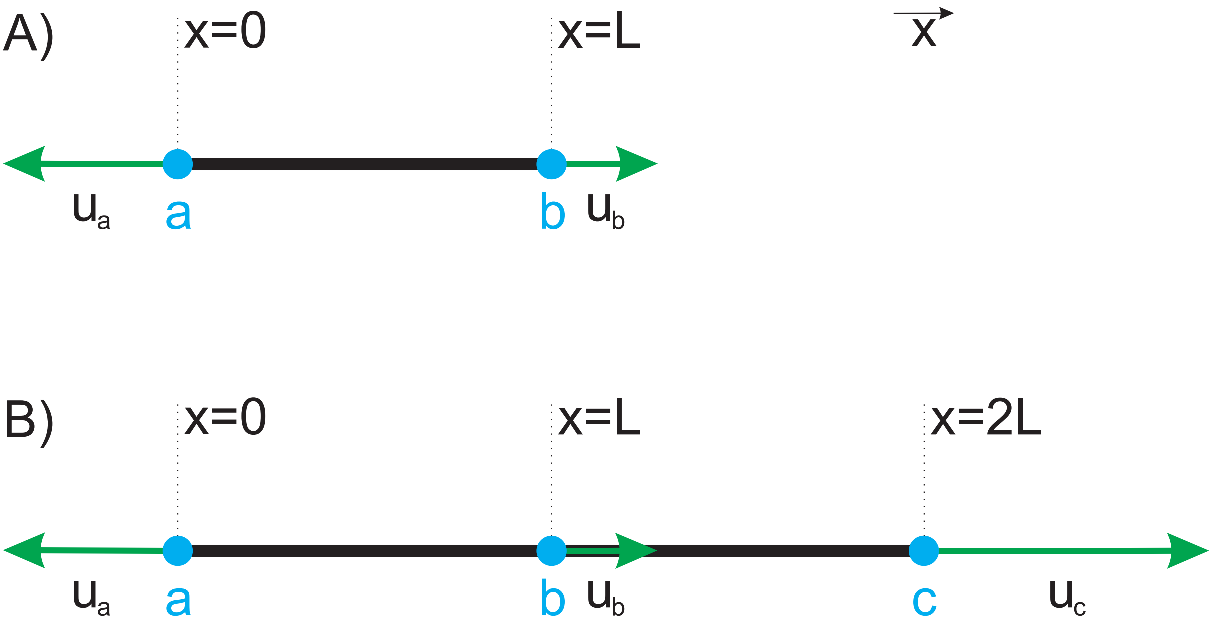

Figure 1.15: (A) Linear finite element in $1D$ and (B) a finite element model made up of 2 linear elements.

and the compact matricial form is,

$$F_e = K_{glo} U_{nodes} \ , \tag{1.85}$$

where K_{glo} is the global stiffness (or rigidity) matrix of the model composed of 2 elements, and can be generalized to larger number. Solving the FEM problem consists then of inverting the global rigidity matrix K_{glo} to express the nodal displacement U_{nodes} as a function of the imposed nodal forces F_{nodes}. Then the continuous displacement u is directly obtained by interpolation of the nodal displacement U_{nodes} using the shape functions.

This method is global and is neither limited to linear elements in $1D$ nor to elasticty. When considering large models made up of a large number of nodes, inverting the global rigidity matrix can result in extensive computational cost. Two methodologies are classicaly implement in FEM to solve this system: (1) Implicit methods in which the static system Eq. 1.85 is linearized into a large system of algebraic equations. These methods are computationally expensive. (2) Explict methods such as the Dynamic Relaxation (DR) (*Underwood*, 1983) which is employed in ADELI. In the following I present the basic methodology of DR.

3.1.2 ADELI: a Tool for Lithospheric Mechanics

ADELI is a Fortran 77 finite element software developed by *Hassani et al.* (1997) to model the thermo-mechanical behaviour of the lithosphere at geological time scales in $2D$. A $3D$ version exists but has not been used in the following. The FEM analysis is performed in large strain using the concept of objective (i.e. Lagrangian) derivative. While the space is discretized using linear triangular elements, the time approximation is done using an explicit finite difference method based on the Dynamic Relaxation method, and more specifically on the algorithm proposed by *Cundall and Board* (1988). The main capabilities of ADELI are:

1. Meshes of various sizes and shapes can be automatically generated starting from the definition of their boundaries, and an arbitrary number of materials can be defined.
2. The rheology can be chosen elastic (linear compressible), elastoplastic (Von Mises or Drucker-Prager), viscoelastic (linear or non-linear Maxwell body), or a combination of two anelastic behaviours.
3. Contact problems between bodies are treated using Coulomb friction via an implicit algorithm for steep contact and dry friction.
4. Thermal properties can be used in order to compute a transient or steay-state thermal solution.
5. Body forces corresponding to a constant gravity field can be included.
6. Boundary conditions are given in terms of velocities and/or stress on the mesh border, and in terms of temperature and/or heat flow for the thermal problem.
7. Initial conditions can be adjusted for internal stress and temperature.

I have developed and implemented new features into ADELI:

1. Possibility of using local remeshing with the Dynamical Lagrangian Remeshing algorithm of *Braun and Sambridge* (1994) and/or with the Surface Lagrangian Remeshing of *Steer et al.* and/or global remeshing/refining of *Hassani et al.* (1997).
2. A large variety of $1D$ surface erosion laws including linear diffusion (*Avouac and Burov*, 1996), stream-power using stochastic or effective water discharge(*Lavé*, 2005; *Godard et al.*, 2006) with possibility to follow both river or mean topography elevation.
3. Metamorphic Phase Change and associated density changes are implemented consistently with mass continuity and elastic rheology (*Hetényi et al.*, 2010).

In Chapter 8 I use ADELI to model post-orogenic mechanical and thermal evolution in $2D$

3.1.2.a Dynamic Relaxation

The code ADELI (*Hassani et al.*, 1997) employs Dynamic Relaxation to solve the matricial problem associated with FEM (*Underwood*, 1983). This is an explicit iterative procedure, in which the static system (Eq. 1.85) is transferred to an artificial dynamic space by adding artificial inertia and damping forces,

$$M\ddot{U}_{nodes} + C\dot{U}_{nodes} + K_{glo}U_{nodes} = F_e \ , \tag{1.86}$$

where M is a fictious mass matrix chosen in a diagonal form, and C a fictious damping matrix. The steady state solution of this artificial dynamic system (Eq. 1.86) is the solution of the static system. It is reached when the inertial regularizing term

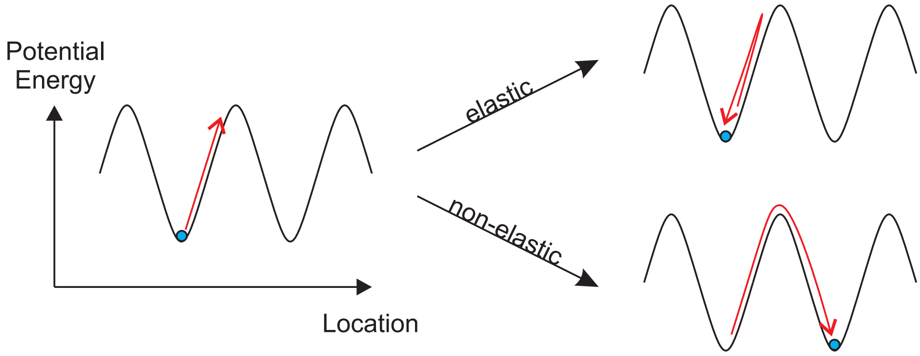

Figure 1.16: Schematic view at atomic scale of elastic (recoverable) and non-elastic (non-recoverable) deformation. In elastic deformation, the increment of potential energy of the atom due to a solicitation is not sufficient to exceed the potential energy of the hill, while in non-elastic it is sufficent.

$M\ddot{U}$ is negligible compared to the forces involved in the problem. Inverting this equation gives an expression of the nodal acceleration,

$$\ddot{U} = M^{-1}(F_{\mathrm{e}} - F_{\mathrm{i}} - C\dot{U}), \tag{1.87}$$

with $F_{\mathrm{i}} = K_{stiff}U$ the internal nodal forces calculated from the integration of the constituve law (Eq. 1.88). Velocity and displacement are then computed by numerical integration.

The main benefits of Dynamical Relaxation is its lower computational cost compared to implicit methods, and its ability to solve finite element problems with non-trivial inversion of the global stiffness matrix. The main counterpart is its high sensitivity to transient instabilities, which can amplify and result in large errors. Thus it is extremely important to limit such instabilities.

3.2 Lithosphere Mechanics

3.2.1 Rheology at Atomic Scale

Rheology is the physical property characterizing flow/deformation behaviour of a material under mechanical, thermal or chemical solicitations (*Karato*, 2008). Let's consider properties of deformation at the atomic scale the scale at which most deformation processes occur (exept fracture). At static equilibrium, each atom occupies a position corresponding to the minimum potential energy (Fig. 1.16). Upon applying a stress, atoms move from their stable positions, and depending on the intensity of the stress, two types of deformation are possible: (1) If the stress is small, or the temperature is low (or time is short), then only small instantaneous displacement will occur. Consequently, when the stress is removed, atoms go back to their initial (and stable position). This is called *elastic* or recoverable or reversible deformation. (2) In contrast when a large stress is applied, or at high temperature (or time is long), then the material will respond not only instantaneously but also through delayed, time-dependent deformation and a fraction of the deformation is not reversible. This is called *non-elastic* deformation. Microscopically , this occurs when the atomic motion is so large that atoms move, over the potential energy hill, to the next stable position.

Two kinds of non-elastic deformation exist: (1) If the stress is removed, the atom will not move back to its initial position, as no energy is added to the system, unless the deformation causes elastic strain inside the material (back stress). In this case after the removal of the external stress, atomic motion occurs in such a way so as to reduce the back stress associated with elastic strain so that the final equilibrium will have no permanent strain: strain is recoverable but time-dependent. This is called *anelastic* deformation. (2) In contrast deformation can be time-dependent and strain is non-recoverable. This is called *viscous* or *plastic* deformation.

The latter deformation can occur nearly instantaneously and be non-recoverable. For instance, fracture is nearly time-independent, but deformation is non-recoverable. Fracture involves the macroscopic breaking of chemical bonds which occurs in most cases in a localized fashion. This is called *brittle* deformation and can be considered as an end-member of plastic deformation.

3.2.2 Rheological laws

In ADELI the elastic part of each component of the strain ϵ_{ij} is function of the stress tensor σ, through Hooke's law,

$$\epsilon_{\mathrm{ij}} = \frac{1+\nu}{E}\sigma_{ij} - \frac{\nu}{E}\mathrm{trace}(\sigma)\delta_{ij} \ , \tag{1.88}$$

where E and ν are the Young's modulus and the Poisson's ratio, respectively. While the viscous part of each component of strain rate is function of the deviatoric stress $(\sigma_1 - \sigma_3)$ and temperature T through the Power law,

$$\dot{\epsilon_{ij}} = \gamma_0(\sigma_1 - \sigma_3)^n e^{(-E_a/RT)} \ , \tag{1.89}$$

where γ_0 is the standard fludity, n the power law exponent, E_a the activation energy and R the universal gaz constant. The limit between the visco-elastic and the elastic-plastic (or -brittle) domains is defined by a Drucker-Prager failure criterion or stress threshold,

$$\sigma_c = \alpha\frac{c}{tan(\Phi)} \ , \tag{1.90}$$

with c the cohesion of the material, Φ its internal angle of friction, and $\alpha = 6\sin(\Phi)/(3 - \sin(\Phi))$. The material becomes plastic when the effective stress σ_{eff} becomes higher than the stress threshold,

$$\sigma_{eff} - \sigma_c > 0 \ , \tag{1.91}$$

where $\sigma_{eff} = J2(\sigma) + J1(\sigma)\alpha$, with $J1$ and $J2$ the first (isotropic, i.e. pressure) and second (deviatoric) invariant of the stress field, respectively. In $2D$ the Drucker-Prager limit is,

$$\frac{1}{2}(\sigma_1 - \sigma_3) = \left(c\cot(\Phi) + \frac{1}{2}(\sigma_1 + \sigma_3)\right) \ . \tag{1.92}$$

Figure 1.17 illustrates the behaviour of the visco-elastic and elasto-plastic rheological law used in ADELI.

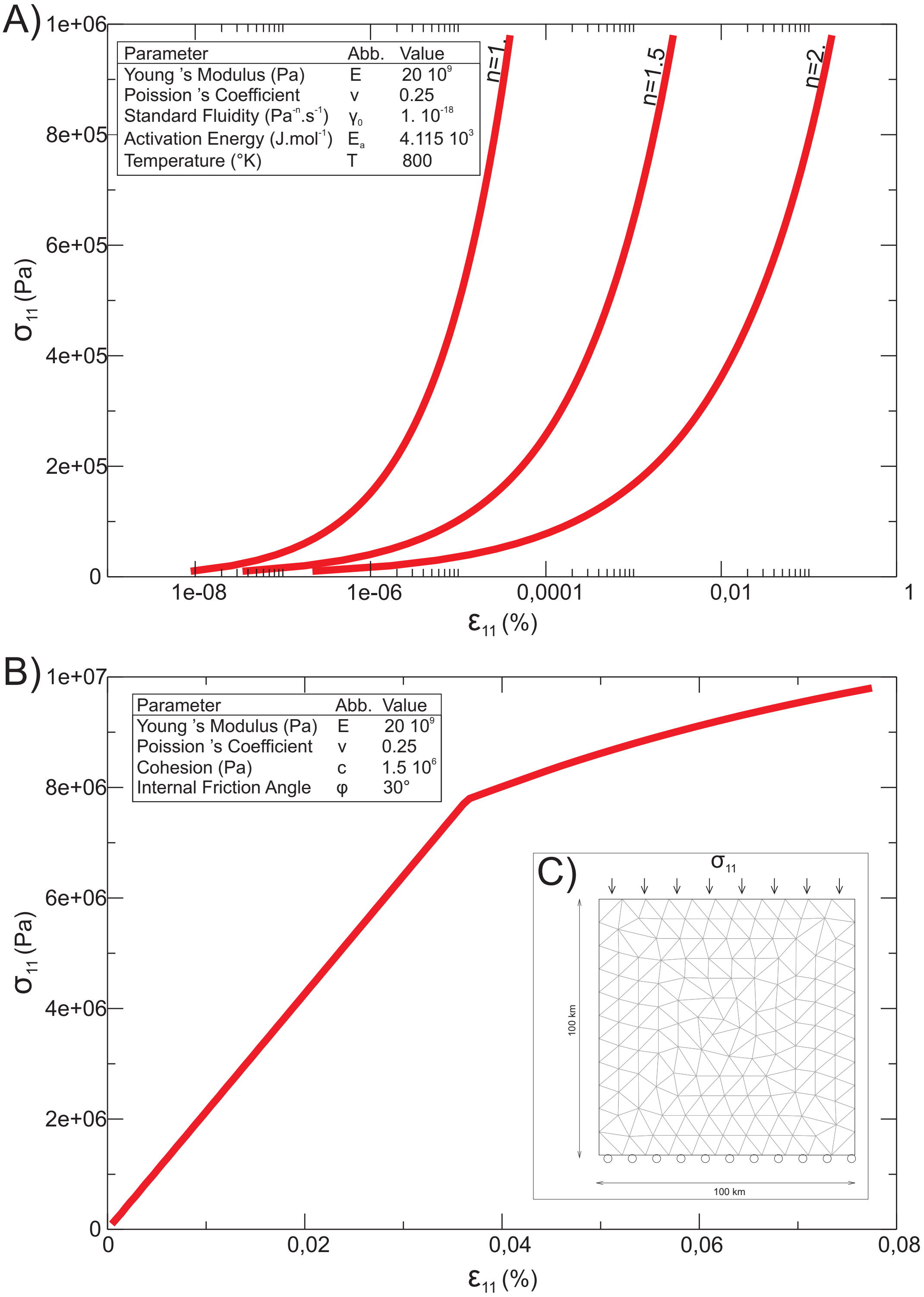

Parameter	Abb.	Value
Young 's Modulus (Pa)	E	$20\ 10^9$
Poission 's Coefficient	v	0.25
Standard Fluidity ($Pa^{-n}.s^{-1}$)	γ_0	$1.\ 10^{-18}$
Activation Energy ($J.mol^{-1}$)	E_a	$4.115\ 10^3$
Temperature (°K)	T	800

Parameter	Abb.	Value
Young 's Modulus (Pa)	E	$20\ 10^9$
Poission 's Coefficient	v	0.25
Cohesion (Pa)	c	$1.5\ 10^6$
Internal Friction Angle	φ	30°

Figure 1.17: Deformation of a (A) visco-elastic or (B) elasto-plastic medium submitted to uniaxial compressive stress using ADELI. (C) Set-up of the numerical experiment.

Last it is possible to a priori define fractures, inside the finite element model, which respect the Coulomb friction law.

3.3 Thermal Behaviour of the Lithosphere and its Modeling

Solid earth rheology is a primary function of the temperature. In geodynamical systems, such as the lithosphere, the temperature varies strongly (for instance slab subduction induces a cooling of its surrounding). Thus it is required in long-term geodynamical models to solve both the mechanics and thermics of the system considered. Here I first present the basic physics of heat transfer and then I present its numerical implementation into ADELI (*Hassani et al.*, 1997).

3.3.1 Physics of Heat Transfers

The basic relation for conductive heat transport is Fourier's law, which states that the flux q at a point in a medium is directly proportional to the spatial gradient of the temperature T at the point,

$$q = -k\vec{\nabla}T \ . \tag{1.93}$$

Combining this equation with heat conservation gives the heat equation, which allows to describe the time evolution of the temperature T in a medium submitted to conduction, convection and in presence of a heat source. In its fundamental form it is expressed as an equation of advection and diffusion:

$$\rho C_p \left(\frac{\partial T}{\partial t} + \vec{u} \cdot \vec{\nabla}T \right) = \nabla \cdot \left(k\vec{\nabla}T \right) + H \ , \tag{1.94}$$

where ρ is the density of the material, C_p its specific heat capacity, k its conductivity, and H is a volumic heat source term (mainly radiogenic heat production in the Earth). The vector $\vec{u}$ is the velocity of the material which results in advection of heat. Note that in ADELI, which is based on a Lagrangian formalism, heat is naturally advected. Under this condition the advection-diffusion equation becomes a diffusion-only equation,

$$\rho C_p \frac{\partial T}{\partial t} = \nabla \cdot \left(k\vec{\nabla}T \right) + H \ . \tag{1.95}$$

3.3.2 Numerical Implementation in ADELI

The diffusion equation is solved in $2D$ using an explicit Euler scheme that computes for each node the heat flux that exists within each linked element. The method is iterative so that the temperature converges toward a steady-state solution, which occurs when the heat fluxes induced by the spatial gradient of the temperature field balance the external heat forcing fluxes generated by boundary conditions and heat sources.

Contrary to many direct solvers, this iterative solver presents the main benefit of being independent of the nature of the boundary conditions.

Table 1.1: Present rates of heat release H_r and half-life $\tau_{1/2}$ of the important radioactive isotopes of the Earth (*Turcotte and Schubert*, 2002).

Isotope	H_r (W.kg^{-1})	$\tau_{1/2}$ (Ma)
^{238}U	$9.46 \cdot 10^{-5}$	$4.47 \cdot 10^{3}$
^{235}U	$5.69 \cdot 10^{-4}$	$7.04 \cdot 10^{2}$
U	$9.81 \cdot 10^{-5}$	
^{232}Th	$2.64 \cdot 10^{-5}$	$1.40 \cdot 10^{4}$
^{40}K	$2.92 \cdot 10^{-5}$	$1.25 \cdot 10^{3}$
K	$3.48 \cdot 10^{-9}$	

3.3.3 Heat Flux, Heat Sources and Temperature of the Lithosphere

The Earth's surface heat flow is the first evidence of a thermal activity in the inner Earth. In the continents the mean surface heat flow is 65 ± 1.6 W.m^{-2} (*Turcotte and Schubert*, 2002). Regions of continental tectonics, such as the Alps or Himalayan collision zone exhibit normal heat flows. In stable continental areas, the surface heat flow is strongly correlated with the concentration of radiocative isotopes in surface rocks. This is due to the production of heat during the fission of the radioactive isotopes of uranium, thorium and potassium. Today heat is produced primary by ^{238}U and ^{232}Th, but in the distant past ^{235}U and ^{40}K were the dominant heat producers due to their shorter half-lives (see Table 1.1). The largest concentrations of heat-producing radioactive isotopes are found close to the surface of the Earth. Typically in continents, the upper crust exhibits higher concentration than the lower crust, which also exhibits higher concentration than the upper mantle.

This production of heat by radioactive isotopes is also called radiogenic heat production, and corresponds to the heat source term in equation 1.95. Note that other mechanisms are able to produce heat in the Earth (*Gerya*, 2009): The shear heating which is related to the dissipation of the mechanical energy during irreversible non-elastic deformation; the adiabatic heat production or comsuption which is related to changes in pressure; the latent heat production or comsuption that is due to phase transformations in rocks subjected to changes in pressure and temperature. However these heat sources are secondary when considering the entire lithosphere as they are very depedent on local conditions (P, T, strain).

Some parts of the surface heat flow are also related to the overall global cooling of the Eart through geologic time. However this cooling flux is poorly constrained. Practically, when considering numerical modeling of the lithosphere, the effect of global cooling is included by defining a basal heat flow.

3.3.4 Steady-State Geotherms

Temerature-depth profiles within the Earth are called *geotherms*. If we consider a $1D$ column with constant bounday conditions, the column may eventually reach a state of thermal equilibrium, a steady-state. At steady-state, i.e. when $\partial T/\partial t = 0$, and if assuming that thermal conductivity is homogeneous, the $1D$ form of the heat

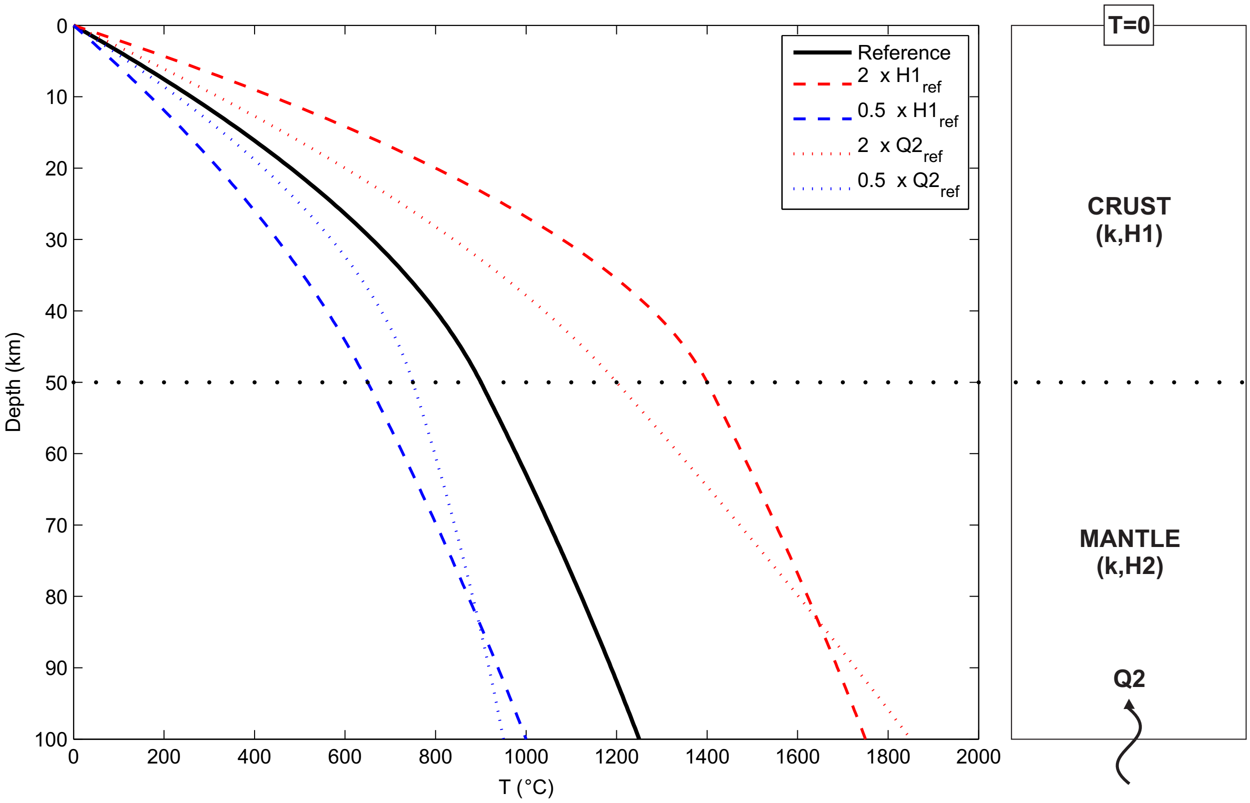

Figure 1.18: Equilibrium geotherms calculated from Eq. 1.99: Reference geotherm (black solid line) is obtained with $H_1 = 1.0\ \mu\mathrm{W.m}^{-3}$ and $H_2 = 0.1\ \mu\mathrm{W.m}^{-3}$, the radiogenic heat production of the crust (1) and mantle (2), respectively, a thermal conductivity of $k = 2.5$ W.m^{-1}.C^{-1} and a basal heat flow $Q_2 = 15$ mW.m^{-2}. The effects of multiplying (red) or dividing (blue) by a factor Q_2 (dotted line) and H_1 (dashed line) is also indicated, to illustrate the sensitivity of the geotherm to these two parameters. Here, the crust is assumed to have a thickness of $d_1 = 50$ km which corresponds to orogenic custal thickness.

equation (Eq. 1.95) is simply,

$$\frac{\partial^2 T}{\partial z^2} = -\frac{H}{k} \ , \tag{1.96}$$

with z the depth. Since this is a second-order differential equation, it can be solved if assuming 2 boundary conditions, such as:

- Temperature $T = 0$ at $z = 0$.
- Heat flow $Q = -Q_d$ at $Z = d$, with d the thickness of the column and Q_d the basal heat flow.

Intergration of Eq. 1.96 and forcing the solution to respect these boundary conditions implies,

$$T = -\frac{H}{2k} z^2 + \frac{Q_d + Hd}{k} z \ , \tag{1.97}$$

with H the radiogenic heat production of the medium considered and k its thermal conductivity.

To express the equation of the steady-state geotherm of the lithosphere, it is required to consider two layers: (1) the crust and (2) the upper mantle. The boundary conditions remain the same for each layer, and forcing the continuity of temperature at the Moho leads to,

$$T = -\frac{H_1}{2k} z^2 + \left(\frac{Q_2}{k} + \frac{H_2}{k}(d_1 - d_2) + \frac{H_1 d_1}{k} \right) z \quad \text{for} \quad 0 \le z < d_1 \ , \tag{1.98}$$

$$T = -\frac{H_2}{2k} z^2 + \left(\frac{Q_2}{k} + \frac{H_2 d_2}{k} \right) z + \frac{H_1 - H_2}{2k} d_1^2 \quad \text{for} \quad d1 \le z \le d_2 \ , \tag{1.99}$$

with H_1 and H_2 the radiogenic heat production of the crust ormantle, d_1 and d_2 their respective thickness, and $Q_2 = Q_d$ the basal heat flow of the lithospheric part of the mantle. Figure 1.18 presents a range of possible geotherms for the lithosphere obtained using previous equations.

4 Coupling of Surface Processes and Lithospheric Deformation

In the last two sections I have described the laws that allow one to model surface processes, lithospheric mechanics and thermics. In the following, after briefly presenting the nature of the interactions between these processes, I introduce the numerical methods to couple them into a single numerical model.

4.1 A Brief Overview

4.1.1 The Earth's Surface Interacts with its External/Internal Envelopes

Earth's surface is by definition the interface between Earth's lithosphere (top internal envelope) and atmosphere (external envelope). As mentioned previously the laws that govern the thermal and mechanical evolution of the lithosphere (and of

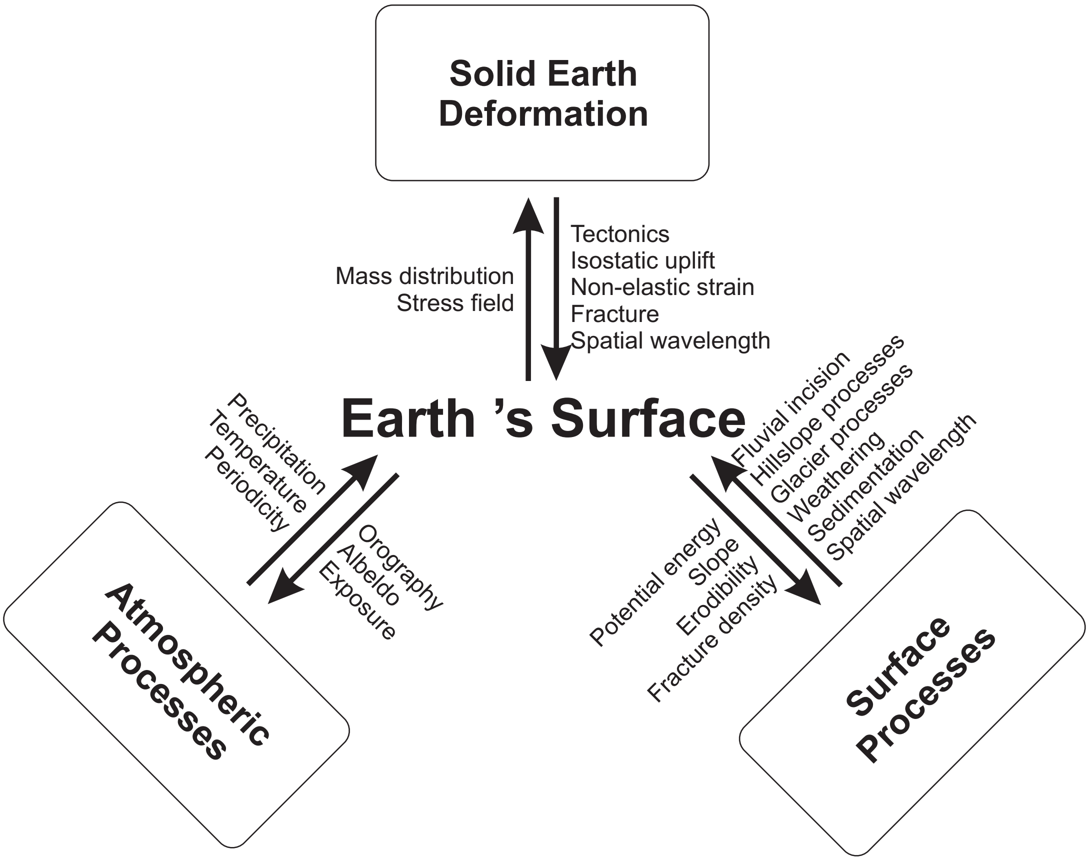

Figure 1.19: Schematic overview of the physical processes that control Earth's surface elevation and properties, including solid earth deformation, atmospheric processes and surface processes.

the atmosphere) are expressed as differential equations, and their solutions are extremely sensitive to boundary conditions. The Earth'surface being the main boundary condition of the lithosphere and of the atmosphere, its mechanical and thermal conditions, such as its temperature (and flow) or its elevation (or slope), are first order forcing terms of the lithosphere and atmosphere evolution.

However it is also observed that the evolution of the lithosphere and of the atmosphere affects the conditions of the Earth's surface. For instance, a convergent tectonic setting can result in building of a mountain belt, with its associated increase of surface elevation. Conversely, climatic cycles such as the Milankovitch ones, which depend on the eccentricity, axial tilt and precession of the Earth's orbit, affect surface temperature. Thus the atmosphere and lithosphere behaviours are first order controls of Earth's surface conditions.

Definition of Interaction and Feebacks: Here it is important to clarify what means *interaction* and *feedback*:

- An *interaction* is an action that occurs as two or more objects have an effect upon one another.
- A (positive or negtive) *feedback* is the effect by which an action that occured in the past, influences (positively or negatively) the same action but occuring afterwards.

Thus the physical system made up of the Earth's surface, the lithosphere and the atmosphere is subjected to interactions, potentially with positive or negative feedbacks. Moreover this physical system is strongly forced and modulated by the physical and chemical processes that occur directly on the surface, such as erosion or sedimentation, and results in changing its elevation and properties. These surface processes are influenced by the behaviour of the atmosphere and of the lithosphere. For instance river incision is dependent on the precipitation input, that modifies the water discharge, and on the spatial patttern of uplift that modifies the river slope.

Figure 1.19 is an attempt to summarize the possible controls of surface processes, atmospheric processes, and lithospheric deformation on the Earth's surface, and inversely.

4.1.2 What are these Interactions?

The last two decades have seen an increasing number of studies focusing on the interactions between climate (meaning here the atmospheric processes that influence surface processes, basically precipitation and temperature), surface erosion, and tectonics (e.g., *Beaumont et al.*, 1992; *Avouac and Burov*, 1996; *Willett*, 1999; *Dadson et al.*, 2003; *Godard et al.*, 2006).

In Taiwan Earthquakes and Typhoons Control Sediment Fluxes *Dadson et al.* (2003) found a positive correlation between present-day erosion rate (river sediment fluxes) with the seismic moment and the pattern of precipitation during large typhoons. This is not really surprising, as earthquakes and typhoons are acknowledged as potential triggering factors of landsliding, which in turn feeds rivers with sediments. However their results also show that erosion predicted by stream-power does not correlate with present-day sediment fluxes whereas it correlates with exhumation rates deduced from Apatite Fission Tracks (AFT) at geologic time scale (> 1 Ma).

Do Precipitation Rates and Patterns Control Erosion Rates? Another issue in geomorphology concerns the potential control of precipitation on erosion. At short time scale (~ 10 yr) extremes precipitation events such as typhoons in Taiwan (*Dadson et al.*, 2003), or abnormaly intense monsoon in the arid part of the Nepal Himalaya (*Gabet et al.*, 2004a,b; *Bookhagen et al.*, 2005a,b), control hillslope erosion by triggering landslides. In contrast to short-term erosion, long-term erosion is strongly influenced by fluvial incision. Rivers set the local base level of erosion for adjacent hillslopes, and thus the rate of river lowering dictates the rate of hillslope erosion (*Burbank*, 2002).

Reiners et al. (2003) and *Grujic et al.* (2006) documented a positive spatial correlation between precipitation and erosion rates at geologic time scale in the Cascades and in the Bhutan Himalayas, respectively. On the other hand, *Burbank et al.* (2003) and *Gabet et al.* (2008) found no significant correlation between precipitation rate and long-term erosion rate (> 0.1 Ma) in the Greater Himalaya of Nepal. This latter observation is consistent with the stream-power formalism, which correlates long-term erosion rates with upslope cumulated precipitation (a proxy for water flow), not with local precipitation. Nontheless it is interesting to relate these observations to orographic precipitation (*Roe et al.*, 2003; *Roe*, 2005), which states that when considering a two-sided range: (1) precipitation rate is greater on the windward side; (2) and intensity of the precipitation increases with increasing slope and elevation. What is the signature of an orogen where erosion is controlled by orographic precipitation?

Mountain Building and Orographic Precipitation *Dahlen and Suppe* (1988) first acknowledged the role of erosion as a driver of tectonics processes in mountain belts, by considering a Coulomb approach that relates deviatoric stress τ_{ij}, to stress σ_{ij} and pressure P:

$$\tau_{ij} = \sigma_{ij} - P\delta_{ij} \ . \tag{1.100}$$

Removal of material from the Earth's surface by erosion should reduce magnitudes of vertical compressive stress (and consequently P), and as a result deviatoric stresses τ_{ij} should increase in regions undergoing horizontal shortening, even with no change in magnitudes of horizontal compressive stress accros the belt. Non-elastic deformation, such as viscous or plastic one, being sensitive to deviatoric stresses, erosion results in an increase of the mountain belt deformation.

Because of the lack of data constraining the evolution of an orogen under an orographic gradient of precipitation, assessing the effect of such process on mountain building is a problem that can typically be addressed with numerical modeling. First numerical result: in actively deforming mountain belts, interactions and feedbacks between tectonics, climate and surface processes influence not only the geomorphology but may also control pattern and rates of strain in orogens (*Beaumont et al.*, 1992). Second numerical result: *Willett* (1999) found that orographic precipitation exerts a fundamental control on the location of zones of high or low strain (Fig. 1.20),

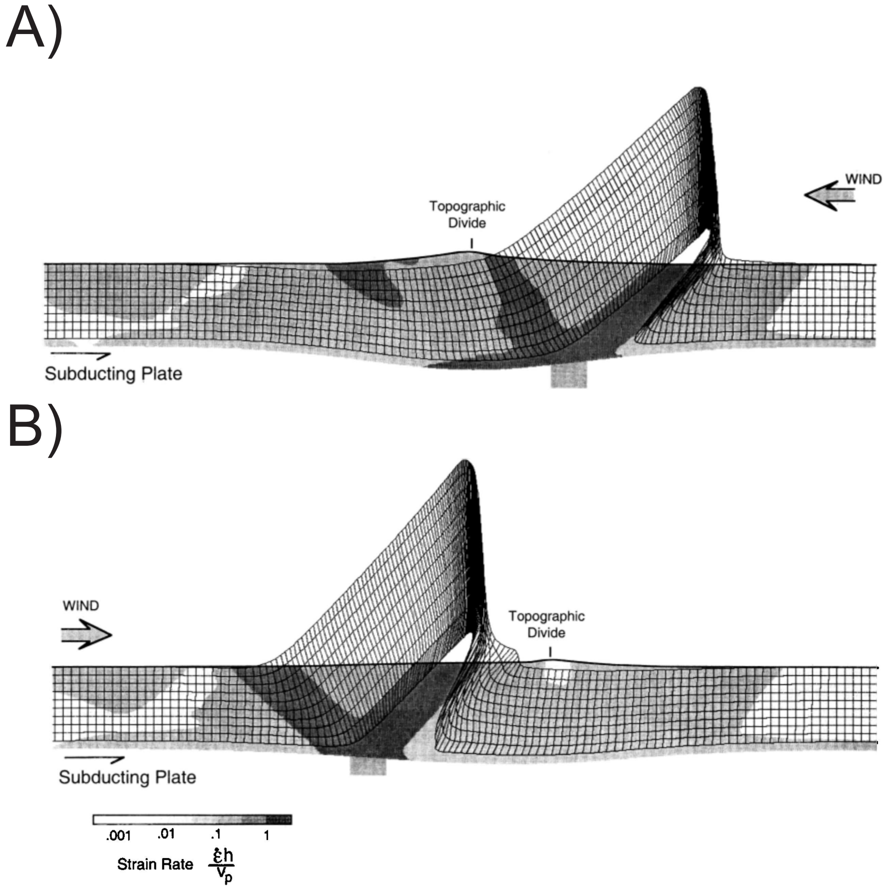

Figure 1.20: Results of the numerical modeling approach of the interaction between orographic precipitation, stream power erosion and visco-plastic deformation during mountain building (*Willett*, 1999). The wet side submitted to precipitation is either located on the retrowedge side (A) or on the prowedge side (B) of the range. The advected mesh shows the total deformation and exhumation relative to the real surface (bold solid line). Strain rate is indicated by a gray scale.

and controls the location of the water divide and its lateral migration. Here appears for the first time, the notion of interaction between atmospheric processes, erosion and lithospheric deformation.

Definition of Uplift: Following *England and Molnar* (1990) we define the meaning of *surface uplift*, *rock uplift* and *exhumation*:

- *Surface uplift* is the net increment of mean elevation of the Earth's surface $U = h(x,t) - h(x,t-1)$.
- Rock uplift is the increment of elevation of the rock particle (without considering erosion), due to a mechanical and internal process.
- *Exhumation* is equal to the thickness of rock removed from the Earth's surface.

Surface Uplift = Rock Uplift + Exhumation

Local Isostasy: The principle of local isostatsy states that there is a region beneath the lithosphere where rocks are so weak that they cannot sustain any horizontal stress gradient over geological times (e.g., *Braun and Robert*, 2005). Isostatic equilibrium implies that the weight of adjacent lithospheric columns must be equal. Mass unloading by surface erosion, disturbs this equilibrium, and leads to vertical motion.

- First let's consider the static case of a mountain belt made up of a topographic elevation H_{topo} and with a crustal root of thickness H_{root}, surrounded by a a crust of thickness H_{crust} with a density ρ_c, and standing on a mantle of density ρ_m. Here local isostatic equilibrium implies,

  $$L\rho_c = (H_{topo} + H_{crust} + H_{root})\rho_c = H_{crust}\rho_c + H_{root}\rho_m \ , \tag{1.101}$$

  which gives an expression of the ratio of the topographic elevation on crustal root thickness R, that only depends on the density of the crust and mantle,

  $$R = \frac{H_{topo}}{H_{root}} = \frac{\rho_m - \rho_c}{\rho_c} \ . \tag{1.102}$$

- Now let's consider the case of a homogeneous erosion of a plateau by an amount E, and let's compute the induced isostatic rock uplift U_{rock}. Isostatic equilibrium relation before and after erosion are,

$$\begin{aligned}(H_{topo} + H_{crust} + H_{root})\rho_c &= H_{crust}\rho_c + H_{root}\rho_m \ , \qquad (1.103)\\ (-E + H_{topo} + H_{crust} + H_{root})\rho_c &= H_{crust}\rho_c + (H_{root} - U_{rock})\rho_m \ ,\end{aligned}$$

  and substracting them leads to expression of rock and surface uplift,

$$U_{rock} = E\frac{\rho_c}{\rho_m} \ \text{ and } \ U_{surf} = E\frac{\rho_c - \rho_m}{\rho_m} \ . \qquad (1.104)$$

  Considering $\rho_c = 2900$ kg.m^{-3} and $\rho_m = 3300$ kg.m^{-3} leads to a net decrease of surface elevation of only ~ 12 % of the amount of vertical erosion.

- Eventually let's consider the case of an non-homogeneous erosion of a plateau only by valley processes such as fluvial or glacier erosion, by an amount E. The mean vertical erosion is $E/2$, and the induced rock uplift is

$$U_{rock} = \frac{E}{2}\frac{\rho_c}{\rho_m} \ . \qquad (1.105)$$

  This rock uplift leads to a net surface uplift of

$$U_{surf} = E\frac{\rho_c - \rho_m}{\rho_m} \text{ for the valleys },U_{surf} = U_{rock} = \frac{E}{2}\frac{\rho_c}{\rho_m} \text{ for the ridges }. \qquad (1.106)$$

  Thus isostasy can lead to surface uplift of the ridges of a topography, only if the hillslopes have not yet reached their slope of equilibrium, for instance the Tibetan plateau before its Cenozoic global uplift (*Molnar and England*, 1990).

Chicken or Egg: Cenozoic Uplift of Mountain Belts Another striking observation of a possible interaction between climate, erosion and tectonics is the concurrence of both global uplift of mountain belts and global cooling of the climate during the late Cenozoic. The first assumption was that uplift of mountain ranges in the late Cenozoic, such as Tibet, has lead to cooling of the climate by: (1) affecting atmospheric circulation (*Raymo et al.*, 1988; *Ruddiman et al.*, 1988; *Ruddiman and Kutzbach*, 1989), and (2) by tectonically driving an increase of chemical weathering, resulting in a decrease of atmospheric CO_2 concentration (*Raymo and Ruddiman*, 1992). Another possible explanation, proposed by *Molnar and England* (1990), is that this global climate cooling has increased glacier erosion, and the frequency of storms and consequently fluvial incision, which in turn has favoured an isostatic uplift of mountain peaks (see Fig. 1.21). In this latter assumption, global cooling is the forcing process of the climate-tectonics interaction, while in the first one the forcing process is an increase of uplift induced by tectonics activity.

It is interesting to note that this debate is still extremely active: (1) Recent observations by *Willenbring and von Blanckenburg* (2010) show that the Cenozoic

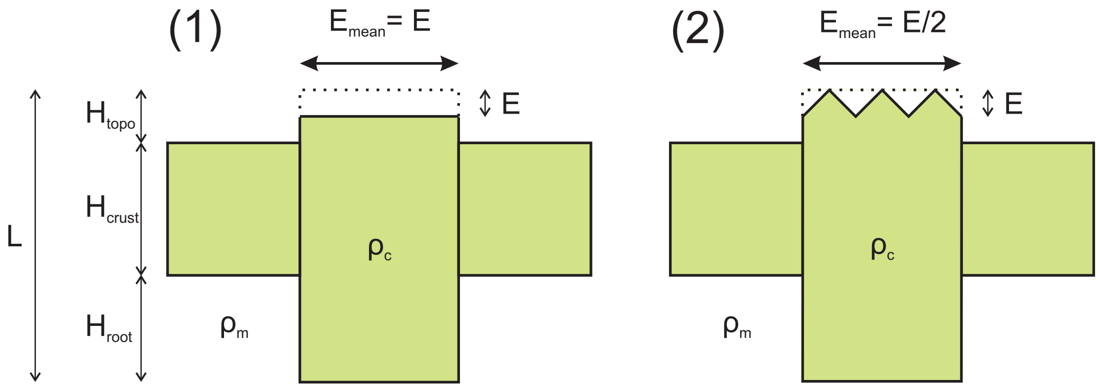

Figure 1.21: Erosion and isostasy in the case of (1) plateau erosion or (2) valley erosion. The setting includes a mountain belt of elevation H_{topo}, and a crustal root of thickness H_{root}, while the thickness of the crust elsewhere is H_{crust}. The density of crust and the mantle are ρ_c and ρ_m, respectively. The amount of vertical erosion in both cases is E, but it translates into a mean vertical erosion of $E/2$ in the case of valley erosion.

uplift of mountain belt has not resulted in a significant increase of sediment fluxes from continents to oceans, which tends to favour the assumption of a tectonic forcing of global uplift (*Goddéris*, 2010). (2) On the other hand *Clift et al.* (2008) observe a correlation between monsoon intensity and exhumation during the past 25 Ma, which can be interpreted as a causal relationship (*West*, 2008). This debate will probably be solved when a clear relationship will be defined between exhumation and sediment fluxes, to decipher whether or not sediment residence time could vary with climate and buffer the erosional signal (e.g., *Allen*, 2008; *Dosseto et al.*, 2010).

Tectonics, Fracturing of Rock and Erosion Another interaction between deformation and erosion (climate is not explicitely involved here) is the role of rock fracturing induced by tectonics (Fig. 1.22). *Molnar et al.* (2007) argue that tectonics plays its most important role with respect to erosion, not by raising topography as it is classicaly admitted, but by fracturing rock so that its fragments can be readily extracted by erosion. The mechanisms of erosion that are directly sensitive to fracture density are mainly glacier or river plucking and hillslope landsliding or rockfalling. Abrasion is also sensitive to fractures as it globally weakens effective properties of rocks. As a corollary, both deeply exhumed lower crust and post-tectonic igneous rocks, undeformed under brittle conditions, should be more resitant to erosion.

In Chapter 5 I explore the influence of fracture density on rock hardness.

4.2 Numerical Method to couple $1D$ SPM and ADELI in $2D$

4.2.1 Coupling Algorithm

As previously mentioned ADELI is a Lagrangian code, where the nodes and elements follow the motion of the model. Implementation of surface erosion in Lagrangian code is conceptually quite direct as it only requires to modify the position of surface nodes accordingly to the erosion rate integrated over the time step. I have coupled

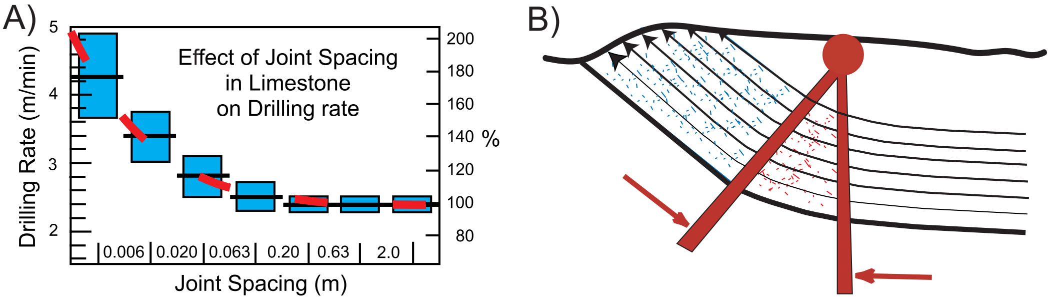

Figure 1.22: Effects of tectonics and subsequent fracturing on erosion. (A) Drilling rates as a function of the spasing of fractures in limestone, modified from *Thuro* (1997) and *Molnar et al.* (2007). The % scale shows the enhancement in drilling rate with decreased spacing of fractures. Red dashed line is an empirical fit. Drilling efficiency informs qualitatively on the resistance of the rock to erosion. (B) Cartoon illustrating the role of tectonics in the generation of faults within rock that is ultimately delivered to the surface of the Earth, from *Molnar et al.* (2007). Fractures here are generated by the strain induced by bending of the hanging wall of the main fault. The resulting fractured rock mass is then translated to the surface, where fractures influence surface erosion.

ADELI with the SPM developped by *Lavé* (2005) following the algorithm proposed by *Willett* (2010):

1. Solve the deformation problem using ADELI, and apply the displacement of the surface to the SPM.
2. Update divide positions and fill closed basins by sedimentation.
3. Update the distribution of precipitation for instance using an orographic law of precipitation.
4. Compute incision of the main river and update its elevation.
5. Compute erosion of the tributaries, update their elevation, and deduce mean topography and drainage density.

4.2.2 Numerical Consequences of the Coupling

Even if suchan algorithm is easy to implement in a FEM, its use raises other practical questions concerning the accuracy of the modeling:

1. First, moving nodes at the surface towards the inner part of the model theoretically requires to update the velocity field of the surface nodes. Indeed, as velocity is a continuous function of the space (using shape functions), moving nodes artificially (for instance by erosion) into this space independently of their velocities, puts them into a ambiguous mechanical condition as their velocities do not correspond to their positions. Rigorous modeling would require to update node velocities, accordingly to the continuous velocity field defined before moving the nodes. However when considering both small artificial displacement compared to the characteristic element dimension, and linear shape

functions, such effects should not significantly influence the accuracy of the modeling. Thus we have neglect this effect in the following.

2. Second deforming surface elements, eroding their nodes belonging to the top surface, results in a decrease of their area, of their shape factor quality, and of their mass. This conjugated effect strongly decreases the accuracy of the finite element solution, and moreover leads to a geometrical dead-end if nothing is done.

In Chapter 2 I present a new local remeshing algorithm that I have developed to solve this problem of Lagrangian FEM.

Chapter 2

Surface Lagrangian Remeshing: a new tool for studying long term evolution of continental lithosphere from 2D numerical modelling

In Press, Computers & Geosciences

Steer, P., Cattin, R., Lavé, J. and Godard, V.

Abstract

In this paper we present a new local remeshing algorithm that is dedicated to the problem of erosion in finite element models whose grid follows the movement of the free surface. The method, which we name Surface Lagrangian Remeshing (SLR), is adapted to 2D Lagrangian models which couple surface erosion with deformation of Earth materials. The remeshing procedure preserves nodes defining the surface submitted to erosion and removes nodes belonging to surface elements whose internal angles or area is critically low. This algorithm is ideally suited to track long term surface evolution. To validate the method we perform a set of numerical tests, using triangular finite elements, to compare the results obtained with the SLR algorithm with global remeshing and with analytical results. The results show good agreements with analytical solutions. Interpolation errors associated with remeshing are generated localy and numerical diffusion is restricted to the remeshed domain itself. In addition this method is computationally costless compared to classical global remeshing algorithms. We propose to couple the SLR method with the Dynamical Lagrangian Remeshing (DLR) algorithm to enable local remeshing only of Lagrangian models coupling large deformation of Earth materials with large erosion.

1 Introduction

Over the last two decades studies based on numerical modelling have demonstrated that the interaction of surface erosion and deformation of continental lithosphere is a key process in orogenic evolution (e.g., *Avouac and Burov*, 1996; *Beaumont et al.*, 1992; *Godard et al.*, 2009; *Willett*, 1999). These numerical approaches are commonly based on both an erosion law controlling the evolution of surface topography and a thermo-mechanical finite element model (FEM) that accounts for lithospheric deformation. However, as previously mentioned (e.g., *Kurfeß and Heidbach*, 2009), the major limitation of coupled models is that the FEM based on a Lagrangian formulation cannot perform simulations over very long time scales, due to the development of large cumulative deformation. Finite element methods are based on the spatial discretization of tensor and scalar values onto a finite number of elements. In the Lagrangian formulation the shape and location of these elements evolve with the deformation within the model together with erosion processes at the top surface. The quality of the numerical solution is closely linked to the shape functions used to interpolate discrete node quantities into continuous field variables. Shape functions are geometrically defined and as a consequence cumulated deformation of elements over long time scales leads to a decrease in the quality of interpolation.

To overcome this major limitation, most of the numerical approaches use remeshing algorithms to work on undistorted and well focused mesh. Remeshing is then associated with transfer of parameter fields between two subsequent meshes. This requires interpolation, which is a common source of numerical diffusion. In geosciences, remeshing is commonly used for the study of crack propagation (e.g., *Belytschko and Black*, 1999), flow description (e.g., *Hwang and Wu*, 1992) or long-time lithospheric deformation (e.g., *Godard et al.*, 2009; *Yamato et al.*, 2007). Most of these algorithms perform global remeshing, which requires transferring the field variables over the entire model.

To reduce numerical diffusion associated with the remeshing procedure many numerical strategies have been developed. For example *Yamato et al.* (2007) use an array of additional passive markers to interpolate field variables. *Fullsack* (1995) has developped a FEM based on the arbitrary Lagrangian-Eulerian (ALE) formulation. In this formulation the finite element calculation is not performed on the tracking mesh (a Lagragian one) but rather on an Eulerian one. Even if those methods (passive markers and ALE) are efficient to reduce interpolation errors, they lead to expensive CPU time-cost or require large amounts of memory. Yet note that ALE methods can be enhanced by the use of adaptative grid based on an octree division of space, which enables to interpolate field variables only for the appropriate elements (*Braun et al.*, 2008; *Thieulot et al.*, 2008).

An alternative approach is local remeshing algorithms, where only the distorted elements and their neighbours are remeshed. The additional benefit of these algorithms is that they reduce CPU time cost associated with remeshing. *Braun and Sambridge* (1994) propose the local Dynamical Lagrangian Remeshing (DLR) algorithm to deal with the distortion of the triangular elements of Lagrangian FEM. This method is suited to address high deformation problems. However it is not adapted to numerical modelling with intense erosion, in which mass removal by erosion not only affects the surface elements shape but also reduces their area.

In this paper, using the Lagrangian FEM code ADELI (*Hassani et al.*, 1997) we propose a complementary approach called Surface Lagrangian Remeshing (SLR hereinafter) algorithm to deal with the distortion and area decrease of surface elements by erosion. In what follows after a detailed presentation and tests of the SLR method, we will focus on the application of this method to study classical surface erosion laws. Coupled with the DLR method, this local remeshing technique can be applied to investigate a wide set of geodynamical problems including interactions between deformation and erosion.

2 Local remeshing algorithms

2.1 Coupling erosion and deformation: remeshing approach

Compared to global remeshing, local remeshing only modifies a small area close to the distorted elements. The Dynamical Lagrangian Remeshing (DLR) algorithm (*Braun and Sambridge*, 1994) was developped to deal with distortion by deformation of the triangular elements of Lagrangian FEM. DLR consists of a permanent reconnection of nodes with their closer neighbours by a Delaunay triangulation (Fig. 2.1). It forces elements to respect the Delaunay condition on the grid: the strict interior of the circumcircle of each triangular element contains no node. As previously mentioned, this method is very efficient to model high deformation problems, but it cannot be applied to remesh surface elements affected by erosion. Here we propose the SLR method as a complementary algorithm to the DLR method and dedicated to surface erosion. At depth the DLR algorithm deals with the remeshing of higly deformed non-Delaunay elements (see Fig. 2.1 bottom image) whereas the SLR algorithm enables to keep unflattened elements at surface (see Fig. 2.1 top image). From now on we focus our study only on the SLR method. We refer the reader to *Braun and Sambridge* (1994) for further details on the DLR method.

2.2 Surface Lagrangian Remeshing (SLR) algorithm

The main difficulty which must be solved by the SLR method consists in the local remeshing of deformed surface elements without altering the topographic profile itself. This latter is a critically important feature of the models investigating coupling between surface processes and tectonics. Thus, in the SLR algorithm only the internal nodes, i.e. the nodes that do not belong to the surface, are concerned by remeshing.

In our approach we use triangular elements initially generated by the Delaunay triangulation. We define the critical elements, with respect to remeshing, as the elements which exhibit at least one small internal angle $\alpha_{int} < \alpha_{cri}$ or a small area $A/A_{ini} < A_{cri}$. Two geometrical conditions apply on the critical angle α_{cri}: (1) $tan(\alpha_{cri})$ must be greater than the ratio of the maximum erosion Δh_{max} during one time step, over the minimum vertical height of the surface elements h_{min},

$$\tan(\alpha_{cri}) > \Delta h_{max}/h_{min} \ . \tag{2.1}$$

(2) α_{cri} must be smaller than 25°to avoid mesh destruction. The critical area A_{cri} is a secondary criterion, which preserves the simulations from both frequent remeshing and major area decrease of surface elements. In the following the critical angle α_{cri} and area A_{cri} are set to 18°and 50% of the initial area, respectively.

The SLR method is applied to the top surface of the model and consists of three stages: (1) internal nodes sharing at least one connection with surface nodes

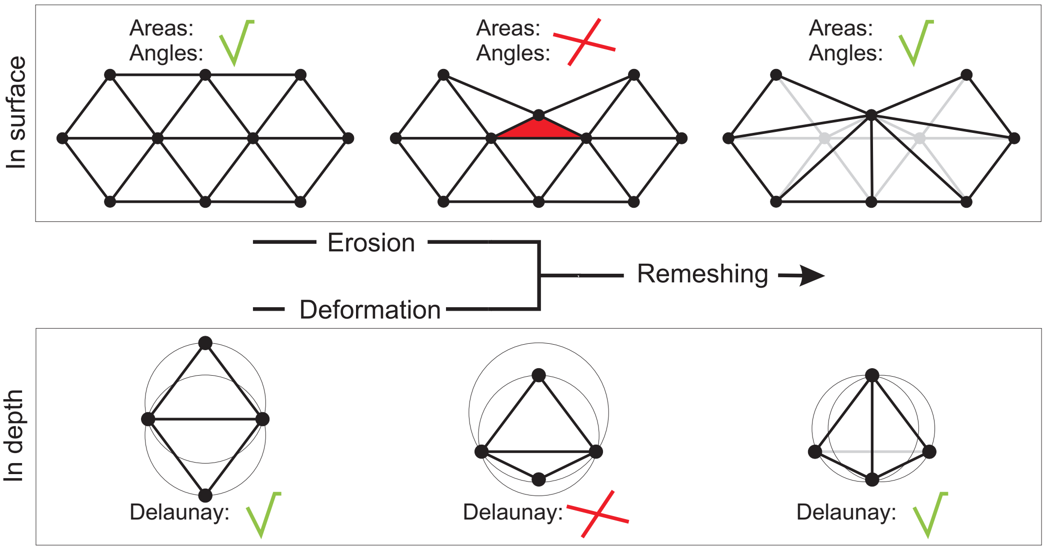

Figure 2.1: Description of the geometric principle of the SLR (top) and DLR (bottom) methods (*Braun and Sambridge*, 1994). Top image: the initial mesh is eroded until at least one angle or one area of a triangular element of the surface becomes critical; After erosion, the area A of the filled triangle is critical, compared to its initial value A_i, $A/A_\mathrm{i} < A_\mathrm{c}$, where $A_\mathrm{c} = 0.5$ is the critical area ratio. A remeshing criterion on the internal angles of the surface triangles is also defined. A triangle with at least one internal angle below 18°becomes critical. Nodes of the critical triangle, which are not at surface, are removed from the mesh. Triangles that include these removed nodes are deleted. Remaining nodes are reconnected by a Delaunay triangulation algorithm. After remeshing, the old mesh is indicated by gray lines. Bottom image: the initial mesh is deformed at depth until the Delaunay condition becomes false, i.e. the strict interior of the circumcircle of each triangular element contains no node. After reconnection of these nodes to their closest neighbours, the Delaunay condition becomes true again.

and belonging to critical elements are removed from the mesh. (2) Next, critical elements and their direct neighbours are also deleted from the mesh and replaced by new triangular elements following a Delaunay triangulation algorithm (*Renka*, 1997). (3) Finally, tensor and scalar values defined by elements are interpolated from the old to the new mesh. We use a simple conservative interpolation scheme, in which each new element value V_{new} is equal to the spatial integral of the old elements value V_{old} on the new element domain Ω divided by the area of Ω,

$$V_{\text{new}} = \frac{\int_{\Omega} V_{\text{old}}(\omega)\ d\omega}{\int_{\Omega}\ d\omega}\ , \tag{2.2}$$

where $d\omega$ is an infinitesimal area.

The SLR algorithm presents three main advantages: (1) by remeshing only critical and highly deformed surface elements, SLR method generates numerical errors only on the local remeshed domain. (2) Nodal values are not interpolated during remeshing as there is no redistribution of node positions during remeshing. (3) The combination of nodes defining the surface is kept constant and thus it does not artificially introduce any surface profile change, which would be a major drawback when considering geomorphological issues.

3 Validation of the SLR method

3.1 SLR and tracking of the surface

To check the ability of the SLR method to preserve surface profile during remeshing, simple models of erosion using SLR are compared with corresponding analytical solutions (Fig. 2.2). The numerical solutions are obtained with the FEM code ADELI (*Hassani et al.*, 1997). These experiments of comparison consist in eroding completely, until peneplanation at $t = t_\star$, a triangular-shaped mountain with a basal width of 100 km and a summit height of 3 km lying over a rigid and incompressible medium. The top surface is subjected to different erosion laws: erosion by diffusion of elevation $\partial h/\partial t = K\partial^2 h/\partial x^2$ (*Avouac and Burov*, 1996) or erosion proportional to slope $\partial h/\partial t = K\partial h/\partial x$ (*Beaumont et al.*, 2001), where K is the coefficient of diffusion and a coefficient of denudation, respectively. Analytical solutions are given in 6.1.

In both cases the numerical results obtained with the SLR method are in very good agreements with the analytical solutions (to the order of 1 cm compared to 3 km of cumulated erosion, see Fig. 2.2) while ~ 200 remeshings were performed in each experiment. However in the slope-dependent erosion law, the numerical solution progressively diverges from the analytical one at the foot of the mountain where the topographic slope varies abruptly. This is due to diffusion of the numerical solution, which is inherent to the upwind-differencing numerical scheme used for numerically solving the surface slope. In these 2 experiments, the ~ 200 SLR phases, which were necesssary to reach peneplanation, have not significantly altered the evolution of the surface.

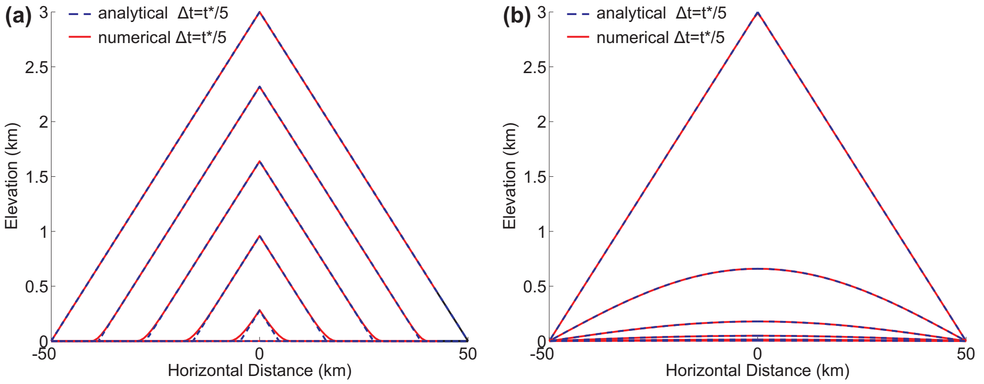

Figure 2.2: Time evolution of the surface of the model for different erosion laws plotted at each 20% ($\Delta t = t_\star/5$) of the numerical experiment: (a) erosion proportional to slope with $K = 4.0 \cdot 10^{-10}$ m.s^{-1}, and (b) erosion by diffusion with $K = 3.0 \cdot 10^{-5}$ m^2.s^{-1}. Results from these numerical experiments are compared with the corresponding analytical solution. Note that in (b) only the erosive component of the diffusion law is simulated.

3.2 Comparison between SLR and global remeshing

To further quantify the robustness of the SLR method, we performed a set of tests, which compare the results obtained with SLR and a global remeshing method using the same interpolation scheme. The set-up of the model (Fig. 2.3) used here is similar to the previous one, apart from the rheology which is elastic and is defined by a Young's modulus, $E = 40$ GPa and a Poisson's ratio $\nu = 0.25$. Each component of the elastic strain ϵ_{ij} is a function of the stress tensor σ, through Hooke's law,

$$\epsilon_{\mathrm{ij}} = \frac{1+\nu}{E}\sigma_{ij} - \frac{\nu}{E}\mathrm{trace}(\sigma)\delta_{ij}. \tag{2.3}$$

The boundaries of the model are fixed except the top surface which is subjected to a more realistic erosion law and follows a classical shear-stress fluvial incision law (*Gilbert*, 1877; *Howard and Kerby*, 1983; *Howard et al.*, 1994; *Lavé and Avouac*, 2001). This approach is not fully compatible with mechanical modeling, which requires to consider mean elevation as the pertinent upper boundary variable (*Godard et al.*, 2006). We refer the reader to *Lavé* (2005) and *Willett* (2010) for further details on how to incorporate erosion in geodynamic models.

Time evolution of the river elevation h is expressed as follow,

$$\partial h/\partial t = KP^\gamma A^\beta (\partial h/\partial x)^\alpha, \tag{2.4}$$

where K is a coefficient related to bedrock erodibility, P the mean precipitation rate of the watershed considered, A the watershed area and α, β, γ, some exponents, set equal to 0.7, 0.27 and 0.33 respectively (*Godard et al.*, 2006; *Lavé and Avouac*, 2001). The area is deduced from Hack's law, $A = k_a L^h$, where L is the length of the river, k_a and h two empirical constants (*Hack*, 1957). The bedrock erodibility and precipitation rate are set to $K = 6.4 \cdot 10^{-10}$ m$^{0.13}$.s$^{-0.67}$ and to $P = 1$ m.a^{-1}, respectively. The model lasts 10 Ma with 10^4 time steps. This setting enables a complete peneplanation of the topography after ~ 6 Ma.

The final stage of these numerical experiments (peneplanation) is compared to the state of strain of an unremeshed reference model, for which erosion is simulated by an instantaneous removal of the mountain load whit no remeshing. As the plate is purely elastic there should be no difference between this modelling and the global or local remeshed numerical experiments with progressive erosion.

In a first approximation both approaches using global and local remeshing algorithms give concordant results showing a localized deformation zone at depth below the initially high elevated area (Fig. 2.3). However a more detailed analysis of the strain pattern and a comparison with the reference model results reveal some major differences including a zone of intense deformation ($< -6.10^{-4}$) at 50-90 km depth obtained in the global remeshed experiment only. The results obtained with the SLR method appear to be significantly closer to the reference model, apart from the top surface where repetitive local remeshing has lead to numerical errors. This illustrates the role of the remeshed domain size: global remeshing interpolates tensor and scalar values defined by elements over the entire model, while SLR interpolate these values only in the remeshed area. Thus SLR prevents the development of widespread numerical diffusion that is inherent to global remeshing methods.

By producing numerical errors, remeshing can affect the stability of the simulation. Here we use the FEM code ADELI which uses an interative explicit approach and solves Newton's second law to obtain the static solution of a steady-state modelling (see a detailed description in 6.2). The convergence of the algorithm is thus associated with the minimization of unbalanced forces (Eq. 2.16), which can be expressed through the inertial ratio,

$$I_{\mathrm{r}} = \frac{\|F_{\mathrm{e}} + F_{\mathrm{i}}\|}{\|F_{\mathrm{e}}\| + \|F_{\mathrm{i}}\|}, \tag{2.5}$$

where F_{e} and F_{i} are the external and internal nodal forces acting on the system, respectively. This parameter can thus be used as a proxy of the numerical stability during an experiment: a decrease (increase) of I_r can be associated to a numerical stability increase (decrease) with time.

For both methods (SLR and global remeshing) we obtain an increase in numerical stability with time affected by large pulses of I_r increase associated with remeshing phases (Fig. 2.4). Our results suggest (1) a lower destabilisation effect due to the SLR method: the inertial ratio exhibits peaks of twice higher amplitude during global remeshing than during SLR and (2) a more frequent remeshing with the SLR method: only 6 global remeshing are needed when 44 SLR are required. These two features can be easily explained by the differences between the two remeshing methods. Global remeshing, contrary to SLR, completely reorganizes the distribution of nodes and in particular those close to the surface. This enables to space out the remeshing phases, but increases the numerical diffusion, due to interpolation on a greater amount of elements.

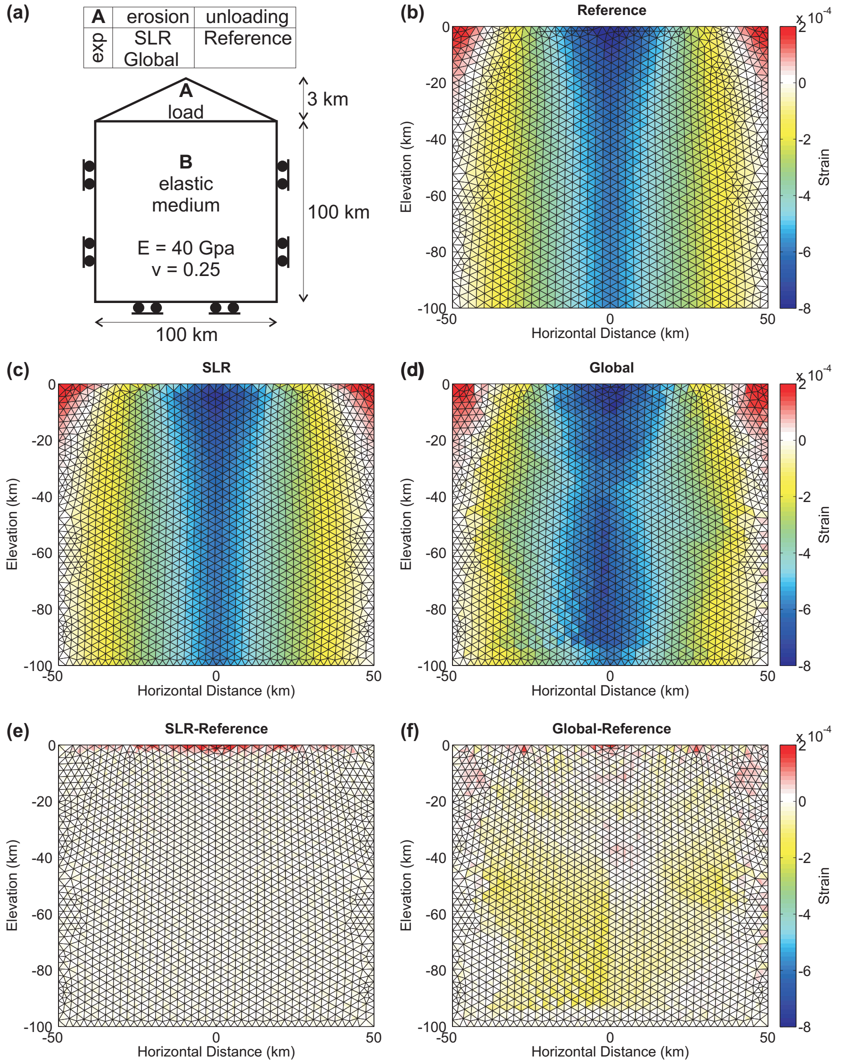

Figure 2.3: Results of the numerical experiments comparing local and global remeshing with the reference one. (a) Set-up of the different experiments. The medium A is submitted either to erosion (SLR, Global) or to instantaneous removal (Reference), while the elastic medium B boundary conditions remain constant in the different experiments. The model counts approximatively 6000 elements. Bulk strain field obtained at 10 Ma for the reference model (b), with the Surface Lagrangian Remeshing (SLR) algorithm (c) and with global remeshing (d). Also are represented the differences of the bulk strain field between (e) the SLR experiment and the reference one, and between (f) the Global and the reference ones. Note that SLR produces errors localized only at the surface of the model, while errors produced by global remeshing are widespreaded accross the simulation domain.

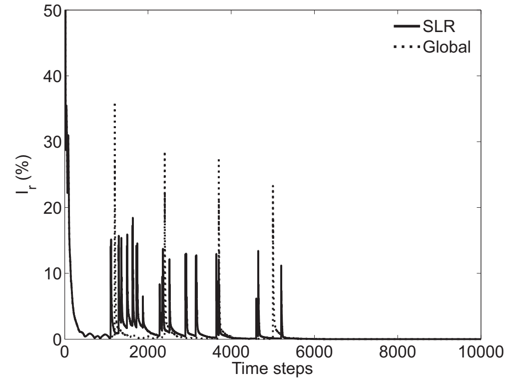

Figure 2.4: Evolution of the inertial ratio I_r for the SLR method (bold line) and for the global remeshing method (dashed line)

3.3 Remeshing and computational cost

In the previous experiments our model is meshed with $\sim$ 6000 elements. The cumulated CPU time for the remeshing and subsequent interpolation is $\sim$ 1.0 s, while it is equal to $\sim$ 400 s for global remeshing.

To test the efficiency of the SLR method in a more general way we compare the CPU time associated with local and global remeshing for models with a number of elements between 500 and 20000 (Fig. 2.5). Our results show that the CPU time for each remeshing phase increases proportionally to the square of the number of elements for global remeshing, whereas it is almost constant for SLR. Accurate simulations require a large amout of elements, which can easily exceed 10^4. In this case each global remeshing phase CPU time largely exceed 100 s. Simultaneously the number of remeshing phases increases proportionally with the number of elements. These two combined effects favour the use of the SLR method, which requires only $\sim$ 5 s of cumulated remeshing time for 20000 elements, while $\sim$ 19 h are needed with global remeshing.

3.4 Remeshing with the Dynamic Relaxation method

ADELI employs the dynamic relaxation (DR) method for time discretization (*Underwood*, 1983). As it is an explicit numerical scheme, the associated FEM is conditionally stable (6.2). Thus we need to check that the errors introduced during remeshing do not lead to numerical divergence. This is likely to occur when the changes in I_r due to each remeshing are cumulated with time. To avoid this accumulation of errors, the time period between each remeshing $\Delta t_{\mathrm{rmesh}}$ must be greater than the numerical relaxation time t_{damp} needed to restore a level of I_r prior to remeshing. For instance in the experiment with $\sim$ 6000 elements and for the SLR method t_{damp} is equal to $\sim$ 50 time steps. The evolution of I_r shows a global decrease except between 1000 and 2000 time steps, where $\Delta t_{\mathrm{rmesh}} < t_{\mathrm{damp}}$ (Fig. 2.4).

Furthermore if we use a visco-elastic rheology instead of the elastic one used in the models presented in this paper, the time between remeshing events needs to be

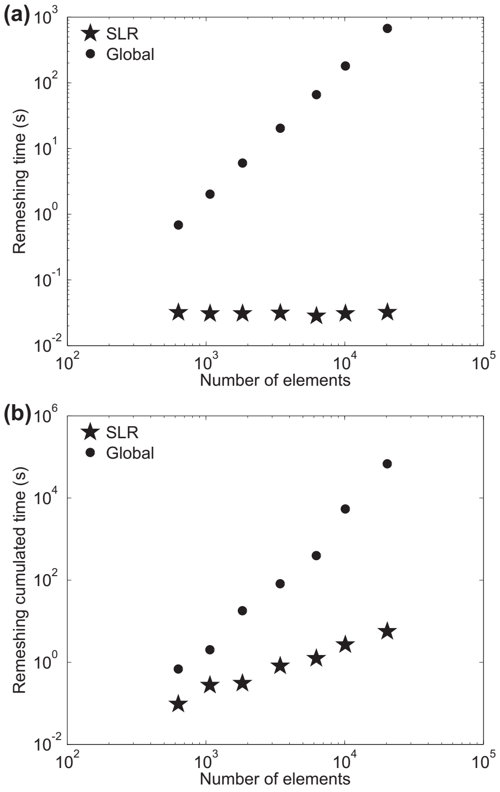

Figure 2.5: Loglog plot of the mean CPU time (s) needed to achieve one remeshing phase (a), and of the cumulated CPU time (b) needed by remeshing for the SLR (stars) and global remeshing (filled circles) methods as a function of the number of elements of the model.

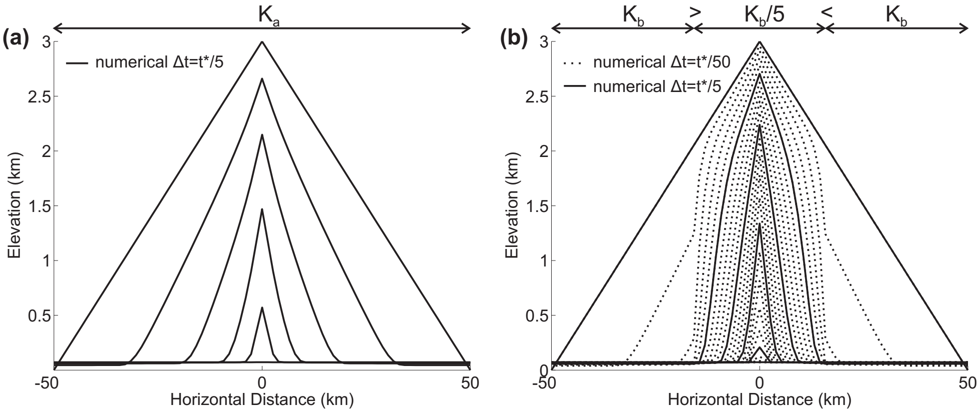

Figure 2.6: Time evolution of the surface of the model for erosion by river incision plotted at each 20% ($\Delta t = t_\star/5$) of the numerical experiment. (a) Homogeneous erodibility with $K = K_a = 6.4 \cdot 10^{-10}$ m$^{0.13}$.s$^{-0.67}$ and the precpitation rate set equal to $P = 1$ m.a^{-1}. Experiment (b) presents a spatial contrast of erodibility to river incision, with $K = K_b = 2.15 \cdot 10^{-9}$ m$^{0.13}$.s$^{-0.67}$ the coefficient of erodibility at the borders of the model being 5 times greater than at the center. Note the elastic rebound associated with unloading by erosion removal.

greater than t_{relax} the viscous relaxation time,

$$t_{\text{relax}} = \frac{min(\mu_{\text{eff}})}{E}, \tag{2.6}$$

where $min(\mu_{\text{eff}})$ is the minimum effective viscosity of the medium considered.

4 Application and limitations

4.1 River incision and rock erodibility

To further assess the abilities and limitations of the SLR algorithm, we apply it to model erosion by river incision (Eq. 2.4). The set-up of the model is the same as in the previous section. In the two experiments presented here (Fig. 2.6) the coefficient of bedrock erodibility is either homogeneous or presents an abrupt contrast, i.e. the borders of the mountain are 5 times more erodible than its center. The SLR algorithm is successful to deal with both and manages to keep constant the number of nodes setting the surface and subsequently the horizontal resolution. Detailed investigations are now required to deepen our understanding of rock erodibility in the interplay between erosion and tectonics.

4.2 Limitations

As a consequence the vertical resolution decreases where the erosion rate exhibits a spatial gradient. Here it happens at the transition zone between high and low erodibility (Fig. 2.6b).

Another limitation, which is not illustrated here, is the singularity that represents, for the SLR method, a single element forming an acute triangular mountain summit. In our models this singularity mainly occurs if the slope of the surface is greater than 45°on both sides of the mountain summit. In this setting it is impossible for the SLR to remesh the element forming the summit, as all its nodes belong to the surface. However this singularity can be avoided by swapping the basal face of such a triangular element with its direct neighbour.

When considering surface processes, the main limitation of the SLR algorithm is that it requires to be modified to allow modelling of sedimentation law. For instance we were not able to simulate the sedimentation part of the diffusion law using SLR (Fig. 2.2). Conversly SLR is not adapted to extensional settings. Both sedimentation and extension would rather require to add nodes where stretching of surface elements is important (small internal angle or large area).

5 Conclusion

Our study has demonstrated the efficiency of the local remeshing algorithm proposed in this paper. Compared to global remeshing, the SLR method is computationally costless, and produces only localized numerical errors, as interpolation occurs locally on the remeshed elements. Since the nodes of the free surface of the model are preserved throughout the simulation, SLR is an appropriate method in the context of numerical modelling with a particular interest in geomorphology. The SLR is thus a robust remeshing algorithm that enables to simulate erosion over long time scale in FEM modelling. It was succesfully applied to study river erosion over an abrupt contrast of rock erodibility.

However it is not suited for studies with both erosion and sedimentation. The applications of the SLR is not limited to $2D$ models using triangular elements. Its fundamental principles can be easily transposed to $3D$ FEM using tetrahedral elements.

Coupled with DLR, these local remeshing algorithms represent both a prospect for FEM based on Lagrangian formulation and an alternative to ALE and passive markers methods by their abilities to deal with both large deformation and high erosion (e.g., *Braun et al.*, 2008; *Fullsack*, 1995; *Thieulot et al.*, 2008; *Yamato et al.*, 2007). The coupled SLR-DLR remeshing algorithm has the potential to provide an efficient way to study a wide range of complex geological settings, which require to couple deformation of Earth materials with surface erosion (e.g., *Godard et al.*, 2006; *Kaus and Becker*, 2008; *Willett*, 1999).

Acknowledgements

Thanks to Cédric Thieulot and Boris Kaus for their careful and helpful reviews. We also thank Riad Hassani and Jean Chéry for providing the finite element code, and to Suzanne Pinder for language corrections.

6 Appendix

6.1 Analytical solutions of erosion laws

Let's consider the elevation of the right side of a triangular mountain belt initially defined as $h(x, t = 0) = -(H/l)x + H$, where H is the elevation of the summit and l is the horizontal distance between the summit and the foot of the mountain. Analytical evolution of this mountain belt $h(x, t)$ submitted to a slope-dependent erosion law,

$$\frac{\partial h(x,t)}{\partial t} = K\frac{\partial h(x,t)}{\partial x} \ , \tag{2.7}$$

is given by

$$h(x,t) = h(x, t = 0) - K\frac{H}{l}t \ , \tag{2.8}$$

where K is a coefficient of denudation.

Analytical evolution of the same mountain belt $h(x, t)$ submitted to diffusion of elevation,

$$\frac{\partial h(x,t)}{\partial t} = K\frac{\partial^2 h(x,t)}{\partial x^2} \ , \tag{2.9}$$

with the boundary conditions,

$$h(x = l, t) = 0 \ , \tag{2.10}$$

$$\partial h(x = 0, t)/\partial x = 0 \ , \tag{2.11}$$

is given by

$$h(x,t) = \int_0^l h(\zeta, 0)G(x, t, \zeta)d\zeta \ , \tag{2.12}$$

where

$$G(x,t,\zeta) = \frac{2}{l}\sum_{n=0}^{l} \cos\left(\frac{\pi(2n+1)}{2l}x\right)\cos\left(\frac{\pi(2n+1)}{2l}\zeta\right)\exp\left(-\frac{K\pi^2(2n+1)^2}{4l^2}t\right) \ , \tag{2.13}$$

with K the coefficient of diffusion. The numerical integration of Eq. 2.12 was carried out by means of a trapezoidal rule.

6.2 Numerical method

Finite element method deduces the nodal displacement U by solving the force-balance equation which results for long-term geodynamic problems in the following system of simultaneous equations,

$$K_{stiff}U = F_{\mathrm{e}}, \tag{2.14}$$

where K_{stiff} is the stiffness matrix and F_{e} the external nodal forces. Two methodologies are commonly used to solve this problem. Implicit methods in which the static system 2.14 is linearized into a large system of algebraic equation. These methods are computationally expensive. The finite element code ADELI (*Hassani et al.*, 1997) used in this study rather employs Dynamic Relaxation (DR) to solve previous equation (*Underwood*, 1983). This is an explicit iterative procedure, in which the static system (Eq. 2.14) is transferred to an artificial dynamic space by adding artificial inertia and damping forces,

$$M\ddot{U} + C\dot{U} + K_{stiff}U = F_{\mathrm{e}}, \tag{2.15}$$

where M is a fictious mass matrix chosen in a diagonal form, and C a fictious damping matrix. The steady state solution of this artificial dynamic system (Eq. 2.15) is the solution of the static system (Eq. 2.14). It is reached when the inertial regularizing term $M\ddot{U}$ is negligible compared to the forces involved in the problem. Inverting Eq. 2.15 gives an expression of the nodal acceleration,

$$\ddot{U} = M^{-1}(F_{\mathrm{e}} - F_{\mathrm{i}} - C\dot{U}), \tag{2.16}$$

with $F_{\mathrm{i}} = K_{stiff}U$ the internal nodal forces calculated from the integration of the constitutive law (Eq. 2.3). Velocity and displacement are then computed by numerical integration of acceleration.

6.3 Erosion rate and Critical Angle

The choice of the critical angle is constrained by the erosion rate and the size of surface elements. Figure 2.7 presents the distribution of successful experiments, i.e. where SLR was able to track the surface, in function of the ratio of erosion rate to element size and of the critical angle. Successful experiments occur when the critical angle is sufficiently small ($< 35°$) to avoid a destruction of the mesh, and when it is sufficiently large so that the amount of element erosion during one time step makes an angulary decrease smaller than the critical angle.

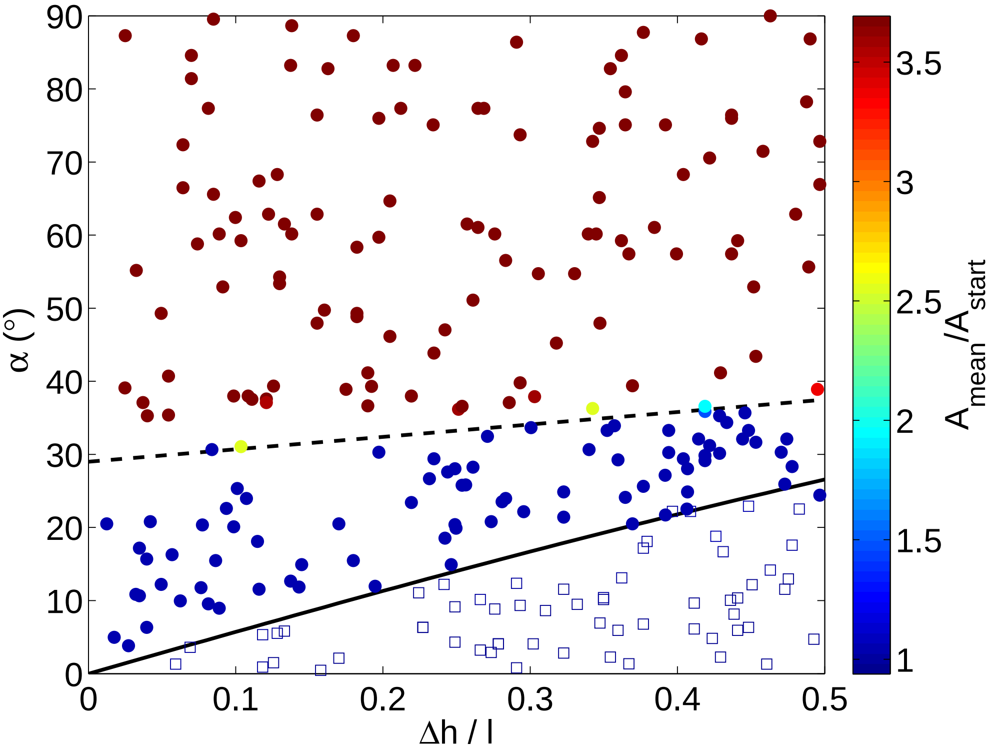

Figure 2.7: Results of the numerical experiments testing the compatibility of the SLR method with triangular elements as a function of the critical angle α and of the ratio of erosion per time steps Δh over the characteric height of elements l. Each point corresponds to a simulation which consists in completely eroding a triangular mountain belt, using here a homogeneous and constant erosion rate. The color code indicates the ratio of mean elements area A_{mean} at the end of the simulation over its initial value A_{start}. Filled circles are succesfull simulations, while empty squares correspond to simulations that have failed to track the top surface. This is likely to happen when $\alpha < arctan(\Delta h/l)$ which is represented with a bold continuous black line. Simulations that exhibits high values of A_{mean}/A_{start} have a low resolution. It happens when the SLR method leads to a destruction of the mesh, as the mesh only presents critical elements. Reasonable values of α lie between 10 and 25°.

Part II

Measuring Rock Erodibility with a Schmidt Hammer

Résumé

Dans cette partie j'examine la possibilité de mesurer l'érodabilité in-situ avec un marteau de Schmidt. Tout d'abord j'analyse les relations entre le rebond R du marteau de Schmidt et l'érodabilité K, prédites par les lois d'érosion déduites de l'étude des processus, en utilisant une relation empirique entre R et l'élasticité ou la résistance. Je confronte ensuite ces relations avec les résultats empiriques d'une experience dédiée. Une loi exponentielle entre R et K est obtenue dans la première approche, alors qu'une loi en puissance est obtenue dans la seconde. Ensuite j'applique cette méthode pour réaliser un transect d'érodabilité à travers Taiwan, qui révèle un contrôle de R à la fois par la lithologie et la fracturation. Je présente aussi les résultats d'une étude de terrain dédiée à la compréhension de l'effet de la diagénèse des Grès d'Annot sur R. A partir d'un jeu de données pétrogénétiques et pétrophysiques, j'évalue le contrôle du grade diagénétique sur R et propose un contrôle par la diagénèse mais aussi par la densité de fracture. Enfin je présente les résultats d'une expérience dédiée à l'étude de la relation entre fracturation et R dans une zone de faille. Les résultats suggèrent que les fractures contrôllent l'élasticité équivalente et donc R, avec une décroissance de l'élasticté équivalente lorsque la densité de fracture augmente. Toutefois l'amplitude de cet effet est dépendante du type de fracture. Cette dernière étude a été soumise à *Journal of Structural Geology*.

Abstract

In this part, I investigate the potentiality of measuring in-situ rock erodibility with a Schmidt hammer. I first analyse relations between Schmidt hammer rebound R and erodibility K that are predicted by process-based laws of erosion, using empirical fitting between R and rock elasticty and strength. I then compare these relations with the empirical results of a dedicated experiment. An exponential relation between R and K is obtained in the first approach while a power law relation is obtained in the second. Then I apply this method to perform a transect of erodibility accross Taiwan mountain belt, which reveals a control of R by both lithology and fracturation. I also presents the results of a field study dedicated to investigate the effect of the diagenesis of the Annot Sandstone on R. Using a set of petrogenetic and petrophysic data, I assess the control of the diagenetic grade on R and propose a control by both diagenesis and fracture density. Last I present the results of an experiment dedicated to study the link between fractures on R in a fault zone. The results suggest that fractures control the effective elasticty and thus R, with an increasing fracture density leading to a decrease of the elasticty. However, the amplitude of this effect of fracture density on R depends on the fracture type.This last study has been submitted to *Journal of Structural Geology*.

Chapter 3

Schmidt Hammer Rebound and Rock erodibility

The Schmidt hammer test is an inexpensive, quick and non-destructive method used for relatively quantifying the hardness of concretes and rocks (*Schmidt*, 1951). Its rebound value is empirically related to the petrophysical parameters or the tested sample, such as its uniaxial compressive strength (σ_{UCS}) or its Young's modulus (E). In this preliminary study we are interested in assessing the potentiality of Schmidt hammer to measure erodibility to abrasion directly in the field. First we present the Schmidt hammer and its measure, then we review empirical constraints on the relations between Schmidt hammer rebound R, rock properties, and erodibility, and discuss the potential models to convert the rebound into relative erodibility.

1 The Schmidt Hammer

The Schmidt hammer consists of a spring-loaded piston made of a steel mass (Fig. 3.1). When the hammer is pressed orthogonally against a surface, the piston is automatically released onto the plunger, and the rebound height of the piston is considered to be an index of surface hardness. Part of the impact energy of the piston is consumed largely by absorption, i.e. plastic deformation under the plunger tip, and by transformation into heat and sound (e.g., *Aydin and Basu*, 2005). The remaining energy represents the impact penetration elastic resistance (or hardness) of the surface and enables the piston rebound. The harder the surface, the shorter the penetration time (smaller impulse) or depth (lesser energy loss), and hence the greater the rebound (smaller momentum change).

First let's consider the case where there are no gravitational forces (Fig. 3.2). The energy released by the key spring is equal to the kinetic energy of the piston when released onto the plunger (*Basu and Aydin*, 2004),

$$\frac{1}{2}kx_1^2 = \frac{1}{2}Mv_1^2 \ , \tag{3.1}$$

with k the key spring elastic constant, x_1 the initial stretch of the spring, M the mass of the piston, and v_1 the velocity of the piston when it first touches the plunger.

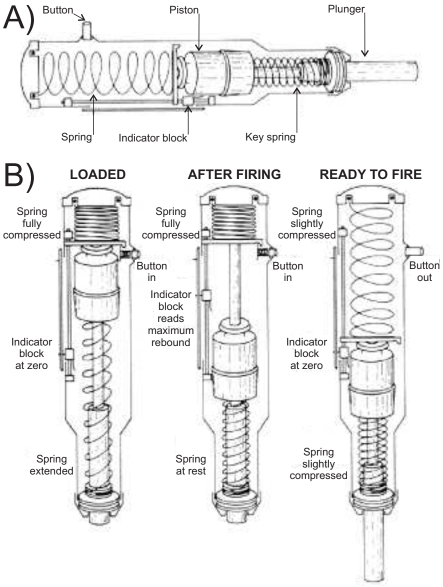

Figure 3.1: Presentation of the mechanical pieces of the Schmidt hammer (A) and its working principle (B) (*Basu and Aydin*, 2004)

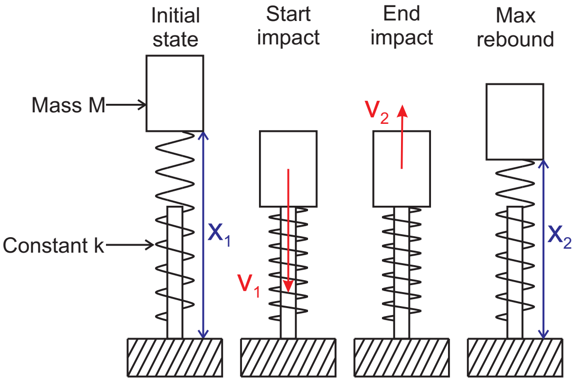

Figure 3.2: Simple schematic presentation of the physics of the Schmidt hammer.

Similarly, the kinetic energy of the piston when the rebound starts, is equal to the energy of the key spring stretched by x_2 when the piston is at it maximum rebound height,

$$\frac{1}{2}kx_2^2 = \frac{1}{2}Mv_2^2 \ , \tag{3.2}$$

with v_2 the initial rebound velocity of the piston. Combining these previous equations leads to,

$$\frac{x_2}{x_1} = \frac{v_2}{v_1} \ , \tag{3.3}$$

and to the expression of the rebound number R,

$$R = \frac{x_2}{x_1} \times 100 = \frac{v_2}{v_1} \times 100 \ . \tag{3.4}$$

Accurate measurements requires to consider gravitational forces and to correct the rebound number for its effect (*Basu and Aydin*, 2004).

2 Schmidt Hammer Rebound, Rock Properties and Erodibility: Empirical Constrains

Rock properties and Schmidt Hammer Rebound Due to its simplicty, Schmidt hammer has been widely used in petrophysics as it offers a quick and inexpensive mechanical test of rock hardness. Many studies find empirical relations between R and the weathering grade of rocks, their moisture content, their uniaxial compressive strength σ_{UCS}, their Young's modulus E or P-wave velocity V_P (see *Aydin and Basu* (2005) or *Goudie* (2006) for a review). In particular R and σ_{UCS} or E are found to be related either by a power or exponential function, which can be generalized by the following expressions,

$$\sigma_{UCS} = ae^{bR} \quad E = ce^{dR} \ , \tag{3.5}$$

$$\sigma_{UCS} = aR^{b} \quad E = cR^{d} \ , \tag{3.6}$$

where a, b, c, and d are postive constants that mainly depends on the rock type.

Erodibility and Schmidt Hammer Rebound: Empirical Models As already mentioned, *Sklar and Dietrich* (2004) proposed that the volume V_i of bedrock that is removed by abrasion during an impact by a pebble is,

$$V_i = \frac{\pi \rho_p \phi_p^3 v_p^2 E}{6 k_p \sigma_t^2} \ , \tag{3.7}$$

with ρ_p the impacting particle density, ϕ_p its diameter and v_p its vertical velocity, k_p a dimensionless coefficient that depends on the mechanical properties of the impacting particle, E the Young's modulus of the impacted susbtrate and σ_t its tensile strength. From this equation it is possible to extract an expression of bedrock erodibility K, i.e. the capacity of the bedrock to be eroded, by removing the terms that depend on the pebble properties,

$$K \propto \frac{E}{\sigma_t^2} \ . \tag{3.8}$$

On the other hand *Sklar and Dietrich* (2001) found empirically that erodibility scales with the inverse of the square of tensile strength, not with Young's modulus,

$$K \propto \frac{1}{\sigma_t^2} \ . \tag{3.9}$$

Moreover assuming that tensile strength is proportional to compressive strength, $\sigma_t \propto \sigma_{UCS}$, gives at first order a relation of proportionality between erodibility K_m and Schmidt hammer rebound R assuming *Sklar and Dietrich* (2004) model,

$$K_m \propto e^{(d-2b)R} \quad \text{or} \quad K_m \propto R^{(d-2b)} \ , \tag{3.10}$$

or *Sklar and Dietrich* (2001) model,

$$K_m \propto e^{(-2b)R} \quad \text{or} \quad K_m \propto R^{(-2b)} \ . \tag{3.11}$$

We employ K_m rather than K to differentiate erodibility obtained from empirical modeling, from measured erodibility

These relations give a theoretical basis that motivated us to asses relative rock erodibility with a Schmidt hammer. However it is also important to understand the limits of these expressions:

- First, it can only be applied to rock that does not exhibit fractures or mechanical discontinuities that have or exceed the characteristic size of the sampled volume by the Schmidt hammer (radius of $\sim$ 30cm). Otherwise the tensile strength would clearly diverges from compressive strength, and ultimately tending towards zero. Moreover in such conditions, the model of *Sklar and Dietrich* (2004) does not apply.

- Second, the different published relations between R and E or σ_{UCS} were derived empirically and only for a limited range of rock types (sometimes only one). In consequence this relation is probably correct when comparing erodibility of different rocks that share the same type, but is hypothetical when considering different rock types. Indeed, the constants a, b, c, d, and the coefficient of proportionality between σ_t and σ_{UCS} are likely to vary with rock type.

On the other hand *Dubille* (2008) directly compared erodibility and Schmidt hammer rebound (N-type) for different rock types. Erodibility was determined from a circular flume using realistic flow and pebble velocities (*Attal and Lavé*, 2006). In the experiments of *Dubille* (2008), erodibility is related to the rate of mass loss by abrasion for impacts between pebbles during transport, everyting else than lithology being equal. Using argillites, pelites, and sandstones with a wide range of densities, he found a power relation between K and R,

$$K = 10^{14.5} R^{-9.1} \ . \tag{3.12}$$

Practical Considerations

Table 3.1: Table that summarizes the potential relations between erodibility K and Schmidt hammer rebound R, using empirical exponenetial or power relations between R and Young's modulus E and compressive strength UCS. The models of *Sklar and Dietrich* (2001) and *Sklar and Dietrich* (2004) are tested. The range of the exponents b and d that are tested represent a compilation of values obtained from *Aydin and Basu* (2005).

	b (UCS)	d (E)	*Sklar and Dietrich* (2001)	*Sklar and Dietrich* (2004)
Exponential	0.055	0.055	$K \propto e^{-0.11R}$	$K \propto e^{-0.055R}$
	0.04	0.07	$K \propto e^{-0.08R}$	$K \propto e^{-0.01R}$
	0.07	0.04	$K \propto e^{-0.14R}$	$K \propto e^{-0.10R}$
Power	1	1	$K \propto R^{-2}$	$K \propto R^{-1}$
	4.3	1	$K \propto R^{-8.6}$	$K \propto R^{-7.6}$

Quite remarkably, b and d, which set the exponent of the power or exponential relation determined from comparison between R and UCS or E, are found to be quite independent of the rock type:

- b and d are both equal to $\sim 0.055 \pm 0.015$ for the exponential relation (*Xu et al.* (1990): Mica-schist, Prasinite, Serpentinite, Gabro; *Aydin and Basu* (2005): Granite weathered or not; *YIlmaz and Sendr* (2002): Gypsum; *Katz et al.* (2000): Limestone, Sandstone).
- For the power law relation, scattering of b (UCS) and d (E) is more important: between 1 and 4.3 for the b, with most values close to 1; 1 for d (*YIlmaz and Sendr* (2002): Marl; *Dearman et al.* (1978): Granite; *Shorey et al.* (1984): Coal; *Haramy and DeMarco* (1985): Coal; *Ghose* (1986): Coal; *Singh et al.* (1983): Sandstone, Siltsone, Mudstone, Seatearth; *O'Rourke* (1989): Sandstone, Siltsone,Limestone, anhydride; *Sachpazis* (1990): 33 different Carbonates; *Tugrul and Zarif* (1999): Granite; *Yaşar and Erdoğan* (2004): Carbonates, Sandstone, Basalt).

Table 3.1 summarizes the different relations that are expected from these sets of parameters with an exponential or power relation and using either the *Sklar and Dietrich* (2001) or the *Sklar and Dietrich* (2004) model. As expected, it is important to note that each relation predicts a decreasing erodibility with increasing value of Schmidt hammer rebound.

Figure 3.3 presents the relative range of erodibility K_m obtained with the models proposed in Table 3.1 assuming classical exponents. It is interesting to note that for the exponential model, K_m varies between 1 and 2 orders of magnitude for the range of rebound to which is sensitive the Schmidt hammer (10-70), and between 1 and 7 orders of magnitude for the power law relation. As expected, the model of *Sklar and Dietrich* (2001) gives a broader range of variation than the model of *Sklar and Dietrich* (2004). Note that the empirical fit obtained by *Dubille* (2008) predicts that erodibility can vary over 8 orders of magnitude for a realistic range of R values.

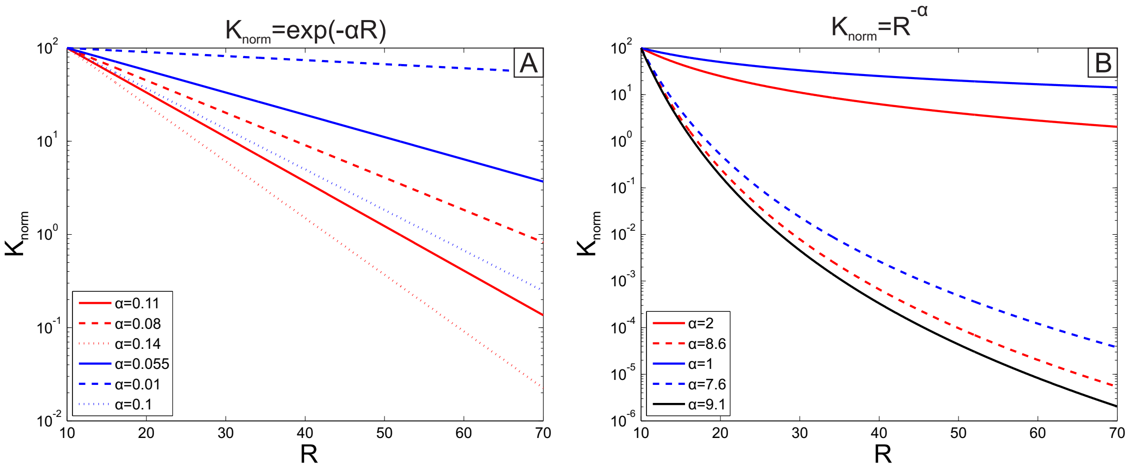

Figure 3.3: Semi-log plot of the relation between erodibility K_{norm} and Schmidt hammer rebound R for the exponential (left) or power law (right) relation testing either the model of *Sklar and Dietrich* (2001) (red) or *Sklar and Dietrich* (2004) (blue). The range of exponents α that are tested represent the range documented by *Aydin and Basu* (2005). K_{norm} is the normalized value of K_m, so that K_{norm} equates 100 for $R = 10$. Note that the empirical fit obtained by *Dubille* (2008) is also indicated in black.

3 Testing the Models

Erodibility and Schmidt Hammer Rebound Datasets

To test the model, two sets of data are compared (Fig. 3.4):

- The erodiblity dataset of *Attal and Lavé* (2009) based on a broad range of rock types using schists, sandstones, marbles, limestones, gneiss, granites, volcanic rocks and quartzite. Similarly to *Dubille* (2008) erodibility was determined from a circular flume with realistic flow and pebble velocities (*Attal and Lavé*, 2006). To the dataset presented by *Attal and Lavé* (2009) were added other values obtained from a smaller flume (M. Attal, unpublished data).
- The Schmidt hammer rebound (N-type) dataset compiled in this study from several studies referenced in *Aydin and Basu* (2005).

From these distributions, K and R are clearly anti-correlated at first order. For instance, schists have high K and low R, while quartzites have low K and high R. Even if including a broad range of lithologies, it is important to note that erodibility varies between 2 to 3 orders of magnitude only. This is not supporting power relations between K and R with large negative exponents, which clearly predict too large variations of erodibility deduced from R.

Models vs Datasets

We use the models defined previously (Table 3.1) to compare Schmidt hammer deduced erodibility K_m with measured erodibility (*Attal and Lavé*, 2009). Figure 3.5

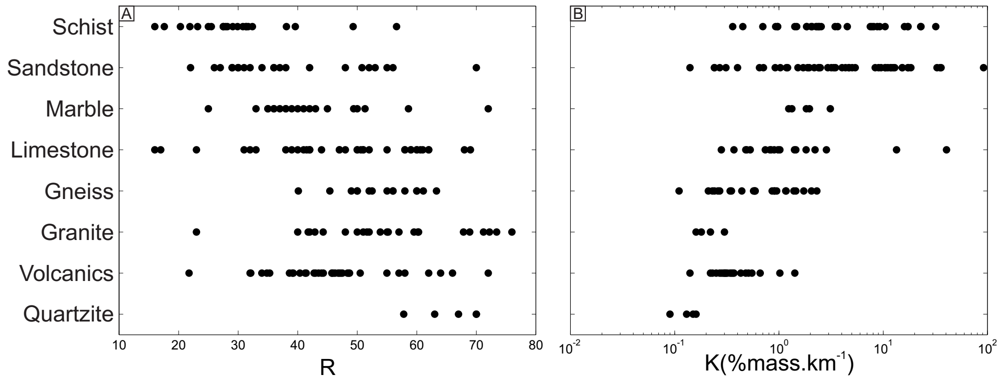

Figure 3.4: Distribution of (A) erodibility K (*Attal and Lavé*, 2009) and (B) Schmidt hammer rebound R (compilation of previous studies, see *Aydin and Basu* (2005)) for different lithologies. Note that the two datasets are not the same, and that these distributions only give indications on the effect of lithology on both K and R.

presents the comparison. We assess the sets of of coefficients and exponents that give the best qualitative fits between the measures and the models, for the exponential and power models. Interestingly, the exponent of the best fit exponential model ($exp(-0.11R)$), is in agreement with both the model of *Sklar and Dietrich* (2001) and empirical parametrization (*Aydin and Basu*, 2005), while it represents an extreme value of the model of *Sklar and Dietrich* (2004). The power model gives a good fit for an intermediary exponent close to -4. Alternatively, the empirical fit obtained by *Dubille* (2008) leads a to broader range of K_m than measured K (*Attal and Lavé*, 2009).

4 Discussion and Preliminary Conclusion

From this preliminary study, it appears that Schmidt hammer is a suitable tool to assess relative erodibility for different lithologies. Even if it is not clear which model to use to convert Schmidt hammer rebound R into erodibility K by abrasion. Building such a model requires either to measure both K and R and to assess an empirical fit (*Dubille*, 2008), or to use empirical relations between R and rock properties (*Aydin and Basu*, 2005), and between K and the same rock properties (*Sklar and Dietrich*, 2001, 2004). Even if the first approach is conceptually better, it appears that the results of *Dubille* (2008), which predict a power relation, are not in good agreement with R compiled from previous studies (see *Aydin and Basu* (2005)) when considering a broader range of lithologies. On the other hand, the second approach which a priori predicts either an exponential or a power relation between K and R, allows one to obtain a good qualitative fit between K_m deduced from the R dataset (see *Aydin and Basu* (2005)), and measured K dataset (*Attal and Lavé*, 2009). The exponents of the power or exponential relations are moreover consistent with the exponents obtained by previous studies of the relation between R and rock properties. From the two models of *Sklar and Dietrich* (2004) and *Sklar and Dietrich* (2001) that relate K_m to rock properties, the latter give the best results.

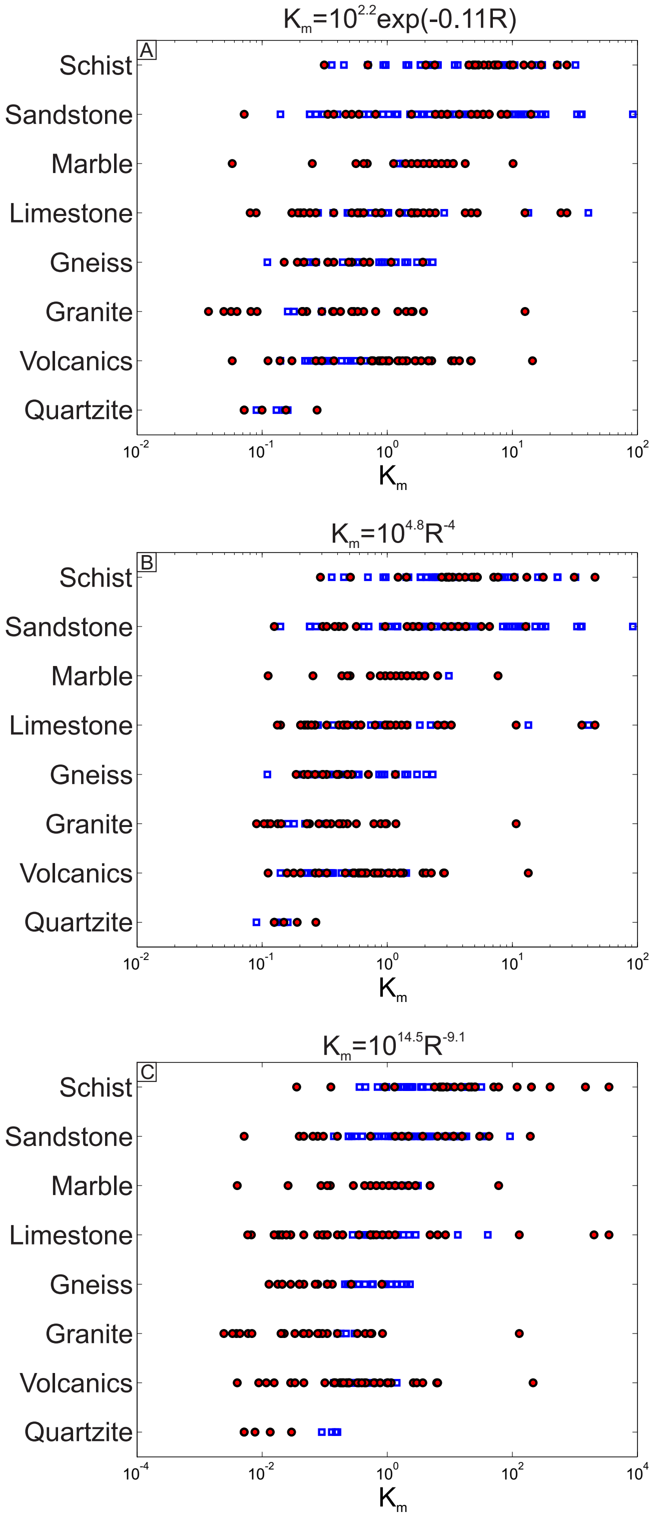

Figure 3.5: Distribution of measured erodibility (blue square) *Attal and Lavé* (2009) and of modeled erodibility (red dots) obtained in this study from a compilation of R values: (A) exponential and (B) power model and (C) power empirical fit o.btained by (*Dubille*, 2008). For the first two models, only the best fit models (assessed qualitatively) are presented.

Chapter 4

A Preliminary Experimental Study of Rock Hardness across the Taiwan Mountain Belt

In Prep.
Steer, P., Simoes, M., Huang, C. and Cattin, R.

Abstract

A preliminary experimental study of rock hardness across the Taiwan mountain belt was carried out. Rock hardness was measured with a Schmidt hammer. 23 outcrops localised in the Western Foothills, in the Slate Belt and in the Tananao Schist, were studied. Our results show a weak to moderate lithological control on the Schmidt hammer rebound values, with Tananao metamorphic schists having a higher hardness than the consolidated sandstones of the Western Foothills, and the slates of the Slate Belt having the lowest hardness. In addition our results do not correlate with uniaxial compressive strength measured in laboratory. This result could indicate a control by rock mass discontinuities such as fracture or schistosity. It also highlights the need to consider effective properties of rock mass when investigating rock properties such as erodibility.

1 Introduction

The erosion of mountain belts controls their topographic and structural evolution, and influences the pattern and rates of rock advection towards Earth's surface (*Avouac and Burov*, 1996; *Beaumont et al.*, 1992; *Willett*, 1999). The Taiwan mountain belt represents a key natural experimental field of interactions between tectonics and fluvial or hillslope erosion with unmatched tectonic activity, erosion rates (*Dadson et al.*, 2003) and extreme climatic conditions (*Fuller et al.*, 2006; *Simoes and Avouac*, 2006). First, convergence rate across the belt is high, estimated by GPS to 80 $\mathrm{mm.yr^{-1}}$ (*Yu et al.*, 1997; *Loevenbruck et al.*, 2001). It results in high exhumation rate $5 - 7$ $\mathrm{mm.yr^{-1}}$ (*Liu*, 1982; *Fuller et al.*, 2006; *Simoes et al.*, 2007), and frequent earthquakes, i.e. twelve seisms with $M_W > 6$ during the last century for the southern part of Taiwan. Second, precipitation is important, $\sim$ 2.5 $\mathrm{m.yr^{-1}}$, and occurs mainly during the typhoon season with an average of four typhoons per year (*Shieh et al.*, 2000). Third, rock resistance to fluvial erosion is estimated to be at least one order of magnitude lower than in the Himalayas, i.e. with higher erodibility (*Hilley and Strecker*, 2004). These three combined effects result in high erosion rates, estimated to $3-6$ mm.yr^{-1} within the actively deforming mountains during the last 30 years (*Dadson et al.*, 2003), and are in agreement with mean exhumation deduced from kinematic modeling (*Simoes et al.*, 2007). Moreover erosion rates are expected to be high at all timescales (*Dadson et al.*, 2003).

Erosion of the Taiwan mountain belt is dominated by hillslope landsliding and fluvial erosion. This latter sets the location of the local lower points of the landscapes and concordingly dictates the pace of hillslope landsliding. At decadale time scale, erosion rates of Taiwanese river basins are controlled by earthquake and typhoon events (*Dadson et al.*, 2003, 2004). In contrast, at geological time scale, erosion rates are controlled mainly by the erodibility of the river bedrock, the topographic signature of landscapes such as local slope or the organisation of the fluvial network. These two latters aspects are strongly dependant on tectonic deformation. In this study we assess rock erodibility across the southern part of the Taiwan mountain belt using a Schmidt hammer. Schmidt hammer permits the non-destructive estimate of uniaxial compressive strength (UCS) and Young's modulus (E) of rock materials (*Aydin and Basu*, 2005). In addition, we make the assumption that rock hardness measured by a Schmidt hammer is a proxy for erodibility.

First we introduce the geological and geodynamical settings of the studied area. Then we present the Schmidt hammer measurements and show the results. Finally we compare our results with existing datasets and discuss their implications on erosion in Taiwan.

2 Geodynamical and Geological Settings

The Taiwan mountain belt has resulted from the collision between the Luzon volcanic arc and the Chinese continental margin, which started about 6.5 Ma ago in the north (e.g., *Lin et al.*, 2003), and has sinced propagated southward (*Byrne and Liu*, 2002; *Simoes and Avouac*, 2006; *Suppe*, 1981). The Taiwan mountain belt is considered as a critical wedge growing essentially by frontal accretion and therefore submitted to distributed shortening (e.g., *Willett et al.*, 2001). However this classical model is challenged by recent observations and modeling that call for a significant contribution of underplating to the growth of the orogenic wedge (*Simoes and Avouac*, 2006; *Simoes et al.*, 2007).

The studied area (Fig. 4.1) is located in the southern part of Taiwan, and includes from West to East: parts of the Western Foothills, of the Slate Belt and of the the Tananao Schists. Lithologies encountered consist of poorly consolidated to consolidated sandstones, shales and slates in the Western Foothills thrust belt, slates, schists and sandstones in the Slate Belt, schists and greenschists (chlorite) in the Tananao Schist belt (Fig. 4.2) (*Ho*, 1986; *Beyssac et al.*, 2007). If refering to the circular flume experiments of *Attal and Lavé* (2009), all these lithologies are associated with high erodibility, and are likely to depend on the diagenetic or metamorphic grade for the sandstone and the schists, respectively.

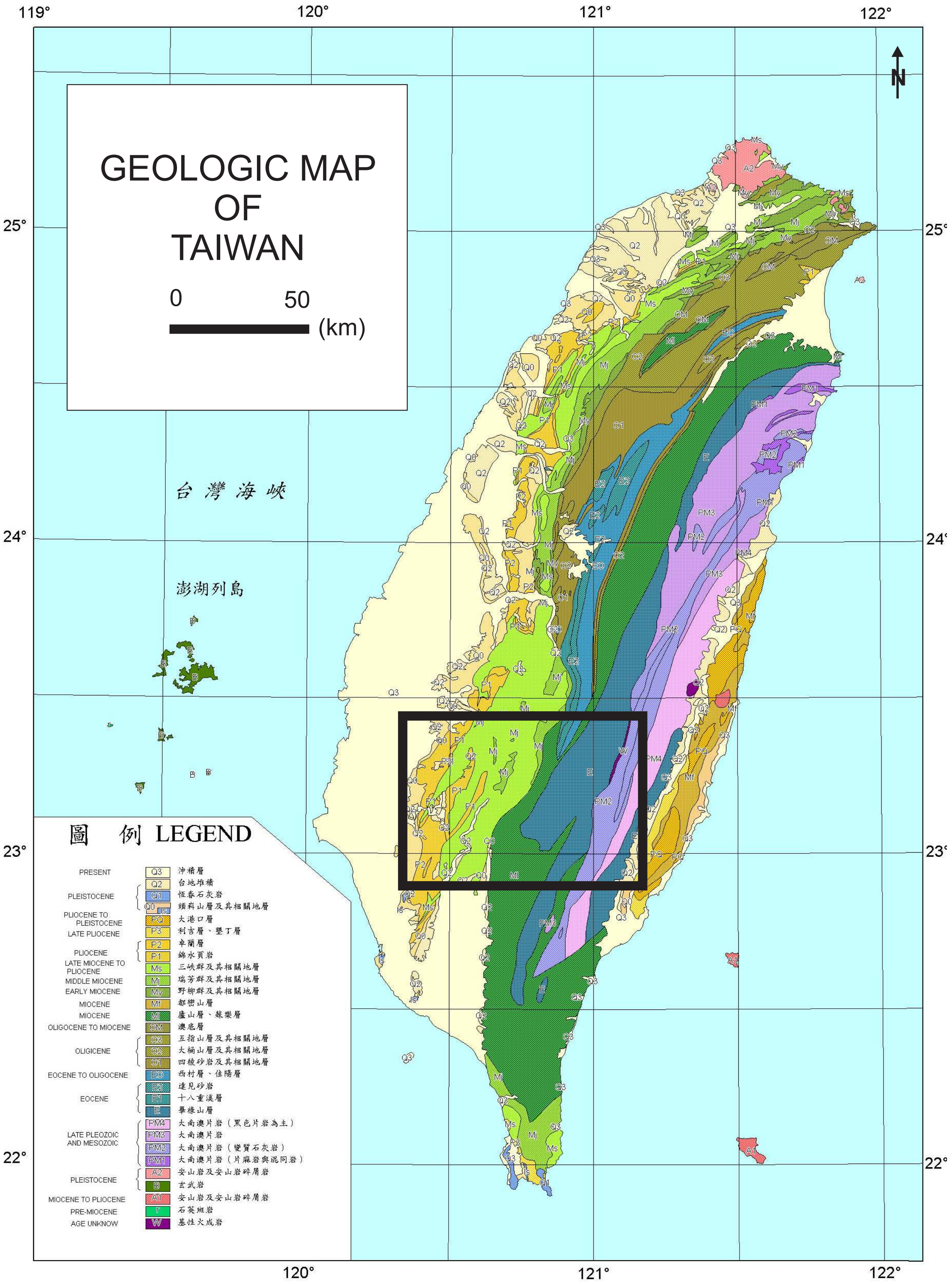

Figure 4.1: Geologic map of the Taiwan Mountain Belt. The black square indicates the location of the studied area.

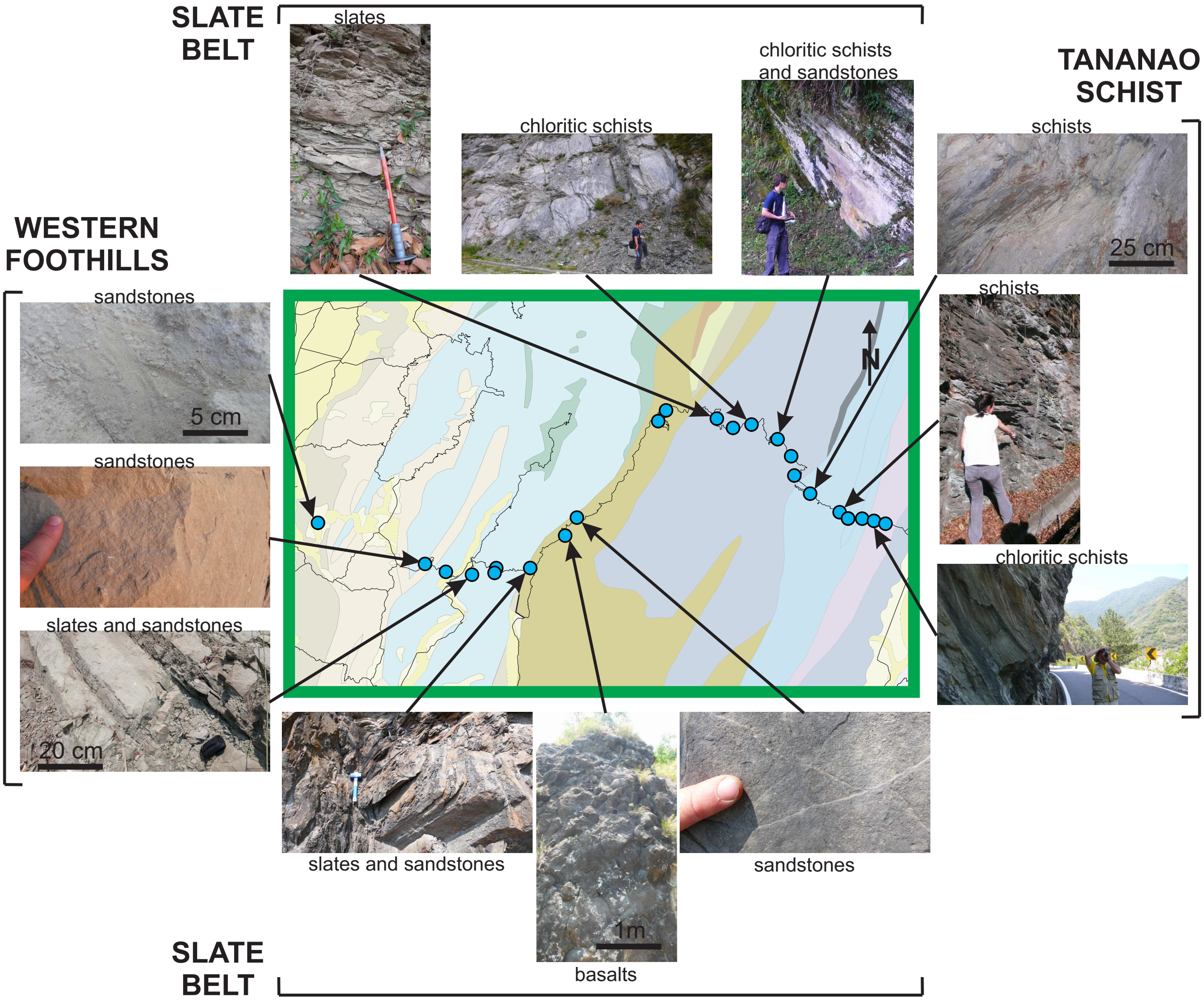

Figure 4.2: Detailed geologic map showing the location of the Schmidt hammer measures (blue points) across the south of the Taiwan mountain belt, with associated photographies of the outcrops.

Table 4.1: Table comparing Schmidt hammer rebound values (R) obtained in this study and uniaxial compressive strength (UCS) from *Dadson et al.* (2003).

	Western Foothills			Slate Belt			Tananao Schist		
	mean	σ	min-max	mean	σ	min-max	mean	σ	min-max
R	38.6	12.1	15-61	32.9	11.7	13-63	40	13.8	15-67
UCS (MPa)	20	13.8	0.1-109.2	39.2	34.4	1.5-253.4	45.3	23.1	1.2-189.9

3 Schmidt Hammer Rock Hardness across Taiwan

Data were collected during 3 days in May 2009, and 23 outcrops were studied with the Schmidt hammer. In parallel, samples were extracted at each outcrop for potential future studies. For practical reasons all the outcrops were selected along the Southern Cross-Island Highway in order to perform a full transect across the Taiwan mountain belt. A total of ~ 120 measures were realised, with 10 impacts per measure. At the scale of the outcrop, the selection of measure points was done randomly. Very weak lithologies with rebound values below the sensitivity limit of the Schmidt hammer (~ 15) were not sampled. Figure 4.3 show the variations of Schmidt hammer rebound values (R) across the Taiwan mountain belt. Globally the highest rebounds R are obtained for the metamorphic schists of the Tananao Schist and for the cemented sandstones of the Western Foothills. The Slate Belt exhibits low values of R in the western part dominated by slates, whereas high values are obtained in the eastern part dominated by schists. Sandstones in the Western Foothills globally show an increasing gradient of R from West to East, probably due to an increase of rock cohesion with cementation and diagenesis.

Figure 4.4 presents the values of R as a function of the lithology. This sorting confirms that the chloritic schists (or greenschists) and the sandstones have the highest hardness of the lithologies encountered in the studied area, with median values around 40. Actually, basalts have the highest hardness 45, but are not representative of Taiwanese lithologies. Slaty sandstones and schists have medium to low R values, with high dispersion which could be associated with varying proportion of slates or of the spacing between the plans of schistosity, respectively. Finally slates have the lowest R values.

4 Discussion and Conclusion

4.1 Comparing Schmidt Hammer Hardness with Uniaxial Compressive Strength

Taking advantage of a pre-existing geotechnical dataset on Taiwan (supplementary materials, *Dadson et al.*, 2003) we compare the in-situ rock hardness obtained in this study with a Schmidt hammer, with the uniaxial compressive strength measured in laboratory (see Table 4.1). Note that we only have access to the dataset published in *Dadson et al.* (2003) and not to the details of this dataset such as the

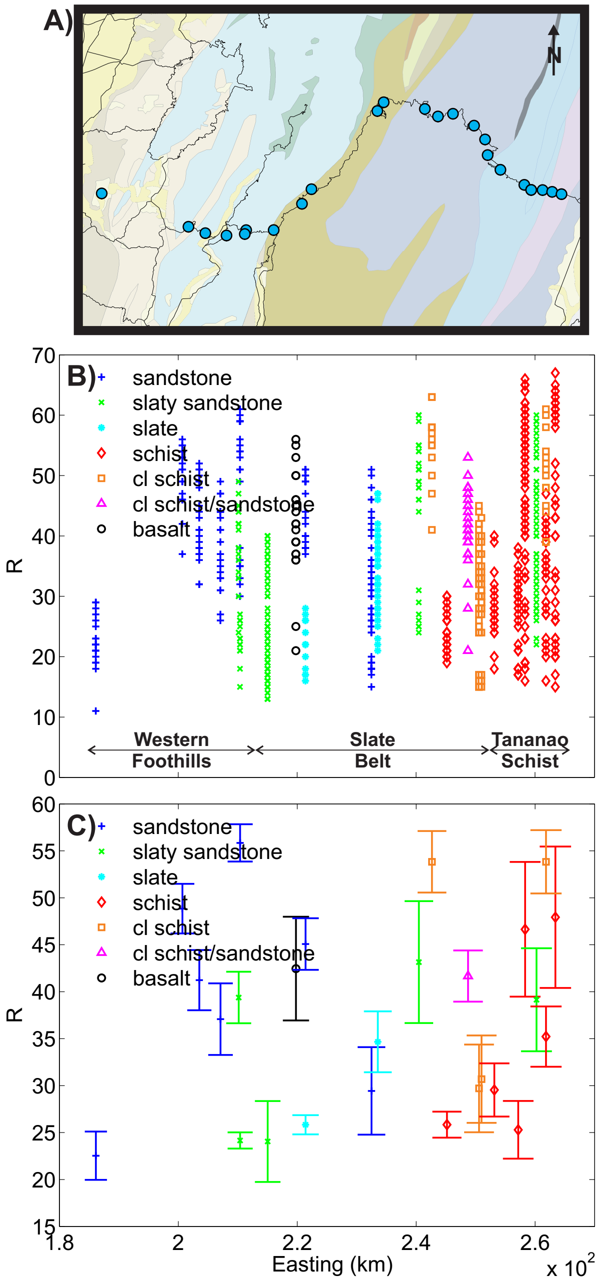

Figure 4.3: A: Detailed geologic map showing the location of the Schmidt hammer measures (blue points) accross the south of the Taiwan mountain belt. B: Schmidt hammer rebound values R for each outcrop, with each measure representing one impact. Lithology of measured rock is indicated: sandstone (blue plus signs), slaty sandstone (green cross), slate (cyan asterisk), schist (red diamond), chloritic schist (yellow square), chloritic schist/sandstone (magenta triangle), and basalt (black circle). C: Schmidt hammer rebound mean values for each outcrop with the errors bars being equal to the standard deviation. Mean values were corrected to remove noise, mainly due to weathering.

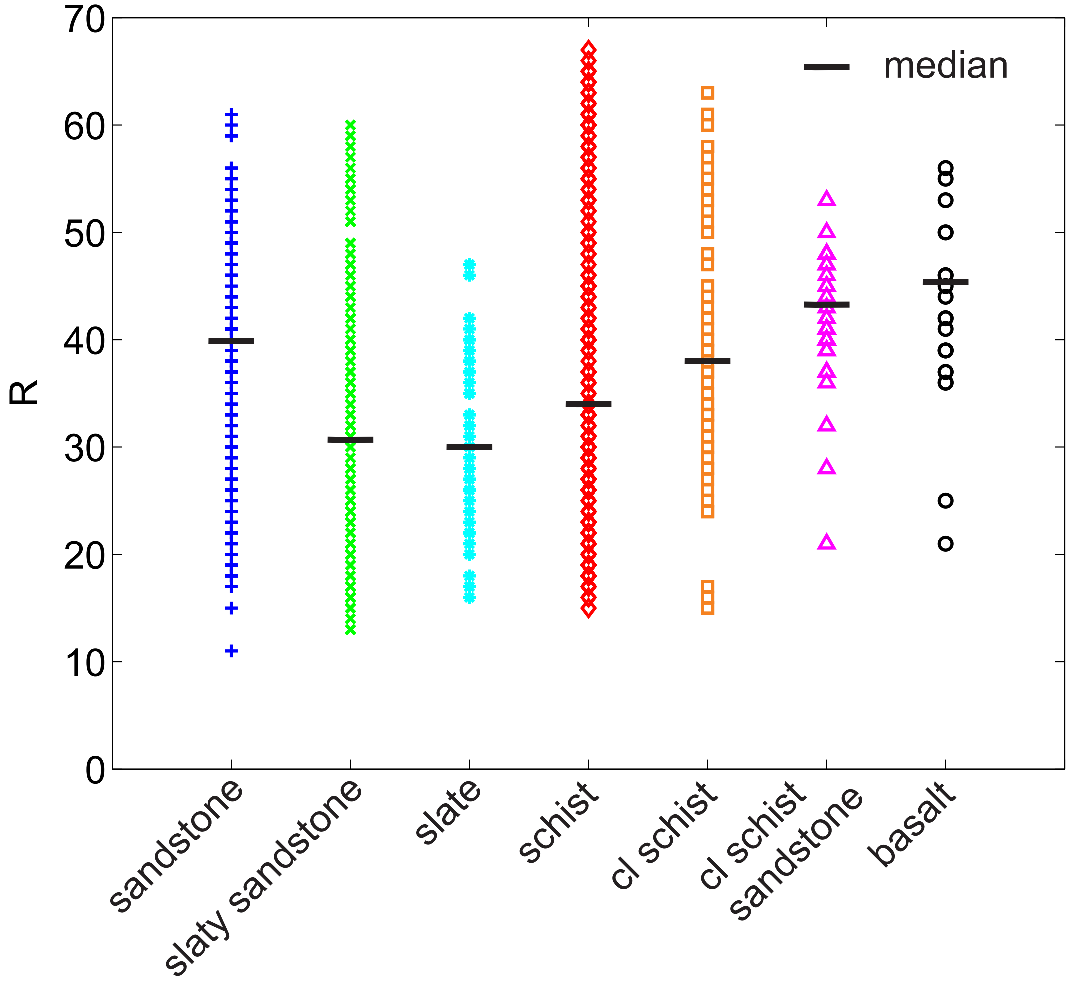

Figure 4.4: Distribution of Schmidt hammer rebound values (R) as a function of rock type or lithology: sandstone (blue plus signs), slaty sandstone (green cross), slate (cyan asterisk), schist (red diamond), chloritic schist (yellow square), chloritic schist/sandstone (magenta triangle), and basalt (black circle). Values were corrected.

location or the lithologies of the samples used in *Dadson et al.* (2003). Thus it is not possible to extensively interpret the comparison. At first order R and UCS are not correlated. This is surprising as many robust empirical relationships exist between UCS and R (see *Aydin and Basu* (2005) for a review). This absence of correlation can be explained by different factors: (1) A possible difference between the representativity of the lithologies measured with the Schmidt hammer and lithologies of the samples used for determination of UCS. It is important to note that the comparison is realised here for stuctural units and not for lithological untis. (2) The effect of rock mass discontinuities, such as fractures or schistosity plans, which probably have a stronger effect on R than UCS, as the volume sampled with a Schmidt hammer (~ 30 cm of characteristic radius) is probably one order of magnitude greater than the volume of the samples used for the determination of UCS (classicaly $1-10$ cm). (3) A discrepancy between R and UCS that has not been documented yet.

4.2 Implications for Erosion of Taiwan at Geologic Timescale

Long-term river erosion, and by extension landscape erosion in mountaineous area, is controlled mainly by the spatial and temporal distribution of precipitation, by the topographic properties of the fluvial network (slope, uplslope area) and by the capacity of the corresponding bedrock to be eroded, i.e. erodibility. This latter is difficult to quantify directly as it depends on the mechanisms of erosion (e.g., abrasion, plucking), on the characteristic scale at which erosion occurs, and on the effective properties of the bedrock (e.g., composition, cohesion of grains or minerals, fracture density). Thus at first order it is useful to simplify this appraisal to isolate the dominant control on erodibility. *Sklar and Dietrich* (2001) empirically deduced from abrasion experiments that erodibility negatively correlates with the square of rock tensile strength. In parallel, tensile and compressional strength are empirically related (e.g., *Bieniawski*, 1967), which supports the initial assumption of this study, that R is a proxy for erodibility.

Under this assumption, our results can be interpreted in terms of relative erodibility: the Tananao Schist is the less erodible part of the studied area, while the central part of the Taiwan mountain belt is the more erodible (Slate Belt); the Western Foothills are more erodible on their western part, while the erodibility of the eastern part is comparable to the Tananao Schist. This spatial pattern of erodibility is not classical, as many mountain belts exhibit mechanically strong units (probably with low erodibility) coinciding with their central area (e.g., Pyrenees, Himalayas, Sierra Nevada, European Alps). However this appraisal needs to be modulated by the relative small variations of R values between the different lithologies encountered.

4.3 Afterwords

This work represents a preliminary study that requires future works in order to lead to a publication. In particular, a comparison between Schmidt hammer rebound and erodibility measured with a circular flume (*Attal and Lavé*, 2009) is needed to clarify the relation between R and erodibility. For that purpose a large number of samples, that correpsond to the tested outcrops, were extracted. We also suggest that the tectonic or metamorphic fabrics of tested rocks influence R. Unfortunately we lack information on the local discontinuities that are potentialy of great influence for our results. Thus a second field investigation is also probably required with a particular focus on the effect of effective properties and rock mechanical anisotropy on R and on erodibility and erosion.

N°	$\bar{R}$	$\sigma(R)$	**1**	**2**	**3**	**4**	**5**	**6**	**7**	**8**	**9**	**10**
01	25,4	5,9	22	11	27	22	26	28	29	29	30	30
	19,5	2,2	14	19	20	21	21	21	19	18	21	21
	21,9	1,9	18	23	25	22	23	22	22	22	22	20
02	47,1	5,9	40	42	49	54	55	47	46	37	50	51
	48,8	4,7	39	51	49	51	46	54	54	51	49	44
	52,3	3,5	46	46	52	53	55	56	54	53	54	54
03	43,5	5,3	40	44	37	50	49	43	49	48	38	37
	36,3	3,0	35	32	32	38	36	38	40	41	35	36
	44,2	7,8	50	37	41	39	52	45	51	51	48	28
04	41,2	7,3	30	47	44	47	44	26	41	44	43	46
	32,1	2,8	28	34	31	33	27	33	31	35	35	34
	40,6	4,4	35	39	37	41	43	49	36	44	38	44
05	56,8	3,8	52	51	59	61	53	54	59	60	60	59
	54,6	4,1	48	55	51	49	56	59	59	54	59	56
	33,0	3,4	26	30	32	35	33	38	35	36	34	31
	23,2	2,9	16	26	26	25	23	23	22	22	24	25
	21,1	4,1	25	27	21	26	21	23	18	15	18	17
06	37,3	7,0	23	45	38	45	42	30	33	38	42	37
	40,3	5,1	40	41	34	33	44	47	42	42	46	34
	39,4	7,2	41	49	38	44	36	42	37	24	48	35
07	16,2	1,2	15	15	15	17	15	17	18	16	18	16
	26,7	4,3	24	31	20	20	27	28	25	32	30	30
	38,4	1,8	40	40	40	37	39	39	39	39	35	36
	18,7	2,4	15	16	18	21	17	20	19	19	19	23
	34,8	4,4	23	33	34	36	37	37	36	37	38	37
	15,7	,5	15	16	16	16	16	16	16	16	15	15
	32,7	4,3	32	33	38	30	30	32	36	40	25	31
	23,6	2,0	25	25	23	26	25	24	19	23	24	22
	33,7	3,6	25	33	34	37	35	35	36	37	31	34
	21,4	2,7	16	20	19	24	25	23	24	21	21	21
	16,5	2,1	14	16	17	18	20	15	17	13	17	18
	17,5	3,6	14	15	16	14	19	24	17	14	21	21
	16,0	2,9	10	13	13	17	17	18	18	18	17	19
	19,7	3,1	17	19	13	20	20	22	22	24	21	19
	22,6	3,3	20	15	22	25	27	25	24	22	23	23
08	42,0	12,5	23	37	36	50	50	46	21	45	55	57
	42,8	12,0	23	25	42	53	36	55	56	39	51	48
	39,9	3,5	34	44	42	41	46	39	39	37	40	37
09	49,6	1,0	48	51	49	51	49	50	49	50	49	50
	38,9	2,4	36	40	42	38	38	39	40	43	36	37
	43,9	6,3	32	38	49	47	44	37	49	51	49	43

	24,6	2,6	24	26	26	26	28	27	22	24	24	19
	18,8	2,4	22	22	16	22	20	17	17	18	17	17
10	30,6	4,3	24	33	26	32	30	36	36	31	33	25
	23,2	3,6	21	20	26	27	25	26	19	24	27	17
	17,3	1,2	16	15	18	18	18	19	17	18	17	17
	32,0	2,7	28	33	31	28	35	35	32	34	30	34
	25,5	1,8	23	26	28	27	25	24	26	28	24	24
	44,0	6,8	47	48	51	46	40	46	50	30	47	35
	40,1	4,0	40	42	38	34	44	41	41	43	33	45
11	27,8	5,0	21	23	28	32	31	32	28	32	32	19
	39,3	4,5	37	38	38	37	35	39	47	35	39	48
	40,8	5,6	41	29	41	35	39	46	47	40	46	44
	29,8	4,6	32	27	33	36	26	25	37	28	30	24
	31,8	8,0	22	33	40	40	30	22	42	21	32	36
12	51,4	6,3	42	60	48	54	60	55	44	49	55	47
	27,6	4,3	22	24	25	26	29	25	31	27	30	37
	47,9	4,9	45	51	48	51	51	51	54	46	37	45
	51,3	4,4	46	55	46	52	49	55	59	49	48	54
13	49,3	8,9	32	57	41	53	58	58	56	47	41	50
	56,6	4,3	57	50	63	63	58	55	58	55	56	51
14	23,2	1,4	23	26	23	23	24	22	24	24	22	21
	27,5	1,8	28	29	30	30	26	28	27	26	25	26
	20,3	,9	19	21	19	20	22	20	21	21	20	20
15	40,0	2,7	37	37	41	37	39	40	39	44	42	44
	41,4	5,7	33	41	40	41	45	48	48	42	45	31
	44,5	6,9	28	41	46	47	43	53	48	50	41	48
	35,8	3,8	33	40	32	40	39	28	36	37	36	37
	40,1	10,5	21	21	42	40	45	42	47	48	46	49
16	30,8	5,5	19	30	26	32	35	39	33	28	33	33
	16,0	,9	17	16	16	15	17	17	15	15	17	15
	38,1	4,8	30	33	33	40	37	42	40	45	39	42
	25,0	1,5	23	24	24	24	25	25	27	24	27	27
	39,6	3,0	44	42	41	38	39	36	37	44	38	37
	32,4	3,4	26	32	34	30	34	33	37	28	35	35
17	31,3	11,9	14	17	15	28	39	37	35	43	44	41
	28,2	7,0	24	34	16	31	33	31	40	27	21	25
	27,5	4,2	17	24	28	30	30	29	29	32	27	29
18	27,9	7,2	19	20	31	34	40	27	26	26	36	20
	29,1	5,4	21	29	32	39	28	28	24	26	28	36
	25,5	4,0	20	25	18	24	27	28	26	30	27	30
19	17,6	,5	18	17	17	18	17	18	18	17	18	18
	29,9	2,5	24	28	29	31	32	32	30	30	32	31
	21,9	3,2	17	22	27	21	25	26	21	18	21	21
	31,4	2,2	28	31	30	29	33	35	31	31	32	34
	31,7	6,3	16	30	30	37	38	37	34	30	31	34
20	17,9	1,4	15	19	19	19	16	18	18	19	18	18
	50,2	6,7	48	40	53	53	57	45	56	52	40	58

	25,6	3,0	20	27	27	23	23	29	25	28	29	25
	50,3	2,6	46	51	50	54	55	49	49	50	50	49
	41,4	5,9	28	36	40	42	46	45	43	40	48	46
	55,5	8,9	49	60	58	55	55	61	62	60	33	62
	46,1	11,0	24	33	41	56	56	53	44	58	50	46
	60,6	3,7	52	57	65	64	61	62	61	60	62	62
	50,2	9,2	32	37	58	55	46	58	55	58	49	54
	59,2	7,6	42	57	65	66	64	59	62	65	51	61
	41,7	4,1	40	34	42	36	41	44	45	45	43	47
	48,7	7,4	47	48	44	54	33	44	49	57	53	58
21	27,3	2,5	25	28	28	30	27	26	28	22	30	29
	56,1	2,5	58	59	59	58	55	57	53	53	56	53
	44,4	5,5	49	44	54	40	46	45	34	40	47	45
	29,8	4,3	25	27	32	33	36	23	27	29	35	31
	42,3	5,1	35	37	47	48	47	43	48	41	36	41
	34,2	3,1	32	37	35	36	30	31	32	33	36	40
	52,1	5,9	46	48	51	42	56	60	49	59	57	53
22	35,0	1,6	35	34	36	35	34	34	37	34	38	33
	38,1	2,3	38	40	40	40	40	35	39	36	39	34
	25,3	2,8	23	22	23	27	27	28	29	27	26	21
	43,1	4,7	35	42	39	42	41	43	47	42	51	49
	26,7	7,0	24	20	31	29	16	21	33	36	35	22
	53,0	5,6	49	60	45	61	58	48	51	54	56	48
	45,0	5,8	47	53	48	52	44	50	39	39	38	40
23	58,5	8,2	40	60	50	60	67	65	64	61	55	63
	58,6	3,2	57	52	60	61	58	61	62	61	55	59
	61,2	2,0	58	59	63	60	62	62	64	63	59	60
	43,0	4,3	34	40	43	43	45	45	48	46	47	39
	30,5	8,0	19	26	33	33	29	33	40	43	18	31
	26,1	7,4	15	17	20	22	26	27	31	34	35	34
	21,8	4,2	16	20	20	21	23	15	23	26	27	27

N°	**East (m)**	**North (m)**	**Alt (m)**	**Rock Type**	**Formation**
01	186146	2559410	40	Sandstone	Q
02	200694	2553301	220	Sandstone	Pc
03	203534	2552134	319	Sandstone	MP
04	207092	2551710	287	Sandstone	MP
05	210396	2552668	562	Slaty Sandstone	M3
06	210159	2551955	581	Slaty Sandstone	M3
07	215025	2552665	402	Slaty Sandstone	M3
08	219786	2551429	508	Basalt	
09	221393	2560072	565	Slate	Mi
10	232482	2574257	1003	Sandstone	Mi
11	233548	2575831	1264	Slates	Mi
12	240451	2574618	2258	Slaty Sandstone	Pilushan
13	242651	2573251	2535	Chloritic Schist	Pilushan
14	245165	2573749	2865	Schist	Pilushan

15	248713	2571585	2071	Sandstone/Chloritic Schist	Pilushan
16	250564	2569082	1828	Chloritic Schist	Pilushan
17	250993	2566237	1208	Chloritic Schist	Pilushan
18	253142	2563566	699	Schist	Wulu
19	257152	2560841	650	Schist	Wulu
20	258310	2559917	561	Schist	Pilushan
21	260221	2559898	482	Slaty Sandstone	Hsin-Wu
22	261829	2559567	396	Chloritic Schist	Wulu
23	263403	2559154	408	Schist	Yuli Belt

Acknowledgments

We thank Olivier Beyssac as well as the members of the ANR Taiwan project. We also acknowledge National Taiwan University and Central Geological Survey for their supports. This study was funded by the ANR Taiwan project.

Chapter 5

Experimental Study of Rock Hardness - Diagenetic Grade Relationship: Application to the Annot Sandstone, French-Italian Alps

In Prep.
Steer, P., Cattin, R., Gibert, B., Labaume, P., Loggia, D., Soliva, R., Taboada, A., Jolivet, M., Lavé, J. and Sizun, J.P.

Abstract

In the large scale studies of landscape evolution, rock erodibility is a key parameter which controls the capacity of rocks to be eroded under the action of erosive agents. This parameter is primary controlled by lithology. However, it also integrates both microscopic and macroscopic parameters such as grain cohesion or fracture density. Despite its extensive use in erosion laws for field or numerical studies, quantifying river bedrock erodibility is still an ongoing issue. Previous studies have highlighted the first order control of rock nature on bedrock erodibility. Here we rather investigate the effect of diagenetic grade using both laboratory measurements and rock hardness data collected in the field with a Schmidt hammer. We consider Schmidt hammer rebound as a proxy for erodibility. Our approach is applied to the well-studied Annot sandstones localized in the southern part of the external French-Italian Alps. Due to thrust front propagation in the external Alpine domain, this Upper Eocene - Lower Oligocene foreland basin formation has been partly buried below allochtonous units during the Oligocene. Exhumed by thrusting during the late Miocene, this formation now exhibits a clear diagenetic gradient increasing from West to East. Taking advantage of the availability of a large petrographic and petrophysic dataset, we study the spatial variation of the Annot Sandstone erodibility with the estimated diagenetic grade. Our preliminiary results reveal that erodibility is correlated to the diagenetic grade, with the external (western) part of the Annot Sandstone exhibiting higher erodibility than the internal (eastern) part. At the scale

of the outcrop, erodibility is characterized by a high variability which statistically does not correlate with density, elastic parameters, porosity or mineral content. We rather suggest that for equivalent diagenetic grade, erodibility is mostly controlled by the density of fracturation.

1 Introduction

Earth surface topography is the result of the motion of tectonic plates, that deforms Earth's exterior and forms topographic relief, and of erosion which shapes uplifted regions. Last decades have seen a growing awareness of the effect of climate on river erosion and on its interactions with teconics (e.g., *Willett*, 1999; *Dadson et al.*, 2004; *Roe*, 2005). Even if bedrock lithology is predicted by river incision formalism to be as well a primary control on river erosion (*Howard et al.*, 1994; *Godard et al.*, 2006), its effects on erosion have not been extensively documented. Lithological variations are difficult to account for and bedrock characteristics are often combined into a single coefficient of erodibility (*Stock and Montgomery*, 1999). Rock properties that control the resistance to mechanical erosion, i.e. erodibility, are scale dependent (*Godard et al.*, 2009): (1) at the mineral scale, resistance is controled by mineral hardness; (2) when upscaling at the mineral assemblage scale which is the relevant scale for river abrasion processes (*Sklar and Dietrich*, 2001), resistance is in addition controlled by the cohesion of the mineral assemblage which depends on porosity, fabrics and fractures, and on their respective orientations and spatial density. Some recent efforts have lead to an experimental characterization of rock erodibility for different lithologies using rounded fragments in a circular flume (*Attal and Lavé*, 2006, 2009; *Godard et al.*, 2009). Despite that, erodibility and more particularly its relation to rock effective properties remains badly constrained.

Some other studies propose that rock erodibility can be quantified using in-situ devices such as the Schmidt hammer (*Duvall et al.*, 2004; *Goudie*, 2006; *Goode and Wohl*, 2010; *Viles et al.*). Schmidt hammer permits the non-destructive estimate of uniaxial compressive strength (UCS) and Young's modulus (E) of rock materials (*Aydin and Basu*, 2005). *Sklar and Dietrich* (2001) demonstrated an inverse relation between erodibility (K) and the square of tensile trength (σ_t). If assuming that UCS and σ_t are proportional (e.g., *Bieniawski*, 1967), thus K and R are anti-correlated.

Here we consider that R is a proxy for K. We investigate the effect of diagenesis on erodibility using: (1) a pre-existing petrogenetic datatset (*Labaume et al.*, 2008b) with samples that were measured in laboratory; (2) and R values collected in-situ. Our approach is applied to the well-studied Annot Sandstone formation, localized in the southern part of the external French-Italian Alps, which presents a clear diagenetic gradient (*Labaume et al.*, 2008a). First we both introduce the geological setting of the Annot Sandstone and the studied outcrops chosen at different diagenetic grade. We then present the spatial variations of Schmidt hammer rebound in relation to the diagenetic grade. Next Schmidt hammer rebound is compared to a range of petrogenetic indexes including elastic properties. Last we disscuss our results in relation to fracturation of the tested outcrops, and conclude on the effects of diagenetic grade on erodibility.

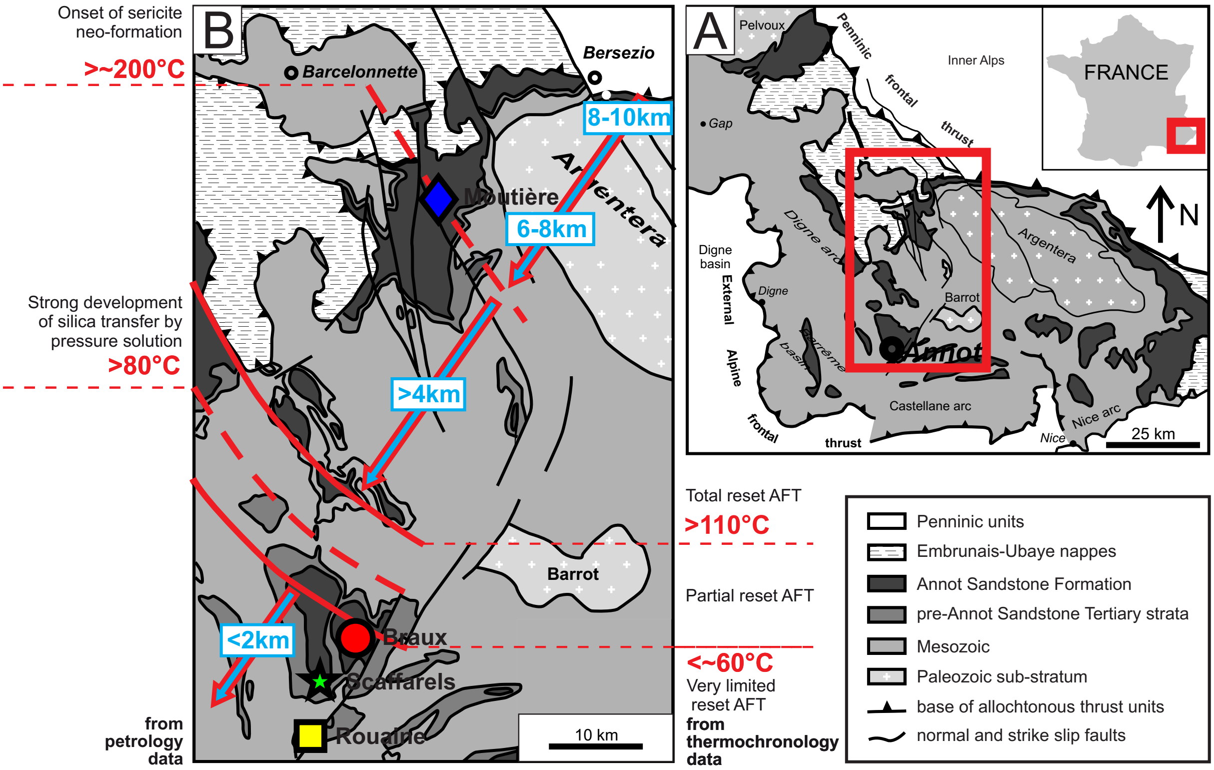

Figure 5.1: Structural sketch of the SW external Alps (A) and of the studied area (B) with distribution of the maximum temperatures and possible related burial depths reached by the Annot Sandstone formation (modified from *Labaume et al.* (2008a)). Temperatures are inferred from a petrographic study and apatite fission track (AFT) thermochronology. Burial depths are calculated assuming a paleo-geothermal gradient of $25 - 30$ °C.km^{-1}. Location of the four studied outcrops is indicated with color markers.

2 Regional Setting

2.1 Geological Setting

The Annot Sandstone formation caps the inner part of the external Alpine units (Digne, Castellane and Nice arcs), the Paleozoic substratum of which forms the Argentera and Barrot massifs (Fig. 5.1). The northern part of this formation is covered by the allochtonous Embrunais-Ubaye nappes, issued from the internal Alps east of the Penninic front.

The Annot Sandstone, which corresponds to a sand-rich turbidite system (*Du Fornel et al.*, 2004; *Joseph and Lomas*, 2004), was mainly sourced in the crystalline basement of the Corsica-Sardinia massif (*Jean et al.*, 1985; *Garcia et al.*, 2004). This formation corresponds to a sand-rich turbidite system (*Du Fornel et al.*, 2004; *Joseph and Lomas*, 2004) and was deposed during the foreland subsidence of the external Alps in the Late Eocene - Early Oligocene (*Ravenne et al.*, 1987). Then in Late Oligocene, thrusting above the Annot Sandstone formation occurs at the emplacement of the Pennininc front and upper Embrunais-Ubaye (*Kerckhove*, 1969; *Fry*, 1989; *Corsini et al.*, 2004). The Annot Sandstone formation was then partially

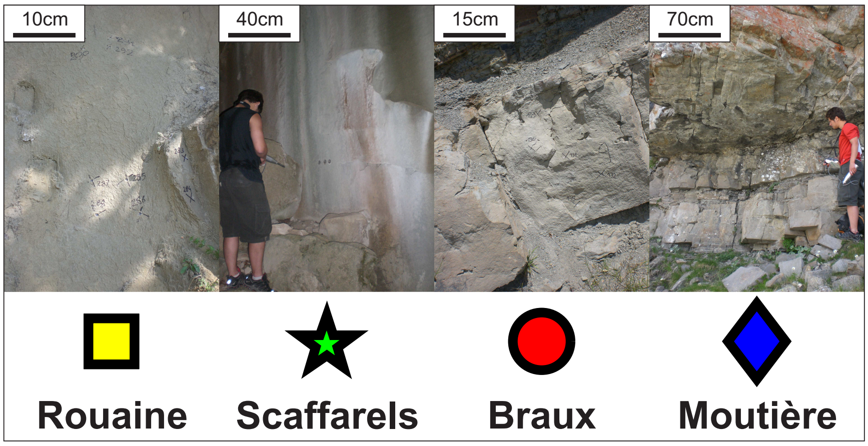

Figure 5.2: Pictures of the Rouaine, Scaffarels, Braux and Moutière outcrops and their correspind markers. Diagenetic grade increases from left (SW) to right (NE).

exhumed by uplifting of the Argentera and Barrot massifs (*Bigot-Cormier et al.*, 2006) which resulted in the erosion of nappes covering the Annot Sandstone formation, and to the formation of normal faults that cutted through the nappes (*Labaume et al.*, 1989). Since then these normal faults were reactivated as strike-slip faults by N-S compression during the Plio-Quaternary.

2.2 Diagenetic Gradient and Studied Outcrops

The Annot Sandstone formation now exhibits a strong diagenetic gradient, from relatively unconsolidated sandstones in the SW to strongly lithified sandstones in the NE. This field observation is consistent with petrologic observations and aptite fission tracks (AFT) thermochronology data, which both indicate an increase of the maximum temperatures reached during burial by the Annot Sandstone formation from SW to NE (*Labaume et al.*, 2008a). Associated burial depths range from less than 2 km in the SW up to 10 km in the NE.

Four outcrops were tested with a Schmidt hammer. The Rouaine outcrop (Fig 5.2) is located in the SW of the Annot Sandstone formation and presents the lowest diagenetic grade with unconsolidated sandstones. The Scaffarels and Braux outcrops are of higher diagenetic grade and exhibit some main layers of consolidated sandstones ($\sim 0.1 - 2$ m thick), separated by thin layers dominated by marls. Last, the Moutiére outcrop located in the NE of the Annot Sandstone formation exhibits the highest diagenetic grade, with layers of strongly lithified sandstones ($0.1 - 10$ m thick) separated by a few thin layers of shales. Secondary macroscopic fractures are present at the three last outcrops, with a qualitative increase of apparent fracture density with diagenetic grade.

3 Method: Schmidt Hammer Measures

Each outrcop was measured with a Schmidt hammer of type N. It was initially conceived to test the hardness of concrete in-situ. Since then it has been applied

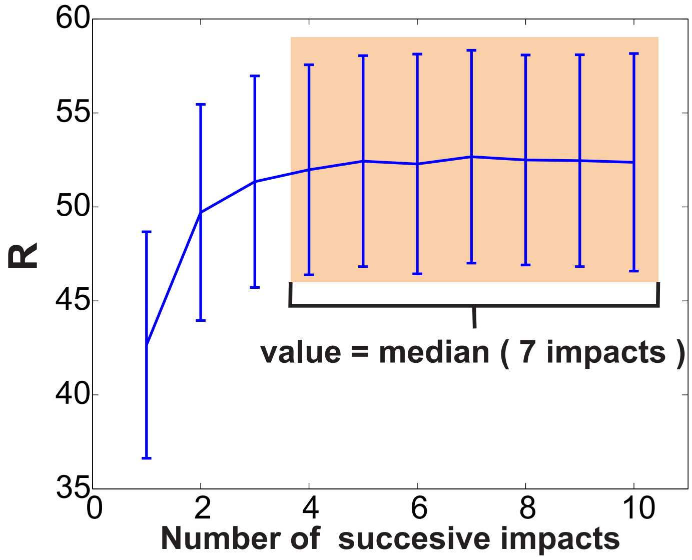

Figure 5.3: Statistical distribution of the mean Schmidt Hammer rebound value (R) as a function of the number of impacts. Errorbars indicates the standard deviation that affects the distribution of each impact when considering the $\sim$ 250 measures of this study. Note that only the last seven impacts present the same statistical distribution, and we consider its median value as representative.

to geomorphology to assess either rock weathering (e.g., *Aydin and Basu*, 2005; *McCarroll*, 1991) or mechanical erodibility (*Duvall et al.*, 2004; *Goudie*, 2006; *Goode and Wohl*, 2010; *Viles et al.*). As previously mentioned the intensity of its rebound value (R) correlates well with rock uniaxial compressive strength (UCS) and Young's modulus (E) measured in laboratory (see *Aydin and Basu* (2005) for a review of the empirical laws).

During this study, a total of $\sim$ 250 measures was acquired. The Rouaine outcrop was measured only 10 times due to the spatial homogeneity of its sandstone. On the other hand the Scaffarels, Braux and Moutière ones include between 50 and 100 measures so as to capture lithological variability. Only layers dominated by sandstones were tested. We have measured R at the same approximate location than the extracted samples of a petrogenetic study (*Labaume et al.*, 2008b). The distance between the location the measures of R and the extracted samples is $\sim$ 10 cm. We make the assumptions that: (1) this distance is sufficiently small to allow a comparison of the two datasets; (2) this distance is large enough so that the void volumes of the extracted samples do not significantly affect R measures.

For each measure 10 impacts were realized. The distribution of R as a function of the number of impact shows a global increase during the three first impacts and then converges towards a constant value (Fig. 5.3). This increase can be related to rock weathering (*Aydin and Basu*, 2005). However this is out of the scope of this paper, and we rather focus on the median value of the last seven impacts which seems to be statistically representative of the rebound of the rock.

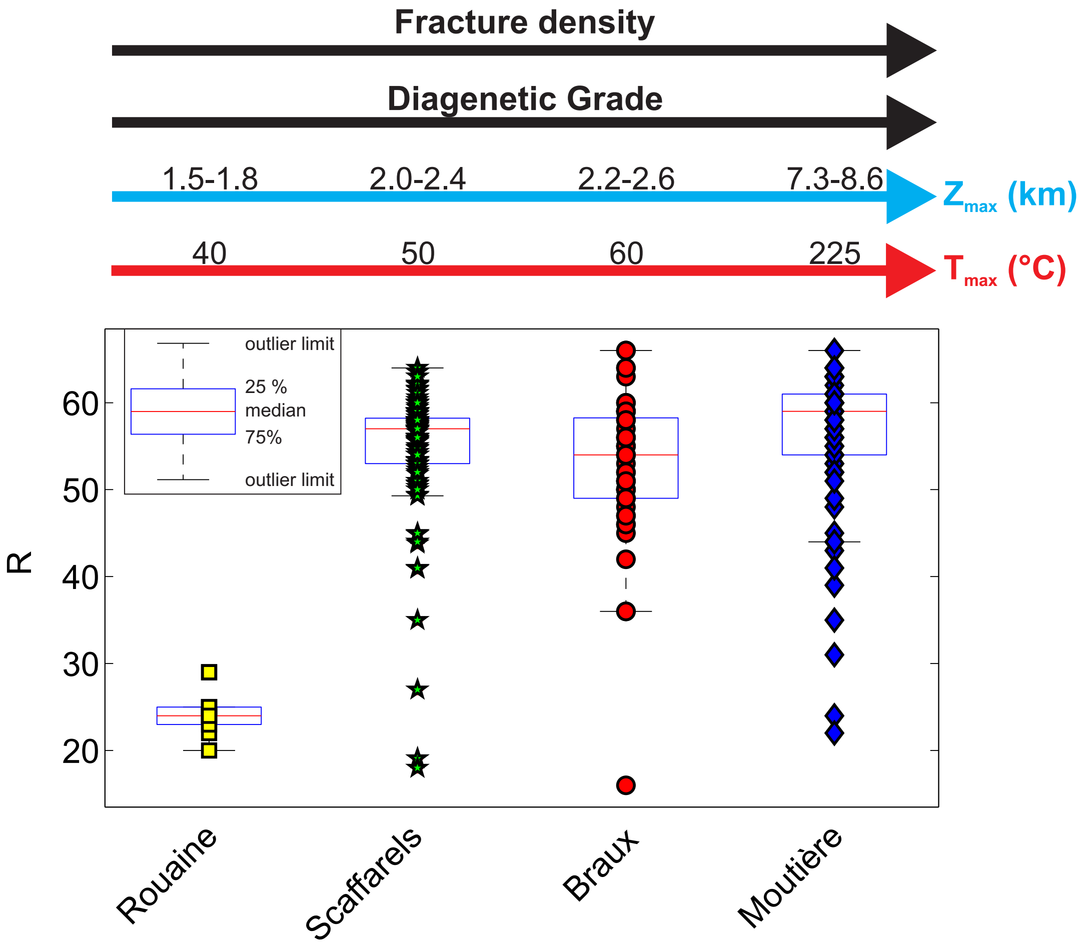

Figure 5.4: Boxplot of the distribution of Schmidt Hammer rebound value (R) for the Rouaine, Scaffarels, Braux and Moutière outcrops. The diagenetic grade increases from letf to right. The temperature and maximum burial depths are indicated with a red and a blue arrow, respectively.

4 Results

4.1 Schmidt Hammer Rebound and Diagenetic Grade

Figure 5.4 shows the distribution of R as a function of the diagenetic grade of each outcrop. The Rouaine and Moutière sandstones, which present the lowest and highest diagenetic grade, clearly also exhibit the lowest and highest R values, respectively. The mean R value is 24 for Rouaine, whereas 59 was obtained for Moutiére. Thus at first order there is a correlation between R and the diagenetic grade. However this observation does not hold at second order, when considering low to intermediary diagenetic grade, at the Scaffarels and Braux outcrops. They have mean R values of 57 and 54 respectively, which is high and very close to the value obtained for the Moutiére sandstones, while it is closer to the Rouaine one when considering the diagenetic grade. Qualitatively, R values seem to correlate with the apparent cohesion and compaction of rock materials, which strongly increases between the Rouaine and Scaffarels or Braux outrcops. The scattering of the R values is important except for the Rouaine outcrop. Interestingly this absence (or presence) of scattering qualitatively correlates with the absence (or presence) of apparent macrosopic fractures.

4.2 Schmidt Hammer and Petrogenetic Indexes

To futher assess the effect of diagenetic grade on R values, we compare our dataset with a pre-existing petrogenetic study of the same outcrops (*Labaume et al.*, 2008a). Due to the unconsolidated nature of the Rouaine sandstones, which does not allow for sample extraction, only the Scaffarels, Braux and Moutière sandstones were extensively studied. Moreover each measure previously done with the Schmidt Hammer does not necessary correspond to an extracted sample. These measures were consequently excluded. The petrogenetic dataset includes: (1) qualitative clay and calcite cement indexes ranging from 0 to 3; (2) rock bulk density ρ_{bulk}; (3) P-wave accoustic velocity V_p; (4) water porosity; (5) and rock permeability K.

Figure 5.5 presents R values as a function of each of these petrogenetic indexes. Clay content decreases with the diagenetic grade, while calcite content is apparently not correlated to the diagenetic grade. As expected, porosity and permeability decrease with the diagenetic grade. Concordingly rock bulk density increases with the diagenetic grade, such as P-wave velocity. As a consequence and quite surprisingly R does not significantly correlate at first order with any of these indexes. This is unexpected, as previous studies have proposed some empirical relations between R and elastic parameters or P-wave velocity (see *Aydin and Basu* (2005)). We related this absence of correlation to the effective properties of rocks which are known to be scale dependent. Petrogenetic samples have a characteristic dimension of 1 to 10 cm, while Schmidt Hammer characeristic sampling size ranges between 10 cm and 1 m, from our estimates. The observed apparent increase of fracture density with the diagenetic grade can potentially explain this scale effect.

5 Discussion and conclusion

In this paper we have studied the effect of the diagenetic grade of the Annot sandstones on rock erodibility measured with a Schmidt hammer. Our study has highlighted a first order correlation between the diagenetic grade of sandstones and the values of Schmidt Hammer rebound. The change from a non-cohesive to a cohesive rock mass seems to explain most of this correlation. As a consequence rock erodibility is likely to strongly increase with the diagenetic grade of sandstones mainly when going from a non-cohesive to a cohesive rock mass.

No qualitative correlations between petrogenetic properties and Schmidt Hammer rebound values are observed for cohesive sandstones, and in particular between elastic properties measured in laboratory and Schmidt Hammer rebound values, whereas a correlation exists between diagenetic grade and the elastic and petrogenetic properties. This can be explained by the scale dependency of rock mass effective properties. In this paper, we assume that the apparent macroscopic fracture density, which qualitatively increases with the diagenetic grade, is the main factor responsible of this scale effect. As a consequence rock erodibility deduced from laboratory experiments (*Sklar and Dietrich*, 2001; *Attal and Lavé*, 2009) can

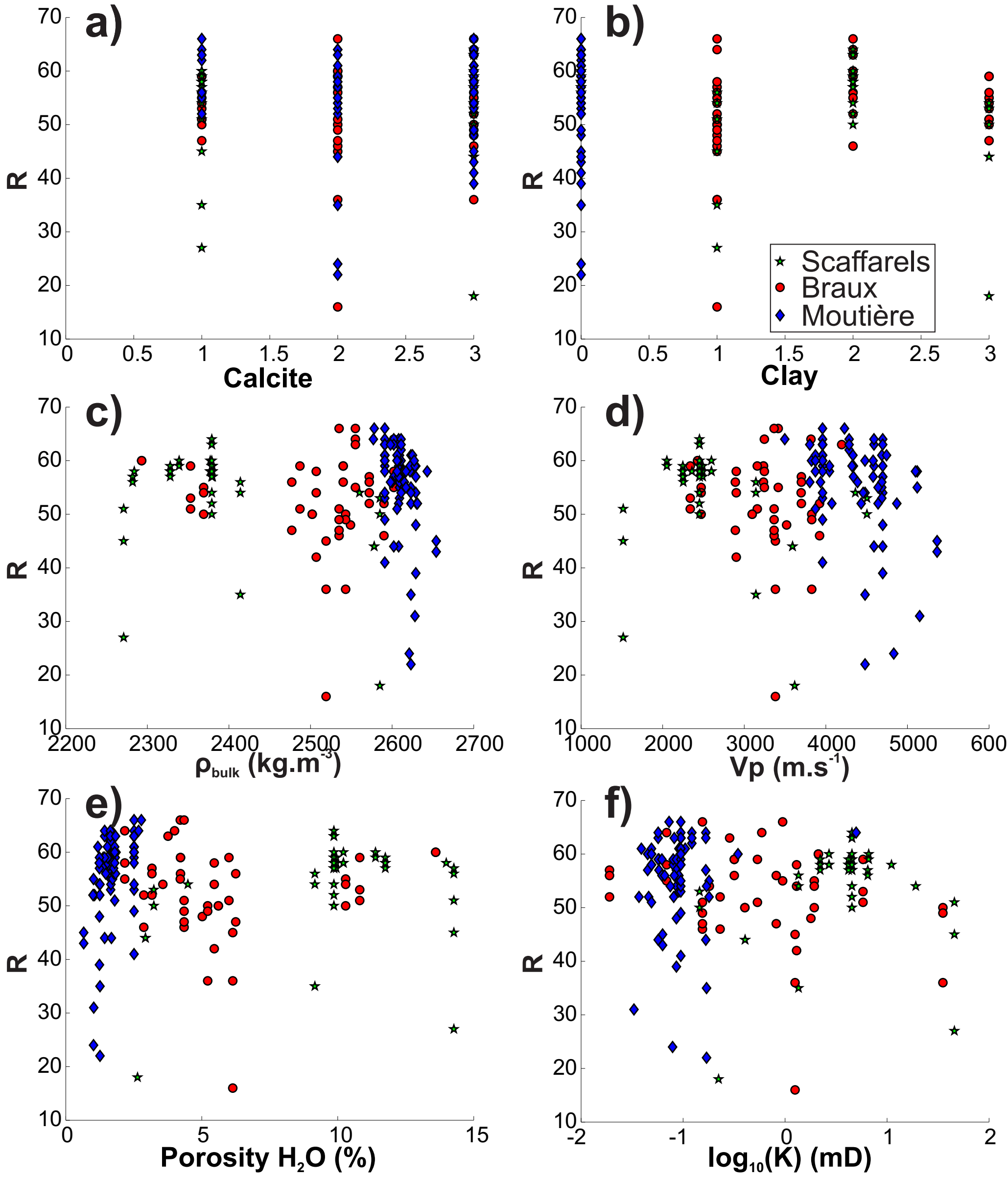

Figure 5.5: Plot of the distribution of Schmidt Hammer rebound values (R) as a function of petrogenetic indexes: (a) calcite index, (b) clay index, (c) rock bulk density ρ_{bulk}, (d) P-wave accoustic velocity V_p, (e) water porosity and (f) rock permeability K (semi-log plot).

not be directly extrapolated to larger spatial scale, without an estimate of macroscopic fracture density. Our observations are consistent with mechanical theories acknowledging the contribution of fracture on rock rheology (e.g., *Hudson*, 1980). It also supports the idea that fracturation is possibly the dominant factor controling rock erodibility (*Molnar et al.*, 2007).

5.1 Afterwords

This study represents a preliminary study that requires future works to lead to a publication. In particular a comparison between in-situ parameters, including P- and S-wave velocity and fracture density, and the parameters deduced in laboratory and presented in this study is needed.

Acknowledgments

We acknowledge the National Parc of Mercantour. This study was funded by the ERODROCK project of Geosciences Montpellier.

Chapter 6

In-situ quantification of the effective elasticity of a fault zone, and its relationship to fracture density

Submitted, Journal of Structural Geology

Steer, P., Bigot, A., Cattin, R. and Soliva, R.

Abstract

Up to now, most studies set up to assess effective elastic properties of fractured rock masses, have employed theoretical or numerical approaches based on laboratory measurements that may not be representative of the scale of fault zones. In this paper, we study the effect of fracture properties such as density and types at the scale of an outcrop, on the effective elasticty measured with a Schmidt hammer. The outcrop studied, dominated by limestones, is part of the deformation zone of the St Clément fault, in the south of France. First, we find relationships between fracture density and effective elasticty, with a negative correlation for faults and open fractures and with a positive correlation for sealed fractures. These correlations are compatible with theoretical models of effective elasticity. Then we define a linear model, to consider simultaneously each fracture type density, that we invert using the least squares method so as to match the spatial distribution of effective elasticity. The results of the inversion confirm that sealed fractures have a positive effect on effective elasticity, while open fractures and faults, depending on the lithology considered, have the strongest negative effect. Moreover, the inversion allows to constrain the representative volume to which are sensitive Schmidt hammer measures (30 to 50 cm of radius). This study represents to our knowledge the first in-situ attempt to quantify the relative effect of fracture types on the effective elasticty of a rock mass in a fault zone. Our results may have geodynamical consequences, related to the interseismic stress build-up of major faults by sealing of fractures in the damage zone.

1 Introduction

Rock discontinuities, such as faults or fractures, play a major role in geological systems, leading to large heterogeneity and anisotropy in hydraulic, thermal as well as geomechanical properties of rocks. The spatial density of mechanical discontinuities significantly affects the elastic behaviour of a fractured rock medium (*Bristow*, 1960; *Walsh*, 1965; *O'Connell and Budiansky*, 1974; *Kachanov*, 1980; *Hudson*, 1980; *Schoenberg*, 1980; *Bieniawski*, 1993), its compressive strength (*Kemeny and Cook*, 1986) and its permeability to fluids (*Renshaw*, 1996), the brittle strain of a fault population (*Scholz and Cowie*, 1990; *Schultz*, 2003) and the efficiency of river or glacier erosion of a fractured bedrock (*Molnar et al.*, 2007). For instance, the architecture of major fault zones is commonly represented by a central zone of protocataclasite and ultracataclasite, surrounded by a large damage or process zone containing micro and macro-fractures (*e.g.*, *Caine et al.*, 1996). These latter affect the mechanical effective properties of the damage zone and thus the behaviour and growth of major fault (*Segall and Pollard*, 1980; *Cowie and Scholz*, 1992; *Katz et al.*, 2000; *Aydin*, 2009) and their slip distributions (*Bürgmann et al.*, 1994).

A common way to characterize the effects of fractures on a rock mass, consists in assessing the resulting effective properties from both laboratory experiments (*e.g.*, *Sayers and Kachanov*, 1995) and theoretical approaches (*e.g.*, *Kachanov*, 1992). Because of potential scale effects associated with mechanical disconituies (*e.g.*, *Schlische et al.*, 1996; *Bonnet et al.*, 2001), the representativity of effective properties, determined from laboratory samples or other small-scale measurements (< 10 cm) when upscaling to the dimension of a fault zone (> 1m), must be seriously questioned. The Schmidt hammer offers the possibility to obtain a direct and in-situ estimate of the effective properties of a rock mass at a greater scale than laboratory experiments (10−100 cm). It was developed in the late 1940s for non-destructive testing of concrete hardness (*Schmidt*, 1951), and later to estimate rock hardness. In particular its measures are found to correlate with the Young's modulus of a rock mass (*e.g.*, *Aydin and Basu*, 2005; *Goudie*, 2006).

In this paper we investigate the effect of fractures, and more specifically their types and spatial densities, on the effective elasticty of a fault zone, estimated with an un-matched density of Schmidt hammer measures of 25 measures per m^2. Qualitative as well as a quantitative comparisons of rock effective elasticity with fracture properties are carried out. This analysis is applied to an outcrop (19 m × 3 m) located close to the St Clément fault zone, in the south of France. First, we briefly present the outcrop and its geological setting. Then the collected data and methods are described and illustrated by preliminary results. Next we present the results of a statistical analysis and discuss the robustness and validity of the proposed model with respect to theoretical and empirical predictions.

2 Data and Preliminiary Results

The study area is located close to the St Clément fault zone ($\sim$ 10 km North of Montpellier, France, Fig. 6.1), where fracturation, in relation to the local tectonic setting, has already been documented (*Taha*, 1986; *Soliva et al.*, 2010) and is similar to other related faults (*Etchecopar et al.*, 1981; *Rispoli*, 1981). Data were collected

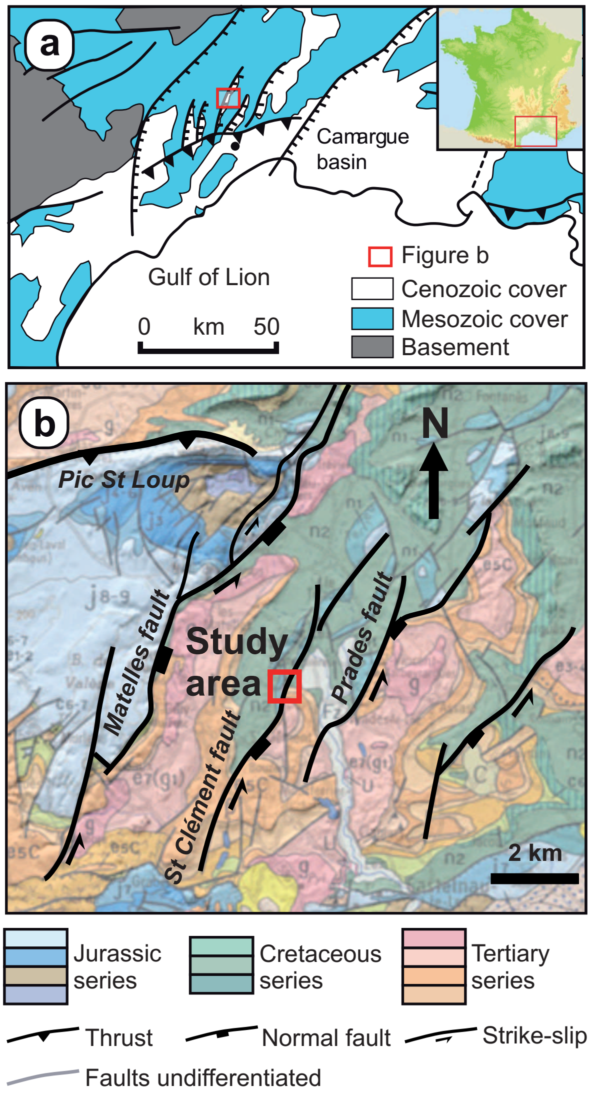

Figure 6.1: (a) Geological and tectonic setting of southern France. Red box shows the location of subsequent figure. Inset shows location of study area (box) relative to France. (b) Simplified geological map of the area. Heavy black lines show the major faults. The red box precises the location of the studied area.

over four weeks in April and May of 2010 along an outcrop oriented perpendicular to the major fault within the study area. The dataset comprises both a detailed mapping of fractures and a dense set of Schmidt hammer measurements (Fig. 6.2), which is a simple method to quantitatively assess in situ rock hardness (*e.g.*, *Aydin and Basu*, 2005; *Aydin*, 2009).

2.1 Studied outcrop: St Clément Fault Zone

The brittle tectonic structures observed (Fig. 6.2a) were formed during a main phase of extension related to the onshore landward part of the Oligocene-Aquitanian Gulf of Lion rifted margin (*Auzende et al.*, 1973; *Séranne et al.*, 1995; *Benedicto*, 1996). As suggested by the presence of a fault scarp and a hanging wall depression in-filled by syn-rift Oligocene sediments, the main part of the brittle deformation observed in the study area is due to the NW-SE extension related to Oligocene-Aquitanian rifting. However, the main surface of the studied fault, which is 60°dipping, also shows oblique and sinistral strike slips and therefore potential fractures related to these horizontal slip components. This suggests that the fault was initiated first as a normal fault, during a not well documented NW-SE middle Cretaceous extension, and reactivated as a sinistral strike slip during the Paleocene-Eocene Pyrenean compression, before the main normal fault Oligocene movement (*Arthaud and Mattauer*, 1969). Therefore, even if a minor part of the deformation is related to a strike slip movement, most of the fractures, the stylolites, the cataclastic fault core and the fault surfaces are consistent with normal faulting.

In the study area, the faults appear to be limited at depth by a Triassic mechanically soft layer (evaporitic level) allowing a major décollement in which the St Clément fault probably ends (*Benedicto*, 1996; *Séranne et al.*, 1995). The St Clément fault therefore cuts the entire sedimentary cover and the cumulative displacement has been estimated to be close to 500 m in the study area. At the surface, the fault cuts the lower Cretaceous series composed of Berriasian micritic limestone, that sometimes contains marly layers in its upper part. The study outcrop exposes the footwall of the eroded main fault zone, which is composed of these lower Cretaceous limestones.

2.2 Mapping of Fractures

The outcrop contains two secondary faults both of decametric normal displacement, containing a cataclastic core (NW fault) and a shale smeared core (SE fault) (Fig. 6.2a). These two faults are surrounded by their kinematically coherent damage zones composed of minor normal faults, sparite sealed mode I fractures, bed parallel stylolites and also unsealed deconfinement fractures (open fractures hereinafter) that are randomly oriented and potentially related to the late events of exhumation of the outcrop. To assess their spatial distribution, these different types of fractures have been mapped and reported in Figure 6.2b. For resolution issues, only fractures with a minimum planar length of ~ 5 cm are mapped. A coordinate mesh composed of squares with dimension of 1 m × 1 m is used to give a common spatial referential with the Schmidt hammer dataset.

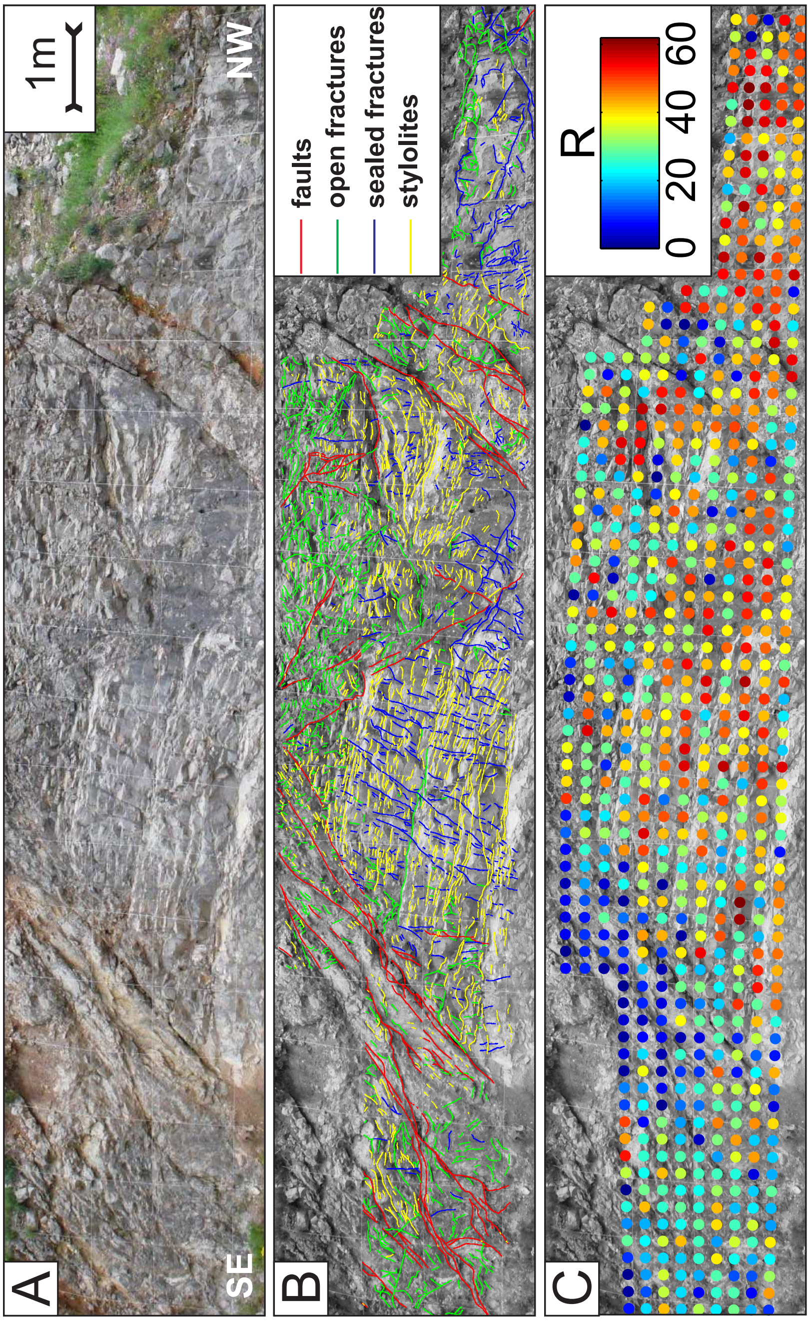

Figure 6.2: (A) In terms of lithology, the studied outcrop mostly consist of gray limestones with parts of brown marlstone and cataclasites located within the SE and NW secondary fault zones, respectively. (B) Four types of fractures are considered: faults (red lines), open fractures (green lines), sealed fractures (blue lines) and stylolites (yellow lines). (C) Spatial distribution of Schmidt hammer rebound values.

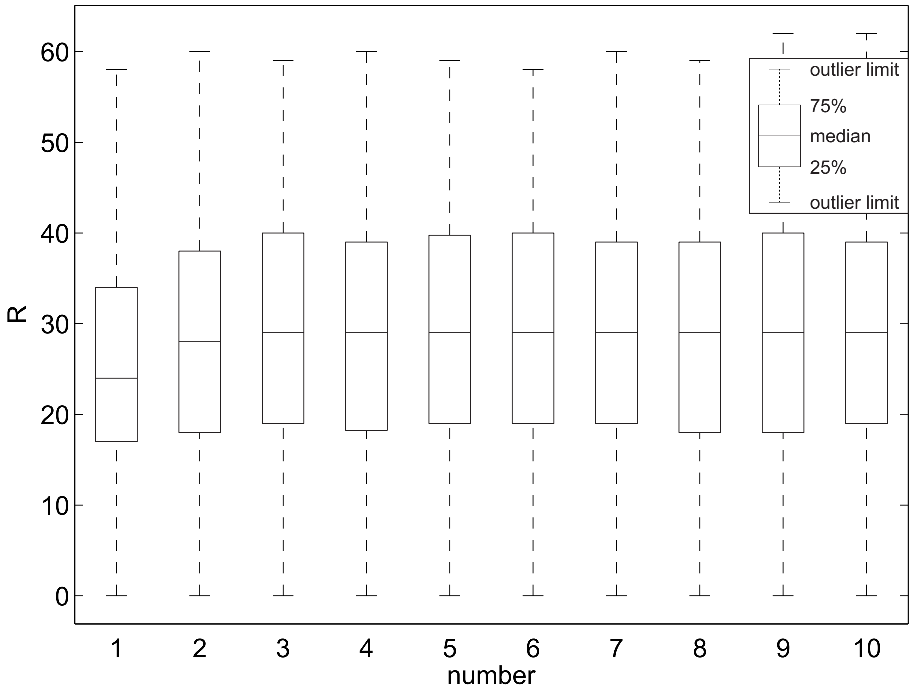

Figure 6.3: Whisker plot showing the evolution of R as a function of the number of impact, for the entire dataset (739 measures). In this study 10 impacts were necessary for each measure (a total of 7390 impacts).

2.3 Schmidt Hammer Rebound

The Schmidt hammer consists of a spring-loaded mass that is released against a plunger when the hammer is pressed onto a hard surface. Part of the impact energy is consumed by absorption, *i.e.* plastic deformation under the plunger tip, and by transformation into heat and sound. The remaining energy represents the impact penetration resistance (or hardness) which induces the rebound of the mass (*Basu and Aydin*, 2004). The distance traveled by the mass after the rebound (expressed as a percentage of its initial distance to the plunger) is called the rebound (R hereinafter). At first order, the Schmidt Hammer hardness correlates with the uniaxial compressive strength (UCS) and Young's modulus (E) of rock materials (see *Aydin and Basu* (2005) or *Yagiz* (2009) for a review). However, it is also sensitive to other rock mass properties such as surface smoothness, rock density, cementation, weathering and moisture content (*e.g.*, *McCarroll*, 1991; *Sumner and Nel*, 2002; *Goudie*, 2006).

In-situ rock strength measurements are performed using the standard (N-type) Proceq Schmidt hammer that releases an impact energy of 2.207 N.m. Rebound is corrected for the influence of gravitational forces using the automatic normalization provided by the manufacturer. All the rebound values R are obtained from a total of ten consecutive mostly horizontal impacts. In general, the rebound value increases between the first and the second impact, while the subsequent impacts only produce minor changes (Fig. 6.3). As previouly mentioned by *Aydin and Basu* (2005), the rebound increase between the first and the second impact can be associated to the weathering grade of the outcrop, and the change in subsequent rebounds can be

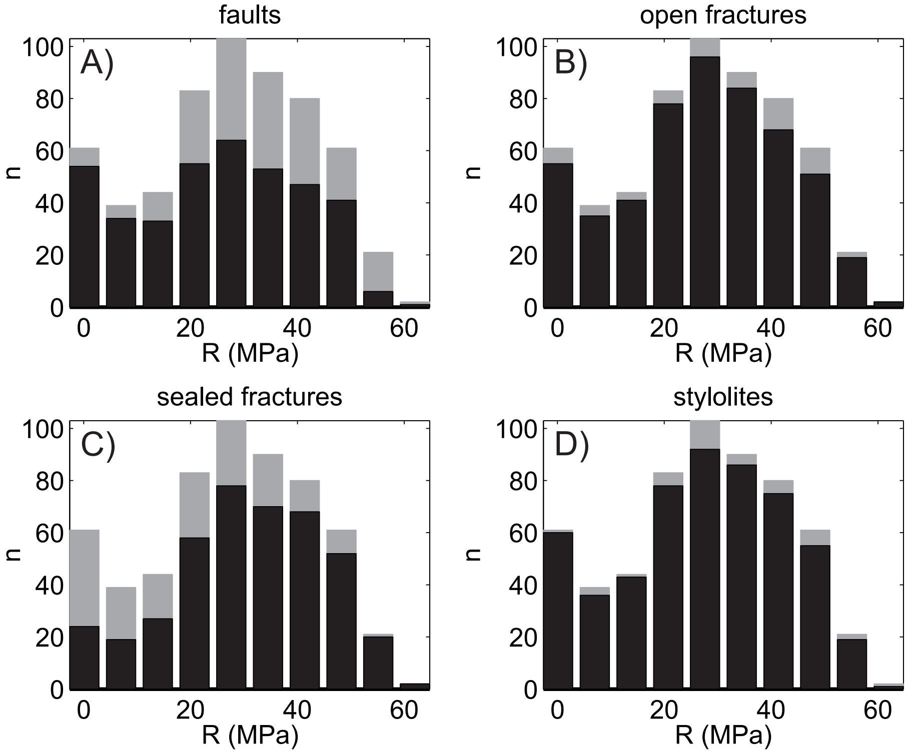

Figure 6.4: Schimdt hammer histogram distribution (10 bins) associated with each type of fracture (black bars): (A) faults, (B) open-fractures, (C) sealed fractures, and (D) stylolites. The gray bars give the total distribution related to all fractures. n is the number (or count) of Schmidt hammer measures which are closer than 20 cm to a fracture. The distribution of R for each fracture type was assessed independently of the others. Note that the total sum of the distributions obtained in this way, is not equal to the total distribution related to all fractures.

related to minor collapse or cracking beyond the original zone of compaction. In the following, the mean rebound value R_{mean} at each site will be used ($R = R_{mean}$). In this study, the Schmidt hammer was found to be empirically sensitive to R ranging from 15 to 62. Rebounds lower than 15 were not measured by the Schmidt hammer. However these unmeasured rebounds ($0 < R < 15$) contain physical information which can not be ignored, as they are related to very low rock hardness. Thus we have arbitrarily decided to randomly distribute these values between 0 and 15.

To assess the real inhomogenity of the study outcrop we use a closely spaced grid of observation points that forms over the study outcrop a dense array of field measurements. Five to twelve rows of nearly equally spaced observation points are distributed over all the exposed surface (Fig. 6.2c). A spacing of 25 cm between measure points is used, leading to a total amount of 739 rebound values (*i.e.*, 7390 impacts).

2.4 Distribution of Fractures and Schmidt Hammer Rebound

To assess a preliminary relationship between fracture and R, we compute the distribution of R associated with each fracture type considered independently. Note that each point of Schmidt hammer measure is potentially representative of several fracture types (Fig. 6.4). Therefore for each point of Schmidt hammer measure, the presence of each fracture type is evaluated: if a fracture is at distance less than 20 cm from a point of measure, then this point is considered as representative of this type of fracture and is included in the distribution (one count). This radius of 20 cm was chosen to be close to the a priori window size, $\sim$ 30 cm, at which the Schmidt hammer is sensitive, and to be below the distance between Schmidt hammer measures 25 cm to prevent from spatial overlap.

The resulting distributions show three different relations between fracture types and R: (1) faults are less represented at high values of R (> 20) compared to the total distribution, considering all fracture types; (2) sealed-fractures are less represented at low values of R; (3) open-fractures as well as stylolites are equally represented at each value or R.

In addition, stylolites and open-fractures are present at almost every point of Schmidt hammer measure as their distributions are very close to the total distribution. Thus, they are not expected to have a significant statistical effect on R, compared to the total distribution. In contrast, faults and sealed-fractures are not present at each point of Schmidt hammer measure and are under-represented for high or low values of R, respectively. Thus, they are expected to have a statistical effect on R with respect to the total distribution: positive effect for the sealed-fractures and negative effect for the faults.

To verify this hypothese we make further statistical analysis of these data, and in particular we focus on the relations between the spatial distribution of fracture density and R.

3 Statistical Analysis Method

3.1 Smoothing R

In order to further compare Schmidt hammer rebound values and fracture density, we make the assumption that statistically, a non-negligible part of the spatial variations of R is not related to the presence of mapped fractures only. This is justified at least by: (1) fractures with a planar length below 5 cm are not mapped, and the microfactures that are not mapped can affect R; (2) local variations of surface roughness, weathering grade and moisture content are expected to affect R (*Aydin and Basu*, 2005; *McCarroll*, 1991; *Sumner and Nel*, 2002); (3) a possible undersampling for R, as *Niedzielski et al.* (2009) suggested the use of 10-40 impacts at each site to statisticaly assess the rebound value R for limestones (rather than 10 in this study). Thus, in order to minimize these local effects, we smooth (or blur) the values of R, using a centered box with a size of 3 points in each direction. Henceforth, only smoothed values of R will be considered.

3.2 Fracture Density

A common feature of effective mechanical models is that fractures are represented by a single continuous spatial parameter, the fracture density ρ (*e.g.*, *Bristow*, 1960; *Walsh*, 1965), which can be expressed in its two- or three-dimensional form. As we lack good constraints on the $3D$ geometry of fractures that are observed at the surface of the outcrop (in $2D$), we only focus on the $2D$ form of fracture density,

$$\rho = \frac{1}{A}\sum_{i=1}^{N} a_i^2 \ , \tag{6.1}$$

where a_i is the radius or half-length of the i-th fracture, and N is the number of fractures that intersect the area A considered. Practically we use a circular window centered on each point of Schmidt hammer measure to determine fracture density. Here we make the a priori assumption that Schmidt hammer rebound is sensitive to rock mass properties for a spherical volume with a radius of $\sim$ 30 cm. Thus fracture density is estimated using a sliding-window with a radius $L_{window} = 30$ cm.

3.3 Effective Stiffness and Fracture Density

Following *Hudson* (1980) we assume a first-order linear relation between the effective stiffness tensor of a fractured rock mass c_e and the contribution of a single set of fractures to stiffness Δc,

$$c_e = c_0 + \Delta c \ , \tag{6.2}$$

where c_0 is a background stiffness of the host rock. If L differently oriented fracture sets are present, their stiffness contributions Δc_j, are simply summed up (*Hudson*, 1981),

$$\Delta c = \sum_{j=1}^{L} \Delta c_j \ . \tag{6.3}$$

For each fracture set, Δc_j is proportional to the scalar fracture density of the corresponding set of fractures, with a coefficient of proportionality K that depends on both the Young's modulus and Poisson's coefficient of the host rock, E_0 and ν_0, and of the fracture infill, E_f and ν_f (*Hudson*, 1980, 1981). Note that K is expected to be negative, so that fractures decrease the effective stiffness compared to the background stiffness. Then we can explicitely express the effective stiffness tensor as a linear function of fracture density for each fracture sets ρ_j,

$$c_e = c_0 + \sum_{j=1}^{L} K(E_0, \nu_0, E_f, \nu_f)\rho_j \ . \tag{6.4}$$

3.4 Fracture Density and R: a Linear Model

We are interested in the effective stiffness of the fractured rock, as seen by the Schmidt hammer. Outcomes from empirical studies propose either a linear, power or exponential relation between R and Young's modulus E of the rock (*e.g.*, *Aydin and Basu*, 2005; *Goudie*, 2006). Here we make two important assumptions: (1) The relation between R and E is linear as empirically observed by *Sachpazis* (1990) or by*Dearman et al.* (1978), and (2) we equate effective stiffness and Young's modulus, which is equivalent to assume that elastic deformation induced by Schmidt hammer impact is uniaxial in the direction of the impact. Under these assumptions we

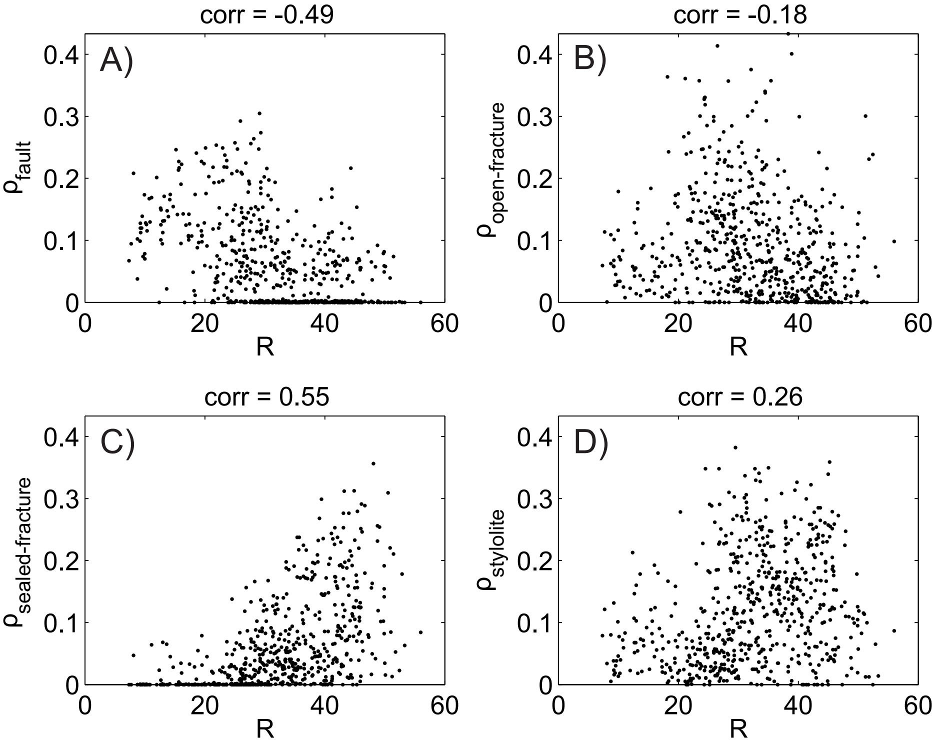

Figure 6.5: Relationship between Schimdt hammer rebound R and fracture density ρ for each type of fracture considered independently: (A) faults, (B) open-fractures, (C) sealed fractures, and (D) stylolites. The coefficients of correlation give estimates of the relation between fracture density and R. The radius of the fracture density sliding-window is 30 cm.

can define a linear model between R and fracture. Each R_i measurement is thus described by a linear combination of each fracture type density ρ_{ji},

$$R_i = \sum_j m_j \rho_{ji} + R_0 \ , \tag{6.5}$$

where m_j are the coefficients associated to the fracture density of the j-th fracture type, *i.e.* fault, open-fracture, sealed-fracture or stylolite, and R_0 is the background R value. Note that this latter is related to the background stiffness c_0, and that the m_j coefficients are related to the elastic parameters of the host rock, assumed to be homogeneous, and to the elastic parameters of the fracture infills, which are expected to vary with fracture type. This model is supported by our measurements, which suggest a relation between R and fracture density for each fracture type (Fig. 6.5): (1) a negative correlation between fault density ρ_{fault} and R; (2) a positive correlation between sealed-fracture $\rho_{sealed-fracture}$ density and R; (3) an almost neutral relation between open-fracture $\rho_{open-fracture}$ or stylolite $\rho_{stylolite}$ density and R. In the following, we set the background value R_0 equal to the mean of the R values for the entire outcrop ($R_0 = 32$). This implicitely assumes that fractures statistically exhibit, as expected, a negative effect (negative correlation), but also a positive effect (positive correlation) on the effective stiffness. This is only dependent on the choice of the background value. For instance, taking $R_0 = \max(R)$ will lead to fractures only exhibiting a negative effect.

3.5 Linear Model Inversion

Equation 6.5 can be arranged into the following matrix equation,

$$d = Gm \ , \tag{6.6}$$

with d a vector of N rebound measurements, m a vector of dimension 4 related to the coefficient m_j and

$$G = \begin{bmatrix} \rho_{fault,1} & \rho_{open-fracture,1} & \rho_{sealed-fracture,1} & \rho_{stylolite,1} \\ \rho_{fault,2} & \rho_{open-fracture,2} & \rho_{sealed-fracture,2} & \rho_{stylolite,2} \\ . & . & . & . \\ . & . & . & . \\ \rho_{fault,N} & \rho_{open-fracture,N} & \rho_{sealed-fracture,N} & \rho_{stylolite,N} \end{bmatrix} . \tag{6.7}$$

The weight m_j of each fracture type is thus obtained from the well-known least squares solution to the inverse problem of the equation 6.6 (*Menke*, 1989),

$$m^{est} = [G^T G]^{-1} G^T d \ . \tag{6.8}$$

The quality of the inversion is then estimated by the misfit Φ, which we define as the $2D$ coefficient of correlation between the data R_{blur} and the result of the inversion R_{inv}:

$$\Phi = \frac{\sum_m \sum_n (R_{inv}(m,n) - \bar{R}_{inv})(R_{blur}(m,n) - \bar{R}_{blur})}{\sqrt{\left(\sum_m \sum_n (R_{inv}(m,n) - \bar{R}_{inv})\right)\left(\sum_m \sum_n (R_{blur}(m,n) - \bar{R}_{blur})\right)}} \ , \tag{6.9}$$

where m and n are the $2D$ spatial index, and $\bar{R}_{inv}$ and $\bar{R}_{blur}$ are the averaged values. Φ is free to vary between -1 (perfect anti-correlation), 0 (no correlation) and 1 (perfect correlation).

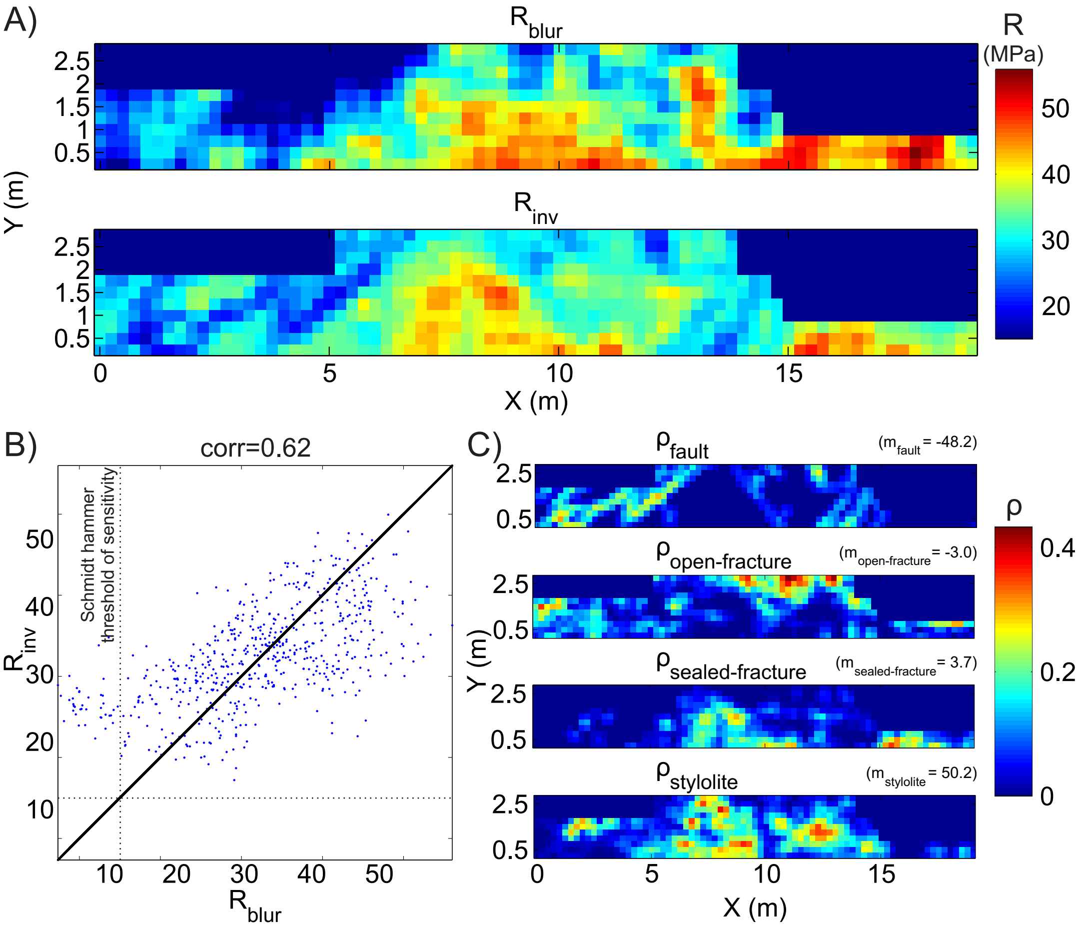

Figure 6.6: (A) Observed R_{blur} (top) and inverted R_{inv} (bottom) Schmidt hammer distribution along the study outcrop. (B) Relationship between calculated and observed Schmidt hammer rebound, with its associated coefficient of correlation. The threshold of sensitivity of the Schmidt hammer is indicated with a dotted line. (C) Fracture density for each fracture type used as data in the inversion. The m_j coefficients represent the weight of each j-th fracture type in the linear model (R_{inv}) deduced from the least square inversion.

4 Statistical Results and Parametric Study

Figure 6.6a compares the results of the least-squares linear inversion R_{inv} with the data R_{blur}. At first order the spatial distribution of R_{inv} and R_{blur} are consistent, the misfit Φ being equal to 0.62 (Fig. 6.6b). However, a closer look at the details reveals some second order discrepancies between the inverted model and the data: (1) Especially at the bottom of the cataclasite core of the seconday fault ($X \sim 14$ m, $Y \sim 0.5$ m) where $R_{blur} > R_{inv}$. This could be explained by potential heterogeneities on both the dimension of the blocks that make up the cataclasite cores, and on their cohesion, which should affect the effective elasticity. (2) The fault that affects the center of the outcrop ($X \sim 10$ m) does not seem to have a significant effect on R and leads in its zone of influence to $R_{blur} > R_{inv}$. (3) Other discrepancies are also present at the left of this secondary fault ($X \sim 13$ m, $Y \sim 1.8$ m) and at the extreme right of the outcrop ($X \sim 18$ m, $Y \sim 0.5$ m), and both exhibit $R_{blur} > R_{inv}$. We suggest that these discrepancies could be related to the presence of small sealed fractures, that were not taken into account due to their size. These observations imply that a linear combination of fracture density can successfully explain the main spatial variations of R.

4.1 Fracture Type and R

Each fracture type has a different effect on R. These effects can be relatively quantified from the results of the inversion. Indeed R_{inv} is the sum of each fracture type density (see Eq. 6.5), weighted by their inverted coefficient: $m_{fault} = -48.2$, $m_{open-fracture} = -3.0$, $m_{stylolite} = 3.7$ and $m_{sealed-fracture} = 50.2$. It is crucial to understand that these weighting coefficients are defined relative to the backround R_0 value, which here equates the mean R value. Under this condition: (1) faults and sealed-fractures have a strong negative or positive effect on R, respectively; (2) stylolites and open-fractures have almost no apparent effect, as their contributions to R_{inv} is negligible compared to the the two other types of fractures. As a result of the inversion, only faults and sealed fractures significantly affect the mean of the R values.

4.2 Optimal Window Size

Until now, we have computed fracture density using a spherical sliding-window with a radius $L_{window} = 30$ cm. Here we test the effect of varying L_{window} on the misfit value Φ of the inversion, and on the weighting coefficient m_j of each fracture type (Fig. 6.7). The misfit quickly increases between 0 and 50 cm to reach a value of $\Phi \approx 0.7$. Then it remains approximativley constant between 50 and 150 cm. These results give somes constraints on the sensitivity of the Schmidt hammer to rock mass volume: (1) The misfit (or coefficient of correlation) is more significant ($\Phi > 0.5$) for $L_{window} > 15$ cm; (2) Schmidt hammer is sensitive to fracture for at least a radius of $L_{window} = 50$ cm; (3) It is not possible from this evolution to rule out the possibility that Schmidt hammer is sensitive to a greater volume, even if it seems unlikely (no increase of Φ for $L_{window} > 50$ cm); (4) 90 % of the highest misfit value ($\Phi = 0.7$) is reached for $L_{window} = 30$ cm, which can be seen as a sufficient radius to capture most of the correlation between fracture density and R. This is consistent which the choice of $L_{window} = 30$ cm as the a priori window size to study the effect of fracture density with the Schmidt hammer.

Furthermore, the weighting coefficient of the faults and sealed fractures decreases or increases with L_{window}, respectively, while it remains almost nil for the stylolites and open fractures, or at least negligible. These results validate the robustness of the inversion, as varying L_{window} to a small extent does not dramatically change neither the misfit nor the weighting coefficients.

4.3 Lithological Control on R

The outcrop is dominated by limestones, but also includes marls and cataclastites which are mostly located in the secondary fault zones of the outcrop (see Fig. 6.2a).

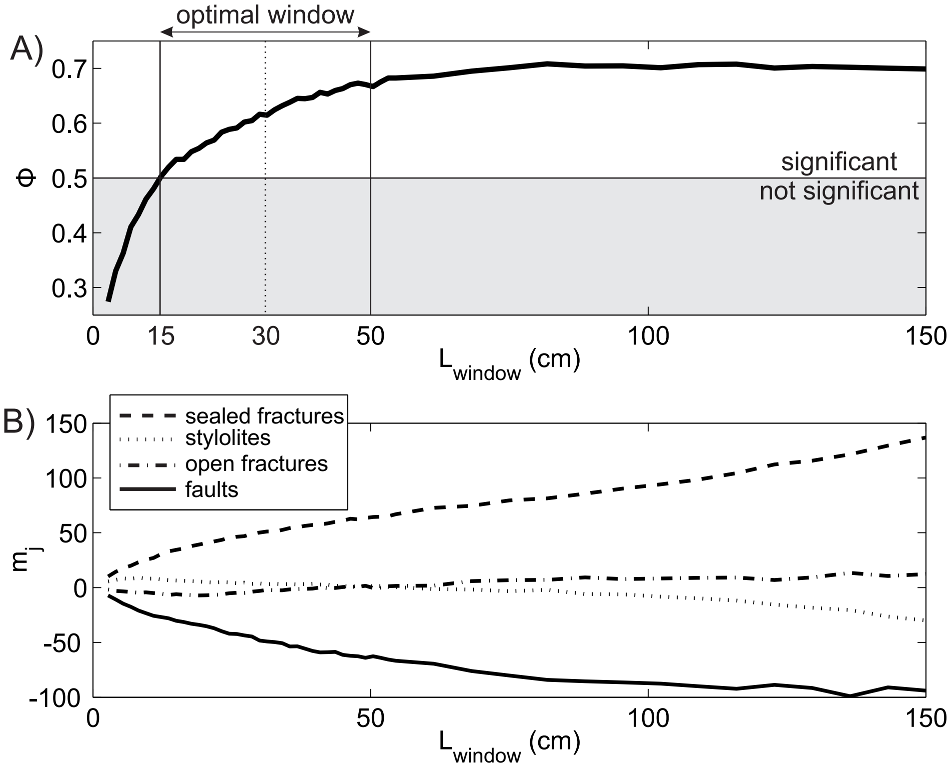

Figure 6.7: Effect of the window size L_{window} used in the density fracture calculation on: (A) the correlation coefficient or misfit (Φ) between the calculated and the measured Schmidt hammer rebound, and on (B) the weighting coefficients m_j for each j-th fracture type infered from the least squares inversion of R. The optimal window size zone is bounded by $L_{window} = 15$ cm where the correlation becomes significant and by $L_{window} = 50$ cm where the correlation stops to significantly increase when increasing L_{window}.

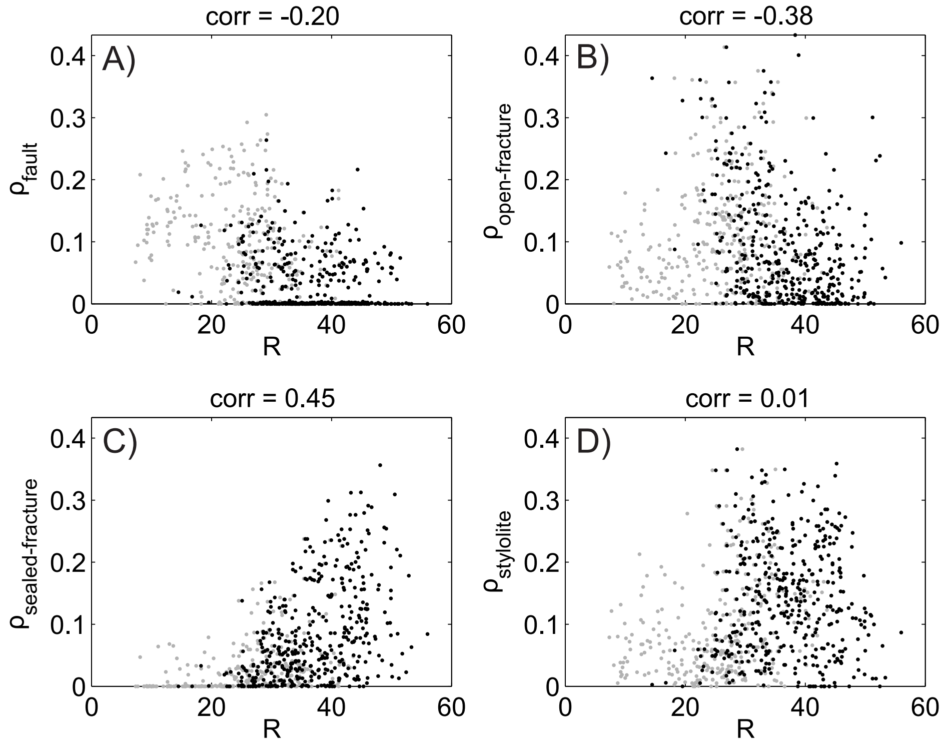

Figure 6.8: Same as figure 6.5, except that black dots show the relationship between Schimdt hammer rebound and fracture density for limestone only, while gray dots represent the entire outcrop (including marls).

This is generally inherent to faults, which in contrast to fractures, allow significant relative displacement (here decametric) of associated lithological units. Consequently these lithological heterogeneities are concordant with high fault density zones. This coincidence may have led us to mis-understand the effect of fault density on R, due to a lithological bias. On this outcrop, marls are the most probable source of lithological control on R, as their effective properties strongly differ from limestones.

To test the importance of a lithological control by marls, we removed from the dataset R values which are located in the marly parts of the outcrop (SE fault zone), so as to consider only limestones and cataclasites. Figure 6.8 presents the new distribution of R values as a function of fracture density for each fracture type. As expected faults seem to have a reduced effect on R, as the coefficient of correlation between ρ_{fault} and R has dropped from -0.49 to -0.20, when comparing with the entire outcrop (Fig. 6.5). Simultaneously, open fractures have no longer a negligible effect, as their coefficient of correlation has decreased from -0.18 to -0.38. Distributions of R as a function of stylolites or sealed fracture density do not significantly vary between the entire outcrop and limestone part of the outcrop.

To further test the effect of the lithology, an inversion using the linear model was performed on the limestones and cataclasites only. The weighting coefficients resulting from the inversion are: $m_{fault} = -3.2$, $m_{open-fracture} = -17.1$, $m_{stylolite} = -7.9$ and $m_{sealed-fracture} = 34.2$. Contrary to the inversion considering the entire outcrop, faults do not have a strong negative effect, whereas open-fractures have a stronger negative effect. On the other hand, the influence of sealed-fractures and

Table 6.1: Table summarizing the weighting coefficients associated with the fracture density of each fracture type, resulting from the inversions performed considering different background value R_0 or different lithologies.

Lithology	R_0	Fault	Open-fracture	Stylolite	Sealed-fracture
All	$R_0 = \text{mean}(R)$	-48.2	-3.0	-3.7	50.2
	$R_0 = \max(R)$	-132.4	-93.3	-73.8	-35.0
No marls	$R_0 = \text{mean}(R)$	-3.2	-17.1	-7.9	34.2
	$R_0 = \max(R)$	-72.1	-91.0	-75.0	-36.1

stylolites remains approximately constant, independently of the lithology. These results are consistent with the direct observations (Fig. 6.8).

5 Discussion

5.1 Background R_0: Mean or Max?

The results of the inversion of the linear model are dependent on the R_0 which sets the background value. As mentioned, R_0 is related to the bacrgound stiffness of the rock excluding the contributions of the fractures considered in this study. Until then R_0 was defined as the mean R value of the outcrop. The inversion has lead to positive (sealed-fracture) or negative coefficients (fault, open-fracture), which can be interpreted in terms of positive or negative effects of the associated fracture type compared to the background value. However there is no a priori physical basis for setting R_0 equal to the mean value. Indeed, R_0 should be equal to the mean R value that would exhibit the outcrop if it was not fractured by the fractures that are considered in the inversion.

If we assume that: (1) the effective stiffness of the host rock is homogeneous over the outcrop, (2) that other fractures than the ones considered in the inversion, for instance fractures with a length < 5 cm, have a negligible effect on R, (3) and that fractures only have a negative effect, then the maximum R value represents a lower bound for the background value R_0. Thus if we set R_0 equal to the maximum R value (64), we obtain after inversion the following set of coefficients: $m_{fault} = -132,4$, $m_{open-fracture} = -93.3$, $m_{stylolite} = -73.8$ and $m_{sealed-fracture} = -35.0$. As expected, all the weighting coefficients are negative, and all fracture types have a negative effect. This is consistent with the theory of *Hudson* (1980) that predicts a negative effect of fractures on the effective stiffness compared to the host background stiffness. Table 6.1 compares the coefficients associated with each fracture types for the different inversions perfomed in this study.

Despite that, we can not rule out the possibility that fractures, for instance sealed-fractures, have a positive effect, and that R_0 is lower than the maximum R value. Especially if we consider that R_0 reflects the background value of the rock mass with other mechanical defaults, such as the fractures that were not considered in the version, *i.e.* fractures that were not mapped. The distribution of the misfit (coefficient of correlation) as a function of the background R_0 value (Fig. 6.9) offers a constraint on this latter. In particular, the maximum misfit, or coefficient of

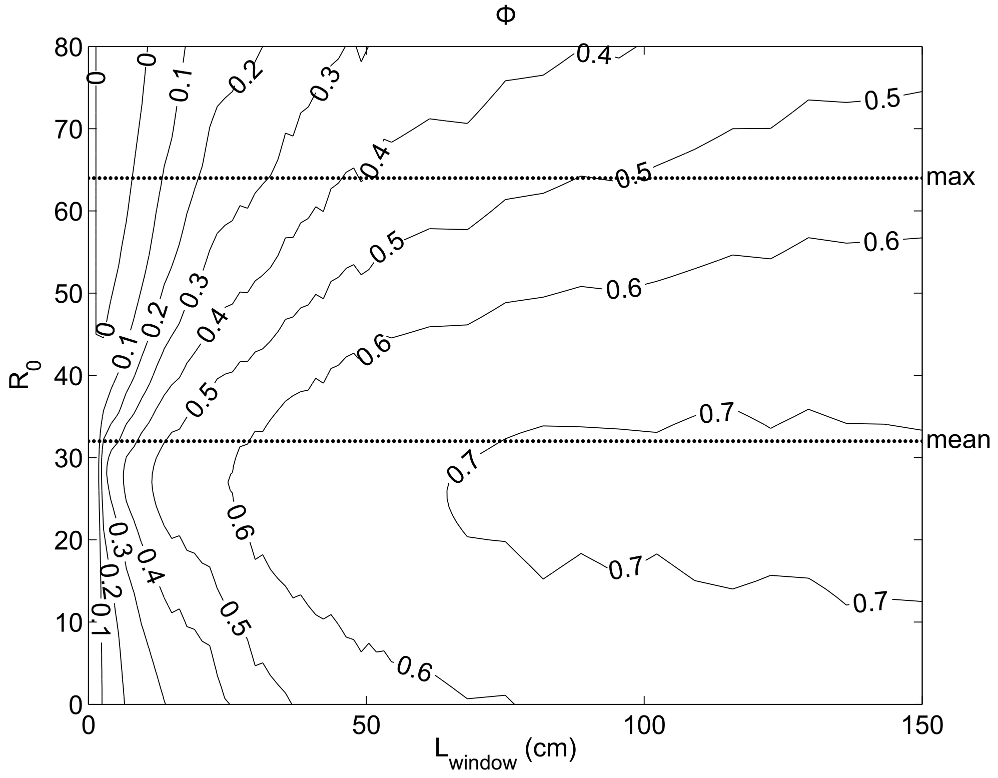

Figure 6.9: Contour plot of the misfit Φ resulting from the inversion, as a function of the circular windows radius L_{window} and of the background value R_0. The mean and maximum R values are indicated with dotted lines. The entire outcrop was taken into account in the inversion.

correlation, is obtained for $20 < R_0 < 35$, close to the mean R value (32). Note that the misfit is lower for R_0 equals to the maximum R value than for the mean R value. This result validates a posteriori the approach of setting the background value R_0 equal to the mean R value.

5.2 Fracture Density and Effective Stiffness: Linear Relation?

Following *Hudson* (1980) we have assumed that the effective stiffness was at first-order a linear function of fracture density. The assumption underlying this relation, is that the contribution to stiffness of each single fracture can be summed up. As illustrated by *Grechka and Kachanov* (2006a) it is a correct approximation for fracture density close to zero, whereas it overpredicts the negative effect of high-fracture density, ultimately leading to negative stiffness. Alternatively, *Schoenberg* (1980) or *Kachanov* (1980) propose that the effective compliance, and not the effective stiffness, is a linear relation of fracture density for non-interacting fractures. Moreover the validity of this latter is confirmed numerically for strongly interacting and intersecting fractures with arbitrary shapes (*Grechka and Kachanov*, 2006b; *Grechka et al.*, 2006; *Grechka and Kachanov*, 2006a). We favor the theory proposed by *Hudson* (1980) only for convenience, as it makes possible to define a linear model between R and fracture density. A discussion on the constrains that our results provide on the validity of effective medium theories is clearly out of the scope of this paper.

More importantly, we have assumed that the Schmidt hammer is a suitable tool to study the effective properties of a fractured rock, with fracture lengths > 5 cm. However the linear relation between effective stiffness or compliance and fracture density is valid if the characteristic fracture dimension is small compared to the wavelength of the elastic waves dynamically generated by the Schmidt hammer impact. To our knowledge, no constraints exist on this latter in limestones nor for any other rock types. However, *Rotonda* (2001) found that Schmidt hammer impact generates body and surface waves with a velocity around 2 km.s^{-1} for Rayleigh waves and 3 km.s^{-1} for P-waves in concretes. The frequencies of both have a broad spectrum, and the maximum frequency recorded is 45 kHz (*Rotonda*, 2001). This provides an estimate of the lower bound for the wavelength of the waves generated by Schmidt hammer impact: 4.5 cm and 6.5 cm for Rayleigh and P waves, respectively. If assuming that these wavelengths apply for limestones, then this supports the choice of considering only fractures with a planar length greater than ~ 5 cm.

5.3 Effective Stiffness and R: Linear Relation?

We have defined a linear model that combines fracture density for each type of fracture into a single parameter R_{inv}, in order to compare it statistically with the rebound value R of the Schmidt hammer. As mentioned, it is debated whether this model is a correct approximation with respect to the effect of fractures on effective elasticity. Morover it is valid only if there is a linear relation between R and Young's modulus E. This latter is debated as well, as different empirical studies (see *Aydin and Basu* (2005) or *Yagiz* (2009) for a review) find either a linear (*e.g.*, *Sachpazis*, 1990; *Dearman et al.*, 1978), a power (*e.g.*, *Katz et al.*, 2000), or an exponential (*e.g.*, *Xu et al.*, 1990; *YIlmaz and Sendr*, 2002; *Aydin and Basu*, 2005) relation between R and E,

$$E \propto R\ , \tag{6.10}$$

$$\text{or } E \propto R^{\alpha}\ , \tag{6.11}$$

$$\text{or } E \propto e^{\alpha R}\ , \tag{6.12}$$

with α a constant that depends mainly on the lithology considered. Injecting the combination of fracture density (Eq 6.5) into these empirical relations leads to,

$$R = \sum_j m_j \rho_{ji} + R_0\ , \tag{6.13}$$

$$\text{or } R = \beta \left(\sum_j m_j \rho_{ji} \right)^{\frac{1}{\alpha}} + R_0\ , \tag{6.14}$$

$$\text{or } R = \frac{\beta}{\alpha} \log \left(\sum_j m_j \rho_{ji} \right) + R_0\ , \tag{6.15}$$

with β a coefficient of proportionality that vanishes for the linear relation into the m_j coefficients. Once again, there is no physical basis to favor a linear relation between E and R, except that conceptually it represents the simplest approach which requires fewer paramaters to invert.

5.4 Implications for Fault Zone Rheology

Our results present new insights into the rheology of a fault zone. Our statistical results suggest that fracture contributions to stiffness, relative to the background value, depend on the fracture type: faults, open-fractures and stylolites have a moderate to strong negative effect on effective stiffness; whereas sealed-fractures have a slightly negative to positive effect on effective stiffness, depending on the choice of the background stiffness value. Faults and fractures are created during the coseismic phase of the seismic cycle, while sealed-fractures result from sealing (or healing) that occurs during the interseismic phase (*e.g.*, *Sibson*, 1992; *Gratier et al.*, 1994; *Renard et al.*, 2000). Fracture sealing is the consequence of external material precipitation or deposition in the related veins (*Gratier et al.*, 1994; *Evans and Chester*, 1995; *Renard et al.*, 2000). It is likely to occur after previous pressure solution of the same material in stylolites (*Gratier et al.*, 1994; *Renard et al.*, 2000). According to experiments, the time scale of such fracture sealing, controlled by the kinetics of pressure solution and associated with deposition processes, is in the order of several tens of years to several millions of years, and is strongly dependent on temperature, fluid circulation, and rock texture (*Rutter and Elliott*, 1976; *Hickman and Evans*, 1991; *Gratier*, 1993; *Renard et al.*, 2000). Fractures, such as sealed-fractures, are located in the damage zone of main faults. We suggest that changing the effective elasticity around a major fault, by fracture sealing during the interseismic phase of a seismic cycle, may have geodynamical effects. In particular it could potentially affect the relation between plate tectonics far-field motion, and the interseismic stress build-up of major faults. Our results are consistent with an increase of the rate of interseismic stress build-up with sealing of fractures present in the damage zone.

6 Conclusion

Here we have investigated the effective elasticty of a fault zone dominated by limestones, using high-density Schmidt hammer measures (25 measures per m^2). Our study demonstrates that Schmidt hammer can be used to assess rock fractures at the scale of an outcrop. Indeed, our results suggest that rock mass effective elasticity is strongly sensitive to the $2D$ form of fracture density: effective stiffness is anti-correlated to the density of faults and open fractures density, while it is correlated to the density of sealed fractures. These results are consitent with theoretical models which predict a linear relationship between effective stiffness and fracture density (*Hudson*, 1980). A least squares inversion using a linear model has led us to a set of weighting coefficients, which represents the sensitivity of effective Young's modulus or stiffness to the fracture density of each fracture type. These coefficients are consistent to the ones that were determined independently: a negative effect of faults and open-fractures on effective elasticty, and a positive effect for sealed-fractures, if considering a mean background R_0 value. It is important to note that this result is extremely dependent on the choice of R_0. For instance taking into account a R_0 equals to the maximum R value, leads to a set of negative weighting coefficients, but still with sealed-fractures having a higher weighting coefficient than the other fracture types.

In addition, the best values of misfit are obtained for a sliding-window (where fracture density is determined) with a radius greater than 15 cm and probably lower than 50 cm. This empirical result gives some new constraints on the representative volume of Schmidt hammer measures, when considering a fractured rock mass. Only the $2D$ form of fracture density was considered due to the lack of good constrains on the $3D$ geometry and orientation of each fracture type. Thus, our results possibly hide dependencies on $3D$ effects. In particular open fractures, which are randomly orientated in $2D$, may also be randomly orientated in $3D$. However, some field evidences make us confident that most of the faults, sealed fractures and stylolites are cutting perpendicularly the plan of the outcrop.

This study represents to our knowledge the first attempt to constrain in-situ the relations between fracture density and effective elasticty of a rock mass. We believe it could represent a step forward in the comprehension of mechanical processes which are dependent on rock effective properties. For instance it could help to clarify and quantify the relation between fracture density and the resistance of a rock to erosion, which is assumed to be a key factor of the interactions between tectonics and erosion (*Molnar et al.*, 2007). We also suggest that our results may have geodynamical consequences, related to the interseismic stress build-up of major faults by sealing of fractures in the damage zone.

Acknowledgements

We especially thank Emmanuel David for fruitful discussions about effective elasticty, and Dimitri Lague for providing help with acquiring fracture networks from the field. We also thank Benoît Gibert, Didier Loggia, Jérôme Lavé, Thomas Theunissen and Magali Rizza for helpful discussions. This study was funded by the Geosciences Montpellier laboratory research program ERODROCK.

Epilogue on Schmidt Hammer

The first application of Schmidt hammer was to perform a transect of erodibility across the Taiwan mountain belt. The lithologies encoutered include sandstones, slates, schists, and green schists, which represent high to moderate erodibility (*Attal and Lavé*, 2009). Statistically, slates have the lowest hardness (possibly highest erodibility), while sandstones and schists have the highest hardness (possibly lowest erodibility). Spatially, slates are localised in the central area of Taiwan mountain belt, in the Slate Belts, which also is the most elevated part of Taiwan. This pattern of erodibility differs from most mountain belts which exhibit low erodibility in their central area (e.g., Pyrenees, Himalaya, Longmen Shan, European Alps). To validate this pattern of erodibility, abrasion tests using samples from the same outcrops are now needed.

The second application of Schmidt hammer was dedicated to measure the effect of diagenesis on R and erodibility, using the well documented Annot Sandstone formation (Southern French Alps) (*Labaume et al.*, 2008b,a). Four outcrops were tested, chosen to capture a strong diagenetic gradient, with the external outcrop being made-up of poorly consolidated sandstones, while the internal one has been buried up to $6-8$ km and exhibits consolidated (and fractured) sandstones. R is at first order correlated to the diagenetic grade, as the R is greater in the internal part than in the external one. However most of the spatial evolution of R seems to be controlled by the transition from poorly consolidated to consolidated, not directly with the burial depth. Surprisingly, R is not correlated to bulk density, P-wave velocity, porosity, permeability, or to the content of calcite or clay. This is not expected since most studies (see *Aydin and Basu* (2005) for a review) have documented an empirical link between R and Young's modulus or P-wave velocity. We suggest that this absence of correlation is related to the increase of apparent fracture density with the diagenetic grade, which counter-balances the effect of diagenesis. Therefore it is required to quantify fracture density and its effect on rock elasticty for the Annot sandstones tested in this thesis.

The last application was consequently dedicated to assess the effect of fracture type and density on the effective elasticity as seen by the Schmidt hammer, at the scale of an outcrop located in a fault zone. This experiment consists in an unmatched number of Schmidt hammer measures (750 with 7500 impacts), parallel to a recording of open-fractures, sealed-fractures, faults and stylolites. As expected, the comparison of the two revealed that increasing fracture density decreases the effective stiffness, with an amplitude that varies with fracture type. A linear model that sums up fracture density for each fracture type into a single parameter is then inverted to fit the observed map of R. The correlation between both maps is significant ~ 0.7 for the best fitting models. The weighting coefficients associated with each fracture type reaveal that faults and open-fractures have a greater negative impact than the sealed fractures. These results confirm the assumption expressed from Annot sandstones observation, that fractures and effective properties affect Schmidt hammer rebound.

From the experiments presented in this thesis, it is possible to summarize the potentiality of Schmidt hammer rebound R to capture erodibility K:

- R can be empirically related to K either by a power $K \propto R^{\alpha}$ or exponential $K \propto \exp(\alpha R)$ function, with α a negative exponent;
- Compared to classical abrasion experiments (*Sklar and Dietrich*, 2001; *Attal and Lavé*, 2009), R captures the effective properties of rock medium at a characteristic scale that corresponds to erosion processes (1 to 30 cm);
- It is a cheap, portable and quick device which is suitable for field studies and in-situ experiments.

Part III

Rock Erodibility and the Spatial and Temporal Evolution of Orogens: a Modeling Approach

Résumé

Dans cette partie j'étudie, à l'aide de la modélisation numérique, la relation entre érodabilité et morphologie des paysages en temps et en espace. D'abord, j'explore la relation entre érodabilité et longueur d'onde des paysages, en utilisant un modèle planaire, qui considère à la fois l'érosion fluviale par stream-power et un angle critique de déclenchement des glissements de terrain pour les versants. Le modèle permet de reproduire un espacement constant entre les rivières pour un rapport constant d'érodabilité sur le taux de soulèvement à l'état d'équilibre dynamique, ce qui est cohérent avec la théorie du stream-power. Je montre que les indices classiques utilisés pour déterminer la longueur d'onde du paysage, tels que la densité de drainage basé sur un seuil arbitraire de l'aire drainée, ne sont pas adéquats pour évaluer le lien entre longueur d'onde du paysage et l'érodabilité ou le taux de soulèvement. Deuxièmement, j'explore l'effet de l'érosion et de la rhéologie sur le temps de décroissance des chaînes de montagnes post-orogéniques, à partir d'un modèle numérique $2D$ qui couple le comportement mécanique ou thermique de la lithosphère à l'érosion de surface. Je démontre que l'efficacité de l'érosion, qui est fortement dépendante de l'érodabilité, est le premier facteur de décroissance de la topographie au cours de la phase post-orogénique. Associé à l'érosion de surface, une transition d'isostasie locale à isostasie régionale permet de reproduire la diminution du ratio de l'élévation de la surface sur l'épaisseur de la racine crustale, qui est observée dans les chaînes de montagnes post-orogéniques.

Abstract

In this part I investigate with numerical modeling the relation between erodibility and the temporal and spatial evolution of landscape morphology. First, I explore the relation between erodibility and the wavelength of landscapes, using a plan-view model that considers a stream power formalism for river erosion and a landslide criterion angle for hillslope. The model reproduces a constant spacing between rivers for a constant ratio of erodibility to uplift rate at steady-state, which is consistent with stream-power prediction. I show that classical morphological indexes used to assess landscape wavelength, such as drainage density using an arbitrary threshold on the drainage area, are not suitable to assess the link betweeen landscape wavelength and erodibility or uplift. Second, I explore the effect of erosion and rheology on the time decay of post-orogenic mountain belt, using a $2D$ numerical model that couples lithospheric deformation and thermal behaviour to surface erosion. As expected, I demonstrate that erosion efficiency, that is strongly dependent on erodibility, is the first controling factor of the time scale of topographic decay. Associated with surface erosion, a transition from local isostasy to regional isostasy reproduces the decrease of the ratio of surface elevation to crustal root thickness that is observed for real post-orogenic mountain belts.

Chapter 7

Relief Wavelength and Scale-dependent Metrics: A Preliminary Numerical Approach

In Prep.

Steer, P., Godard, V., and Hurtrez, J.E.

Abstract

We used a plan view landscape evolution model to assess the relation between topographic wavelength, uplift rate and erodibility. From theoretical prediction, topographic wavelength is expected to be a power function of the ratio of uplift rate to erodibility with a positive exponent. Synthetic topographies outcoming from the model present 3 different types: topographies with only fluvial network, with only hillslopes, and with both hillslopes and fluvial network. Only this latter type is consistent with the modeling approach, the other two having either a theoretical wavelength below the pixel resolution or above the model size. Studying type 2 synthetic topographies we find a dependency of drainage density on the ratio uplift rate to erodibility following a power law with a positive exponent, as expected. Last we show that this relation only emerges when considering the true fluvial network, while considering drainage density based on arbitrary threshold over drainage area to identify the fluvial network leads to a strong bias.

1 Introduction

Numerical landscape evolution models are useful tools to determine the spatial implications of river incision laws. Many studies have focused on the $1D$ river geometries predicted by the stream-power erosion law (e.g., *Howard*, 1980; *Whipple and Tucker*, 2002). At steady-state the concavity of a river profile is expected to be directly dependent of the uplift rate, erodibility, and on the slope and drainage area exponents that define the river incision law. On the other hand, only a few studies have investigated the $2D$ landscape geometries predicted by stream-power incision law (*Tucker and Whipple*, 2002; *Lague and Davy*, 2003; *DeLong et al.*, 2007; *Perron* *et al.*, 2009). In this technical note, using a simple $2D$ plan view landscape evolution model including river incision and hillslope landsliding, we explore the effect of varying uplift rate and erodibility on the wavelength of outcoming synthetic topoggraphies. We first present the modeling approach, then we assess the limits of the model in terms of resolution and associated wavelength. Last, we assess the effect of using landscape metrics based on arbitrary threshold to chararcterize landscape wavelength on their potential to capture uplift or erodibility.

2 Modeling Approach

Recent studies have underlined the key role played by fluvial incision in driving unglaciated landscape denudation (*Whipple and Tucker*, 1999). Two leading classes of models describe the long-term erosion rate of a river: transport- or detachment-limited (e.g., *Tucker and Whipple*, 2002). In this study we only use a detachment-limited relation that links erosion rate to the unit stream-power of river channel (*Howard et al.*, 1994; *Perron et al.*, 2008). In this formalism, the evolution of the elevation z of a river is

$$\frac{\partial z}{\partial t} = U - K\left(\left(\frac{A}{w}\right)^p S^n - \tau_c\right) \text{ if } \left(\frac{A}{w}\right)^p S^n > \tau_c \ , \tag{7.1}$$

$$\frac{\partial z}{\partial t} = U \text{ if } \left(\frac{A}{w}\right)^p S^n \leq \tau_c \ , \tag{7.2}$$

with U the uplift rate, K a coefficient of erosion efficiency that includes bedrock erodibility and climatic dependences, A the contributing area, w the width of flow in the dominant fluvial pathway, S is the along-channel local slope, p and n are dimensionless coefficients, and τ_c is the detachment threshold below which no erosion takes place. In uniform lithological and tectonic settings, the mean channel width increases downstream with the water discharge according to a power law (*Leopold and Maddock*, 1953; *Montgomery and Gran*, 2001a; *Snyder et al.*, 2003). Mean channel width can be taken as a reference for the effective flow width of this channel, and contributing area as a proxy for water discharge. Using these assumptions leads to,

$$w = k_w A^{\omega} \ , \tag{7.3}$$

with k_w an amplitude factor, and ω is a scaling exponent. Combining last equations gives,

$$\frac{\partial z}{\partial t} = U - K\left(A^m S^n - \tau_c\right) \text{ if } A^m S^n > \tau_c \ , \tag{7.4}$$

$$\frac{\partial z}{\partial t} = U \text{ if } A^m S^n \leq \tau_c \ , \tag{7.5}$$

by integrating k_w into K and τ_c, and with $m = p - \omega$.

Rivers downcut the landscapes and set the low points of the topography and force the hillslopes to adapt (*Burbank et al.*, 1996). In active orogens, hillslope erosion is dominated by landslides (*Hovius et al.*, 1997). Thus, we assume in the following that hillslopes display a critical slope of repose S_c, and that they react instantaneously to any local base level drop (*Lavé*, 2005; *Godard et al.*, 2006). For the sake of simplicity no other hillslope processes are considered in this study. Sedimentation only occurs in closed basins which are filled with sediments to the spill point, so that the rivers flow downhill to the edge of the model. Otherwise sediments are instantaneously and efficiently flushed out of the system.

Following *Pelletier* (2004), we apply both the river unit stream-power erosion law and the hillslope landsliding slope criterion to a two dimensional plan view surface processes model. The numerical model solves Equation 7.5 on a rectangular grid, made up of pixels, that is subjected to a uniform rate of rock uplift and to a fixed elevation boundary condition on every side of the model. The contributing area is determined using a bifurcation method that routes flow to multiple downslope directions, weighted by slope (*Freeman*, 1991; *Pelletier*, 2004). Contrary to *Pelletier* (2010) we do not minimize the grid-resolution dependence of the flow routing algorithm, although we recognize it might influence our modeling results.

The main benefit of this simple modeling approach is that it requires only a small set of model parameters: U, K, S_c, τ_c, m and n. Moreover other simple assumptions allow to reduce the number of free parameters: (1) The landsliding threshold slope is kept constant, $S_c = 0.8$, which corresponds to an angle of $\sim 40°$, a value commonly observed for the angle of respose of hillsopes in active mountain belts; (2) We neglect the critical erosion threshold; (3) Following *Snyder et al.* (2000), we set $n = 1$ and we impose $m/n = 0.5$ as it is classically assumed in the unit stream-power formalism. As a consequence, the parameters of the model are only the uplift rate U and the coefficient of erosion efficiency K.

3 Resolution and Relief Scale of Synthetic Landscapes

3.1 Relief Scale of Synthetic Landscapes

We test the effect of varying U and K on the scaling of synthetic topographies which outcome from our model (see Fig. 7.1). Each model is represented by a square box with a total dimension $\Delta x = 45$ km, and a pixel resolution $\delta x = 90$ m. Each simulation is performed until a dynamic topographic steady state is reached (*Willett and Brandon*, 2002).

The first qualitative observation is that both the wavelength and the maximum elevation reached by the model increase with the ratio U/K. As previously observed by *DeLong et al.* (2007) 3 types of synthetic topographies emerge from this modeling approach: (1) Type 1 topographies have no pixels that have reached the critical slope S_c, i.e. rivers only; (2) Type 2 topographies have some pixels that exhibit the critical slope and others that have lower slope, i.e. a combination of rivers and hillslopes; (3) Type 3 topographies only have pixels with a critical threshold, i.e. hillslopes only. *DeLong et al.* (2007) relates these 3 types of synthetic topographies to the dominant erosion process taking place in the model, with type 1 being completely dominated by fluvial incision (i.e., for each pixel), type 3 by hillslope landsliding, and type 2 representing a state where the dominant erosion process varies spatially. However this classification hides some more fundamental dependencies on the resolution and

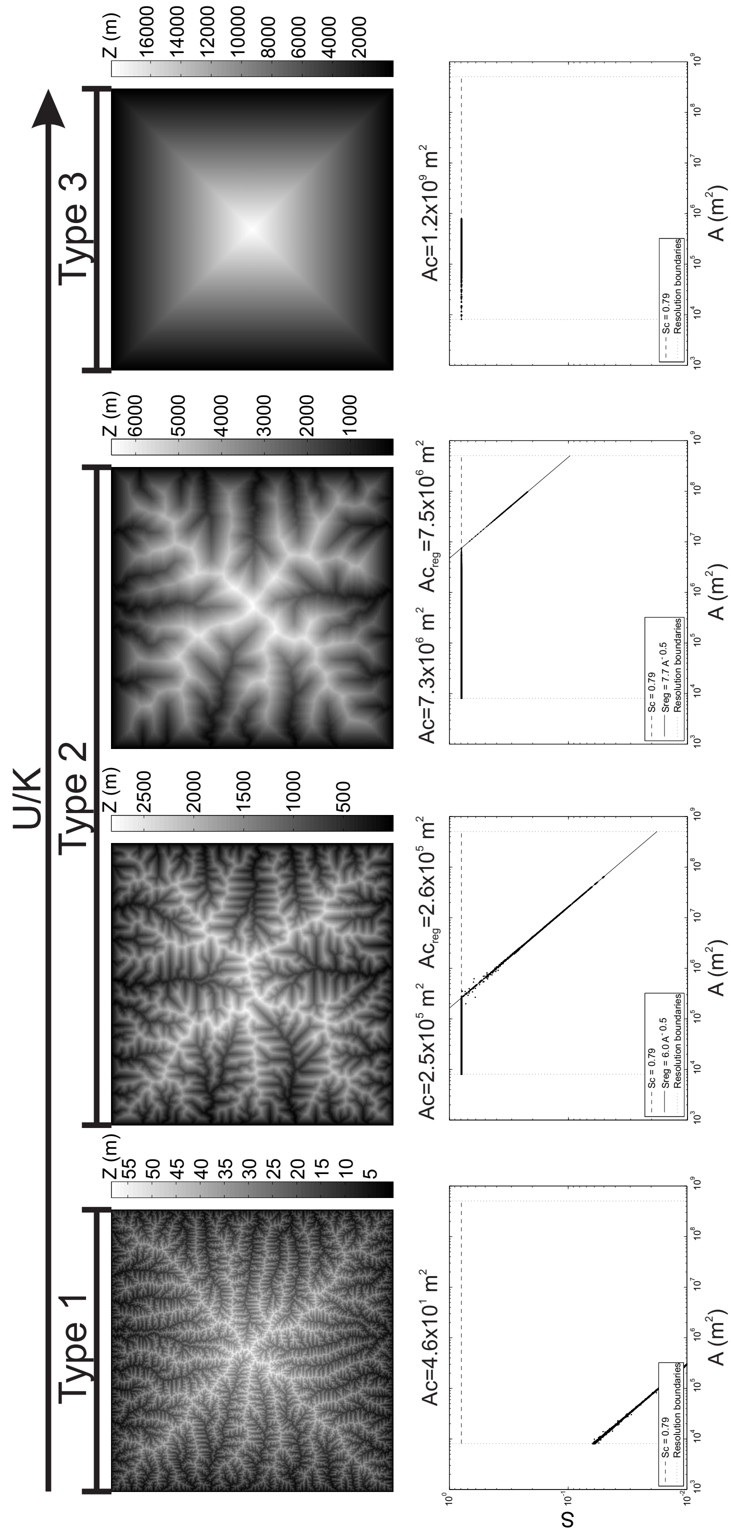

Figure 7.1: Left: Elevation of synthetic topographies resulting from our models as a function of the ratio U/K, and distribution of corresponding topographic types. Right: Slope-area log-log distribution associated with each topography. Type 1 topography presents only river pixels, while type 3 presents only hillslope pixels. Type 2 topographies present both hillslope and river pixels. Intersection of the critical slope with the linear regression of the fluvial pixel gives the critical area Ac_{reg} of the topography which can be compared to its theoretical value Ac deduced from the ratio U/K.

dimension of the model.

3.2 Theoretical prediction of Relief Scales

To investigate these dependencies we need to consider the dynamic steady-state of a $1D$ river, when erosion rate balances uplift rate. At steady-state, river erosion law predicts a power law relation between A and S all along the river channel,

$$S = \left(\frac{K}{U}\right)^{1/n} A^{-m/n} \ . \tag{7.6}$$

In synthetic landscapes dominated by river erosion and hillslopes landsliding, this relation theoreticaly implies a scaling criterion of relief. Indeed at the head of river channels, where the junction between rivers and hillslopes occurs, local slope is equal to S_c. At this point the contributing area is also critical A_c, as it represents the minimum contributing area that allows to initiate a river channel with a critical slope. Under this condition, Equation 7.6 allows to express A_c as an explicit function of S_c,

$$A_c = \left(\frac{U}{K}\right)^{1/m} S_c^{-n/m} \ . \tag{7.7}$$

Conversely this critical area also implies a critical horizontal distance between the river channel and divide d_c, and a critical hillslope relief R_c. In our approach A_c, d_c and R_c are functions of the ratio U/K as S_c, m and n are kept constant. Consequently the wavelength and amplitude of synthetic topographies are a function of U/K.

3.3 Resolution Limits

As observed in our modeling (Fig. 7.1) the formalism of unit stream-power predicts an increase of A_c with an increase of the ratio U/K. However our modeling approach presents two theoretical limits of resolution: The lower limit which corresponds to the pixel resolution $\delta x = 90$ m, and the upper limit which corresponds to the total dimension of the model $\Delta x = 45$ km. These limits can be translated in terms of contributing area, and represents the lower , $A_c^{low} = \delta x^2$, and upper, $A_c^{up} = \Delta x^2$, critical area that can be modeled with this resolution and dimension. Practically because the model is symetrical in the two horizontal directions, the upper critical area is necessary below $A_c^{up} = \frac{1}{4}\Delta x^2$.

In the following we test the implication of these resolution limits on the classification proposed by (*DeLong et al.*, 2007). For this purpose we perform a uniform Monte Carlo sampling of the paramater space $\Omega(U, K)$ with 100 models (Fig. 7.2). A comparison between the types of synthetic topographies and their critical area A_c reveals that the resolution limits control the distribution of the topographic types: below A_c^{low} all models are of type 1 and above A_c^{up} all models are of type 3. However it appears that A_c^{up} is not the true limit between type 2 and type 3 as some models of type 3 are located below A_c^{up}. The true limit is found empirically to be $A_c^{up} \simeq \frac{1}{50}\Delta x^2$. We suggest this is due to the low degree of flow convergence on a

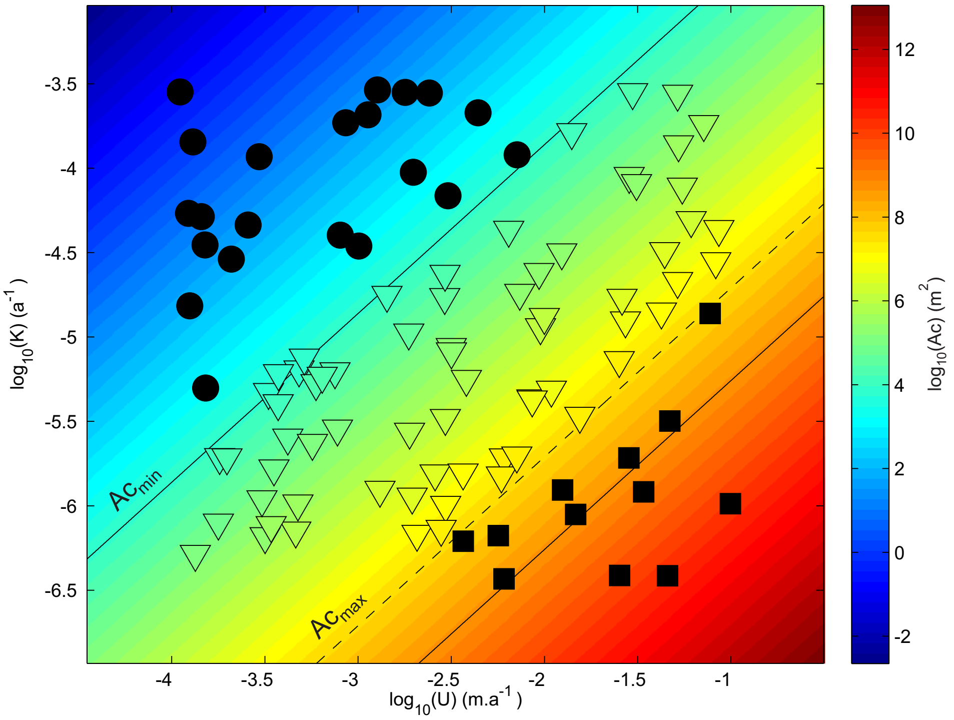

Figure 7.2: Distribution of the topographic model types in the parameter space $\Omega(U, K)$ in log-log: type 1 (circle), type 2 (triangle) and type 3 (square). The color of the markers indicates the critical area A_c deduced from their topography. Black models indicate that it was not possible to measure A_c, and was observed only for type 1 and type 3 which presents only river or hillslope pixels, respectively. Continuous pseudocolor plot shows the evolution of the analytical critical area $A_c = \left(\frac{U}{K}\right)^{1/m} S_c^{-n/m}$. Black solid lines indicate the theoretical upper and lower resolution limits and the black dashed line indicates the true upper resolution limit deduced from the distribution of type 2 and type 3 models.

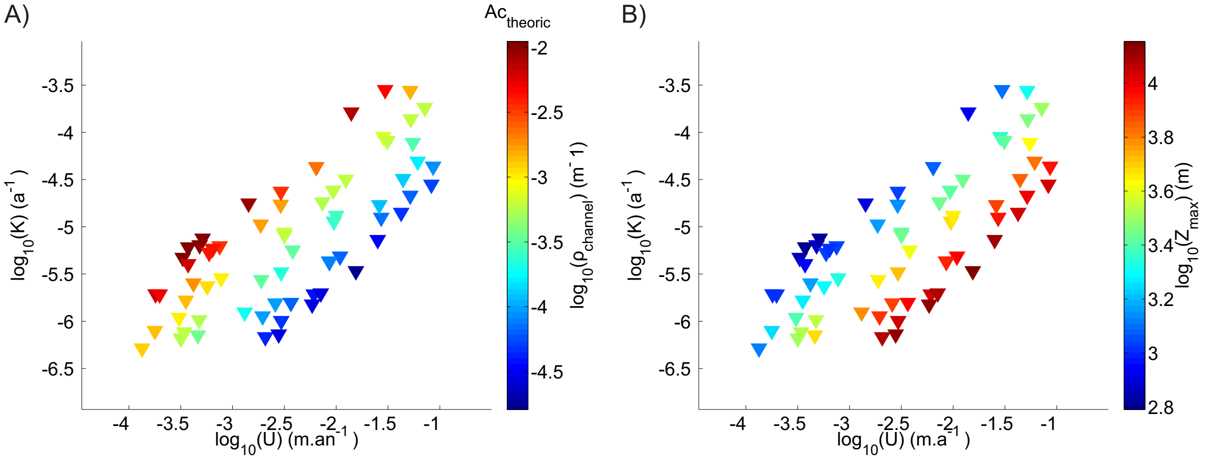

Figure 7.3: Distribution of (A) the true channel density $\rho_{channel}$ and (B) of the maximum elevation Z_{max} for models of type 2 in the parameter space $\Omega(U, K)$ in log-log.

tilted plane (e.g., type 3 topography), which prevents from reaching the critical area A_c.

Type 1 and type 3 models exhibit topographies with a relief scale that does not fit in the resolution limits of the model. Increasing the resolution or the dimension of the model would result in a modification of the distribution of model types. It implies that synthetic topographies emerging from surface processes modeling are valid with respect to the resolution, only when exhibiting type 2 topography.

4 Scale-dependence of Landscapes Metrics

4.1 Head-source Area and Drainage Density

Another conclusion of the Monte Carlo sampling is that the critical area A_c measured from the topographies of the models and the one deduced analytically (Eq. 7.7) are consistent for models of type 2. First this result validates the robustness of the numerical method of our modeling approach. More importantly it gives a robust criterion for distinguishing river pixels ($A > A_c$) from hillslope pixels ($A < A_c$), which enables identifying the fluvial network in each model of type 2.

A classical metric of fluvial network is drainage density $\rho_{channel}$ (*Horton*, 1932, 1945). It is equal to the total length of river channels divided by the total basin area, and is a dimensional parameter (m^{-1}). Figure 7.3 presents the drainage density for each model of type 2. As expected drainage density, which is inversely proportional to the root of A_c, increases with the ratio U/K. We consider it is the true drainage density as it was determined using the actual river network produced by our simulations.

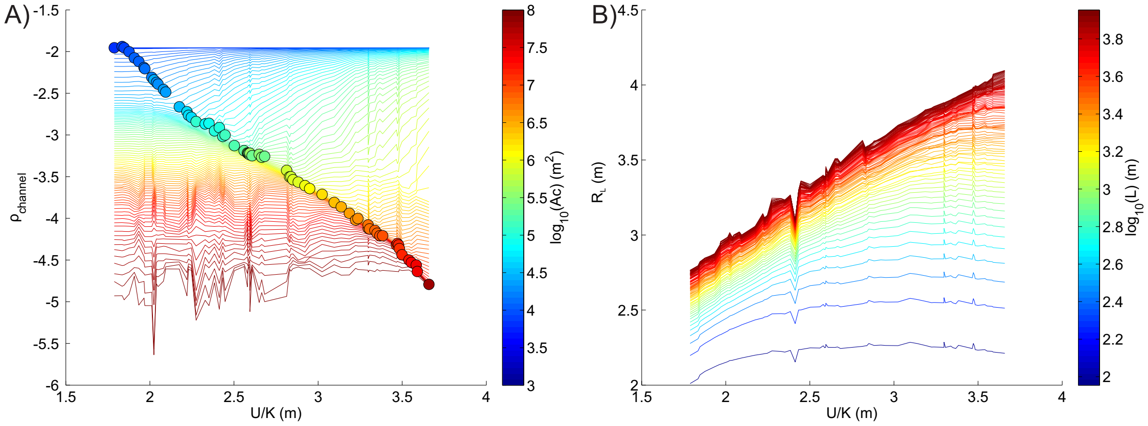

Figure 7.4: A: Log-log plot of drainage density $\rho_{channel}$ as a function of the ratio of uplift on erodbility U/K for different threshold on the critical area A_c used for identifying the fluvial network. The colorbar indicates the values of these thresholds A_c. Moreover color circles indicates the true drainage density with its corresponding A_c indicated by the color. B: Log-log plot of the local relief R as a function of the ratio U/K for different window size L.

4.2 Arbitrary Head-Source Area Criterion and Drainage Density

Contrary to our approach many studies have extracted the fluvial network and its associated drainage density from Digital Elevation Model (DEM) using an arbitrary threshold on the contributing area (e.g., *Hurtrez et al.*, 1999). We investigate the influence of the value of this threshold on the relationships between U, K and drainage density. Figure 7.4 presents the distribution of drainage density for each model as a function of U and K for different critical area thresholds. Surprisingly, the pattern of drainage density varies significantly with the critical area threshold: (1) For a threshold below the pixel resolution δx^2, drainage density is homogeneously equal to $1/\delta x$, as all the pixels are considered as river channels. (2) Inversely for a threshold close to the total area of the topography Δx^2 drainage density approaches 0. (3) In between, the pattern of drainage density is inverse to the true one for $A_c \leq 0.1$ km^2, while it is approximatively consistent with the true one for $A_c \simeq 1$ km^2. However, none of these patterns allow to clearly establish a strong relationship between drainage density and the ratio U/K. The amplitude and pattern of drainage density as a function of the ratio U/K varies considerably with the threshold. This highlights the real limit of landscape metrics based on arbitrary threshold to decipher physical properties from DEM or synthetic topographies.

5 Conclusion

In this technical note we have investigated the relation between erodibility, uplift rate and the wavelength of synthetic lanscapes at steady-state. Following *DeLong et al.* (2007) three types of synthetic topographies are obtained. We argue that only type 2 topographies, i.e. with both critical hillslopes and developed fluvial network, are consistent with the modeling approach. Type 1 and 3 that exhibit only river or only hillslopes, respectively, represent outcomes of models that suffer from resolution issues. Type 1 and 3 topographies are associated with critical head-source area below pixel resolution or too large with respect to the size of the model, respectively. Wavelengths of type 2 topographies exhibit clear dependencies on the ratio of uplift rate to erodibility, which is consistent with theoretical prediction at steady-state (*Tucker and Whipple*, 2002). Drainage density is a landscape metric classicaly used to determine topographic wavelength. We show that the relation between drainage density and the ratio U/K exhibits the predicted increasing trend only when considering the true fluvial network. On the other hand, drainage density associated with fluvial network determined from arbitrary threshold on drainage area, does not exhibit the same trend. This technical note illustrates the necessity of using only true fluvial networks to assess the ratio U/K from drainage density determined from a digital elevation model .

Chapter 8

Post-Orogenic Evolution of Mountain Belts: Insights from Numerical Modeling

Submitted, Journal of Geophysical Research

Steer, P., Cattin, R., Lavé, J. and Godard, V.

Abstract

In this study we are interested in constraining the erosional and rheological conditions that allow one to repoduce the progressive temporal decrease of surface elevation divided by crustal root thickness (R) after orogeny. A finite element model that couples surface processes to lithospheric deformation and thermal behavior is used to investigate the long-term evolution of mountain belts. Using a range of realistic values for the geometry of the initial range, coefficient of erosion efficiency, and thermal conditions, we show that a topographic decay driven by erosion and compensated by regional isostasy is consistent with the temporal decrease of R observed in most mountain ranges. Sampling the model space with a uniform Monte-Carlo algorithm and using a least absolute value criterion, leads us to constraining the combinations of paramater values that are consistent with the decrease of R. The first prominent factor that controls the quality of the fit is the coefficient of erosion efficiency, with best fitting models associated with moderate to high values. Second is the initial geometry of the range with higher or narrower ranges requiring lower coefficient of erosion efficiency. A temporal decrease of R is reached independently of the initial geometry. The viscosity of the crust on the other hand does not appear as a controlling factor. Best fitting models are obtained for conditions of erosional collapse, not for gravitational collapse, which suggest that this latter is not associated with a temporal decrease of R. In addition best fitting models exhibit a topographic decay that is similar to the temporal distribution of the elevation of post-orogenic mountain belts.

1 Introduction

The persistence of mountainous topography in post-orogenic mountain belts over hundreds of millions of years is an observation that questions classical concepts of surface erosion and its interactions with lithospheric deformation (*Baldwin et al.*, 2003). Analyses of modern sediment-load data versus relief amplitude implies decay time of the order of ~ 25 Ma (*Pinet and Souriau*, 1988). Even taking into account rock uplift generated by isostatic compensation further increases the decay times up to ~ 70 Ma (*Pazzaglia and Brandon*, 1996; *Pelletier*, 2008). This value is still five fold smaller than the age of Paleozoic orogens with peak elevation well above 1 km (e.g. Appalachians, Urals). On the other hand by considering time-scales associated with river erosion by stream-power, *Baldwin et al.* (2003) demonstrated that the decay time can be increased up to a factor 20 by taking into account some specific features of river driven erosion such as stochastic distribution of flood events and critical incision threshold.

Futhermore, post-orogenic mountain belts are also associated with very thick crustal roots that geometrically correspond to over-compensated surface topography. The ratio between surface topography elevation and the thickness of the crustal root (R hereinafter) is smaller in post-orogenic belts than in orogenic belts and decreases with the age of the orogen (*Fischer*, 2002; *French et al.*, 2009) (Fig. 8.1). This distribution suggests a rapid decrease of R during $\sim$ 25 Ma, followed by a slowdown of the R decrease until reaching an almost constant value around 300 Ma. Two geodynamical mechanisms are proposed by *Fischer* (2002) to explain this decrease of R: (1) A rapid increase of the lithospheric strength which inhibits crustal root uplift associated with erosional unloading at surface; (2) A progressive decrease of the density contrast between crust and mantle due to metamorphic reactions, that decreases the buoyancy of the crustal root. The latter is supported by Bouguer gravity anomalies which are best explained by a decrease of the density contrast at the Moho between the crustal root and the mantle (*Fischer*, 2002; *French et al.*, 2009). However metamorphic reactions that could account for this progressive increase of the density of the crustal root after orogeny are still unconstrained.

These two challenging observations of post-orogenic evolution, i.e. large decay time and a progressive decrease of R, are closely related: unloading by surface erosion sets the pace of internal deformation, acting to balance the gravitational forces at lithospheric scale, and consequently controls rock uplift of the crustal root and surface (e.g., *Beaumont et al.*, 1992; *Avouac and Burov*, 1996; *Willett*, 1999). As a consequence the evolution that leads post-orogenic topography to peneplenation over hundreds of millions years and to the over-balancing of the underlying crustal root, can not be fully understood without a coupled modeling of surface erosion and internal deformation.

Thus in this paper to explore potential scenarios of post-orogenic evolution of mountain belts in the framework of the interactions between erosion and deformation we use a coupled $2D$ Finite Element Model (FEM), which includes both solid Earth deformation and Surface Processes Model (SPM). The main purpose of this modeling approach is to point out the basic physics which control post-orogenic evolution, with a reduced set of parameters, rather than trying to mimic the geometry and features of a specific mountain range. In particular, we focus on the erosional and rheological conditions that enable reproducing the observed decrease of R with the age of the

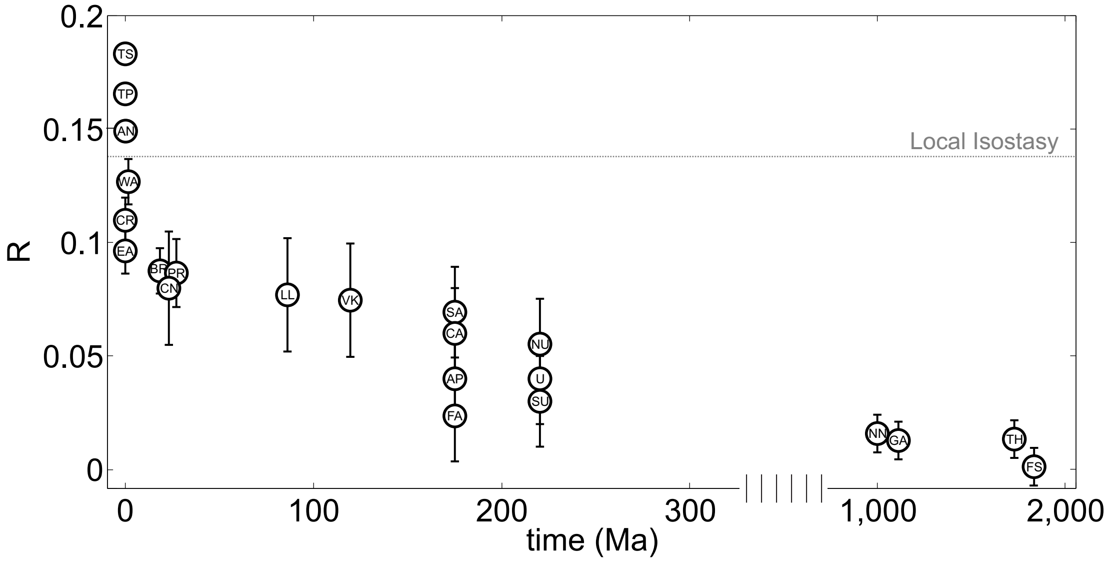

Figure 8.1: Comparison of the evolution of surface topography/crustal root thickness (R), for young and old orogens (modified from *Fischer* (2002) and *French et al.* (2009)). Error bars are 95% confidence limits. The gray horizontal dashed line indicates the value of R corresponding to geometrical isostasy assuming no density variations during post-orogenic evolution. TS, Tien Shan; TP, Tibetan Plateau; AN, Central Andes; WA, Western Alps; CR, Carpathians; EA, Eastern Alps; BR, Brooks Range; PR, Central Pyrenees; CN, Cantabrians Mountains; LL: Lachlan Orogen; VK, Verkhoyansk Mountains; SA, Southern Appalachians; CA, Central Appalachians; AP, Appalachians Plateau; FA, Florida-to-Edmonton Broadband Seismometer Experiment, extreme Southern Appalachians; NU, Northern Urals; CU, Central Urals; SU, Southern Urals; NN, Namaqua-Natal Orogen; GA, Northwest Greenville Orogen; TH, Trans-Hudson Orogen; FS, Svecofennian Orogen.

orogen.

First we detail the FEM and SPM used in the modeling approach. Then we present the behaviour of an arbitrary model and test its sensitivity to the model parameters. Then we present the results of the inversion of R using a Monte Carlo sampling algorithm of the model space with a least absolute criterion. Finally we propose and discuss physical models of post-orogenic evolution that are consistent with both the data presented by *Fischer* (2002) and with the geometrical properties of real inactive orogens.

2 Modeling of Post-Orogenic Evolution

Following *Lambeck and Stephenson* (1985) we assume an already developed mountain range as initial condition, formed by unspecified mechanisms. We assume for convenience that, (1) the initial topography is locally compensated and (2) during the post-orogenic phase surface erosion is balanced by regional isostasy and by lateral viscous flow of the crustal root.

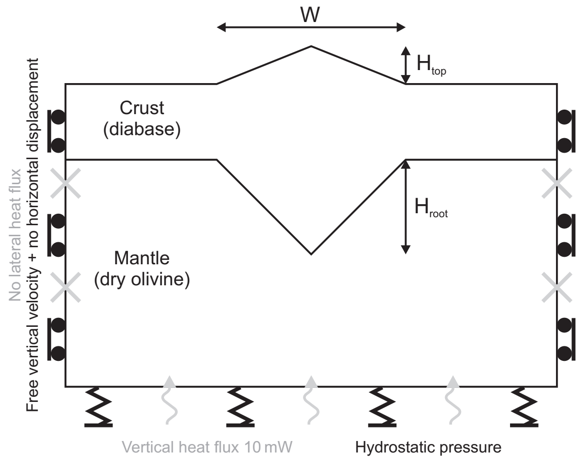

Figure 8.2: Geometry of the initial stage of the reference thermo-mechanical model used in this study. The mantle and the crust are represented by two layers with different rheologies and thermal properties (Table 8.1). As an initial condition, the topography is isostatically compensated by a crustal root. Surface is submitted to erosion. Temperature varies with depth, and is dependent on radiogenic heat production and basal vertical heat flow. Free vertical displacements are allowed at both ends of the model, which is supported at its base by hydrostatic pressure.

2.1 System Geometry

Following *Avouac and Burov* (1996) the initial geometry of our 2D model is a simple conceptual orogen (Fig. 8.2). It includes a triangular mountain, with a basal width W and a summit height H. This topography is balanced by a crustal root with a thickness H_{root}, and respects local isostasy as an initial condition. Local isostasy implies that the ratio $R = H/H_{root}$ equals $(\rho_m - \rho_c)/\rho_c$. The crust, 35 km thick, lies over an upper mantle. The entire model is 2000 km wide and 200 km thick to prevent the center of the model from boundary effects.

2.2 Thermo-Mechanical Modeling and Boundary Conditions

We use ADELI, a 2D Lagrangian FEM (*Hassani et al.*, 1997) consisting in a coupled thermo-mechanical solver, to model the post-orogenic evolution of the mountain range. It accounts for the mechanical layering of the lithosphere and the non-Newtonian viscous rheology of rocks as a function of temperature and stress. The elastic part of each component of strain ϵ_{ij} is function of the stress tensor σ, through Hooke's law,

$$\epsilon_{\mathrm{ij}} = \frac{1+\nu}{E}\sigma_{ij} - \frac{\nu}{E}\mathrm{trace}(\sigma)\delta_{ij}, \tag{8.1}$$

where E and ν are the Young's modulus and the Poisson's ratio, respectively. While the viscous part of the strain rate $\dot{\epsilon}$ is defined as,

$$\dot{\epsilon} = \gamma_0(\sigma_1 - \sigma_3)^n e^{(-E_a/RT)}, \tag{8.2}$$

where T is the temperature,γ_0 the standard fludity, n the power law exponent, E_a the activation energy and R the universal gas constant.

Table 8.1: Rheological parameters and material properties used for the thermo-mechanical model: density, ρ; Young's modulus, E; Poisson's ratio, ν; standard fluidity, γ_0; power law exponent, n; activation energy, E_a; coefficient of thermal conductivity, λ; specific heat capacity, C_p. Parameters from *Carter and Tsenn* (1987); *Tsenn and Carter* (1987); *Kirby and Kronenberg* (1987). Universal gas constant $R = 8.314$ J.mol^{-1}.K^{-1}.

	Crust (Diabase)	Mantle (Olivine)
ρ (kg.m^{-3})	2900	3300
E (GPa)	20	70
ν	0.25	0.25
γ_0 (Pa$^{-\mathrm{n}}$.s^{-1})	$6.31 \cdot 10^{-20}$	$7.00 \cdot 10^{-14}$
n	3.05	3.0
E_a (kJ.mol^{-1})	276	510
λ (W.m^{-1}.K^{-1})	3.0	3.0
C_p (J.kg^{-1}.K^{-1})	1070	1070

Two lithological layers are used: the continental crust and the upper mantle, which are assumed here to have the rheological properties of diabase and olivine, respectively (see Table 8.1). Those rheologies are dependent on temperature T, which is calculated from the heat equation,

$$\rho C_p \left(\frac{\partial T}{\partial t} + \vec{u} \cdot \vec{\nabla} T \right) = \mathrm{div} \left(\lambda \vec{\nabla} T \right) + P_r \ , \tag{8.3}$$

where ρ is the density, λ the coefficient of thermal conductivity, C_p the specific heat capacity, P_r the radiogenic heat production, and $\vec{u}$ the velocity of the material.

The model is supported by hydrostatic pressure at its base, and free vertical velocity conditions on its sides. Those boundary conditions allow the model to balance surface unloading either by regional isostasy or by internal deformation. Thus they enable a coupling between unloading by erosion at surface and rock-uplift. This coupling depends on the mechanical and thermal properties of the lithosphere. Surface temperature respects a Dirichlet condition with $T = 273$ K. The base of the lithosphere and both vertical boundaries of the model are submitted to Neumann conditions. To avoid lateral heat loss horizontal heat flow remains zero. Further on, a basal vertical heat flow of 10.0 mW.m^{-2} will be used as the reference value (*Turcotte and Schubert*, 2002). In the following, we detail the surface processes model applied to the upper boundary (i.e. topographic surface) of the model.

2.3 Surface Processes Model with a Stochastic Approach

Many surface processes contribute to erosion in orogenic or post-orogenic settings. However, fluvial downcutting is believed to be the controling factor of landscape erosion (*Burbank et al.*, 1996; *Lavé and Avouac*, 2001; *Godard et al.*, 2010). Rivers downcut the landscapes and set the local base level for topographic denudation: Despite their prominent role, rivers do not account for the mean topography of landscapes, which is the pertinent variable for the upper boundary condition in mechanical modeling (*Godard et al.*, 2006; *Willett*, 2010). We therefore use the

Table 8.2: Paramaters used in the surface processes model, from *Lavé* (2005); *Lague et al.* (2005).

Discharge parameters		Basin geometry		Fluvial network	
m	0.6	L_{basin} (km)	50	K_L ($km^{1.88}$)	868
k_w ($s^{0.45}.m^{-0.35}$)	0.45	A_{Omin} (km^2)	0.1	ω	1.44
ω_a	0.45	ϕ_c (°)	40	s_0	1.5
ω_s	0.2	Effective discharge		Stochastic discharge	
χ	1	α	0.7	α'	2.9
		β	0.33	β'	1.4
		γ	0.28	γ'	1.2

method proposed by *Lavé* (2005) to compute the $1D$ mean topography of a $2D$ landscape controlled by river incision and hillslope landsliding.

2.3.1 Description of the $2D$ Model

Following *Lavé* (2005), the surface model is divided into several rectangular parallel basins characterized by regular outlet spacing (*Hovius*, 1996). They are made up of a main river that is oriented perpendicular to the range axis, and a series of tributaries feeding the main river.

In our modeling the erosion rate of the main river follows a simple detachment-limited relation that has provided satisfactory first-order results accross the Subhimalaya rivers (*Lavé and Avouac*, 2001). This relation states that the instantaneous bedrock incision rate of a river i is proportional to its unit stream power,

$$i = k\left(\left(\frac{Q}{w}\right)^m S^\alpha - \tau_c\right) , \tag{8.4}$$

with S the local channel slope, Q the water discharge, w the width of the river channel, m and α the stream power exponents, τ_c a critical unit stream-power threshold for incision, and k a dimensional erodibility coefficient.

Sedimentation occurs in closed basins which are filled with sediments to the spill point, so that the main river flows downhill to the edge of the model. This implies that there is sufficient sediment supplied to fill basins, and excludes the existence of endorheic basins.

In active orogens the erosion of hillslopes is dominated by landsliding (*Hovius et al.*, 1997). In post-orogenic settings hillslopes are also submitted to diffusive processes, such as soil creep (e.g., *Dietrich et al.*, 1987; *Heimsath et al.*, 1997; *Roering et al.*, 1999). However, in order to simplify our model, we hereinafter assume that hillslopes are only controlled by instantaneous landsliding, and display a critical angle of repose ϕ_c.

2.3.2 A Stochastic Approach for Water Discharge

In orogenic settings it is classically assumed that river geometries reflect the effect of both long-term tectonics and erosion, and that this latter is controlled by a dominant or effective river water discharge (e.g., *Howard and Kerby*, 1983; *Lavé and Avouac*, 2001). In addition, models of river erosion, such as stream power incision, generally consider that the critical threshold for incision is negligible compared to the effective stream power. However in post-orogenic settings the progressive decay of topography results in the decrease of the effective stream power. In such configuration the effect of the critical threshold for incison becomes increasingly important with topographic decay (*Baldwin et al.*, 2003). This implies a complete cessation of erosion when the effective stream power equals the critical threshold, and an infinite post-orogenic topography decay time. Thus the concept of effective discharge is not appropriate to model post-orogenic evolution.

Following *Lague et al.* (2005) we instead include a stochastic distribution of discharge to express the long-term river erosion law. We make the simple assumption that the temporal variability of the local at-a-station river water discharge can be expressed through a power law distribution,

$$pdf(Q_\star) = k_{pdf} \frac{\chi^{\chi+1}}{\Gamma(\chi+1)} Q_\star^{-(\chi+2)} dQ_\star \ , \tag{8.5}$$

with $Q_\star = Q/\bar{Q}$ the water discharge ratio and $\bar{Q}$ the average water discharge, χ an exponent, that decreases with increasing water discharge variability, ranging commonly between 0 and 2 (*Lague et al.*, 2005; *Turcotte and Greene*, 1993) and eventually up to 5 (*Molnar et al.*, 2006), and k_{pdf} a constant (see appendix 6)). This distribution is consistent with real discharge distribution for high-flow events, but largely over-predicts the frequency of low-flow events (*Lague et al.*, 2005). It is only suitable in settings where the erosive impact of low-flow events is negligible. Henceforth we assume that post-orogenic mountain belts are compatible with this distribution, yet acknowledging that we lack constraints to support this in detail. Accordingly, it implies a decrease of the frequency of erosive-flow events, i.e. above the erosion threshold, with topographic decay during the post-orogenic phase. Then we can integrate the instantaneous incision rate i to express the long-term incision rate I,

$$I = \int_{Q_{c\star}}^{Q_{m\star}} pdf(Q_\star) i(Q_\star) dQ_\star, \tag{8.6}$$

with i the instantaneous incision rate defined in Eq. 8.4. $Q_{c\star}$ is the critical water discharge ratio and is defined such that $i(Q_\star \leq Q_{c\star}) = 0$, and $Q_{m\star}$ is the maximum water discharge ratio at the timescale considered. Extending the analytical derivation first proposed by *Lague et al.* (2005), the integration (see appendix 6) ultimately leads to an equation that shares the same generic expression as the effective stream-power or shear-stress incision law,

$$I = k' A^{\gamma'} S^{\alpha'} \ , \tag{8.7}$$

where $k' = k_{sto} k \bar{P}^{\beta'} / \tau_c'$ is a coefficient of erosion efficiency that depends on the erodibility coefficient k, discharge variability χ, the mean precipitation rate $\bar{P}$ over the drained area A, the apparent critical unit stream-power threshold for incision τ_c' and on a constant k_{sto}. These latter both depend on discharge variability χ, such as the slope α', precipitation β', and area γ' exponents. We refer the reader to appendix 6 and to *Lague et al.* (2005) for more details on the integration, and on the assumptions that lie behind.

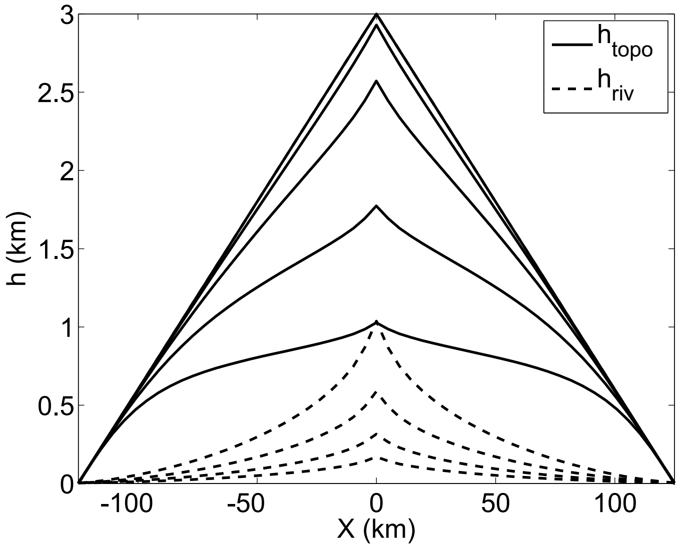

Figure 8.3: Evolution of the main river h_{riv} (dashed line) and of the mean topography h_{topo} for a rigid lithosphere with no isostasy, for an arbitrary set of model parameters, at $t = 0, 9, 27, 90, 300$ Ma. The initial river and mean topography profils consists in a triangular mountain belt with a width of $W = 250$ km and a height of $H = 3$ km. The coefficient of erosion efficiency is set to $k' = 3.8 \cdot 10^{-17}$ m$^{-1.4}$.s^{-1}.

2.3.3 From $2D$ to $1D$ Model

In space we integrate the previous equation to express both the evolution of the main river profile and of the mean relief profile in $1D$ (*Lavé*, 2005). The mean relief h_{mean} is the sum of the main river elevation h_{riv}, of the mean tributary relief $\bar{h}_{trib}$ and of the mean hillslope relief $\bar{h}_{hill}$. The time evolution of the main river profile river is,

$$\dot{h}_{riv} = U - I \ , \tag{8.8}$$

where U is the rock uplift deduced from the finite element model. Assuming that the tributary rivers follow the same incision law as the main river and that they are in steady-state, leads to the following expression of the denudation rate of the mean topography,

$$\begin{aligned} \dot{h}_{mean} &= k' \left(\frac{(2-\omega-\gamma'/\alpha')A_T}{K_L(A_T^{2-\omega-\gamma'/\alpha'} - A_0^{2-\omega-\gamma'/\alpha'})} \bar{h}_{trib} \right)^{\alpha'} \ , & (8.9) \\ \text{with } \bar{h}_{trib} &= h_{mean} - h_{riv} - \bar{h}_{hill} & (8.10) \end{aligned}$$

where A_0 and A_T are the tributary head source area and total area respectively, K_L and ω are the exponents of the density function $f_L(A) = K_L A^{-\omega}$ that defines in a given watershed the length of a fluvial network that drains an area A. In addition, as $\bar{h}_{hill}$ depends on A_0, which is related to the denudation rate of the mean topography, this equation needs to be computed iteratively. We invite the reader to refer to *Lavé* (2005) for more details on the spatial integration of surface processes form $2D$ to $1D$. Figure 8.3 illustrates the time evolution of a river profile and of its corresponding mean topography in the case of a rigid lithosphere with no isostasy.

2.4 Coupling Erosion and Deformation in Numerical Models

We couple this SPM with the FEM following a method similar to *Willett* (2010): (1) Solve the deformation problem using the FEM, and apply the displacement of the surface to the SPM; (2) Update divides position and fill close basins by sedimentation; (3) Compute incision of the main river and update its elevation; (4) Compute erosion of the tributaries, update their elevation, and deduce mean topography. Note that, comparatively to *Willett* (2010), the distribution of precipitation is not updated at each time step as it is assumed to be homogeneous all over the surface.

In addition, we use a local remeshing algorithm, called Surface Lagrangian Remeshing (SLR) (*Steer et al.*), which is dedicated to the problem of erosion in Lagrangian FEM. It is combined with a global remeshing method (*Hassani et al.*, 1997) which deals with deformation of elements at depth. This combination enables minimizing numerical errors associated with remeshing in post-orogenic modeling, where erosion is the dominant process. ADELI employs the dynamic relaxation (DR) numerical scheme for time discretization (*Underwood*, 1983), which is an iterative explicit method solving Newton's second law to obtain the static solution of a steady-state modeling (see *Hassani et al.* (1997) and *Steer et al.* for more details). This method is fully compatible with post-orogenic settings, where geodynamics inertial terms are negligible.

The initial profile of the river follows the mean topographic profile (triangular shape, see Fig. 8.2). Thus to overcome this nonrealistic initial condition, 2 mm.a^{-1} of convergence are imposed to the lateral boundary of the model during the first 3 Ma to force the river to tend towards its steady-state profile.

In each of the following experiments, 3 millions of time steps were necessary to model post-orogenic evolution over 300 Ma. The models were discretized in $\sim$ 20.000 triangular elements with smaller elements at surface than at depth. It allows for a horizontal resolution of $\sim$ 3 km in surface, which is an appropriate scale for the description of surface processes in our formalism.

2.5 Range of Parametric exploration

The main purpose of our modeling approach is to assess the conditions of surface erosion and lithosperic deformation that are compatible with a temporal decrease of R. In particular we want to quantify: (1) the influence of the initial topographic (and associated crustal root) amplitude and wavelength, as it controls the gravitational and erosional perturbation; (2) the effect of surface erosion efficiency as it sets the pace of elevation decay, erosional unloading and subsequent rock uplift generated by isostasy; (3) the influence of the crustal root lateral viscous flow which is a potential mechanism of compensation accounting for surface unloading.

As a consequence we need to choose a set of relevant parameters that allow encompassing of each of these potential mechanism of post-orogenic evolution. This set includes: (1) the initial basal width W of the orogen ranging between 100 and 400 km, which corresponds to the range of width of present-day active orogens (Fig. 8.4); (2) the elevation of the mean topography at the center of the range, H ranging between 2 and 5 km and also corresponds to observed values for active orogens; (3) the coefficient of erosion efficiency or k' ranging between 10^{-18} and

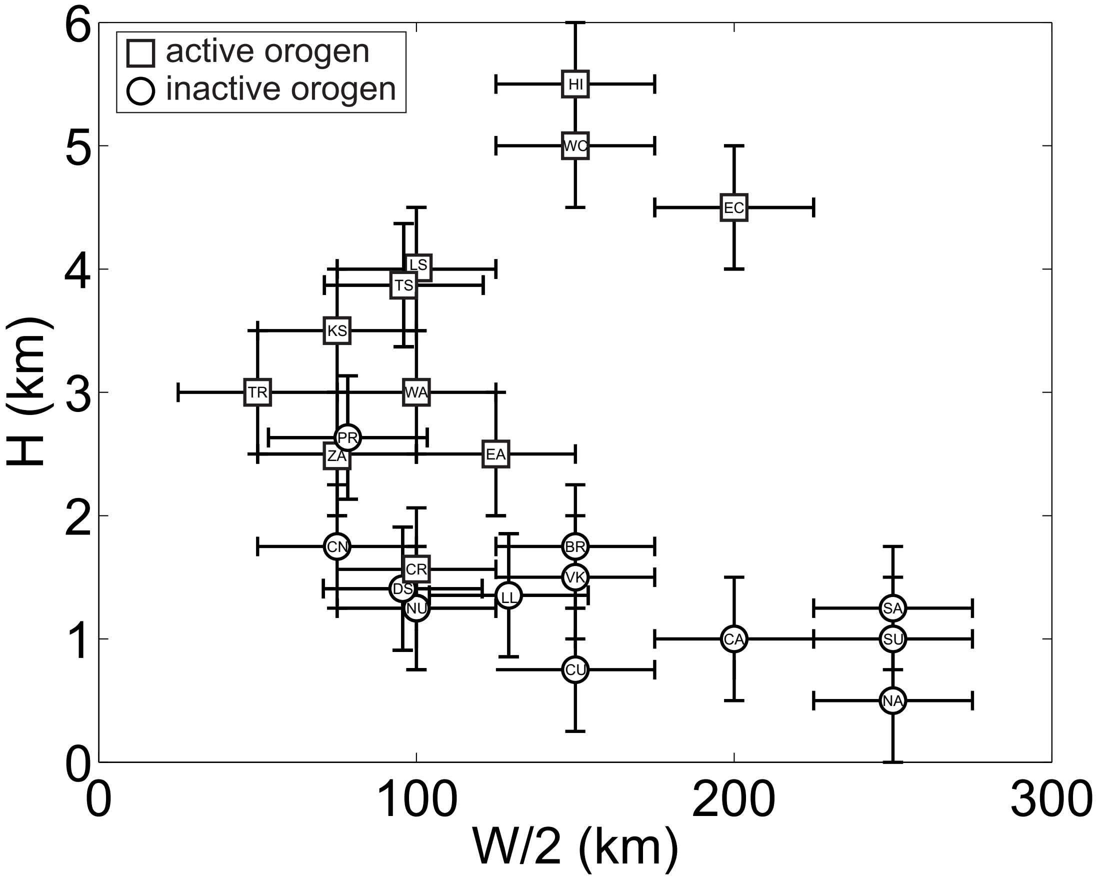

Figure 8.4: Approximate elevation (H) and half-width ($W/2$) of active and inactive orogens, excepted for plateau shape topography. Data were acquired using cross-sectional topographic mean profile, with averaging on 50km width. Elevation is computed relatively to the local base level of each orogen or relative to sea level, and half-width was defined as the width of topography above this base level. The uncertainty is about 0.25 km for H, 25 km for $W/2$, and 5 Ma for t_{post}. HI, Himalaya; WC, Andean Western Cordillera; EC, Andean Eastern Cordillera; LS, Longmen Shan; TS, Tien Shan; KS, Kunlun Shan; WA, Western Alps of Europe; EA, Eastern Alps of Europe; ZA, Southern Alps of New Zealand; TR, Taiwan Range; CR, Carpathians; PR, Central Pyrenees; BR, Brooks Range; CN; Cantabrians Mountains; LL, Lachlan Orogen; DS: Dabie Shan; VK, Verkhoyansk Mountains; SA, Southern Appalachians; CA, Central Appalachians; NA: Northern Appalachians; NU, Northern Urals; CU, Central Urals; SU, Southern Urals.

10^{-15} $m^{-1.4}.s^{-1}$, which corresponds to a realistic range of terrestrial values for $\chi = 1$ (J. Lavé, unpublished data); (4) the radiogenic heat production of the entire crust P_r ranging between 0 and 1 $\mu W.m^{-3}$, which corresponds to an average range of values (*Krešl et al.*, 1978; *Furukawa*, 1995; *Furukawa and Shinjoe*, 1997; *Pinet and Jaupart*, 1987; *Brady et al.*, 2006). Several variables can impact the amplitude of viscous spreading: in a search for simplicity we assume here that varying the thermal stucture through radiogenic heat production variations, enables accounting for the effect of other variables like the ones induced by the chosen viscosity rheology. For this last point we recognize large potential variations. Similarly, the coefficient of water discharge variability is kept constant $\chi = 1$ for all the models, and we admit that varying it would modify the sensitivity of the model to erosion and the time scale of topographic decay. Moreover we do not consider temporal or spatial variations of any parameters.

This set of parameters makes it possible to test the effect of the initial geometry, of the surface erosion efficiency and of the crustal root effective viscosity on the evolution of post-orogenic belts with realistic values. In this set, k' is the less constrained parameters, which presents the greater range of realistic values, several orders of magnitude, while the range of the other parameters is more limited, approximatively extending over one order of magnitude.

3 Model Results and Sensitivity

3.1 Surface Topography and Crustal Thickness Evolution

To illustrate the behavior of the model during post-orogenic conditions, we test the following arbitrary set of parameters: $H = 3$ km, $W = 250$ km, $P_r = 0.5$ $\mu W.m^{-3}$ and $k' = 3.8 \cdot 10^{-17}$ $m^{-1.4}.s^{-1}$ (Fig. 8.5). As expected, the evolution of the mean elevation shows a global decrease, especially in the summit area. This decrease is controlled by a joint effect of both erosion and rock uplift induced by isostatic compensation. Rock uplift affects topographic mean elevation but also Moho depth, which contrary to the surface is not affected by erosion. In this model elevation of the summit has decreased from 3 to 1.6 km in 300 Ma, and has experienced about 0.9 km of cumulated rock uplift if considering that rock uplift at surface is equal to the uplift of the Moho. Under this assumption the cumulated exhumation at the summit is about 2.3 km. To maintain local isostasy, the cumulated uplift of the Moho should have been $U = 2.3\rho_c/\rho_m = 2.0$ km. Clearly this condition is not reached, and it results in a decrease of R. However note that this decrease is not as intense as what is suggested by data from post-orogenic belts (Fig. 8.1).

In this model erosion is focused on the range, while uplift is more widespread and also affects the foreland. This difference of wavelength between erosion and uplift in surface is the consequence of the rheological properties of the lithosphere. In this model, the elastic core of the lithosphere is too thick to allow strict local isostatic compensation of erosion. It results in a decrease of the R ratio relatively to its isostatic value $R = (\rho_m - \rho_c)/\rho_c$. This decrease is controlled by the transition from local to regional isostasy, which mainly depends on the rheological properties of the lithosphere, and on the pattern of surface erosion of the mean elevation. This

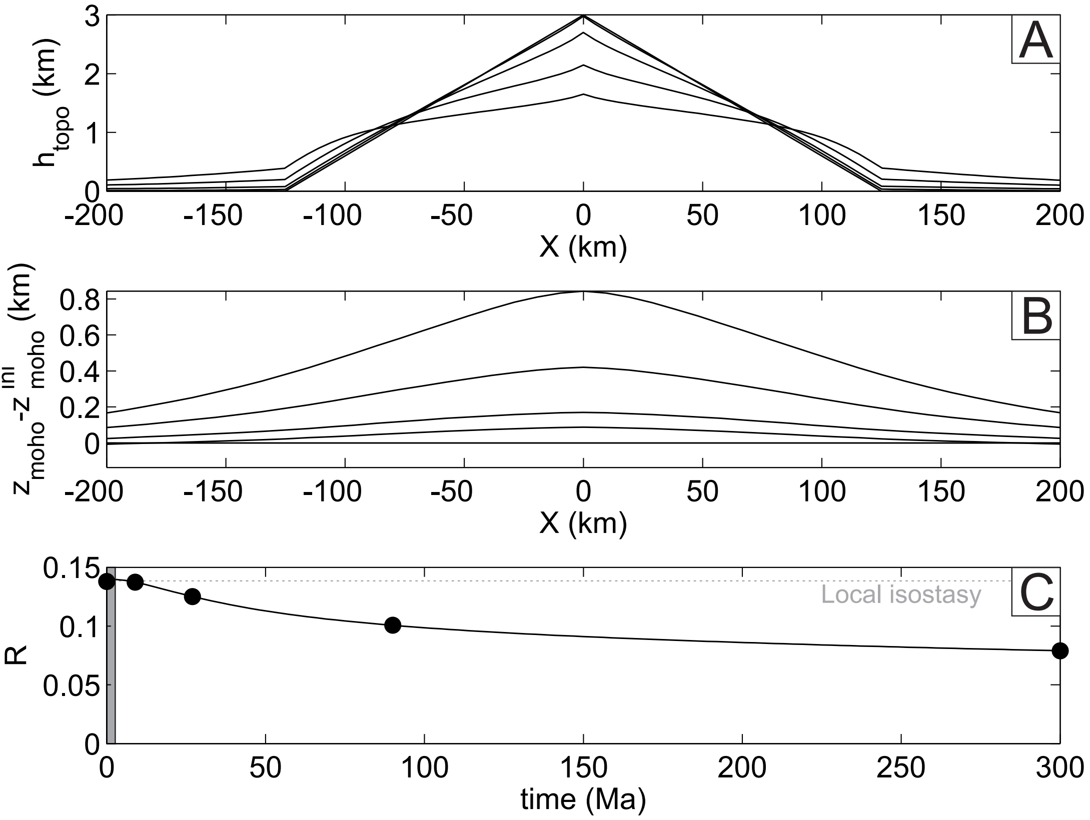

Figure 8.5: Evolution of the profiles of (A) mean elevation h_{topo}, and (B) Moho's depth z_{moho} relatively to its initial value z_{moho}^{ini}, for an arbitrary model at $t = 0, 9, 27, 90, 300$ Ma. (C) Time evolution of the ratio R of surface elevation on crustal root thickness, with the black filled circles indicating timing of profiles presented in A and B. Gray shading corresponds to tectonic forcing phase during 3 Ma. The parameters of the model are: the width of the initial mountain belt $W = 250$ km, its summit elevation $H = 3$ km, the radiogenic heat production rate $P_r = 0.5$ μW.m^{-3} and the coefficient of erosion efficiency $k' = 3.8 \cdot 10^{-17}$ m$^{-1.4}$.s^{-1}. The model is similar to the one presented in Fig. 8.3 except for the rheology.

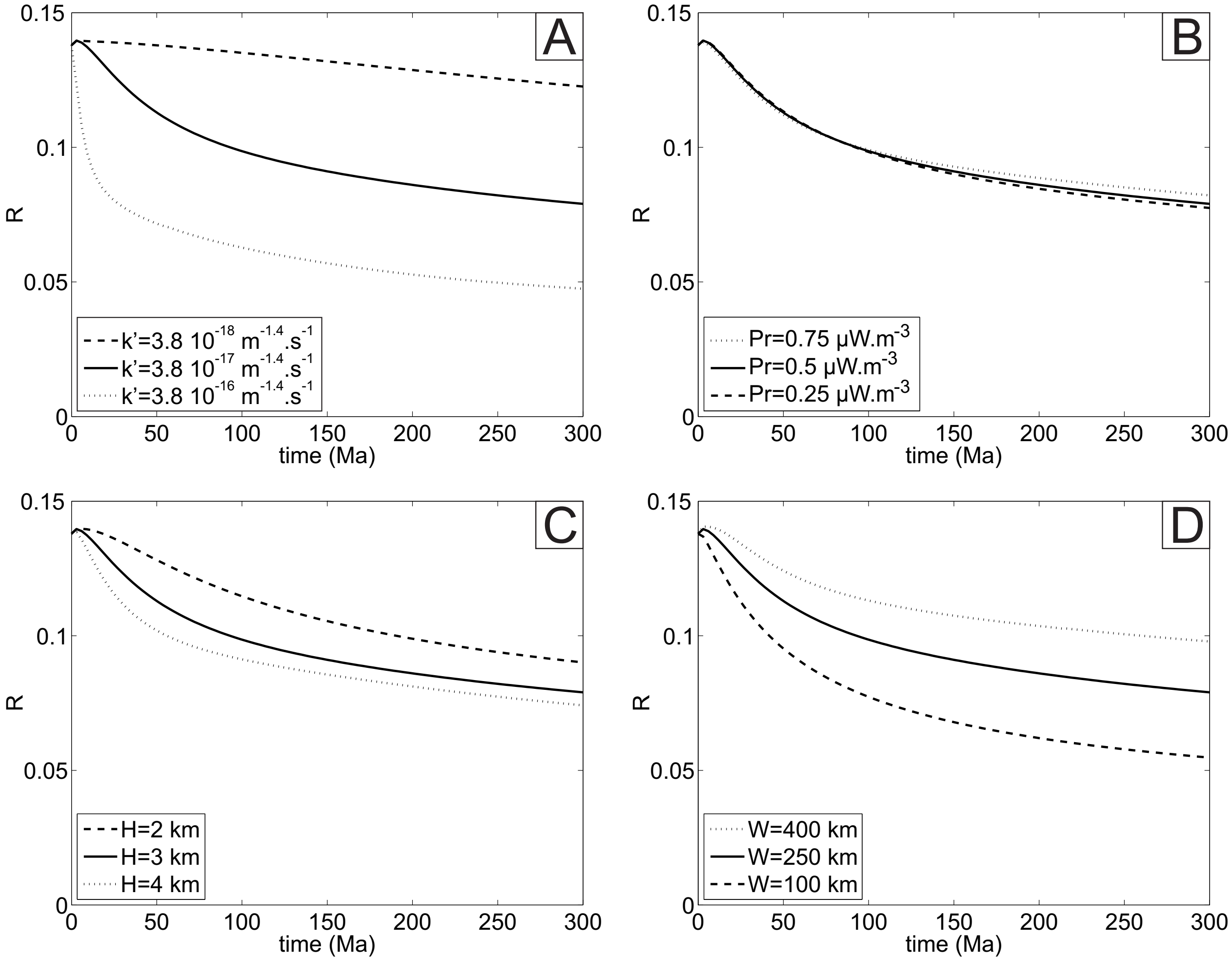

Figure 8.6: Sensitivity of the ratio R of surface elevation on crustal root thickness to the parameters of the models: (A) the coefficient of erosion efficiency k', (B) the radiogenic heat production rate P_r, (C) the summit elevation H, and (D) the width of the range W. The black solid line corresponds to the model presented in the Figure 8.5, while the dashed and dotted lines correspond to a decrease or an increase of the parameter considered, respectively.

outcome highlights the influence of the initial structure of the modeled orogen, that we have assumed for convenience to be in a state of local isostasy. Dynamically, the model also exhibits a progressive slowing of the rate of R decrease. This is due to the progressive decrease of the erosion rate associated with the decrease of elevation and slope.

3.2 Model Sensitivity: Geometry, Surface Processes and Crustal Rheology

Before detailing the tests of sensitivity it is important to recall that k' varies over several orders of magnitude, whereas H, W and P_r are restricted to approximatively one order of magnitude. To constrain the sensitivity of this arbitrary post-orogenic model, we use the previous parameter set and vary each parameter independently of the others in the range of their realistic values (Fig. 8.6). (1) Clearly, the model is first sensitive to the coefficient of erosion efficiency as increasing or decreasing it by an order of magnitude results in a dramatical increase or decrease of the rate of R evolution, respectively. In a purely elastic model, increasing or decreasing k', increases or decreases the rate of evolution of R correspondingly. In a visco-elastic model, this behavior is modulated by the viscous response of the lithosphere to erosion, that acts to damp the erosional forcing. (2) The model is also sensitive to the initial geometry of the range, with a higher or narrower range resulting in a lower R, and vice versa. The slope of the initial belt $2H/W$ partly controls the erosion rate: higher or narrower range results in higher initial transverse river slope and therefore induces higher initial erosion rate as well as faster R decrease. On the other hand, the wavelength and the amplitude of the the range load, controls the pattern and amplitude of the flexural rebound. When considering a constant range load equal to $HW/2$ (i.e. the gravitational perturbation) and a constant rheology, the ratio of the uplift wavelength to W increases when W decreases (and consequently H increases). As a consequence the uplift is more widespread than the pattern of erosion that is focused on the range, which results in a decrease of R. (3) The model is apparently not significantly sensitive to the radiogenic production rate of the crust, which only induces minor changes of R.

However, these first observations are dependent of the arbitrary set of parameters that were used in these models. Moreover, the sensitivity tests were performed for each parameter independently of the others. This does not make it possible to predict the effect on R of varying several parameters simultaneously and in particular the existence of eventual trade-offs between those parameters.

4 Post-Orogenic Over-Compensation and Erosional Decay

Each mountain range is unique in terms of rheology, initial width and height, climatic and erosional conditions, and consequently has followed a distinctive decay history. However, data proposed by *Fischer* (2002) on young and old mountain ranges (Fig. 8.1), suggest that they follow a relatively common destiny in terms of R evolution. Using the forward model defined previously, we seek through a Monte Carlo approach to determine the combination of model parameters that allow reproducing of this global tendency. In other words, we invert the model to determine values of each variable compatible with the mean R decrease. Yet we acknowledge that variable values of each specific mountain range can depart from this mean trend given sligthly different settings.

The dataset that is used in the inversion (Fig. 8.1), consists in the time evolution of R (i.e. the ratio of surface topography on crustal root thickness), restricted to the last 300 Ma (*Fischer*, 2002; *French et al.*, 2009). We do not explore Proterozoic orogens in our modeling because the characteristic time for the evolution of R appears to be typically shorter than 300 Ma, and because practically modeling Proterozoic would require to multiply by 10 the time cost associated with each single model. Moreover, we consider the scatter in R values for each active and inactive orogen around the average trend as an estimate of the standard deviation on R.

4.1 Monte Carlo Sampling and Least Absolute Values Inversion

To explore the sensitivity of the model to its parameters, the model space is sampled by ~ 300 models using a Monte Carlo algorithm with a uniform search. This latter has the main advantage of being robust and easily implemented. To assess the agreement between the modeled evolution of R and the real R dataset, we compute a misfit Φ for each model that is determined from a least absolute values criterion (Fig. 8.7),

$$\Phi = \frac{1}{N} \sum_{i=1}^{N} \frac{|R_{i,m} - R_{i,d}|}{\sigma_i} , \tag{8.11}$$

where N is the number of orogen, $R_{i,m}$ and $R_{i,d}$ are the R values extracted from the model and from the data, respectively, and σ_i is the standard deviation of $R_{i,d}$. We do not seek to find a single best fitting model for the entire dataset, and thus the least absolute values method is well suited as it is robust, i.e. less sensible to outliers.

4.2 Temporal Evolution of R

Our results suggest that part of our models can explain the major trend of the observed R decrease (Fig. 8.7): (1) the progressive decrease of surface mean elevation driven by river incision which downcuts the landscapes; (2) the accommodation of erosional mass unloading at surface by a global uplift of the lithosphere due to regional isostasy, and not only of the crustal root. (3) the progressive slowing of erosion rate with time and topographic decay, which control the dynamic trend of the evolution of R.

The low values of misfit obtained (~ 0.2) a posteriori confirm that the modeling approach is consistent with post-orogenic evolution. Moreover this global trend, obtained with the best fitting models, is also consistent with R values of Proterozoic orogens ($R < 0.025$), even if they are not considered in the inversion.

4.3 Exploring the Model Space

The inversion gives an a posteriori constraint on each parameter of the model space. Figure 8.8 shows the distribution of the misfit Φ as a function of each couple of parameters of the model space. The main outcome of these distributions is that erosion efficiency k' has a strong control on the misfit, as all the best fitting models ($\Phi < 1$) range between $5 \cdot 10^{-17}$ and $1 \cdot 10^{-15}$, almost independently of the other parameters. This result confirms the outcomes of the arbitrary model, suggesting that the rate of R decrease is proportional to erosion efficiency.

The distribution of misfit shows a secondary control by the geometry of the initial belt, which slightly modulates the previous result: lower or wider orogens require higher erosion efficiency to yield a good fit. This geometrical control is associated with river erosion which is affected by the initial slope of the orogen $2H/W$: a lower

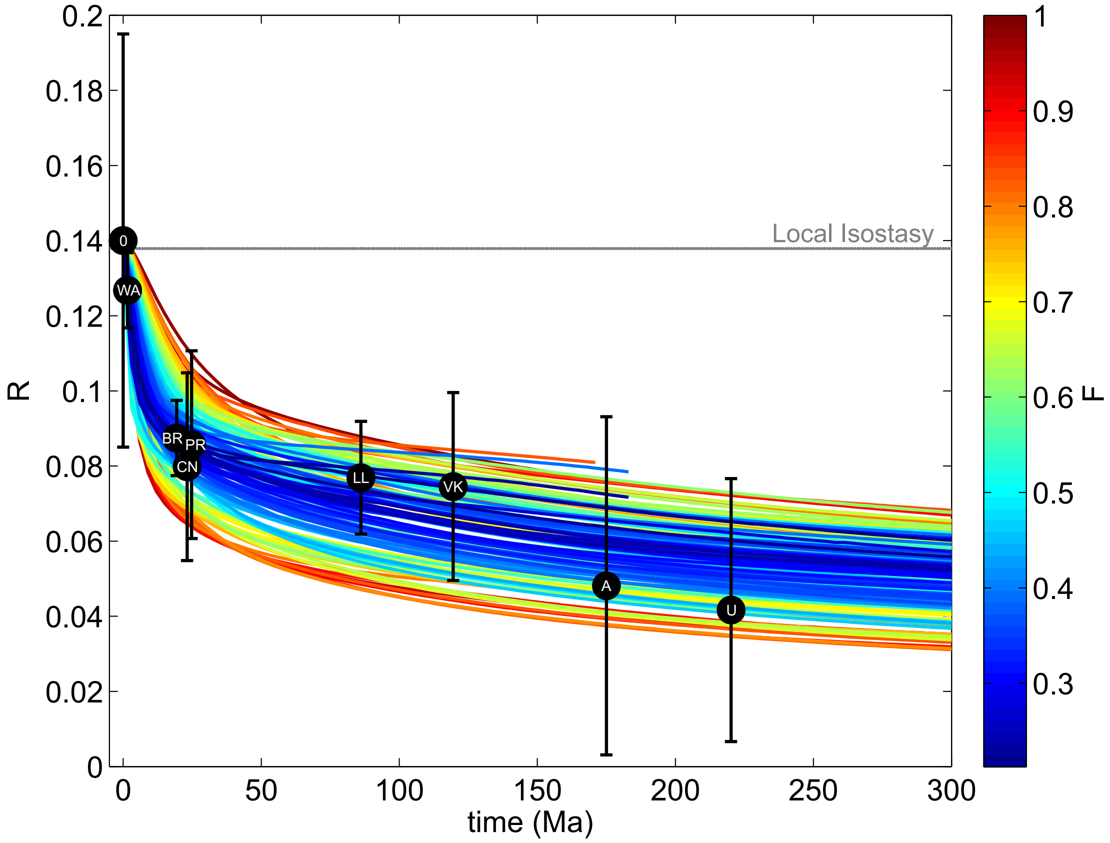

Figure 8.7: Comparison of the evolution of surface topography/crustal root thickness (R), for young and old orogens (modified from *Fischer* (2002) and *French et al.* (2009)), and for the best fitting models ($\Phi < 1$) with respect to the least absolute values inversion with Φ the misfit (Lower values indicating better fitting models). We only consider the average R values for the entire active orogens and for each post-orogenic belts. The data used in the inversion is represented with black filled circles. Error bars represents the sparsity of the raw data taking into account their error bars (see Fig 8.1). It is used as an approximation of the standard deviation σ_i in the inversion. The horizontal gray dashed line indicates the value of R corresponding to geometrical isostasy assuming no density variations during post-orogenic evolution. O, average for the active orogens; WA, Western Alps; BR, Brooks Range; PR, Central Pyrenees; CN, Cantabrians Mountains; LL: Lachlan Orogen; VK, Verkhoyansk Mountains; A, average for the Appalachians; U, average for the Urals.

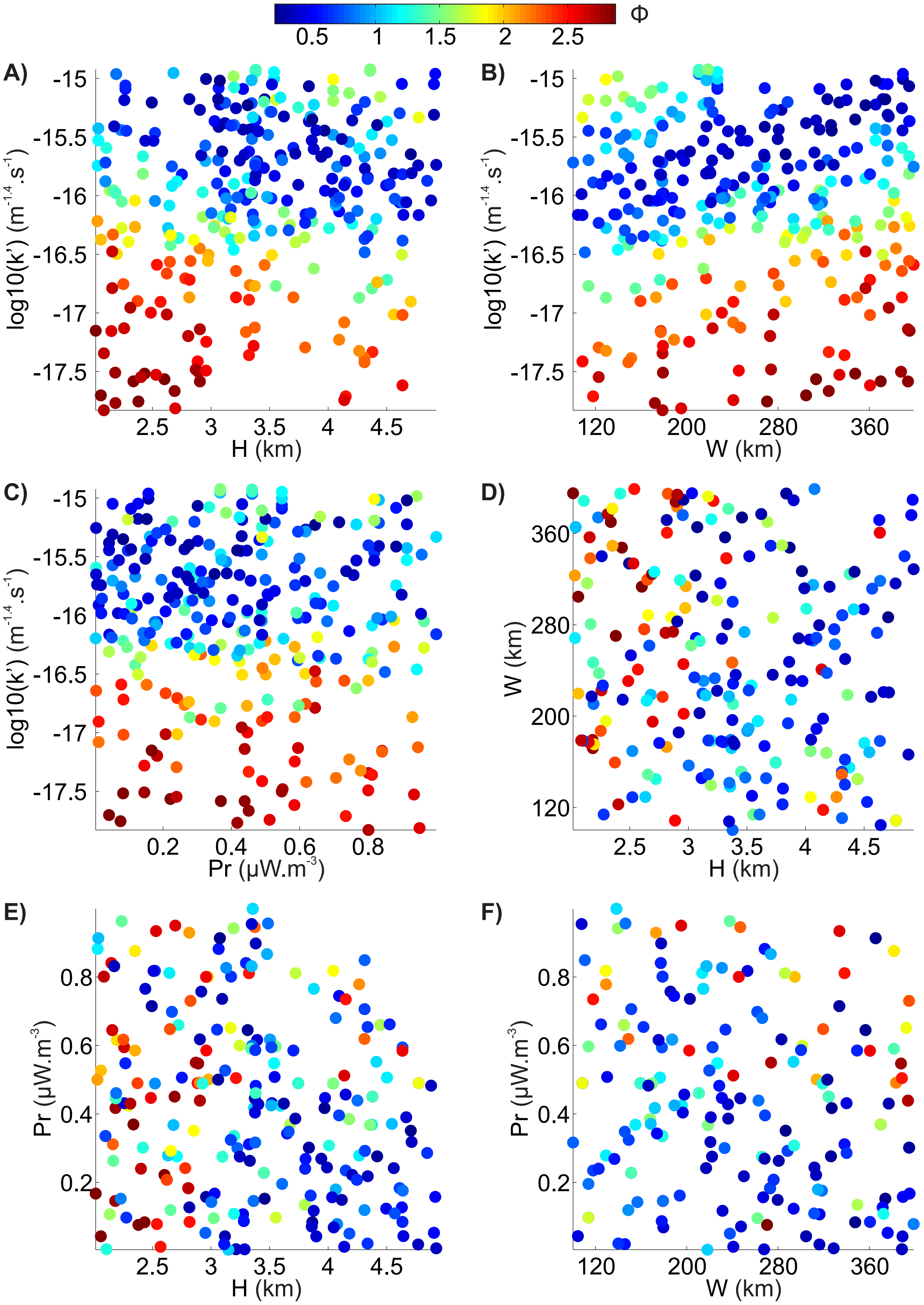

Figure 8.8: Distribution of the misfit versus each couple of parameters of the model space: erosion efficiency k', crustal radioactive heat production P_r, initial mountain width W and height of the mean topography summit H.

or a wider range requiring a higher erosion efficiency to maintain the high erosion rate required to fit the decrease of R with time.

Interestingly, the best fitting models are not restricted to a particular range of initial width W or height H of the mountain belt. As expected from the outcomes of the arbitrary model, the radiogenic heat production rate does not influence the distribution of the misfit.

4.4 Interactions between Erosion and Deformation

In this study, we are in particular interested in understanding the competition between surface erosion and the long-term visco-elastic deformation of the crustal root. Thus to simplify the intertwinned dependencies of the explored parameters through the constitutive laws of the model, we define two variables that characterize explicitely viscous deformation and surface erosion: the effective viscosity of the crustal root (e.g., *Godard et al.*, 2009),

$$\mu_{\text{eff}} = \frac{J_2(\sigma')^{1-n}}{2\gamma_0 \cdot e^{(-E_a/RT)}}, \tag{8.12}$$

where $J_2(\sigma')$ is the second invariant of the deviatoric stress tensor σ',

$$J_2(\sigma') = \sqrt{3(\sigma'^2_{xx} + \sigma'^2_{yy} + \sigma'_{yy}\sigma'_{xx} + \sigma'^2_{xy})}, \tag{8.13}$$

and the geometrical initial characteristic erosion rate,

$$\begin{aligned} I_{geo} &= k'(L_{basin}\frac{W}{2})^{\gamma'}(\frac{H}{W/2})^{\alpha'} , && (8.14) \\ &\propto k'W^{-1.7}H^{2.9} , && (8.15) \end{aligned}$$

which characterizes both the effect of the initial geometry, with W and H, and of the erosion efficiency (k') on the erosion rate. It is equal to the maximum initial erosion rate of the river (Eq. 8.7), which is obtained at the edges of the initial triangular belt at a distance $W/2$ of the divide. At these points, the drained area and slope are equal to $A = L_{basin}W/2$ and $S = 2H/W$, respectively.

Figure 8.9 shows the distribution of the misfit as a function of I_{geo} and of the minimum value of μ_{eff} obtained for each model in the crustal root below the main divide. At first order the distribution is concentric with most of the best fitting models ($\Phi < 1$) converging towards I_{geo} around 0.1 m.a^{-1}. This suggests that the erosion rate is the prominent factor that controls post-orogenic topographic decay. Best fitting models are obtained for a large range of crustal effective viscosities, from 10^{21} to 10^{24} Pa.s. This suggests that this latter does not represent a limiting factor for R decrease, at least in the range of parameters values explored in our modeling approach.

Nonetheless, effective viscosities of 10^{21} to 10^{24} Pa.s correspond to Maxwell relaxation time, $t_{\text{relax}} = \frac{\mu_{\text{eff}}}{E}$, between 1 ka and 1 Ma, assuming a Young's modulus of $20-60$ GPa. As a consequence delayed viscous deformation occurs in the models, as the relaxation time is much smaller than the post-orogenic time scale (> 100 Ma). Thus even if erosion is the main factor that controls post-orogenic evolution in our

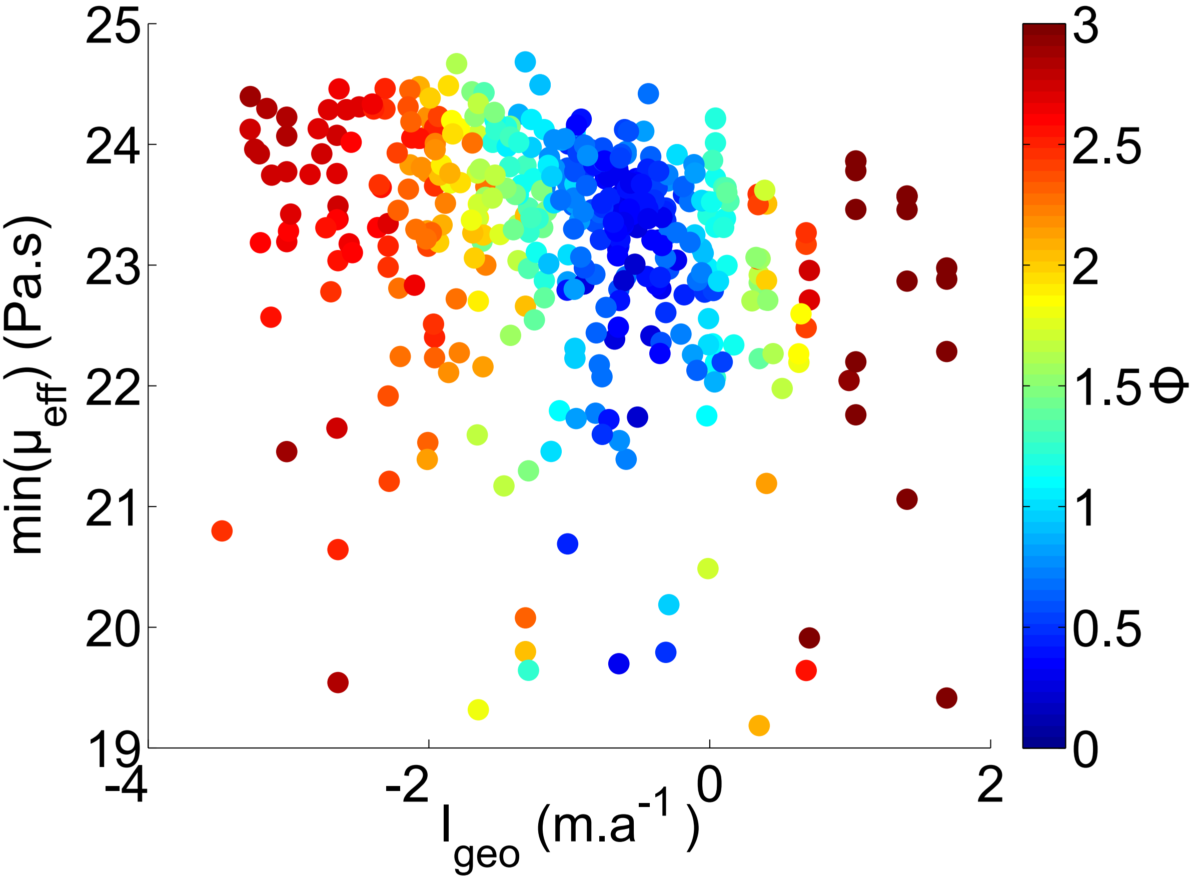

Figure 8.9: Log-log plot of the Distribution of the misfit Φ as a function of the minimum effective viscosity $min(\mu_{\text{eff}})$ obtained in the crustal root below the main divide, and of the geometrical initial characteristic erosion rate I_{geo}.

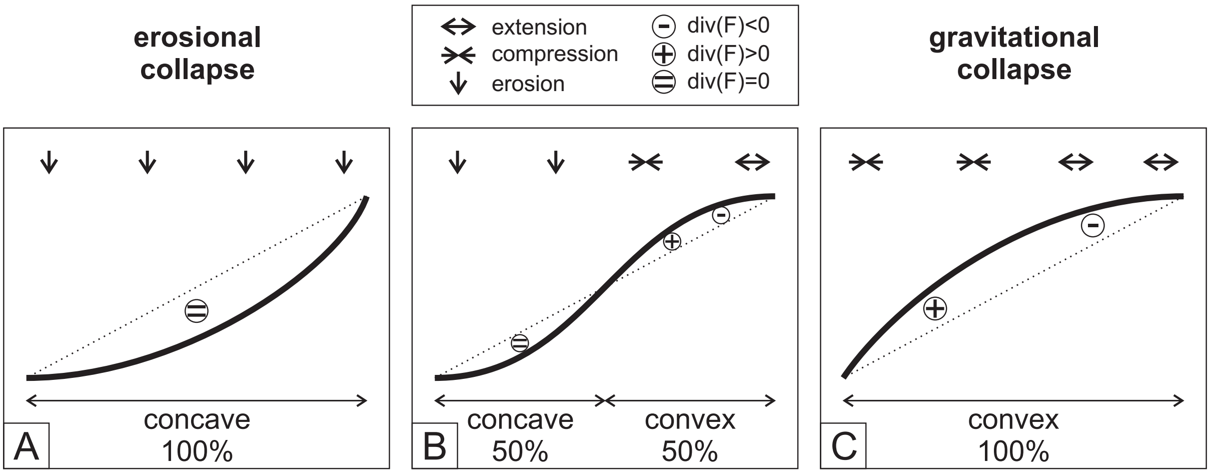

Figure 8.10: Schematic representation of a river profile under (A) erosional collapse, (C) gravitational collapse, and (B) for an intermediary case where the upper part of the river profile is dominated by gravitational collapse whereas the lower part is dominated by erosional collapse. Under erosional collapse the river profile is concave, while it is convex under gravitational collapse. Extension occurs where the divergence of the crustal viscous flow is negative, whereas compression occurs where it is positive.

models, viscous behavior of the lithosphere needs to be considered. In particular it is assumed to control the type of post-orogenic collapse (e.g., *Jadamec et al.*, 2007).

5 Discussion

5.0.1 Erosional or Gravitational Collapse?

Two types of collapse mechanisms are commonly considered for post-orogenic evolution: (1) an erosional driven collapse of the topography coupled to an elastic isostatic uplift (e.g., *Baldwin et al.*, 2003); (2) a gravitational collapse by viscous extension of the crustal root associated with a decrease of surface topography (e.g., *Rey et al.*, 2001).

In our model, we implicitly assume a strong mechanical coupling between the lower and upper parts of the crust as we have defined only one rheological layer for the crust. As a consequence, if gravitational collapse of the crustal root occurs, it is likely to deform the upper part of the crust as well. As neither faulting nor plasticty are allowed in the model, crustal collapse is expected to leave a distributed visco-elastic fingerprint on the surface of the model, including surface extension where the divergence of viscous flow F in the crust is negative, and surface compression where it is positive (Fig. 8.10). In particular, river profiles are expected to record both incision and gravitational collapse, which are associated with concavity and convexity, respectively.

To decipher if gravitational collapse occurs, we compute for each model the degree of convexity of the river profile. We defined it as the ratio of profile length that is convex over the total profile length, i.e. river profile that is above the base level,

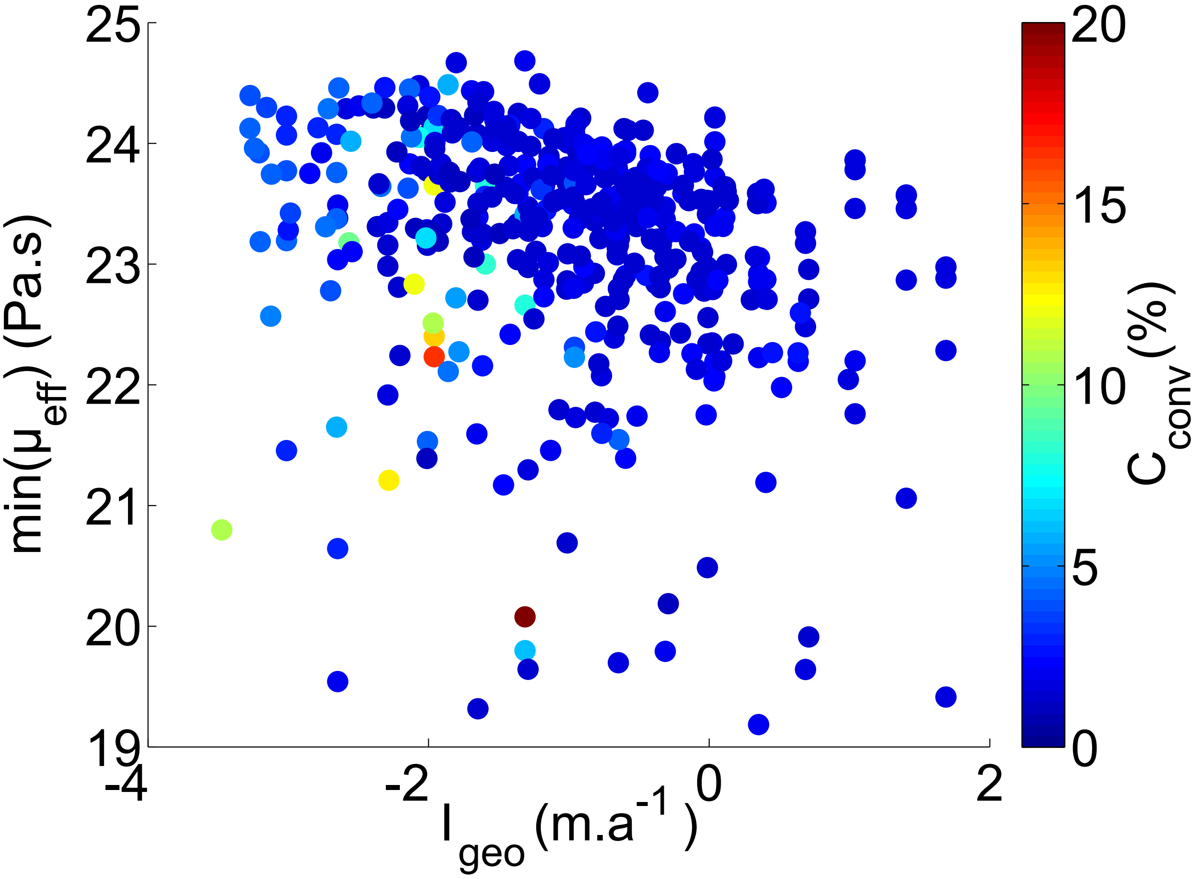

Figure 8.11: Log-log plot of the Distribution of the convexity C_{conv} as a function of the minimum effective viscosity $min(\mu_{\text{eff}})$ obtained in the crustal root below the main divide, and of the geometrical initial characteristic erosion rate I_{geo}.

and retain the temporal maximum as the characteristic value C_{conv}. It records the maximum amplitude of the gravitational spreading during the whole post-orogenic decay (Fig. 8.11). The maximum convexity index ranges between 0 and $\sim 20\%$, but for most of the models convex reaches represent less than 5% of the river profile along the range. Thus, the range of the parameters of our models allow mainly for erosional collapse, with a few models being partly controlled by gravitational collapse. Gravitational collapse, when it occcurs, mainly affects the center of the orogen, which is the hotter part of the crust and the less viscous. It is important to note that in the range of parameters that were tested, no models present river profile that are strongly dominated by gravitational collapse. The distribution of C_{conv} as a function of μ_{eff} and I_{geo} (Fig. 8.11) indicates that: erosional collapse strongly dominates for high erosion rates and high effective viscosity; partial gravitational collapse, when occuring, is associated with low effective viscosity and low erosion rates. These results are consistent with the outcomes of the analytical approach of *Jadamec et al.* (2007).

In addition, good fitting models ($\Phi < 1$) are strongly dominated by erosional collapse. This result suggests that a majority of orogens presents a dominant post-orogenic erosional decay with surface topography isostatically over-compensated by crustal root. However the existence of mountain ranges with active extension and lateral crustal escape like in Tibet (*Armijo et al.*, 1986) or in the French Hercynian belt (*Gibson*, 1991; *Faure et al.*, 2002), demonstrates that gravitational orogenic collapse definitively can control the orogenic decay. Further modelings including plateau like geometry, or evolving boundary conditions during orogenic decay are required to provide a framework to gravitational collapse.

5.1 Comparison With Previous Studies

5.1.1 Erosional Decay or Root Densification?

Here we present the evolution of the mean elevation of the axial part of the range H for the 10 best models, i.e. with the lowest misfit (Fig. 8.12). All the models follow the same trend, which consists of a rapid decrease followed by a progressive slowing of the decrease. This trend is mainly driven by surface erosion and by partial subsequent regional isostatic uplift. From these models mean topography is predicted to be below 2 km after 100 Ma, and below 1.5 km after 300 Ma. This temporal decay of surface elevation is consistent with the temporal distribution of elevation of natural mountain belts. Thus, our modeling approach is in agreement with the distribution of both mountain belt elevations and R values. Moreover this agreement is obtained using realistic values of the model parameters. This suggests that surface erosion driven by river incision following a stream-power law with a stochastic distribution of water discharge, associated with a transition from local to regional isostatic uplift, is a potential mechanism of post-orogenic topographic decay and temporal decrease of R.

The best model solutions converge towards moderate to high values of erosion efficiency k' in the range of realistic values. On the other hand, post-orogenic mountains belts used to invert the model, represent a wide range of climatic or surface lithological conditions, which are not necessary associated with high k' values nor

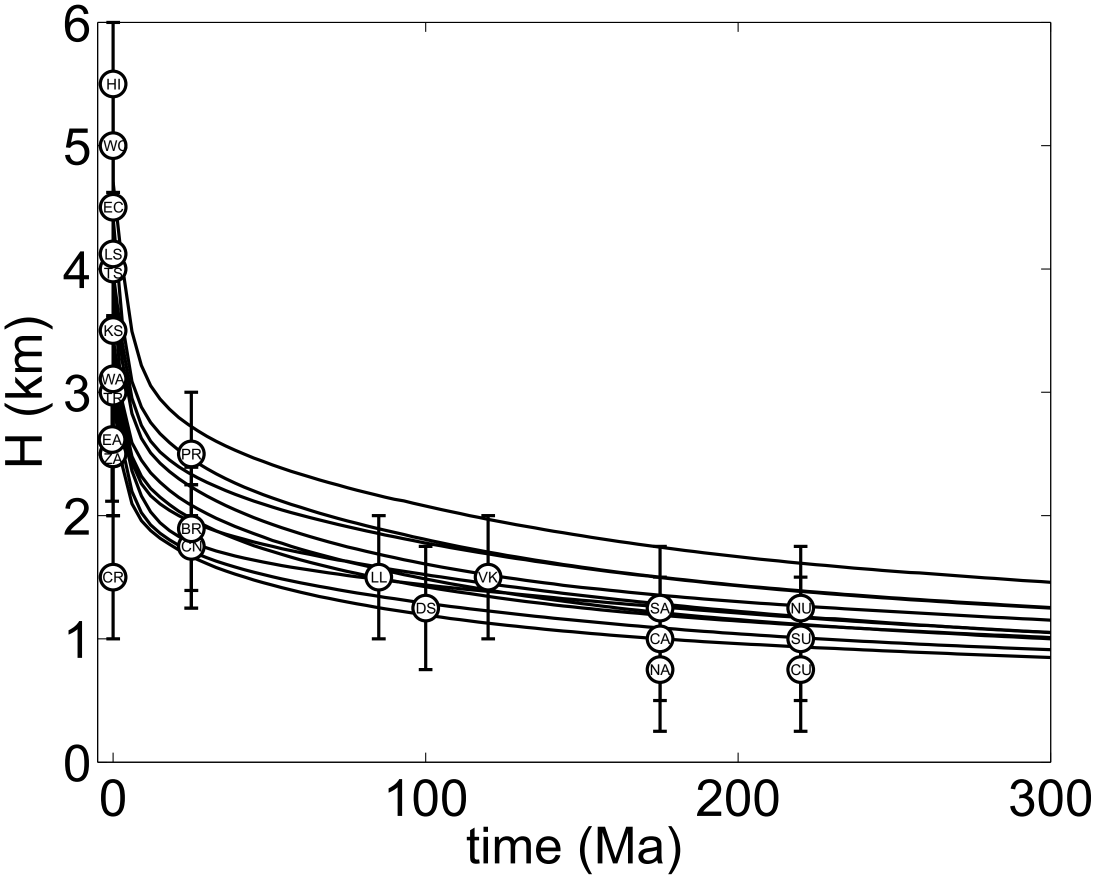

Figure 8.12: Comparison of the time decay of the mean topography at the center of the range H for the 10 best fitting models with respect to the inversion, and with the temporal distribution of elevation for real orogen. *Fischer* (2002) contains reference for these time durations, except for the Dabie Shan (*Reiners et al.*, 2003). HI, Himalaya; AN, Central Andes; LS, Longmen Shan; TS, Tien Shan; KS, Kunlun Shan; WA, Western Alps of Europe; ZA, Southern Alps of New Zealand; TR, Taiwan Range; CR, Carpathians; BR, Brooks Range; PR, Central Pyrenees; CN; Cantabrians Mountains; LL, Lachlan Orogen; DS: Dabie Shan; VK, Verkhoyansk Mountains; SA, Southern Appalachians; CA, Central Appalachians; NA: Northern Appalachians; NU, Northern Urals; CU, Central Urals; SU, Southern Urals.

with discharge distribution parameter $\chi = 1$. This may suggest that our modeling approach could be associated with other mechanisms leading to both a partial decrease of R and surface elevation with time. Compared to previous studies for which post-orogenic evolution of R is related to to a temporal decrease of of density contrast across the Moho (*Fischer*, 2002; *French et al.*, 2009), our approach represents an alternative or a complementary explanation for both R decrease and topographic decay.

Densification of the crustal root, relative to the underlying mantle, by metamorphic reactions should reduce its buoyancy. Two ways of metamorphic reactions can be evoked to explain a decrease of R with time: (1) Metamorphic reactions induced by lithospheric cooling and resulting in an increase of density (*Fischer*, 2002). Increasing the volume fraction of garnet inside the granulite facies of a mafic lower crust, or changing to the eclogite facies, would result in an overall densification of the crustal root. Whether such reactions starting from e.g. granulite facies at quasi-constant pressure and decreasing temperature would increase density is strongly dependent on the availability of fluids (*Hetényi et al.*, 2010). (2) Delayed prograde reactions catalysed by aqueous fluids, such as eclogitisation, could increase crustal root density, with a delay between reaching the pressure-temperature (P-T) conditions of the facies and resulting densification (e.g., *Hetényi et al.*, 2007). The source of fluids can be either from dehydratation reactions or external supply (e.g., *Leech*, 2001). However, both geophysical and field evidence suggests that the densification by eclogitisation occurs during the construction of the orogenic wedges, at least for the Himalayas and Scandinavian Caledonides (*Hetényi et al.*, 2007; *Labrousse et al.*, 2010). The aformentioned time delay between reaching P-T conditions of the eclogite facies and subsequent metamorphic reactions was estimated to be between 7 and 10 Ma for the mafic Himalayan lower crust (*Hetényi et al.*, 2007). This order of magnitude for the delay of eclogitisation does not support a progressive increase of crustal root density during hundreds of million years.

Thus, if metamorphic densification of the crustal root could play a role on the initial buoyancy of mountain range, it is not clear whether or not it could be the main factor controling the temporal decrease of R for most post-orogenic mountain belts. Contrary to surface erosion driven by fluvial incision, crustal root densification requires particular conditions, mostly depending on the availability of fluids, to be effective, and it is still speculative if it could be progressive in time.

5.1.2 Initial Condition: Local or Regional Isostasy?

For practical reasons, we have assumed the initial orogen to be in a state of local isostasy, i.e. the thickness of the crustal root compensates the load associated with the mean elevation of the topography. This represents an end member model, its opposite being a complete regional isostasy, where the topographic load is fully supported by the flexure of the elastic lithosphere. Departures from local isostasy are mainly observed near the border of mountain belts, which indicates that their topography may be partly compensated by regional flexure (*Karner and Watts*, 1983; *Lyon-Caen and Molnar*, 1985; *Royden*, 1993; *Watts et al.*, 1995; *Cattin et al.*, 2001). On the other hand, local isostasy successfully predicts the crustal thickness and gravity anomaly over the central parts of many natural mountain belts (*Woollard*, 1969). This is supported by the distribution of R for active orogens (Fig.8.7), which suggests a state close to local isostasy at the center of the orogens, despite a wide range of values. As we are particularly interested in the evolution of the central part of orogens, not of their borders, the assumption of local isostasy as an initial condition is justified.

5.1.3 Sedimentation and Transport-limited or Detachment-limited

Following *Godard et al.* (2006) river incision is driven by a detachment-limited law and sedimentation is limited to closed basins so that the main rivers flow downhill to the edge of the model. This approach prevents from feedbacks between piedmont sedimentation on the border of the range and the dynamics of fluvial incision. Piedmont sedimentation, by raising the effective base level of rivers bedrock erosion, is expected to decrease the erosion rate and to increase the time scale of topographic decay (*Baldwin et al.*, 2003; *Pelletier*, 2004). It has been proposed to be a governing factor which explains the constancy of topographic characteristics such as height and width of the Appalachians and Urals (*Pelletier*, 2004), and the applanation of the Pyrennees at high elevation (*Babault et al.*, 2005). Moreover *Baldwin et al.* (2003) propose that a transition from detachment- to transport-limited conditions increases by a factor $2-3$ the decay time of post-orogenic topography. Such a transition is expected during topographic decay (*Whipple and Tucker*, 2002), with alluvial cover protecting river bedrock, and thus inhibiting erosion. A transition from detachment- to transport-limited, and the addition of sediment deposition in the adjacent basins would have to be introduced in future modeling to explore their potential effects on orogenic decay. However as a result of our modeling approach, which explains most of post-orogenic evolution using only a detachment-limited formalism coupled with close basins sedimentation, more complexity is not required at first order.

6 Conclusion

This study investigates the long-term post-orogenic evolution of a mountain belt, using a $2D$ thermo-mechanical finite element model (*Hassani et al.*, 1997) which couples surface processes to lithospheric deformation. The model includes: Fluvial incision by shear-stress (*Lavé and Avouac*, 2001) with a stochastic distribution of water discharge and a critical incision threshold (*Baldwin et al.*, 2003; *Lague et al.*, 2005), and hillslopes landsliding (*Lavé*, 2005); Visco-elastic lithospheric deformation coupled to a regional isostatic support of the lithosphere.

In particular we focus on the conditions and model parameters that make it possible to reproduce the temporal decrease of the ratio R of surface elevation to crustal root thickness (*Fischer*, 2002; *French et al.*, 2009). The model parameters are the initial width W and height H of the range, the coefficient of erosion efficiency k', and the radiogenic heat production rate of the crust P_r. Using an arbitrary set of parameter values, we show that this trend is sensitive at first order to erosion efficiency and to the initial geometry of the mountain belt: higher erosion efficiency or initial mountain belt slope leading to a quicker R decrease. Overcompensation of the crustal root being accommodated by focused erosion on the range, and partial subsequent regional uplift.

Sampling the model space with a uniform Monte-Carlo algorithm and using a least absolute value criterion, leads to combinations of model parameters compatible with the data. The inversion confirms the outcomes of the arbitrary model, and highlights the prominent role of surface erosion efficiency on the temporal decrease of R, including the effect of erodibility, climate and mountain belt geometry. On the other hand, crustal viscosity does not exert a strong control on the results. Interestingly, gravitational collapse (e.g., *Rey et al.*, 2001) does not significantly affect the model behavior in the range of parameter values investigated.

In addition, the topographic decay predicted by the 10 best fitting models is consistent with the temporal distribution of post-orogenic elevation. This demonstrates that post-orogenic evolution can be explained by surface erosion following a detachment-limited formalism of river incision with stochastic floods and a transition from local to regional isostasy. Introducing more complexity into the modeling approach is not necessary at first order. Yet our modeling outcomes represent an alternative or a complement to an erosional control by sediment flux and piedmont sedimentation (*Baldwin et al.*, 2003; *Pelletier*, 2004) and to crustal root densification by metamorphism (*Fischer*, 2002). Taking into account metamorphic phase change (*Hetényi et al.*, 2010) in post-orogenic modelings is now required to assess the potential influence of metamorphism on post-orogenic evolution.

Appendix: Integration in Time of the Incision Law

Following the work of *Lague et al.* (2005), we express the details of the integration of the incision law, with the assumption that the river water discharge is stochastic and follows a power-law distribution (e.g., *Turcotte and Greene*, 1993; *Molnar et al.*, 2006).

The downstream variations of the river width w_a is expressed by,

$$w_a = k_a \bar{Q}^{\omega_a} \ , \tag{8.16}$$

where k_a is an amplitude factor, and ω_a a scaling exponent. The local, at-a-station temporal variation of flow width w with discharge is described as a function of w_a,

$$w = w_a \left(\frac{Q}{\bar{Q}} \right)^{\omega_s} \ , \tag{8.17}$$

with Q the instantaneous river water discharge, $\bar{Q}$ the river average water discharge, and ω_s a scaling exponent. Combining last two equations leads to,

$$w = k_w Q_\star^{\omega_s} \bar{Q}^{\omega_a} \ , \tag{8.18}$$

with $Q_\star = Q/\bar{Q}$ the water discharge ratio. Combining last equation with Eq. 8.4 gives,

$$i = k \left(k_w^{-m} Q_\star^{m(1-\omega_s)} \bar{Q}^{m(1-\omega_a)} S^\alpha - \tau_c \right) \ . \tag{8.19}$$

Now we make the assumption that the temporal variability of the at-a-station river water discharge can be expressed through a power law distribution,

$$pdf(Q_\star) = k_{pdf} Q_\star^{-(\chi+2)} dQ_\star \ , \tag{8.20}$$

with χ an exponent and $k_{pdf} = \frac{\chi^{\chi+1}}{\Gamma(\chi+1)}$ a constant that was chosen so that to be consistent with the formalism of *Lague et al.* (2005). Γ is the Gamma function such that if χ is an integer then $\Gamma(\chi+1) = \chi!$. Then we can integrate the instantaneous incision rate to express the long-term incision rate,

$$I = \int_{Q_{c\star}}^{Q_{m\star}} pdf(Q_\star) i(Q_\star) dQ_\star, \tag{8.21}$$

with i the instantaneous incision rate defined in Eq. 8.4. $Q_{c\star}$ is the critical water discharge ratio and is defined such that $i(Q_{star} \leq Q_{c\star}) = 0$, and $Q_{m\star}$ is the maximum water discharge ratio at the timescale considered. Note that a power law distribution for water discharge is an approximation that holds if $Q_{c\star}$ is large, as it does not reproduce the decrease of number of events for discharge below the average discharge. Here we also make the assumption that previous equation can be integrated with the parameters of the incision law independant of the water discharge, and we obtain for $m(1-\omega_s) - (\chi+1) \neq 1$,

$$\begin{aligned} I = kk_{pdf} \Bigg(& k_w^{-m} \bar{Q}^{m(1-\omega_a)} S^\alpha \frac{(Q_{m\star}^{m(1-\omega_s)-(\chi+1)} - Q_{c\star}^{m(1-\omega_s)-(\chi+1)})}{m(1-\omega_s) - (\chi+1)} \\ & - \tau_c \frac{(Q_{m\star}^{-(\chi+1)} - Q_{c\star}^{-(\chi+1)})}{-(\chi+1)} \Bigg) . \end{aligned} \tag{8.22}$$

At large timescale and in most settings $Q_{m\star} \gg Q_{c\star}$, and if $m(1-\omega_s) - (\chi+1) < 1$ (which is true with our model parameters) then any dependency with $Q_{m\star}$ rapidly vanishes in Eq. 8.22, and I converges on a constant whose approximate expression is:

$$\begin{aligned} I = -kk_{pdf} \Bigg(& k_w^{-m} \bar{Q}^{m(1-\omega_a)} S^\alpha \frac{Q_{c\star}^{m(1-\omega_s)-(\chi+1)}}{m(1-\omega_s) - (\chi+1)} \\ & + \tau_c \frac{Q_{c\star}^{-(\chi+1)}}{\chi+1} \Bigg) . \end{aligned} \tag{8.23}$$

In order to simplify previous equation, let's notice that $Q_{c\star}^{m(1-\omega_s)} = k_w w^m \bar{Q}^{-m(1-\omega_a)} S^{-\alpha} \tau_c$, which gives,

$$I = -kk_{pdf} \tau_c Q_{c\star}^{-(\chi+1)} \frac{m(1-\omega_s)}{(\chi+1)(m(1-\omega_s) - (\chi+1))} . \tag{8.24}$$

Using $Q_{c\star}$ and $\bar{Q} = k_Q A^\xi \bar{P}$, where $\bar{P}$ is the average precipitation in the drained area A, in the previous equation leads to,

$$I = \left(\frac{k}{\tau_c'}\right) k_{sto} A^{\gamma'} \bar{P}^{\beta'} S^{\alpha'} , \tag{8.25}$$

with,

$$\begin{aligned}
\tau_c' &= \tau_c^{\frac{\chi}{m(1-\omega_s)}} && (8.26)\\
k_{sto} &= -k_{pdf}\frac{m(1-\omega_s)}{(\chi+1)(m(1-\omega_s)-(\chi+1))}k_w^{\frac{-(\chi+1)}{(1-\omega_s)}}k_Q^{\frac{(\chi+1)(1-\omega_a)}{(1-\omega_s)}} && (8.27)\\
\beta' &= \frac{(\chi+1)(1-\omega_a)}{(1-\omega_s)} && (8.28)\\
\gamma' &= \xi\beta' && (8.29)\\
\alpha' &= \frac{\alpha(\chi+1)}{m(1-\omega_s)} && (8.30)
\end{aligned}$$

Ultimately we can even more simplify previous equation by defining an apparent coefficient of erosion efficiency $k' = k_{sto}k\bar{P}^{\beta'}/\tau_c'$, which leads to,

$$I = k'A^{\gamma'}S^{\alpha'} \ . \tag{8.31}$$

acknowledgments

We thank G. Hetényi for his relevant comments about metamorphism and density and J. Braun for suggesting systematical testing of model parameters. We also thank Riad Hassani and Jean Chéry for providing the finite element code. This study benefits from the computing facilities of Geosciences Montpellier.

General Conclusion, Ongoing Studies and Future Prospects

Conclusion

This thesis presents new assessments of the relations between erosion, erodibility and deformation in orogenic settings. This work has been focused on three main axes including improvement of numerical codes, in-situ acquisition of field data, and numerical modeling.

Building Numerical Tools to Study Erodibility, Erosion and Deformation Several numerical tools were developed during this thesis. A $2D$ plan view landscape evolution models that includes river incision and hillslope landsliding was developed. Resolution issues concerning modeling of relief wavelength were investigated and solved (these issues have also motivated the following paper: *Pelletier*, 2010). Following *Lavé* (2005) integration of $2D$ surface processes in $1D$ was extended to a stochastic distribution of water discharge (*Lague et al.*, 2005). It allows to efficiently couple surface processes and solid Earth deformation into $2D$ numerical models. For that purpose, a new remeshing algorithm called Surface Lagrangian Remeshing (SLR) was developed. It allows to take into account long-term erosion into $2D$ Lagrangian numerical codes based on triangular finite elements, such as ADELI (*Hassani et al.*, 1997). It is a complementary algorithm to Dynamical Lagrangian Remeshing (DLR, *Braun and Sambridge*, 1994) or to other remeshing algorithms dealing with internal deformation of triangular elements. The main features of SLR are its speed, accuracy and its applicability to $2D$ and $3D$ numerical models.

Acquiring Data: Schmidt Hammer Rebound, Erodibility and Effective Properties Schmidt hammer rebound has been used by many studies (e.g., *Duvall et al.*, 2004; *Yanites et al.*, 2010) as a proxy for the control of lithology on erosion. Up to now, except for the pioneering empirical work of *Dubille* (2008), the link between erodibility (K) and Schmidt hammer rebound (R) was not really estimated. First I propose, from the abrasion model of *Sklar and Dietrich* (2001) and the results of empirical studies (*Aydin and Basu*, 2005; *Yagiz*, 2009), that R and K are possibly related either by a power or exponential law, $K \propto R^{-4}$ or $K \propto \exp(-0.11R)$. In this thesis, R was measured for several field settings: Taiwan active orogen, the diagenetic Annot sandstones and St Clement fault zone. Taiwan and Annot experiments reveal that effective properties strongly affect R as well as rock nature and geological history, i.e. mainly diagenesis and metamorphism. A linear model based on effective medium theory (*Hudson*, 1980, 1981) that sums up fracture density into a single parameter is proposed. This model was applied to a fault zone that includes secondary faults, dry and sealed fractures, tested with an unmatched number of R measures (750 measures, 7500 rebounds) and resolution

(25 measures per square meter). The modeled $2D$ image significantly correlates with the observed map of R. This result demonstrates that fracture density can be quantified with a Schmidt hammer, and more importantly that effective elasticity is sensitive to fracture type and to healing. Moreover, compared to classical abrasion experiments (*Sklar and Dietrich*, 2001; *Attal and Lavé*, 2009), R captures the effective properties of rock medium at a scale that is corresponding to erosion processes, in the order of 1 to 30 cm.

Numerical Modeling: Erosion, Rheology and Post-Orogenic Evolution
The new version of ADELI, including SLR and $2D$ surface processes integrated in $1D$, was applied to study post-orogenic evolution of mountain belts. In particular I have focused on the parameters, defining the efficiency of surface erosion and lithospheric rheology, allowing to reproduce a temporal decrease of the ratio of surface elevation on crustal root thickness (R) (*Fischer*, 2002) and a topographic decay, which are both observed. Using realistic model parameters, it appears that a model coupling surface erosion governed by river incision intergrating a stochastic distribution of discharge (*Baldwin et al.*, 2003; *Lague et al.*, 2005) and partial subsequent regional isostatic uplift is consistent with both observations. The time scale of both topographic decay and R decrease is controlled at first order by surface erosion rate, which depends on both the initial geometry of the mountain belt and on the coefficient of erosion efficiency. This highlights the control of climate and erodibility on the perseverance of topography. This modeling approach does not consider potential densification of the crustal root associated with metamorphism during post-orogenic evolution, which is suggested by *Fischer* (2002) to be the dominant mechanism controlling the temporal decrease of R. I suggest that the two approaches are not antagonist but rather complementary. From a numerical prospect, metamorphism phase change (MPC) (*Hetényi et al.*, 2010) was implemented into ADELI in order to decipher the respective preponderance of both mechanisms.

Ongoing Studies and Future Work

Metamorphic Phase Change and Post-Orogenic Evolution

As mentioned in Chapter 8, *Fischer* (2002) proposed that density variation induced by metamorphism is a controlling factor of post-orogenic evolution. In particular, a densification of the crustal root would result in a decrease of buoyancy and of the ratio of surface elevation to crustal root thickness R, as observed. This is an alternative or complementary approach to the one investigated in Chapter 8, where surface erosion partially compensated by regional isostasy leads to a decrease of R. To constrain the relative effects and limits of both approaches, requires to model simultaneously surface erosion, lithospheric mechanical and thermal behaviour, and densification associated with metamorphism. The first approach to take into account metamorphism into finite element modeling, would be to change the density of each element, according to the density of the facies corresponding to the pressure P and temperature T conditions. This would lead to "creation" or "suppresion" of mass where density increases or decreases respectively. Thus it is not consistent with mass conservation. To correct this requires changing the volume of each element inversely to the change of density. Implementation of metamorphic phase change (MPC hereinafter) in the finite element Cast3M was developed initially by *Hetényi et al.* (2010). In the following we present the implementation of MPC into ADELI, and present some preliminary results.

Principle of MPC in FEM

Changing element volumes to respect mass conservation can be performed by different approaches:

- Intuitively, moving the nodes of the elements inward (densification) or outward (decrease of density) is the simplest approach. However, such an implementation is not consistent with mechanical solving in finite element, as it rules out the rheological response of the medium considered and the boundary conditions of the model.

- Imposing a deformation field that would act to reduce (densification) or stretch (decrease of density). Once again this approach is not compatible with taking into account the boundary conditions of the model.

- Imposing a stress field.

This latter approach has been implemented into ADELI, and the associated algorithm is presented in Figure 8.13. We make the assumption that deformation associated with metamorphism is elastic which allows to convert a change of density into a stress field increment through Hooke's law.

Stresses resulting from MPC σ_{MPC} can reach 10^5 Pa (*Hetényi et al.*, 2010), which is equivalent to stress drop during earthquakes (*Scholz*, 1990). This is significant compared to the internal stresses σ_{INT} of most geodynamical systems. Thus it prevents from a direct modification of the stresses, at least in the quasi-static

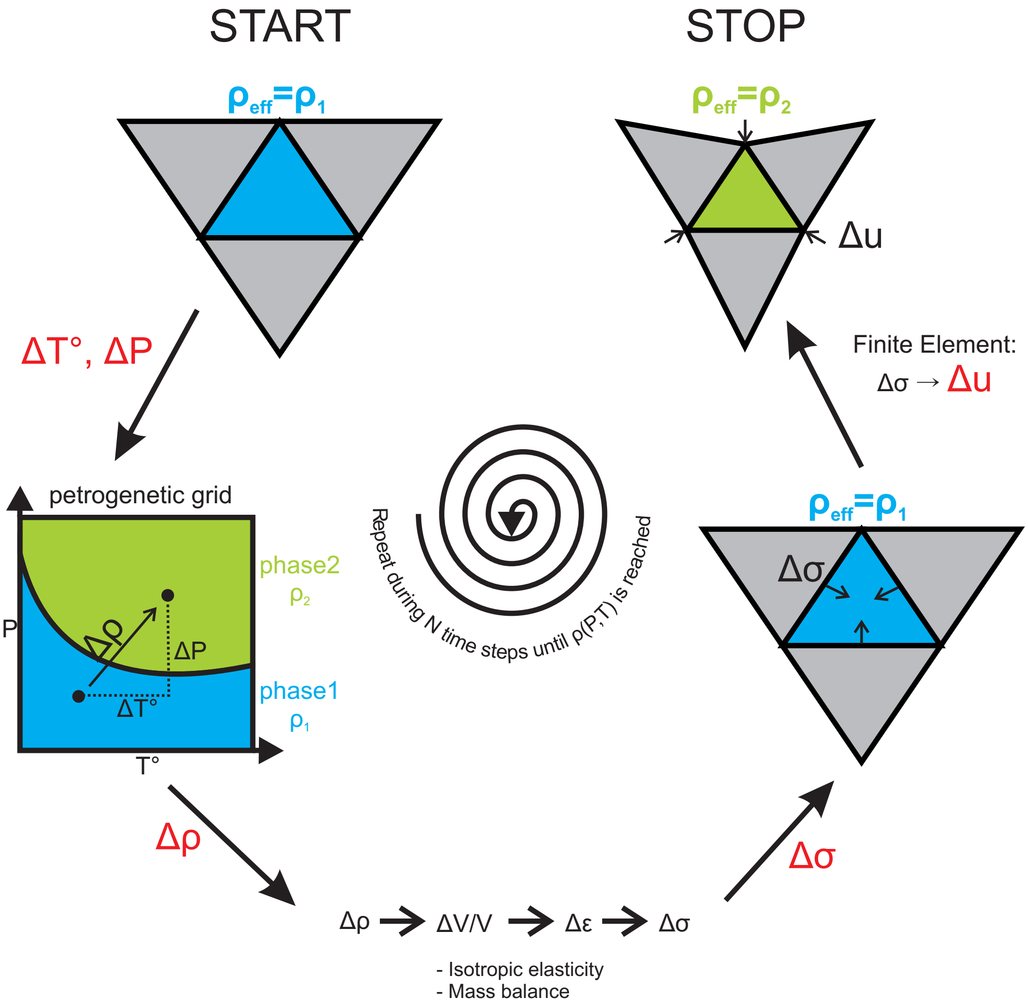

Figure 8.13: The introduction of mineral phase changes into finite element models is a stepwise iterative procedure. The evolving P-T conditions determine the density of the elements through petrogenetic grids. The change in density is translated into volumetric variations, that can be expressed as isotropic strain. In the elastic assumption, these can be converted to stress variations, which provide the feedback to the finite element code. The induced deformation of the mesh converges towards the imposed density (and hence volume) values and verifies conservation of mass.

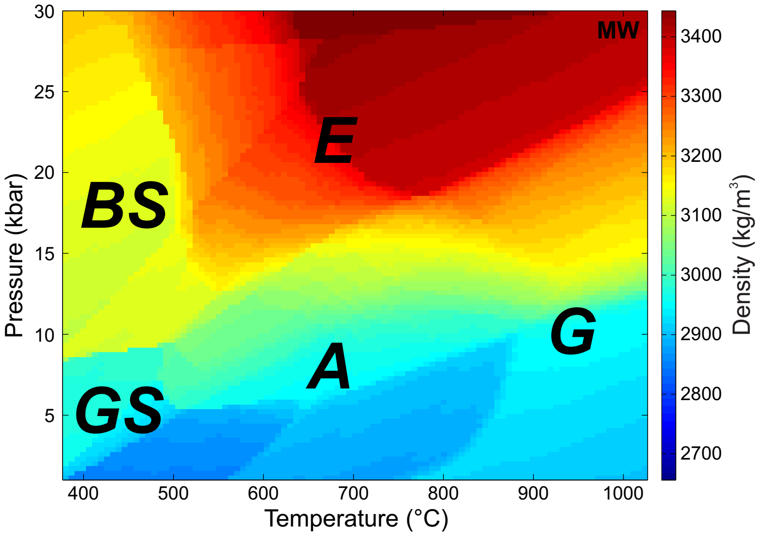

Figure 8.14: Petrogenetic grid for a water-saturated mafic system, representing the continental lower crust. Same exact mineral composition as *Hetényi et al.* (2007), and calculation made with PerpleX (*Connolly*, 2005). The letters denote the main metamorphic facies: GS - greenschist, A - amphibolite, G - granulite, BS - blueschist, E - eclogite. Important variations of density occur as a function of pressure and temperature conditions. This illustratee both the potential control of metamorphic reactions on processes that are buoyancy-dependent, and the possible feedbacks between mechanics, thermics and metamorphism.

approximation used in ADELI. Following *Hetényi et al.* (2010) we rather apply a numerical damping factor F (< 1) to the metamorphic stresses,

$$\sigma_{INT} = \sigma_{INT} + F\sigma_{MPC} \ . \tag{8.32}$$

F can also be interpreted as a kinetic coefficieent associated with density changes. These changes are deduced from variations of P-T conditions with respect to petrogenetic grids (Fig. 8.14) resulting from thermomechanical static solutions (*Connolly*, 2005). It is important to note that petrogenetic solutions are not associated with kinetic coefficients, which prevents from giving a theoretical basis to F. Thus the choice of F is mostly constrained by numerical considerations, such as respecting quasi-static approximation. Nonetheless we acknowledge that F hides a dependency on the kinetics of MPC. Practically, values between 10 and 100 were tested here or by *Hetényi et al.* (2010).

Application to Post-Orogenic Evolution

In a first attempt to illustrate the potental effect of metamorphism, we have run 3 post-orogenic models (Fig. 8.15) similar to the one presented in Chapter 8, except that density in the lower crust is allowed to vary with MPC according to the petrogenetic grid presented in Figure 8.14. Contrary to retrograde reactions, prograde reactions lead to a densification of the crustal root and to a decrease of its buoyancy. Consequently, the thickness of the crustal root is greater for prograde

A) PROGRADE AND RETROGRADE

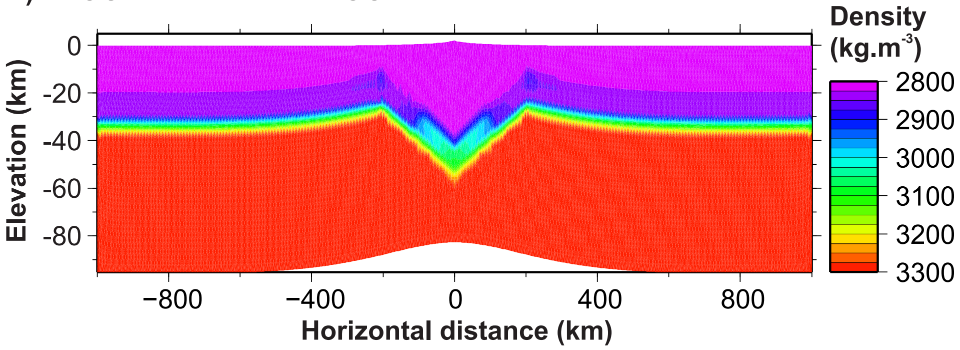

B) RETROGRADE ONLY (Δρ <0)

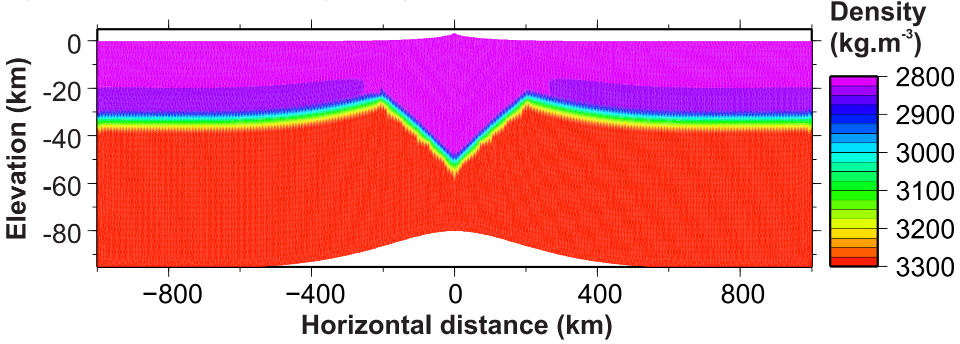

C) PROGRADE ONLY (Δρ >0)

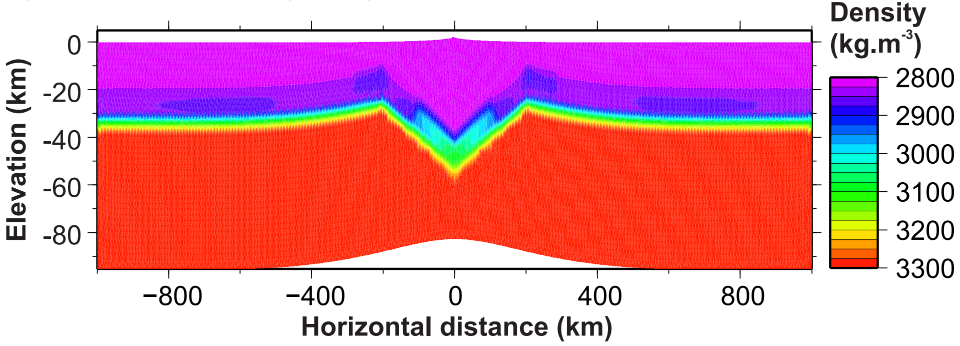

Figure 8.15: Density of post-orogenic models after 150 Ma: (A) with prograde and retrograde reactions, (B) retrograde only and (C) prograde only. The initial model is made up of initial three layers: upper crust (quartz, 2.8 kg.m^{-3}), lower crust (diabase, 2.9 kg.m^{-3}), mantle (olivine, 3.3 kg.m^{-3}). The rheology is visco-elastic, and the model is submited to erosion in surface and to isostasy at the base of the model (Winkler condition).

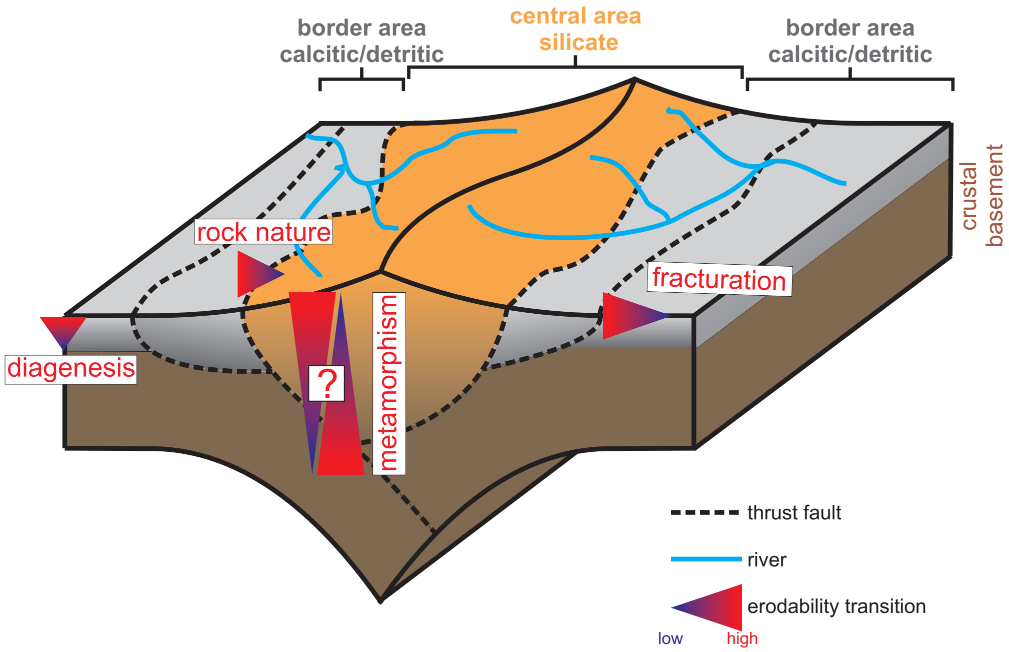

Figure 8.16: Schematic image of the main processes affecting rock erodibility in orogenic and post-orogenic settings. Here we assume that the axial zone or central area of the mountain belt is silicate dominated, and the foothills or border areas are calcitic or detritic dominated. Erodibility varies spatially with the nature of surface rocks: calcitic or detritic rock being generally more erodible than granite or gneiss. Diagenesis decreases erodibility by increasing its density, decreasing its porosity, and by cimenting inter-grains pore or fractures. The effect of metamorphism on erodibility is not direct, as on the one hand it increases rock density, but on the other hand it creates lineation or foliation. Faults and fractures weaken the rock and decrease erodibility with respect to abrasion and favor erosion by plucking (*Molnar et al.*, 2007).

than retrograde reactions, while summit elevation is higher in the retrograde case. Thus prograde metamorphism is a potential factor that could explain decrease of the ratio of surface elevation to crustal root thickness. However further investigations are now required to validate these preliminary results.

Spatio-Temporal Variation of Erodibility and Orogeny

Willett (1999) proposed that a spatial gradient of precipitation, such as the one obtained by orographic precipitation, control orogeny by forcing internal rocks to advect where erosion is the more intense. In rivers dominated by shear-stress incision, erodibility is as well as precipitation a first-order controling factor of erosion efficiency. Moreover erodibility is documented to be a function of rock type (*Sklar and Dietrich*, 2001; *Attal and Lavé*, 2009) which varies both with space and time in most mountain belts (e.g., Himalaya, Pyrenees, European Alps, Andes, Taiwan, Sierra Nevada), deformation (Chapter 6), diagenesis and metamorphism (Fig. 8.16). In particular the foothills of most mountain belts (e.g., Siwaliks) are commonly more erodible than the inner part (e.g., Higher Himalaya). I suggest that spatial and temporal gradient of erodibility can control the amplitude and location of topography

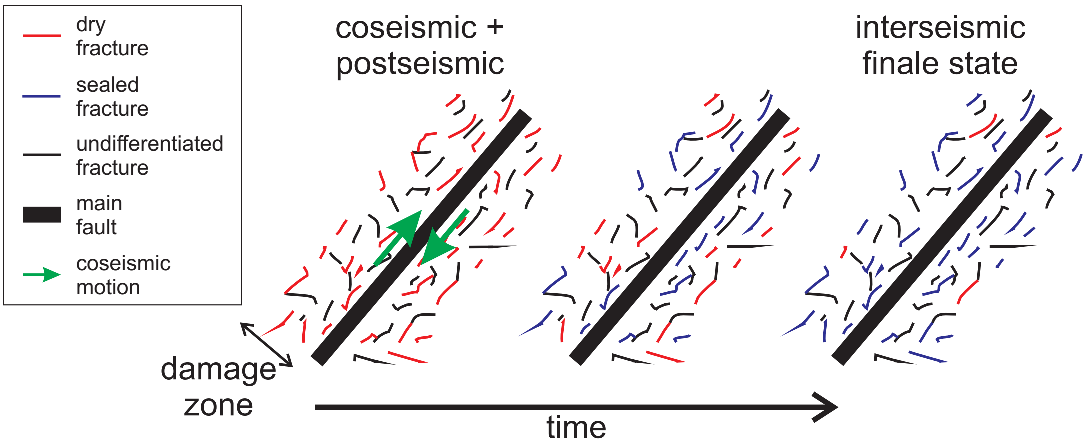

Figure 8.17: Schematic image presenting the distribution of fractures during the seismic cycle of a strike-slip fault.

in mountain belts.

However to better understand the link between erodibility, erosion and rock advection, it is required to define a model of channel width not only as a function of drainage area but also of local slope (*Attal et al.*, 2008). How rivers geometry adjusts to spatial or temporal changes in erodibility is likely to be a controling factor of the effects of erodibility on orogeny.

Cracking and Healing the Damage Zone of Major Faults and Interseismic Stress Build-up: a Numerical Approach

An important result of Chapter 6 is that the negative contribution to stiffness of sealed fractures is less than open fractures. We thus suggested that this could have important implication on the interseismic stress build-up of major faults.

As illustrated by Figure 8.17, faults and fractures are created during the coseismic phase of the seismic cycle, while sealed-fractures result from sealing (or healing) that occurs during the interseismic phase (*e.g.*, *Sibson*, 1992; *Gratier et al.*, 1994; *Renard et al.*, 2000). Fracture sealing is the consequence of external material precipitation or deposition in the related veins (*Gratier et al.*, 1994; *Evans and Chester*, 1995; *Renard et al.*, 2000). It is likely to occur after previous pressure solution of the same material in stylolites (*Gratier et al.*, 1994; *Renard et al.*, 2000). According to experiments, the time scale of such fracture sealing, controlled by the the kinetics of pressure solution and associated with deposition processes, is on the order of several tens of years to several millions years, and are strongly dependent on temperature, fluid circulation, and rock texture (*Rutter and Elliott*, 1976; *Hickman and Evans*, 1991; *Gratier*, 1993; *Renard et al.*, 2000). Fractures, such as sealed-fractures, are located in the damage zone of main faults. We suggest that changing the effective elasticity around a major fault, by creation of fracture during the coseismic and postseismic phase and by sealing of these fractures during the interseismic phase of a seismic cycle, may have geodynamical effects. In particular it could lead to variation of stiffness in the damage zone and consequently to variation of interseismic stress

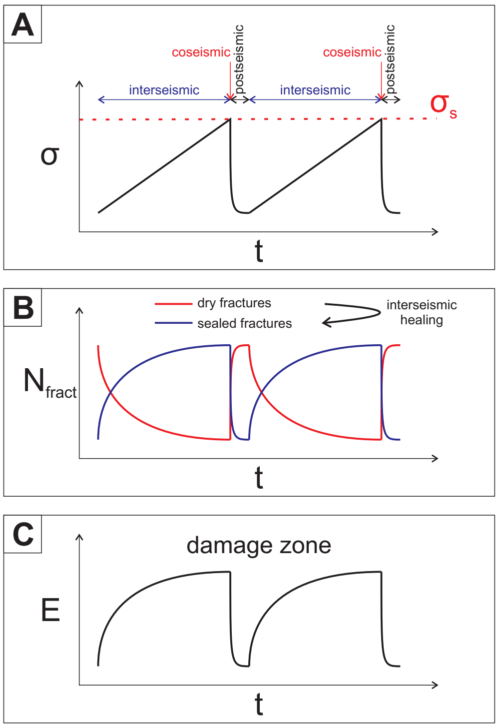

Figure 8.18: Schematic representation of (A) a classical linear model of stress variation during the seismic cycle tangentially to the main fault plane, and (B) of the number of dry (open) and sealed (healed) fractures and of (C) corresponding Young's modulus in the damage zone surrouding the main strike-slip fault. Note that the linear model of stress build-up was defined *independently* of fractures present in the damage zone.

build-up on the main fault.

Classical models of seismic cycle (Fig. 8.18A) consider that the interseismic stress build-up is a linear function of time since the last coseismic event. *Gratier et al.* (2003) proposed that healing rate decreases exponentially with time. From the conclusion of Chapter 6 it is reasonable to assume that healed fractures have a negligible effect on the effective stiffness compared to open or dry fractures, which have a negative contribution that is directly proportional to their spatial density (*Hudson*, 1980, 1981). In a fault zone, fractures are localised in the damage zone. Thus Young's modulus of the damage zone is likely to vary during the interseismic phase of a seismic cycle. Such variation of Young's modulus is expected to affect the interseismic stress build up of the main fault.

When considering a strike-slip fault, the influence of fracture opening and healing on interseismic stress build-up is likely to be dependent on: (1) the initial fracture density of dry fracturex which sets the contrast of Young's modulus between the damage zone E_2 and the host rock E_1 (with $E_1 > E_2$); (2) the kinetics of the exponential healing rate k_{1-2} which sets the kinetics of Young's modulus recovery from E_2 to E_1 in the damage zone; (3) the width of the damage zone W_2 and the width of the intact elastic plate; (4) The elastic thickness of the tectonic plate D and its length L: (5) the velocity V across the fault zone. Following the work of *Jolivet et al.* (2008) I intend to implement this set-up in ADELI 3D (Fig.8.19).

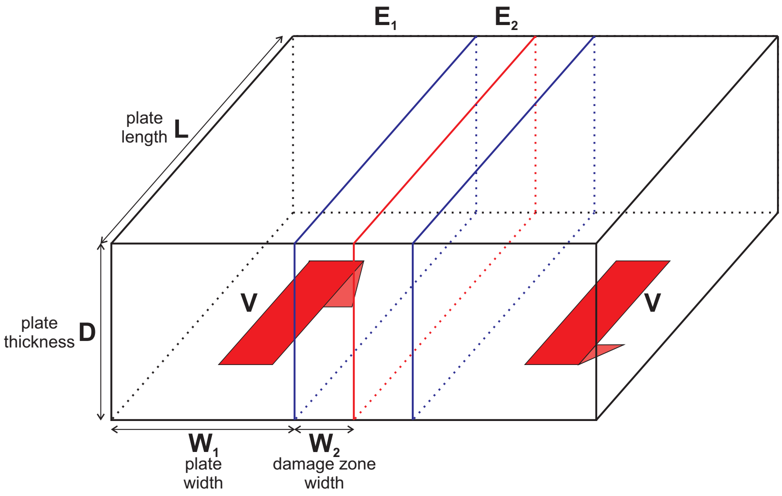

Figure 8.19: Model setup designed for ADELI to take into account the effect of fracture in the damage zone on the elasticity of the medium surrounding the main strike-slip fault. This setup is close to the one used by *Jolivet et al.* (2008).

Bibliography

Allen, P. (2008), From landscapes into geological history, *Nature*, *451*(7176), 274–276.

Armijo, R., P. Tapponnier, J. Mercier, and H. Tong-Lin (1986), Quaternary extension in southern Tibet: Field observations and tectonic implications, *Journal of Geophysical Research*, *91*(B14), 13,803.

Arndt, R. (1981), Cavitation in fluid machinery and hydraulic structures, *Annual Review of Fluid Mechanics*, *13*(1), 273–326.

Arthaud, F., and M. Mattauer (1969), Sur les décrochements NE—SW senestres contemporains des plis pyrénéens du Languedoc, *CR somm. Soc. géol. Fr*, *8*, 290–291.

Attal, M., and J. Lavé (2006), Changes of bedload characteristics along the Marsyandi River (central Nepal): Implications for understanding hillslope sediment supply, sediment load evolution along fluvial networks, and denudation in active orogenic belts, *GSA Special Papers*, *398*, 143.

Attal, M., and J. Lavé (2009), Pebble abrasion during fluvial transport: Experimental results and implications for the evolution of the sediment load along rivers, *Journal of Geophysical Research*, *114*(F4), F04,023.

Attal, M., G. Tucker, A. Whittaker, P. Cowie, and G. Roberts (2008), Modeling fluvial incision and transient landscape evolution: Influence of dynamic channel adjustment, *Journal of Geophysical Research*, *113*(F3), F03,013.

Auzende, J., J. Bonnin, and J. Olivet (1973), The origin of the western Mediterranean basin, *129*, 607–620.

Avouac, J., and E. Burov (1996), Erosion as a driving mechanism of intracontinental mountain growth, *Journal of Geophysical Research*, *101*(B8), 17,747–17,769.

Aydin, A. (2009), ISRM Suggested method for determination of the Schmidt hammer rebound hardness: Revised version, *International Journal of Rock Mechanics and Mining Sciences*, *46*(3), 627–634.

Aydin, A., and A. Basu (2005), The Schmidt hammer in rock material characterization, *Engineering geology*, *81*(1), 1–14.

Babault, J., S. Bonnet, A. Crave, and J. Van Den Driessche (2005), Influence of piedmont sedimentation on erosion dynamics of an uplifting landscape: An experimental approach, *Geology*, *33*(4), 301.

Baldwin, J., K. Whipple, and G. Tucker (2003), Implications of the shear stress river incision model for the timescale of postorogenic decay of topography, *Journal of Geophysical Research*, *108*(B3), 2158.

Basu, A., and A. Aydin (2004), A method for normalization of Schmidt hammer rebound values, *International journal of rock mechanics and mining sciences*, *41*(7), 1211–1214.

Beaumont, C., P. Fullsack, and J. Hamilton (1992), Erosional control of active compressional orogens, *Thrust tectonics*, *99*, 1–18.

Beaumont, C., R. Jamieson, M. Nguyen, and B. Lee (2001), Himalayan tectonics explained by extrusion of a low-viscosity crustal channel coupled to focused surface denudation, *Nature*, *414*(6865), 738–742.

Belytschko, T., and T. Black (1999), Elastic crack growth in finite elements with minimal remeshing, *International Journal for Numerical Methods in Engineering*, *45*(5), 601–620.

Benedicto, A. (1996), Modèles tectono-sédimentaires de bassins en extension et style structural de la marge passive du Golfe du Lion (SE France), *Doctorat, Universitè de Montpellier*, *2*, 242.

Beyssac, O., M. Simoes, J. Avouac, K. Farley, Y. Chen, Y. Chan, and B. Goffé (2007), Late Cenozoic metamorphic evolution and exhumation of Taiwan, *Tectonics*, *26*(6).

Bieniawski, Z. (1967), Mechanism of brittle fracture of rock:: Part I–theory of the fracture process, in *International Journal of Rock Mechanics and Mining Sciences & Geomechanics Abstracts*, vol. 4, pp. 395–404, Elsevier.

Bieniawski, Z. (1993), Classification of rock masses for engineering: the RMR system and future trends, *Comprehensive rock engineering*, *3*, 553–573.

Bigot-Cormier, F., M. Sosson, G. Poupeau, J. Stephan, and E. Labrin (2006), The denudation history of the Argentera Alpine External Crystalline Massif (western Alps, France-Italy): an overview from the analysis of fission tracks in apatites and zircons, *Geodyn. Acta*, *19*, 455–473.

Bitter, J. (1963), A study of erosion phenomena, *Wear*, *6*(1), 5–21.

Bonnet, E., O. Bour, N. Odling, P. Davy, I. Main, P. Cowie, and B. Berkowitz (2001), Scaling of fracture systems in geological media, *Reviews of Geophysics*, *39*(3), 347–383.

Bookhagen, B., R. Thiede, and M. Strecker (2005a), Late Quaternary intensified monsoon phases control landscape evolution in the northwest Himalaya, *Geology*, *33*(2), 149.

Bookhagen, B., R. Thiede, and M. Strecker (2005b), Abnormal monsoon years and their control on erosion and sediment flux in the high, arid northwest Himalaya, *Earth and Planetary Science Letters*, *231*(1-2), 131–146.

Brady, R., M. Ducea, S. Kidder, and J. Saleeby (2006), The distribution of radiogenic heat production as a function of depth in the Sierra Nevada Batholith, California, *Lithos*, *86*(3-4), 229–244.

Braun, J., and X. Robert (2005), Constraints on the rate of post-orogenic erosional decay from low-temperature thermochronological data: application to the Dabie Shan, China, *Earth Surface Processes and Landforms*, *30*(9), 1203–1225.

Braun, J., and M. Sambridge (1994), Dynamical Lagrangian Remeshing (DLR): a new algorithm for solving large strain deformation problems and its application to fault-propagation folding, *Earth and Planetary Science Letters*, *124*(1-4), 211–220.

Braun, J., and M. Sambridge (1997), Modelling landscape evolution on geological time scales: a new method based on irregular spatial discretization, *Basin Research*, *9*(1), 27–52.

Braun, J., C. Thieulot, P. Fullsack, M. DeKool, C. Beaumont, and R. Huismans (2008), DOUAR: A new three-dimensional creeping flow numerical model for the solution of geological problems, *Physics of the Earth and Planetary Interiors*, *171*(1-4), 76–91.

Bristow, J. (1960), Microcracks, and the static and dynamic elastic constants of annealed and heavily cold-worked metals, *British Journal of Applied Physics*, *11*, 81.

Brozovic, N., D. Burbank, and A. Meigs (1997), Climatic limits on landscape development in the northwestern Himalaya, *Science*, *276*(5312), 571.

Bryan, R. (2000), Soil erodibility and processes of water erosion on hillslope, *Geomorphology*, *32*(3-4), 385–415.

Burbank, D. (2002), Rates of erosion and their implications for exhumation, *Mineralogical Magazine*, *66*(1), 25.

Burbank, D., J. Leland, E. Fielding, R. Anderson, N. Brozovic, M. Reid, and C. Duncan (1996), Bedrock incision, rock uplift and threshold hillslopes in the northwestern Himalayas, *Nature*, *379*(6565), 505–510.

Burbank, D., A. Blythe, J. Putkonen, B. Pratt-Sitaula, E. Gabet, M. Oskin, A. Barros, and T. Ojha (2003), Decoupling of erosion and precipitation in the Himalayas, *Nature*, *426*(6967), 652–655.

Bürgmann, R., D. Pollard, and S. Martel (1994), Slip distributions on faults: effects of stress gradients, inelastic deformation, heterogeneous host-rock stiffness, and fault interaction, *Journal of Structural Geology*, *16*(12), 1675–1690.

Byrne, T., and C. Liu (2002), Introduction to the geology and geophysics of Taiwan, *Geology and Geophysics of an Arc-Continent Collision, Taiwan.*

Caine, J., J. Evans, and C. Forster (1996), Fault zone architecture and permeability structure, *Geology*, *24*(11), 1025.

Carter, N., and M. Tsenn (1987), Flow properties of continental lithosphere, *Tectonophysics*, *136*(1-2), 27–63.

Cattin, R., G. Martelet, P. Henry, J. Avouac, M. Diament, and T. Shakya (2001), Gravity anomalies, crustal structure and thermo-mechanical support of the Himalaya of Central Nepal, *Geophysical Journal International*, *147*(2), 381–392.

Chatanantavet, P., and G. Parker (2009), Physically based modeling of bedrock incision by abrasion, plucking, and macroabrasion, *Journal of Geophysical Research*, *114*(F4), F04,018.

Clift, P., K. Hodges, D. Heslop, R. Hannigan, H. Van Long, and G. Calves (2008), Correlation of Himalayan exhumation rates and Asian monsoon intensity, *Nature Geoscience*, *1*(12), 875–880.

Connolly, J. (2005), Computation of phase equilibria by linear programming: A tool for geodynamic modeling and its application to subduction zone decarbonation, *Earth and Planetary Science Letters*, *236*(1-2), 524–541.

Corsini, M., G. Ruffet, and R. Caby (2004), Alpine and late-hercynian geochronological constraints in the Argentera Massif (Western Alps), *Eclogae Geologicae Helvetiae*, *97*(1), 3–15.

Cowie, P., and C. Scholz (1992), Physical explanation for the displacement-length relationship of faults using a post-yield fracture mechanics model, *Journal of Structural Geology*, *14*(10), 1133–1148.

Cruse, R., and W. Larson (1977), Effect of soil shear strength on soil detachment due to raindrop impact, *Soil Science Society of America Journal*, *41*(4), 777.

Culling, W. (1960), Analytical theory of erosion, *The Journal of Geology*, *68*(3), 336–344.

Culling, W. (1963), Soil creep and the development of hillside slopes, *The Journal of Geology*, *71*(2), 127–161.

Cundall, P., and M. Board (1988), A microcomputer program for modeling large-strain plasticity problems, *Numerical methods in geomechanics*, *6*, 2101–2108.

Dadson, S., et al. (2003), Links between erosion, runoff variability and seismicity in the Taiwan orogen, *Nature*, *426*(6967), 648–651.

Dadson, S., et al. (2004), Earthquake-triggered increase in sediment delivery from an active mountain belt, *Geology*, *32*(8), 733.

Dahlen, F., and J. Suppe (1988), Mechanics, growth, and erosion of mountain belts, *Processes in continental lithospheric deformation: Geological Society of America Special Paper*, *218*, 161–178.

Dearman, W., F. Baynes, and T. Irfan (1978), Engineering grading of weathered granite, *Engineering Geology*, *12*, 345–374.

DeLong, S., J. Pelletier, and L. Arnold (2007), Bedrock landscape development modeling: Calibration using field study, geochronology, and digital elevation model analysis, *Geological Society of America Bulletin*, *119*(1-2), 157.

Dietrich, W., S. Reneau, and C. Wilson (1987), Overview: zero-order basins and problems of drainage density, sediment transport and hillslope morphology= Aperçu: bassins d'ordre zéro et problèmes de densité de drainage. Transport des sédiments et morphologie des pentes de collines, *IAHS-AISH publication*, *165*, 27–37.

Dosseto, A., P. Hesse, K. Maher, K. Fryirs, and S. Turner (2010), Climatic and vegetation control on sediment dynamics during the last glacial cycle, *Geology*, *38*(5), 395.

Du Fornel, E., P. Joseph, G. Desaubliaux, R. Eschard, F. Guillocheau, O. Lerat, C. Muller, C. Ravenne, and K. Sztrakos (2004), The southern Grès d'Annot outcrops (French Alps): an attempt at regional correlation, *Geological Society London Special Publications*, *221*(1), 137.

Dubille, M. (2008), Transport solide et abrasion dans les rivières à fond rocheux. De la mesure au modèle sur un exemple himalayen., *Thèse de Doctorat, Université Joseph FOurier, Grenoble.*

Dutton, C. (1882), Tertiary history of the Grand Canyon district: US Geol, *Survey Mon*, *2*(284), 1885.

Duvall, A., E. Kirby, and D. Burbank (2004), Tectonic and lithologic controls on bedrock channel profiles and processes in coastal California, *Journal of Geophysical Research*, *109*(F03002), 18.

Ekern, P. (1950), Raindrop impact as the force initiating soil erosion, in *Soil Science Society of America Proceedings*, vol. 15, pp. 7–10.

Engel, P., and F. Ling (1978), Impact wear of materials, *Journal of Applied Mechanics*, *45*, 458.

England, P., and P. Molnar (1990), Surface uplift, uplift of rocks, and exhumation of rocks, *Geology*, *18*(12), 1173.

Etchecopar, A., G. Vasseur, and M. Daignieres (1981), An inverse problem in microtectonics for the determination of stress tensors from fault striation analysis, *Journal of Structural Geology*, *3*(1), 51–65.

Evans, J., and F. Chester (1995), Fluid-rock interaction in faults of the San Andreas system: Inferences from San Gabriel fault rock geochemistry and microstructures, *Journal of Geophysical Research*, *100*(B7), 13,007.

Faure, M., P. Monié, C. Pin, H. Maluski, and C. Leloix (2002), Late Visean thermal event in the northern part of the French Massif Central: new 40 Ar/39 Ar and Rb-Sr isotopic constraints on the Hercynian syn-orogenic extension, *International Journal of Earth Sciences*, *91*(1), 53–75.

Fischer, K. (2002), Waning buoyancy in the crustal roots of old mountains, *Nature*, *417*(6892), 933–936.

Foufoula-Georgiou, E., V. Ganti, and W. Dietrich (2010), A non-local theory of sediment transport on hillslopes, *Journal of Geophysical Research*, *115*(F0), F00A16.

Freeman, T. (1991), Calculating catchment area with divergent flow based on a regular grid, *Computers & Geosciences*, *17*(3), 413–422.

French, S., K. Fischer, E. Syracuse, and M. Wysession (2009), Crustal structure beneath the Florida to Edmonton broadband seismometer array, *Geophysical Research Letters*, *36*(L0), 8309.

Fry, N. (1989), Short Paper: Kinematics of the Alpine arc, *Journal of the Geological Society*, *146*(6), 891.

Fuller, C., S. Willett, D. Fisher, and C. Lu (2006), A thermomechanical wedge model of Taiwan constrained by fission-track thermochronometry, *Tectonophysics*, *425*(1-4), 1–24.

Fullsack, P. (1995), An arbitrary Lagrangian-Eulerian formulation for creeping flows and its application in tectonic models, *Geophysical Journal International*, *120*(1), 1–23.

Furukawa, Y. (1995), Vertical distribution of heat generation in the Nissho granitic pluton, Hokkaido, Japan, *Geophysical Research Letters*, *22*(6), 711–714.

Furukawa, Y., and H. Shinjoe (1997), Distribution of radiogenic heat generation in the arc's crust of the Hokkaido island, Japan, *Geophysical Research Letters*, *24*(10), 1279–1282.

Gabet, E., D. Burbank, J. Putkonen, B. Pratt-Sitaula, and T. Ojha (2004a), Rainfall thresholds for landsliding in the Himalayas of Nepal, *Geomorphology*, *63*(3-4), 131–143.

Gabet, E., B. Pratt-Sitaula, and D. Burbank (2004b), Climatic controls on hillslope angle and relief in the Himalayas, *Geology*, *32*(7), 629.

Gabet, E., D. Burbank, B. Pratt-Sitaula, J. Putkonen, and B. Bookhagen (2008), Modern erosion rates in the High Himalayas of Nepal, *Earth and Planetary Science Letters*, *267*(3-4), 482–494.

Garcia, D., C. Ravenne, B. Maréchal, and J. Moutte (2004), Geochemical variability induced by entrainment sorting: quantified signals for provenance analysis, *Sedimentary Geology*, *171*(1-4), 113–128.

Gasparini, N., K. Whipple, and R. Bras (2007), Predictions of steady state and transient landscape morphology using sediment-flux-dependent river incision models, *Journal of Geophysical Research*, *112*(F3), F03S09.

Gershenfeld, N. (1999), *The nature of mathematical modeling*, Cambridge University Press.

Gerya, T. (2009), *Introduction to numerical geodynamic modelling*, Cambridge University Press.

Ghose, A. (1986), Empirical strength indices of Indian coals-an investigation, in *The 27th US Symposium on Rock Mechanics (USRMS)*.

Gibson, R. (1991), Hercynian low-pressure-high-temperature regional metamorphism and subhorizontal foliation development in the Canigou massif, Pyrenees, France–Evidence for crustal extension, *Geology*, *19*(4), 380.

Gilbert, G. (1877), Report on the geology of the Henry Mountains: US Geog. and Geol, *Survey, Rocky Moutnain Region, 160*.

Godard, V., J. Lave, and R. Cattin (2006), Numerical modelling of erosion processes in the Himalayas of Nepal: effects of spatial variations of rock strength and precipitation, *Geological Society London Special Publications*, *253*(1), 341.

Godard, V., J. Lavé, J. Carcaillet, R. Cattin, D. Bourlès, and J. Zhu (2009), Spatial distribution of denudation in Eastern Tibet and regressive erosion of plateau margins, *Tectonophysics*.

Godard, V., J. Lavé, J. Carcaillet, R. Cattin, D. Bourlès, and J. Zhu (2010), Spatial distribution of denudation in Eastern Tibet and regressive erosion of plateau margins, *Tectonophysics*.

Goddéris, Y. (2010), Earth science: Mountains without erosion, *Nature*, *465*(7295), 169–171.

Goode, J., and E. Wohl (2010), Substrate controls on the longitudinal profile of bedrock channels: Implications for reach-scale roughness, *J. Geophys. Res.*

Goudie, A. (2006), The Schmidt hammer in geomorphological research, *Progress in physical geography*, *30*(6), 703.

Gratier, J. (1993), Experimental pressure solution of halite by an indenter technique, *Geophysical Research Letters*, *20*(15), 1647–1650.

Gratier, J., T. Chen, and R. Hellmann (1994), Pressure solution as a mechanism for crack sealing around faults, *US Geological Survey Open-File Report*, pp. 94–228.

Gratier, J., P. Favreau, and F. Renard (2003), Modeling fluid transfer along California faults when integrating pressure solution crack sealing and compaction processes, *Journal of Geophysical Research*, *108*(B2), 2104.

Grechka, V., and M. Kachanov (2006a), Effective elasticity of fractured rocks: A snapshot of the work in progress, *Geophysics*, *71*, W45.

Grechka, V., and M. Kachanov (2006b), Effective elasticity of rocks with closely spaced and intersecting cracks, *Geophysics*, *71*, D85.

Grechka, V., I. Vasconcelos, and M. Kachanov (2006), The influence of crack shape on the effective elasticity of fractured rocks, *Geophysics*, *71*, D153.

Grujic, D., I. Coutand, B. Bookhagen, S. Bonnet, A. Blythe, and C. Duncan (2006), Climatic forcing of erosion, landscape, and tectonics in the Bhutan Himalayas, *Geology*, *34* (10), 801.

Hack, J. (1957), Studies of longitudinal stream profiles in Virginia and Maryland, *United States Geological Survey Professional Paper*, *292*, 45–97.

Hancock, G., R. Anderson, and K. Whipple (1998), Beyond power: Bedrock River incision process and form, *Geophysical monograph*, *107*, 35–60.

Haramy, K., and M. DeMarco (1985), Use of the Schmidt hammer for rock and coal testing, in *The 26th US Symposium on Rock Mechanics (USRMS)*.

Hassani, R., D. Jongmans, and J. Chéry (1997), Study of plate deformation and stress in subduction processes using two-dimensional numerical models, *Journal of Geophysical Research*, *102* (B8), 17,951–17,965.

Heimsath, A., W. Dietrich, K. Nishiizumi, and R. Finkel (1997), The soil production function and landscape equilibrium, *Nature*, *388* (6640), 358–361.

Heimsath, A., J. Chappell, N. Spooner, and D. Questiaux (2002), Creeping soil, *Geology*, *30* (2), 111.

Herman, F., and J. Braun (2008), Evolution of the glacial landscape of the Southern Alps of New Zealand: Insights from a glacial erosion model, *Journal of Geophysical Research*, *113* (F2), F02,009.

Hetényi, G., R. Cattin, F. Brunet, L. Bollinger, J. Vergne, J. Nábelek, and M. Diament (2007), Density distribution of the India plate beneath the Tibetan plateau: Geophysical and petrological constraints on the kinetics of lower-crustal eclogitization, *Earth and Planetary Science Letters*, *264* (1-2), 226–244.

Hetényi, G., R. Cattin, and J. Vergne (2010), *Geodynamics of Tibet and the Himalayas: Geophysical advances from imaging and modelling*, LAP Lambert Acad. Publ.

Hickman, S., and B. Evans (1991), Experimental pressure solution in halite: the effect of grain/interphase boundary structure, *Journal of the Geological Society*, *148* (3), 549.

Hilley, G., and M. Strecker (2004), Steady state erosion of critical Coulomb wedges with applications to Taiwan and the Himalaya, *J. Geophys. Res*, *109*, B01,411.

Ho, C. (1986), A synthesis of the geologic evolution of Taiwan, *Tectonophysics*, *125* (1-3), 1–16.

Horton, R. (1932), Drainage basin characteristics, *Transactions of the American Geophysical Union*, *13*, 350–361.

Horton, R. (1945), Erosional development of streams and their drainage basins; hydrophysical approach to quantitative morphology, *Geological Society of America Bulletin*, *56* (3), 275.

Hovius, N. (1996), Regular spacing of drainage outlets from linear mountain belts, *Basin Research*, *8*(1), 29–44.

Hovius, N., C. Stark, and P. Allen (1997), Sediment flux from a mountain belt derived by landslide mapping, *Geology*, *25*(3), 231.

Howard, A. (1980), Thresholds in river regimes, *Thresholds in geomorphology*, pp. 227–258.

Howard, A. (1994), A detachment-limited model of drainage basin evolution, *Water resources research*, *30*(7), 2261–2286.

Howard, A., and G. Kerby (1983), Channel changes in badlands, *Geological Society of America Bulletin*, *94*(6), 739.

Howard, A., W. Dietrich, and M. Seidl (1994), Modeling fluvial erosion on regional to continental scales, *Journal of Geophysical Research*, *99*(B7), 13,971–13,986.

Hudson, J. (1980), Overall properties of a cracked solid, in *Mathematical Proceedings of the Cambridge Philosophical Society*, vol. 88, pp. 371–384, Cambridge University Press.

Hudson, J. (1981), Wave speeds and attenuation of elastic waves in material containing cracks, *Geophysical Journal of the Royal Astronomical Society*, *64*(1), 133–150.

Hurtrez, J., F. Lucazeau, J. Lavé, and J. Avouac (1999), Investigation of the relationships between basin morphology, tectonic uplift, and denudation from the study of an active fold belt in the Siwalik Hills, central Nepal, *Journal of Geophysical Research*, *104*(B6), 12,779.

Hwang, C., and S. Wu (1992), Global and local remeshing algorithms for compressible flows, *Journal of Computational Physics*, *102*(1), 98–113.

Jadamec, M., D. Turcotte, and P. Howell (2007), Analytic models for orogenic collapse, *Tectonophysics*, *435*(1-4), 1–12.

Jean, S., C. Kerckhove, J. Perriaux, and C. Ravenne (1985), Un modèle paléogène de bassin à turbidites: les grès d'Annot du NW du massif de l'Argentera–Mercantour, *Geól, Alpine*, *61*, 115–143.

Jolivet, R., R. Cattin, N. Chamot-Rooke, C. Lasserre, and G. Peltzer (2008), Thin-plate modeling of interseismic deformation and asymmetry across the Altyn Tagh fault zone, *Geophysical Research Letters*, *35*(2), L02,309.

Joseph, P., and S. Lomas (2004), Deep-water sedimentation in the Alpine Foreland Basin of SE France: New perspectives on the Gres d'Annot and related systems-an introduction, *Deep-water sedimentation in the Alpine basin of SE France: new perspetives on the Grès d'Annot and related systems*, p. 1.

Kachanov, M. (1980), Continuum model of medium with cracks, *Journal of the Engineering Mechanics Division*, *106*(5), 1039–1051.

Kachanov, M. (1992), Effective elastic properties of cracked solids: critical review of some basic concepts, *Applied Mechanics Reviews*, *45*, 304.

Karato, S.-I. (2008), *Deformation of earth materials: an introduction to the rheology of solid earth*, Cambridge University Press.

Karner, G., and A. Watts (1983), Gravity anomalies and flexure of the lithosphere at mountain ranges, *Journal of Geophysical Research*, *88*(B12), 10,449–10,477.

Katz, O., Z. Reches, and J. Roegiers (2000), Evaluation of mechanical rock properties using a Schmidt Hammer, *International Journal of Rock Mechanics and Mining Sciences*, *37*(4), 723–728.

Kaus, C., B.J.P. Steedman, and T. Becker (2008), From passive continental margin to mountain belt: insights from analytical and numerical models and application to Taiwan, *Physics of the Earth and Planetary Interiors*, *171*, 235–251.

Kemeny, J., and N. Cook (1986), Effective moduli, non-linear deformation and strength of a cracked elastic solid, *23*(2), 107–118.

Kerckhove, C. (1969), La “zone du Flysch” dans les nappes de l’Embrunais (Alpes Occidentales), *Geól, Alpine*, *45*, 5–204.

Kirby, S., and A. Kronenberg (1987), Rheology of the lithosphere: selected topics, *Reviews of Geophysics*, *25*(6), 1219–1244.

Krešl, M., V. Vaňková, and A. Janáčková (1978), Radioactivity and heat production data from several boreholes in the Bohemian Massif, *Studia Geophysica et Geodaetica*, *22*(2), 165–176.

Kurfeß, D., and O. Heidbach (2009), CASQUS: A new simulation tool for coupled 3D finite element modeling of tectonic and surface processes based on ABAQUS (TM) and CASCADE, *Computers & Geosciences*, *35*(10), 1959–1967.

Labaume, P., J. Ritz, and H. Philip (1989), Failles normales récentes dans les Alpes sud-occidentales: leurs relations avec la tectonique compressive, *Comptes rendus de l’Académie des sciences. Série 2, Mécanique, Physique, Chimie, Sciences de l’univers, Sciences de la Terre*, *308*(17), 1553–1560.

Labaume, P., M. Jolivet, F. Souquiere, and A. Chauvet (2008a), Tectonic control on diagenesis in a foreland basin: combined petrologic and thermochronologic approaches in the Grès d’Annot basin (Late Eocene–Early Oligocene, French–Italian external Alps), *Terra Nova*, *20*(2), 95–101.

Labaume, P., et al. (2008b), Contrôle tectonique de la diagenése d’une formation turbiditique d’avant chaîne, exemple des gré d’Annot, Alpes externes franco-italiennes.

Labrousse, L., G. Hetényi, H. Raimbourg, L. Jolivet, and T. Andersen (2010), Initiation of crustal-scale thrusts triggered by metamorphic reactions at depth: Insights from a comparison between the Himalayas and Scandinavian Caledonides, *Tectonics*, *29*(5).

Lague, D., and P. Davy (2003), Estimating uplift rate and erodibility from the area-slope relationship: examples from Brittany (France) and numerical modelling, *Physics and Chemistry of the Earth*, *25*(6–7), 543–548.

Lague, D., N. Hovius, and P. Davy (2005), Discharge, discharge variability, and the bedrock channel profile, *Journal of Geophysical Research*, *110*(F4), F04,006.

Lamb, M., W. Dietrich, and L. Sklar (2008), A model for fluvial bedrock incision by impacting suspended and bed load sediment, *Journal of Geophysical Research F*, *113*(F3), F03,025.

Lambeck, K., and R. Stephenson (1985), Post-orogenic evolution of a mountain range: South-Eastern Australian Highlands, *Geophysical Research Letters*, *12*(12), 801–804.

Lavé, J. (2005), Analytic solution of the mean elevation of a watershed dominated by fluvial incision and hillslope landslides, *Geophysical Research Letters*, *32*(11), L11,403.

Lavé, J., and J. Avouac (2001), Fluvial incision and tectonic uplift across the Himalayas of central Nepal, *Journal of Geophysical Research*, *106*(B11), 26,561.

Leech, M. (2001), Arrested orogenic development: eclogitization, delamination, and tectonic collapse, *Earth and Planetary Science Letters*, *185*(1-2), 149–159.

Leopold, L., and T. Maddock (1953), The hydraulic geometry of stream channels and some physiographic implications, Professional Paper 252, *US Geological Survey, Washington, DC.*

Lin, A., A. Watts, and S. Hesselbo (2003), Cenozoic stratigraphy and subsidence history of the South China Sea margin in the Taiwan region, *Basin Research*, *15*(4), 453–478.

Liu, T. (1982), Tectonic implication of fission track ages from the Central Range, Taiwan, in *Proc. Geol. Soc. China*, vol. 25, pp. 22–37.

Loevenbruck, A., R. Cattin, X. Le Pichon, M. Courty, and S. Yu (2001), Seismic cycle in Taiwan derived from GPS measurements, *Comptes Rendus de l'Académie des Sciences-Series IIA-Earth and Planetary Science*, *333*(1), 57–64.

Lyon-Caen, H., and P. Molnar (1985), Gravity anomalies, flexure of the Indian plate, and the structure, support and evolution of the Himalaya and Ganga basin, *Tectonics*, *4*(6), 513–538.

McCarroll, D. (1991), The Schmidt hammer, weathering and rock surface roughness, *Earth Surface Processes and Landforms*, *16*(5), 477–480.

McKean, J., W. Dietrich, R. Finkel, J. Southon, and M. Caffee (1993), Quantification of soil production and downslope creep rates from cosmogenic 10Be accumulations on a hillslope profile, *Geology*, *21*(4), 343.

Menke, W. (1989), *Geophysical data analysis: discrete inverse theory*, Academic Press.

Molnar, P., and P. England (1990), Late Cenozoic uplift of mountain ranges and global climate change: chicken or egg?, *Nature*, *346*(6279), 29–34.

Molnar, P., R. Anderson, G. Kier, and J. Rose (2006), Relationships among probability distributions of stream discharges in floods, climate, bed load transport, and river incision, *Journal of Geophysical Research*, *111*(F2), F02,001.

Molnar, P., R. Anderson, and S. Anderson (2007), Tectonics, fracturing of rock, and erosion, *Journal of Geophysical Research*, *112*(F3), F03,014.

Momber, A. (2003), Cavitation damage to geomaterials in a flowing system, *Journal of Materials Science*, *38*(4), 747–757.

Montgomery, D., and K. Gran (2001a), Downstream Variations in the Width of Bedrock Channels, *Water Resources Research*, *37*(6), 1841–1846.

Montgomery, D., and K. Gran (2001b), Downstream Variations in the Width of Bedrock Channels, *Water Resources Research*, *37*(6), 1841–1846.

Niedzielski, T., P. Migoń, and A. Agnieszka Placek (2009), A minimum sample size required from Schmidt hammer measurements, *Earth Surface Processes and Landforms*, *34*(13), 1713–1725.

O'Connell, R., and B. Budiansky (1974), Seismic velocities in dry and saturated cracked solids, *Journal of Geophysical Research*, *79*(35), 5412–5426.

O'Rourke, J. (1989), Rock index properties for geoengineering in underground development, *Mining Engineering*, pp. 106–110.

Pazzaglia, F., and M. Brandon (1996), Macrogeomorphic evolution of the post-Triassic Appalachian mountains determined by deconvolution of the offshore basin sedimentary record, *Basin Research*, *8*(3), 255–278.

Pedersen, H., and B. Hasholt (1995), Influence of wind speed on rainsplash erosion, *Catena*, *24*(1), 39–54.

Pelletier, J. (2004), Persistent drainage migration in a numerical landscape evolution model, *Geophysical Research Letters*, *31*(20), L20,501.

Pelletier, J. (2008), *Quantitative modeling of earth surface processes*, Cambridge University Press.

Pelletier, J. (2010), Minimizing the grid-resolution dependence of flow-routing algorithms for geomorphic applications, *Geomorphology*.

Perron, J., W. Dietrich, and J. Kirchner (2008), Controls on the spacing of first-order valleys, *Journal of Geophysical Research*, *113*(F4), F04,016.

Perron, J., J. Kirchner, and W. Dietrich (2009), Formation of evenly spaced ridges and valleys, *Nature*, *460*(7254), 502–505.

Pinet, C., and C. Jaupart (1987), The vertical distribution of radiogenic heat production in the Precambrian crust of Norway and Sweden: geothermal implications, *Geophysical Research Letters*, *14*(3), 260–263.

Pinet, P., and M. Souriau (1988), Continental erosion and large-scale relief, *Tectonics*, *7*(3), 563–582.

Press, W., B. Flannery, S. Teukolsky, W. Vetterling, et al. (2007), *Numerical recipes*, Cambridge University Press.

Ravenne, C., R. Vially, P. Riche, and P. Tremolieres (1987), Sédimentation et tectonique dans le bassin marin Eocène supérieur-Oligocène des Alpes du Sud= Sedimentation and tectonics in the Upper Eocene-Oligocene marine basin in the southern Alps, *Revue de l'Institut français du pétrole*, *42*(5), 529–553.

Raymo, M., and W. Ruddiman (1992), Tectonic forcing of late Cenozoic climate, *Nature*, *359*(6391), 117–122.

Raymo, M., W. Ruddiman, and P. Froelich (1988), Influence of late Cenozoic mountain building on ocean geochemical cycles, *Geology*, *16*(7), 649.

Reiners, P., T. Ehlers, S. Mitchell, and D. Montgomery (2003), Coupled spatial variations in precipitation and long-term erosion rates across the Washington Cascades, *Nature*, *426*(6967), 645–647.

Renard, F., J. Gratier, and B. Jamtveit (2000), Kinetics of crack-sealing, intergranular pressure solution, and compaction around active faults, *Journal of Structural Geology*, *22*(10), 1395–1407.

Renka, R. (1997), Algorithm 751: TRIPACK: Constrained two-dimensional Delaunay Triangulation Package, *ACM Transactions on Mathematical Software (TOMS)*, *22*, 1–8.

Renshaw, C. (1996), Influence of subcritical fracture growth on the connectivity of fracture networks, *Water Resources Research*, *32*(6), 1519–1530.

Rey, P., O. Vanderhaeghe, and C. Teyssier (2001), Gravitational collapse of the continental crust: definition, regimes and modes, *Tectonophysics*, *342*(3-4), 435–449.

Rigon, R., I. Rodriguez-Iturbe, A. Maritan, A. Giacometti, D. Tarboton, and A. Rinaldo (1996), On Hack's law, *Water Resources Research*, *32*(11), 3367–3374.

Rispoli, R. (1981), Stress fields about strike-slip faults inferred from stylolites and tension gashes, *Tectonophysics*, *75*(3-4), T29–T36.

Roe, G. (2005), Orographic Precipitation, *Annual Review of Earth and Planetary Sciences*, *33*, 645–671.

Roe, G., D. Montgomery, and B. Hallet (2003), Orographic precipitation and the relief of mountain ranges, *Journal of Geophysical Research*, *108*(B6), 2315.

Roering, J., J. Kirchner, and W. Dietrich (1999), Evidence for nonlinear, diffusive sediment transport on hillslopes and implications for landscape morphology, *Water Resources Research*, *35*(3), 853–870.

Rotonda, T. (2001), Applications of dynamic techniques to concrete lining of tunnels, in *Rock mechanics:a challenge for society: proceedings of the ISRM Regional Symposium Eurock 2001, Espoo, Finland.*

Royden, L. (1993), The tectonic expression slab pull at continental convergent boundaries, *Tectonics*, *12*(2), 303–325.

Ruddiman, W., and J. Kutzbach (1989), Forcing of late Cenozoic Northern Hemisphere climate by plateau uplift in southern Asia and the American West, *Journal of Geophysical Research*, *94*(D15), 18,409.

Ruddiman, W., M. Raymo, H. Lamb, and J. Andrews (1988), Northern Hemisphere Climate Regimes During the Past 3 Ma: Possible Tectonic Connections [and Discussion], *Philosophical Transactions of the Royal Society of London. Series B, Biological Sciences*, *318*(1191), 411–430.

Rutter, E., and D. Elliott (1976), The Kinetics of Rock Deformation by Pressure Solution, *Philosophical Transactions for the Royal Society of London. Series A, Mathematical and Physical Sciences*, *283*(1312), 203–219.

Sachpazis, C. (1990), Correlating Schmidt hardness with compressive strength and Young's modulus of carbonate rocks, *Bulletin of Engineering Geology and the Environment*, *42*(1), 75–83.

Sayers, C., and M. Kachanov (1995), Microcrack-induced elastic wave anisotropy of brittle rocks, *Journal of Geophysical Research*, *100*(B3), 4149–4156.

Schlische, R., S. Young, R. Ackermann, and A. Gupta (1996), Geometry and scaling relations of a population of very small rift-related normal faults, *Geology*, *24*(8), 683.

Schmidt, E. (1951), Experiments with the new concrete test hammer, *Schweizer Archive.*

Schoenberg, M. (1980), Elastic wave behavior across linear slip interfaces, *The Journal of the Acoustical Society of America*, *68*, 1516.

Scholz, C. (1990), *The mechanics of earthquakes and faulting*, Cambridge University Press.

Scholz, C., and P. Cowie (1990), Determination of total strain from faulting using slip measurements, *Nature*, *346*, 837–839.

Schultz, R. (2003), A method to relate initial elastic stress to fault population strains, *Geophysical Research Letters*, *30*(11), 1593.

Schumm, S. (1967), Rates of surficial rock creep on hillslopes in western Colorado, *Science*, *155*(3762), 560.

Segall, P., and D. Pollard (1980), Mechanics of discontinuous faults, *Journal of Geophysical Research*, *85*(B8), 4337–4350.

Seidl, M., and W. Dietrich (1992), The Problem of Channel Erosion into Bedrock, *Catena Supplement*, *23*, 101–124.

Séranne, M., A. Benedicto, P. Labaum, C. Truffert, and G. Pascal (1995), Structural style and evolution of the Gulf of Lion Oligo-Miocene rifting: role of the Pyrenean orogeny, *Marine and Petroleum Geology*, *12*(8), 809–816.

Shieh, S., S. Wang, M. Cheng, T. Yeh, and T. Chiou (2000), Users' Guide for Typhoon Forecasting in the Taiwan Area (VIII), *Central Weather Bureau, Taipei.*

Shorey, P., D. Barat, M. Das, K. Mukherjee, and B. Signh (1984), Schmidt hammer rebound data for estimation of large scale in situ coal strength, *International Journal of Rock Mechanics and Mining Sciences Geomechanical Abstracts*, *21*, 39–42.

Sibson, R. (1992), Implications of fault-valve behaviour for rupture nucleation and recurrence, *Tectonophysics*, *211*(1-4), 283–293.

Simoes, M., and J. Avouac (2006), Investigating the kinematics of mountain building in Taiwan from the spatiotemporal evolution of the foreland basin and western foothills, *Journal of Geophysical Research*, *111*(B10), B10,401.

Simoes, M., J. Avouac, O. Beyssac, B. Goffé, K. Farley, and Y. Chen (2007), Mountain building in Taiwan: A thermokinematic model, *Journal of Geophysical Research*, *112*(B11), B11,405.

Singh, R., F. Hassani, and P. Elkington (1983), The application of strength and deformation index testing to the stability assessment of coal measures excavations, in *The 24th US Symposium on Rock Mechanics (USRMS).*

Sklar, L., and W. Dietrich (1998), River longitudinal profiles and bedrock incision models: Stream power and the influence of sediment supply, *Rivers over rock: fluvial processes in bedrock channels, in Geophysical monograph*, *107*, 237–260.

Sklar, L., and W. Dietrich (2001), Sediment and rock strength controls on river incision into bedrock, *Geology*, *29*(12), 1087.

Sklar, L., and W. Dietrich (2004), A mechanistic model for river incision into bedrock by saltating bed load, *Water Resources Research*, *40*(6), W06,301.

Sklar, L., and W. Dietrich (2006), The role of sediment in controlling steady-state bedrock channel slope: Implications of the saltation-abrasion incision model, *Geomorphology*, *82*(1-2), 58–83.

Smolarkiewicz, P. (1983), A simple positive definite advection scheme with small implicit diffusion, *Monthly Weather Review*, *111*, 479–486.

Snyder, N., K. Whipple, G. Tucker, and D. Merritts (2000), Landscape response to tectonic forcing: Digital elevation model analysis of stream profiles in the Mendocino triple junction region, northern California, *Geological Society of America Bulletin*, *112*(8), 1250.

Snyder, N., K. Whipple, G. Tucker, and D. Merritts (2003), Channel response to tectonic forcing: field analysis of stream morphology and hydrology in the Mendocino triple junction region, northern California, *Geomorphology*, *53*(1-2), 97–127.

Soliva, R., F. Maerten, J. Petit, and V. Auzias (2010), Field evidences for the role of static friction on fracture orientation in extensional relays along strike-slip faults: Comparison with photoelasticity and 3-D numerical modeling, *Journal of Structural Geology.*

Steer, P., R. Cattin, J. Lavé, and V. Godard (), Surface Lagrangian Remeshing: a new tool for studying long term evolution of continental lithosphere from 2D numerical modelling, *Computers & Geosciences*, in press.

Stock, J., and D. Montgomery (1999), Geologic constraints on bedrock river incision using the stream power law, *Journal of Geophysical Research. B*, *104*, 4983–4993.

Stolar, D., G. Roe, and S. Willett (2007), Controls on the patterns of topography and erosion rate in a critical orogen, *Journal of Geophysical Research*, *112*(F4), F04,002.

Summerfield, M., and N. Hulton (1994), Natural controls of fluvial denudation rates in major world drainage basins, *Journal of Geophysical Research*, *99*(B7), 13,871–13,883.

Sumner, P., and W. Nel (2002), The effect of rock moisture on Schmidt hammer rebound: tests on rock samples from Marion Island and South Africa, *Earth Surface Processes and Landforms*, *27*(10), 1137–1142.

Suppe, J. (1981), Mechanics of mountain building and metamorphism in Taiwan, *Mem. Geol. Soc. China*, *4*, 67–89.

Taha, M. (1986), *Apport de la microtectonique cassante aux problèmes des trajectoires de contraintes et de leurs perturbations: exemple du nord de Montpellier*, Thèse d'Etat, Université de Montpellier.

Thieulot, C., P. Fullsack, and J. Braun (2008), Adaptive octree-based finite element analysis of two-and three-dimensional indentation problems, *Journal of Geophysical Research*, *113*(B12), B12,207.

Thuro, K. (1997), Drillability prediction: geological influences in hard rock drill and blast tunnelling, *International Journal of Earth Sciences*, *86*(2), 426–438.

Tsenn, M., and N. Carter (1987), Upper limits of power law creep of rocks, *Tectonophysics*, *136*(1-2), 1–26.

Tucker, G., and D. Bradley (2010), Trouble with diffusion: Reassessing hillslope erosion laws with a particle-based model, *J. Geophys. Res*, *115*.

Tucker, G., and R. Slingerland (1996), Predicting sediment flux from fold and thrust belts, *Basin Research*, *8*(3), 329–349.

Tucker, G., and K. Whipple (2002), Topographic outcomes predicted by stream erosion models: Sensitivity analysis and intermodel comparison, *Journal of Geophysical Research*, *107*(B9), 2179.

Tucker, G., S. Lancaster, N. Gasparini, and R. Bras (2001a), The channel-hillslope integrated landscape development model (CHILD), *Landscape Erosion and Evolution Modeling*, pp. 349–388.

Tucker, G., S. Lancaster, N. Gasparini, R. Bras, and S. M. Rybarczyk (2001b), An object-oriented framework for distributed hydrologic and geomorphic modeling using triangulated irregular networks, *Computer & Geosciences*, *27*, 959–973.

Tugrul, A., and I. Zarif (1999), Correlation of mineralogical and textural characteristics with engineering properties of selected granitic rocks from Turkey, *Engineering Geology*, *51*, 303–317.

Turcotte, D., and L. Greene (1993), A scale-invariant approach to flood-frequency analysis, *Stochastic Hydrology and Hydraulics*, *7*(1), 33–40.

Turcotte, D., and G. Schubert (2002), *Geodynamics*, Cambridge University Press.

Turowski, J., D. Lague, and N. Hovius (2007), Cover effect in bedrock abrasion: A new derivation and its implications for the modeling of bedrock channel morphology, *Journal of Geophysical Research*, *112*(F4), F04,006.

Underwood, P. (1983), Dynamic relaxation, *Computational methods for transient analysis*, *1*, 245–265.

Viles, H., A. Goudie, S. Grab, and J. Lalley (), The use of the Schmidt Hammer and Equotip for rock hardness assessment in geomorphology and heritage science: a comparative analysis, *Earth Surface Processes and Landforms.*

Walsh, J. (1965), The effect of cracks on the compressibility of rocks, *Journal of Geophysical Research*, *70*, 381–389.

Watts, A., S. Lamb, J. Fairhead, and J. Dewey (1995), Lithospheric flexure and bending of the Central Andes, *Earth and Planetary Science Letters*, *134*(1-2), 9–21.

West, A. (2008), Geomorphology: Mountains and monsoons, *Nature Geoscience*, *1*(12), 814–815.

Whipple, K., and G. Tucker (1999), Dynamics of the stream-power river incision model: Implications for height limits of mountain ranges, landscape response timescales, and research needs, *Journal of Geophysical Research*, *104*(B8), 17,661.

Whipple, K., and G. Tucker (2002), Implications of sediment-flux-dependent river incision models for landscape evolution, *Journal of Geophysical Research*, *107*(B2), 2039.

Whipple, K., G. Hancock, and R. Anderson (2000), River incision into bedrock: Mechanics and relative efficacy of plucking, abrasion, and cavitation, *Bulletin of the Geological Society of America*, *112*(3), 490.

Willenbring, J., and F. von Blanckenburg (2010), Long-term stability of global erosion rates and weathering during late-Cenozoic cooling, *Nature*, *465*(7295), 211–214.

Willett, S. (1999), Orogeny and orography: The effects of erosion on the structure of mountain belts, *Journal of Geophysical Research*, *104*(B12), 28,957.

Willett, S. (2010), Erosion on a line, *Tectonophysics*, *484*(1-4), 168–180.

Willett, S., and M. Brandon (2002), On steady states in mountain belts, *Geology*, *30*(2), 175–178.

Willett, S., R. Slingerland, and N. Hovius (2001), Uplift, shortening, and steady state topography in active mountain belts, *American journal of Science*, *301*(4-5), 455.

Willgoose, G., R. Bras, and I. Rodriguez-Iturbe (1991), A coupled channel network growth and hillslope evolution model 1. Theory, *Water Resources Research*, *27*(7), 1671–1684.

Woollard, G. (1969), Regional Variations in Gravity, *The Earth's crust and upper mantle: structure, dynamic processes, and their relation to deep-seated geological phenomena*, p. 320.

Xu, S., P. Grasso, and A. Mahtab (1990), Use of Schmidt hammer for estimating mechanical properties of weak rock, in *6th International IAEG Congress*, pp. 511–519.

Yagiz, S. (2009), Predicting uniaxial compressive strength, modulus of elasticity and index properties of rocks using the Schmidt hammer, *Bulletin of Engineering Geology and the Environment*, *68*(1), 55–63.

Yamato, P., P. Agard, E. Burov, L. Le Pourhiet, L. Jolivet, and C. Tiberi (2007), Burial and exhumation in a subduction wedge: Mutual constraints from thermomechanical modeling and natural PTt data (Schistes Lustrés, western Alps), *Journal of Geophysical Research*, *112*(B7), B07,410.

Yanites, B., G. Tucker, K. Mueller, Y. Chen, T. Wilcox, S. Huang, and K. Shi (2010), Incision and channel morphology across active structures along the Peikang River, central Taiwan: Implications for the importance of channel width, *Bulletin of the Geological Society of America*, *122*(7-8), 1192.

Yaşar, E., and Y. Erdoğan (2004), Estimation of rock physiomechanical properties using hardness methods, *Engineering Geology*, *71*, 281–288.

YIlmaz, I., and H. Sendr (2002), Correlation of Schmidt hardness with unconfined compressive strength and Young's modulus in gypsum from Sivas (Turkey), *Engineering Geology*, *66*(3-4), 211–219.

Yu, S., H. Chen, and L. Kuo (1997), Velocity field of GPS stations in the Taiwan area, *Tectonophysics*, *274* (1-3), 41–59.

Zienkiewicz, O., R. Taylor, and R. Taylor (2005), *The finite element method for solid and structural mechanics*, Elsevier Butterworth-Heinemann.

Acknowledgments

Je remercie tout d'abord Rodolphe et Jérôme pour avoir accepté d'encadrer cette thèse.

Rodolphe, j'ai particulièrement apprécié la confiance et la liberté que tu m'as accordé quand à mon travail, tout en assurant une présence pédagogique et un suivit scientifique rassurant et efficace. Tu as toujours été présent lorsque j'avais besoin d'un avis ou d'un coup de main. Et par dessus tout, tu m'as sortis de la grisaille parisienne pour m'emmener "dans tes bagages" à la mer!

Jérôme, merci pour la rigueur et la minutie avec laquelle tu as appréhendé mon travail. J'en avais vraiment besoin, et je suis sûr que cela me sera utile pour le reste de ma carrière.

Je tiens à remercier Jean Braun, Sébastien Carretier, Greg Tucker et Hermann Zeyen pour avoir accepté de juger ma thèse, et je dois bien avouer que je suis heureux de vous compter dans mon jury.

Merci aussi à mes encadrants officieux. Vincent, grâce à toi j'ai connu les joies de la modélisation en 2D (je t'avoue que j'ai joué comme un enfant à construire et à détruire ces jolis paysages!). Merci aussi de m'avoir fais venir à Santa Barbara (ca c'est la classe! Au passage merci à Amandine pour ses cookies made in US!). Gyuri (dit le Yeti d'après Rodolphe) tu as vraiment été efficace lors de nos interactions scientifique, d'ailleurs au passage il va bien falloir qu'on s'y remette sur ces histoires de métamorphisme. Merci aussi pour ton amitié et ton soutient ainsi qu'à Anna. Un petit bémol quand même, Zurich à part l'entrée du labo ca fait moins classe que Santa Barbara! Roger, je ne te connaissais pas avant de venir dans le Sud, et j'avoue que tu as été pour beaucoup dans la réussite de cette thèse. Merci et j'espère qu'on aura encore l'occasion de travailler ensemble (ca a été efficace non? ;)). Un merci aussi à Martine pour cette virée scientifico-gastronomique à Taiwan, j'en garde plein de chouettes souvenirs... heuh je voulais dire plein d'idées à publier (quand est ce qu'on y retourne?).

Un merci particulier à Dimitri, pour avoir été le premier à m'initier à la géomorphologie. Ce stage de licence a vraiment été un déclic! Merci aussi pour avoir déplacé ta playstation à 100000 euros pour numériser l'Hérault, et pour avoir supporté les odeurs de station d'épuration à St Clément!

Je remercie aussi tout les (enseignants-) chercheurs, ingénieurs, techniciens et secrétaires de GM pour m'avoir accueilli comme si j'avais toujours été un des leurs. Merci notamment à Didier (Monsieur Presse), Benoit à qui j'ai physiquement cassé les rotules, à Jean (Monsieur ADELI), à Christel (qui a elle aussi profitée des bagages de Rodolphe), à Pierre pour les coups de mains sur la presse, à l'autre Pierre pour nous avoir lancé sur Annot, à Stéphane pour ses belles manips, à Jeff et Alfredo pour la visite de l'Hérault et à Serge (pour avoir signé ma paperasse universitaire sans

broncher!). Je n'oublie pas pour autant mon laboratoire d'origine, et donc un grand merci à tout les gens de l'ENS pour la recherche mais aussi pour m'avoir formé. Un merci particulier à Christian (il faut bien commencer par le chef!), à Nicolas (le chef en second), à Luce, Marie-Pierre, Julia, Jérôme le strasbourgeois, Yves, Fabrice, Olivier (pour Taiwan, et pour ces parties de foot endiablées), Alex (pour le cocktail offert au sommet du Marriott), Nath (Mr Bio), Françoise, Lina, Laurent B du CEA, et tout ceux que j'ai probablement oublié. Merci aussi aux laboratoires de géologie de l'ETHZ, de Santa Barbara et de Nancy pour leur accueil. Merci aussi à Clément l'homme aux dudunes pour ces bières offertes à l'AGU (ca t'avais fais rire cette histoire de vieille moules bretonnes!) . Merci à tout les moniteurs du Palais de la Découverte à Monica, Manue, Arnaud et Olivier pour leur sympathie et pour m'avoir appris la pédagogie par la pratique.

Bon passons aux choses sérieuses. Merci à mes ex co-bureaux (attention la liste est longue), à Alex (non on aura jamais de bébé ensemble ;)), à Nadaya pour ca gentillesse, à Pauline Miss GRS (bon alors on les couple nos modèles? PS: c'est pas indécent comme proposition!), à Pierrot l'homme du sud qui voit des TEMpêêêêttttes partout (bon faudra quand même travailler ton pointé), à Nono qui fais du bruit sans faire de bruits (je crois que j'ai pompé sur les remerciements de Gyuri, à vérifier!) et qui m'a si souvent accueilli dans son bureau (et alors on y retourne aux Ecrins?). Nico, mon compagnon de pauses café, de foot déjantés, et de virées cyclotouritsiques dont mes rotules se souviendront toujours. Il y a aussi mes co-bureaux d'adoption du 4eme Mag et Tom (et Cooky ou Rose, au choix), avec qui on aura fait un bon bout de chemin. Tom qui est le seul à faire des blagues plus nulles que les miennes (tu m'as sauvé la face plus d'une fois! Merci vieux), et Mag (Mougoulou d'après certains) qui est la seule à pouvoir nous supporter (ou pas)! (bon maintenant tu peux avouer que c'était toi le géoinfo du 1er avril! ;)) .

Merci aussi à tout les thésards footeux que j'ai cotoyé, à l'ENS: Corentin (l'indécrotable), S. Bernard (l'imbougeable), Jérôme C. (le meilleur), Damien et Julien (qui aurait du venir jouer avec nous), à l'IPG: Julien le Rock, Alex le plus fort en rêve, Yoann l'homme qui passe à la télé, et à toute la team. Merci aussi à ceux de Montpel (de loin les meilleurs ;)): Théo (mon nouveau frêre, bonne chance avec Rodolphe!), Flo (bon alors Paris?) et Titou les inséparables au foot comme à la grimpe (vous me manquez les mecs!), à Bruno l'homme qui à appris à jouer en Patagonie (tu m'emmènes alors?), à Lyde le nouveau nancéen et ex-stephanois, et tant qu'on y est à Fab le taiwano-lillois, Mathieu (samba!) et Lara, Rémi, Camille Mr BBQ et Thibault l'Annotien. Et enfin merci au jorkygirls Marie Violette et Neness pour ces supers moments de détentes.

Merci aussi au moins-sportifs, à Aurélie et Marie (les princesses de la promo, on va se boire un petit vers d'Ouzo?), à Mathieu le philosophe des sciences, à Vince, Mickael kael, Kate et Roberto qui représentent le côté obscur de la force, Tom Jacob et Sabrina les larzacois, Yaroub, Nico le régateur de l'extrême (alors ces amibes?), et Greg le talonneur le plus intelligent de la Terre, et Clémence ma soeur de thèse (du coup je t'ai pas mis du côté obscur de la force). Merci aux anciens de promo, à Fab (quand est ce qu'on monte ce fameux cabinet de géomorpho?), J-B, Pierrot. Merci à Aurélien pour son super coup de main à St Clem.

Je remercie aussi les amis: Gilouze et Ludoï, les potes de toujours, Quentin et Olga les néo-toulousaings (on se fait un petit WE?), à Suzanne la future ma-

man belge une fois (ou plus? ;)), les tentanusiens Manus et Manux, Jack Daniel l'australien, Olivier notre oiseau préféré, la p'tite Marina, Célestine la ch'tite voisine, Clara la femme des îles, Mathilde et Nico les tandémistes à carriole bien remplie.

Merci à Steph ma petite chinoise pour ton amour et tes encouragements.

Je dédis cette thèse à toute ma famille, mes parents, mon clone, mes soeurs, mes cousins et cousines, oncles, tantes, et grands parents pour le soutient que vous m'avez apporté et pour m'avoir toujours incité à poursuivre mes études.